Regional Flood Models and Digital Elevation Model (DEM) Uncertainty

By

Laurence Paul Hawker

A thesis submitted to the University of Bristol in accordance with the requirements for award of the degree of Doctor of Philosophy in the Faculty of Science

School of Geographical Sciences

December 2018

Word Count 69,746

For Saori

Abstract

Flooding is a natural hazard that affects millions of people throughout the world every year. Hydrodynamic models are a key tool in delineating current and future flood hazard, and provide a key resource for decision makers to reduce flood risk. However, hydrodynamic models need data to drive them, with many parts of the world not having high-quality data at a high-resolution. These areas are considered data-sparse. Data-scarcity is partially characterised by a lack of high-resolution (<30m) topographic data, with this elevation data previously shown to be a key control on the propagation of a flood. Therefore, hydrodynamic models at the intermediate scale (270-1000m) are needed to estimate flood hazard given the lack of high-resolution data, computational resources and a Monte Carlo approach to estimate uncertainties in predictions. This thesis presents three results chapters assessing the ability of an intermediate scale hydrodynamic model to estimate flooding in a large river delta, before going on to establish the effects of uncertain topographic information of flood predictions and connectivity between river channels and floodplains. In the first chapter, an intermediate scale hydrodynamic model of the Mekong Delta is built, with results showing that a model at this scale has a good level of skill and thus a similar approach could be used to estimate flooding in other data-sparse river deltas. However, it is shown that uncertainty in topography from the global digital elevation models (DEMs) had a large influence on flood predictions. This finding inspired the subsequent chapters. Chapter 2 characterised the spatial error structure of floodplains in two global DEMs, and used these relationships to simulate plausible versions of the DEM. By using DEM ensembles, probabilistic flood hazard maps could be produced, with these maps avoiding the spurious precision compared to flood maps that use a single deterministic DEM. Chapter 3 further explored the influence of DEMs by developing a novel method to quantify river-floodplain connectivity across scales and DEM products. Results demonstrated that the DEM product had more influence on river-floodplain connectivity than scale, with the quantification of river-floodplain connectivity shown to be a useful indicator of the appropriateness of a DEM to be used in a hydrodynamic model. This thesis has subsequently enhanced our understanding of the skill of hydrodynamic models at the intermediate scale to model flooding in large data-sparse river deltas, as well as improving our understanding of the impact uncertain topography has on flood predictions by promoting the treatment of topography as a probabilistic entity as opposed to a deterministic one as it currently is.

Acknowledgements

There are so many people who have believed in me and who I would like to thank for making this thesis possible.

First and foremost, I would like to thank my supervisors Paul and Jeff. I could not have wished for any better mentors and I feel incredibly fortunate to have had you both to guide me through the thesis process. You both gave me energy and enthusiasm and I am especially grateful for the free rein you gave me to pursue interesting research avenues. So thank you for all those hours of your time you gave me and for giving me the opportunity in the first place.

This PhD was made possible through the WISE programme, so I would like to thank those who made it possible – Thorsten, Ross, Dragan and Tom to name but a few. The main benefit of WISE was the fantastic group of people I went through the process with. That first year in Exeter was not without its hiccups but the group around me pushed me through and I can confidently say I have made friends for life. So thank you Barney, Ludo, Wouter, Olivia, Ioanna, Mariano, James, Josh, Josie, Nejc, Jonathan, Dave and Elli!

I would also like to thank all the people who collaborated with me and provided support and guidance. In particular, a special thank you must be extended to Jonty Rougier for whom I am eternally grateful for opening up my eyes to the power of geostatistics. Also thank you to Niall Quinn, Fiachra O'Loughlin, Matt Lewis, Matti Kummu and Dai Yamazaki who helped me through the formative stages and those annoying coding questions. Another I would like to thank Yasuto Tachikawa and his great lab in Kyoto for hosting me on 2 occasions. This really opened my eyes to other research environments and taught me a lot. I would also like to extend a huge thank you to Steve Darby for taking a huge punt and letting me join him on fieldwork in the Mekong Delta. All the time and logistics you went through to get me there for little gain on your part was incredible. Just goes to show that if you don't ask you don't get!

I must also thank the Browns community, in particular Sav, Marius, Soso, Ali, Tom, Leanne and Jeison for making day-to-day PhD life so enjoyable.

I cannot forget to mention the mighty Athletico Geography and everyone involved. It's strange to think that I would look forward to a cold, wet, winter night so much, but the people I shared the pitch with make it so special. I'm sure everyone will not thank me for the countless emails I have sent out in my time as management! A genuine highlight of my PhD has to be the glorious evening of the 24th October when we finally clinched the league title after 6 long years. So a particular thank you to Jon, Jamie, Alex and Tom for making those special memories.

My family have shown support throughout my PhD. It's always been a challenge to explain to my Grandma what a PhD is.

And last but by no means least – Saori. At the beginning of the PhD we were 6,000 miles apart but now we are together. You have been so strong, supportive and loving throughout the PhD. This thesis is for you

Author's Declaration

I declare that the work in this dissertation was carried out in accordance with the requirements of the University's Regulations and Code of Practice for Research Degree Programmes and that it has not been submitted for any other academic award. Except where indicated by specific reference in the text, the work is the candidate's own work. Work done in collaboration with, or with the assistance of, others, is indicated as such. Any views expressed in the dissertation are those of the author.

SIGNED: …….. DATE: …….

Table of Contents

List of Tables

List of Figures

Chapter 1 Introduction

1.1 Background

Floods are a major natural hazard that cause widespread damage to land, property, the economy and humanity. Indeed, there does not seem to be a week that goes by without a report of a devastating flood in some part of the world. In the past two decades alone, UNISDR (2015) estimated that flooding has affected 2.3 billion people, resulting in 157,000 deaths. Deaths from flooding occur predominantly in lower-income countries, whilst economic damages are dominated by a small number of events in higher-income countries, with estimated flood damages in 2016 alone totaling $56 billion (MunichRE, 2016). Flooding in the future is expected to increase in severity and frequency due to a warming climate (Hirabayashi et al., 2013, Kundzewicz et al., 2014, Arnell and Gosling, 2016, Arnell et al., 2018, Dottori et al., 2018, Winsemius et al., 2015), with several studies already demonstrating that recent flood events have been exacerbated by climate change (Schaller et al., 2016, Pall et al., 2011). Moreover, the cumulative cost of frequent events ('nuisance' floods) may exceed the cost of extreme events which societies usually prepare for (Moftakhari et al., 2017a) Coupled with an increased severity and frequency of the hazard, there is an increase in exposure to flooding as world population increases and humans continue to build in more at-risk areas due to land pressures and marginalization (Douglas et al., 2008, Donner and Rodriguez, 2008). The ability to effectively predict flooding is crucial for planning and management to limit the risk from flooding both in the current day and in the future.

Hydrodynamic models have proved to be the key tool in delineating current and future flood hazard, providing crucial information to help manage flood risk (Wing et al., 2018, Sampson et al., 2015, Dung et al., 2011, Apel et al., 2009, Bates and De Roo, 2000, Zanobetti et al., 1970, Hrodadka and Yen, 1986, Ward et al., 2013b). These hydrodynamic models are physically-based computational models that are based on the theory of fluid dynamics

and have been shown to effectively delineate flooding from coastal, fluvial and pluvial sources. To implement hydrodynamic models, information is needed on how much water is going into the catchment/river, how it is routed through the catchment and the topography of the floodplain for when water flows out of bank of the river. Even in this age where information is so readily available, especially with the proliferation of remote sensing, there is still a chronic lack of high-quality data to use within hydrodynamic models. High quality data is typically found in more developed countries which suffer more damages but less casualties than developing countries (MunichRE, 2016). Therefore, in a great deal of the world, lower quality globally available data are used in flood models. These areas can be considered to be data-sparse.

By their very nature, hydrodynamic models are an approximation of reality and even with the highest quality data will always be incorrect to some degree (Beven et al., 2011). The challenge in data-sparse areas is obtaining an acceptable level of flood prediction with the available data. To this end, intermediate scale models are often used in data-sparse areas owing to a lack of data to drive a finer resolution, more detailed model and a limitation in computational resources. For this thesis we define intermediate scale flood models as those with a resolution between 270m to 1km as set out in Table 1-1. Resolutions of 270 m to 1 km are chosen for an intermediate scale as the random vertical error of the most commonly used source of topography (Shuttle Radar Topography Mission; SRTM) has a random height error of approximately 6m (Rodriguez et al., 2006), resulting in a random height error of approximately 2 m for 270 m or 0.6 m at 1 km. These values are suitably appropriate for a flood model as the random error becomes smaller than typical flood wave amplitudes (4-6m) but retains a suitable level of detail that valley shapes and some floodplain topographic features such as relic channels and oxbows can be resolved (Wilson et al., 2007, Neal et al., 2012a). For example, Wilson et al. (2007) justify a model resolution of 270 m as the random height error is less than the flood pulse of the Amazon (~10 m) and the vertical scale of the key controlling floodplain morphologic features (channels, levees, scroll bars of ~3-5 m). Indeed, hydrodynamic model resolution can substantially alter computational runtime, with Savage et al. (2016b) finding that halving the model resolution increases the computational runtime by an order of magnitude. Therefore, a balance needs to be struck for appropriate

complexity given the available computational resources and data and the application the hydrodynamic model results are intended for.

Table 1-1 Definition of hydrodynamic model scale and associated resolution

Scale	Domain Size	Grid Size (m)	Topographic Data Source	Channel Representation	Floodplain Features	Example Studies
Hyper	Building	<5	Terrestrial LiDAR; LiDAR; Airborne Photogrammetry	2D; 3D	Buildings; Rills	Chen et al. (2012)
	Reach	1 – 30	LiDAR; Airborne Photogrammetry; TanDEM-X	1D; 2D	Roads; Levees; Ditches	Neal et al. (2011)
High	Catchment	30 – 270	LiDAR; ASTER; MERIT; TanDEM-X; SRTM	1D; 2D	Channels; Levees; Scroll bars	Wood et al. (2016)
Intermediate	Regional	270 – 1000	ASTER; MERIT; SRTM	1D; 2D	Larger Channels and Levees	Neal et al. (2012a)
Coarse	Global	>1000	ASTER; MERIT; SRTM; GMTED2010	1D	Large Depressions	Alfieri et al. (2014)

ASTER = Advanced Spaceborne Thermal Emission and Refection Radiometer; GMTED2010 = Global Multi-Resolution Terrain Elevation Data 2010; LiDAR – Light Detection and Ranging, airborne unless stated otherwise; MERIT = Multi Error Removed Improved Terrain; SRTM = Shuttle Radar Topography Mission

Data-sparsity is partly characterised by a lack of hyper scale (<30 m) topographic data. Topography is a key control on the propagation of a flood (Horritt and Bates, 2002). For a flood to occur, the river must connect to a floodplain. The ability of a DEM to accurately capture river-floodplain connectivity is therefore crucial to accurately predict flooding. Yet the ability of global DEMs to depict river-floodplain connectivity can be weak, with Trigg et al. (2012) finding that SRTM omitted 96% of river-floodplain channels that were pivotal in the flood dynamics.

Hydrodynamic models use topographic information from a gridded dataset of topographic heights called a digital elevation model (DEM). Despite being almost 2 decades old, the SRTM (Shuttle Radar Topography Mission) DEM remains the most popular choice of topographic information for flood inundation models when high resolution LIDAR (Light Detection and Ranging) is unavailable. Nevertheless, SRTM is characterised by an estimated ~6m vertical error (Rodriguez et al., 2006), with errors stemming from vegetation (Shortridge and Messina, 2011, Carabajal and Harding, 2006, Hofton et al., 2006), steep relief (Falorni et al., 2005), an inability to resolve features in urban areas (Gamba et al., 2002) proximity to metallic objects (Becek, 2008), speckle noise (Rodriguez et al., 2006, Farr et al., 2007) and striping caused by instrument setup (Walker et al., 2007). Error removal has tended to focus on hydrological correction (Jarvis et al., 2008) and vegetation removal (Baugh et al., 2013, O'Loughlin et al., 2016b, Zhao et al., 2018).The recent release of the Multi-Error-Removed-Improved-Terrain (MERIT) DEM (Yamazaki et al., 2017) saw the most comprehensive error removal from SRTM, with notable improvements over SRTM reported particularly in flat areas. Despite calls for a concerted effort to produce a more accurate free global DEM (Schumann et al., 2014), there is little sign that such a dataset will be produced soon. Therefore, a flood modeller has 3 choices to improve the topographic information in their model: 1) Obtain high-accuracy LIDAR data (expensive and/or unavailable); 2) Use an error reduced version of SRTM (e.g. MERIT) or manually edit the DEM (time-consuming); 3) Simulate plausible versions of a global DEM based on spatial error characteristics. This last idea is well-known in the field or geostatistics (Goovaerts, 1997, Holmes et al., 2000, Kydriakidis et al., 1999) but has only been applied in a single fluvial flood study (Wilson and Atkinson, 2005).

A number of intermediate scale hydrodynamic models (270 m-1 km) have been run across the world with examples from the Amazon (270 m) (Baugh et al., 2013, Wilson et al., 2007), Damador (270 m) (Sanyal et al., 2013), Ob (1 km) (Biancamaria et al., 2009), Oti (480-960 m) (Komi et al., 2017), Niger (905 m) (Neal et al., 2012a) and Zambezi (1 km) (Schumann et al., 2013) rivers. An inherent problem with these models has been the poor quality of topographic information, with the models using Shuttle Radar Topography Mission (SRTM) Digital Elevation Model (DEM) data which has a vertical error of ~6m (Rodriguez et al,

2006). Furthermore, examples of intermediate scale models are not always found in areas of high flood risk, with large river deltas typically neglected due to the challenging nature of modeling in these areas primarily because of the incredible flatness of the delta and the uncertainties involved with flow splitting at bifurcations.

Yet, large-scale river deltas form some of the most flood prone areas in the world, with this widely expected to increase (Syvitski et al., 2009, Hallegatte et al., 2013). These areas are among the most productive and economically important ecosystems in the world, acting as a home for an estimated 600 million people, and a nexus of agriculture and trade (Day et al., 2016, Passalacqua, 2017). The most populous of these deltas are mostly located in Asia, which has seen a distinct recent shift to urbanisation in deltas (Seto, 2011). Yet, Asia also bears the brunt of the majority of floods (UNISDR, 2015).

Even though flooding in deltas is widely recognised as a major challenge (Ericson et al., 2006, Syvitski et al., 2009, Tessler et al., 2015), hydrodynamic models focused on large river deltas are scarce. Studies exist in developed countries, such as in the Rhine Delta (Klerk et al., 2015), but in developing countries studies are mostly focussed on the Mekong Delta and the Ganges-Brahmaputra (Karim and Mimura, 2008, Lewis et al., 2013, Ikeuchi et al., 2017) . Data-sparse deltas can be modelled with intermediate (270m-1km) or coarse scale models (>1km) based on open-data but these have been found to perform poorly in such locations (Trigg et al., 2016). Yet, these types of models are important as they do not rely on detailed data so can be applied to data-sparse regions, and are computationally efficient such that Monte Carlo methods can be applied.

Therefore, there is a clear need for intermediate scale flood models that can effectively utilise the limited data available and have an appropriate computation time that allows for Monte Carlo simulations. By applying an intermediate scale hydrodynamic model to large river deltas we can improve our understanding of the flood hazard in these at-risk areas. Owing to the incredibly flat terrain of a delta, topography is very likely to be a key control on uncertainty. To date, the effects of DEM uncertainty on hydrodynamic models have been limited with most studies investigating resolution effects but with access to high resolution DEMs which are not available in data-sparse areas (Horritt and Bates, 2001a, Sanders, 2007,

Neal et al., 2009b, Fewtrell et al., 2011). In data-sparse areas, modellers are thus limited to global DEMs and typically just use a single layer of topography. The impact of varying other hydrodynamic model inputs stochastically have been investigated in hydrodynamic models in data-sparse areas (Wechsler, 2007), but not for topography owing to the lack of datasets. A significant step forward in understanding the implications of topographic uncertainty of flood inundation would be to simulate plausible versions of global DEMs at native resolution so an ensemble of DEMs can be used in a stochastic simulation. Additionally, the ability of a DEM to accurately depict river-floodplain connectivity is a key control in flooding and is inherently related to uncertainties in DEMs. To date, the ability to quantify river-floodplain connectivity has been extremely difficult, so it would be useful to quantify river-floodplain connectivity and assess the ability of a range of DEM products to depict river-floodplain connectivity. This thesis aims to fill these research gaps by first building an intermediate scale hydrodynamic model of a data-sparse delta, before progressing to investigate the impact of DEM uncertainty through stochastic simulation of DEMs and quantifying river-floodplain connectivity amongst various DEM products at various resolutions.

1.2 Research Aims and Objectives

The main aim of this thesis was to further our understanding of how uncertainty in topography impacts flood inundation predictions in data-sparse environments, and specifically deltas. A pre-cursor to fulfil this aim is to build an intermediate scale hydrodynamic model of a large river delta that has a lack of data to distinguish how much of a control topography has on flood inundation prediction. To enhance our understanding of how uncertain topography affects flood inundation predictions, this thesis aims to use geostatistics to characterize the spatial error structure of global DEMs in floodplains and stochastically simulate plausible versions of global DEMs so an ensemble of DEMs can be used in flood studies even in data-sparse locations. This thesis will further assess and quantify river-floodplain connectivity of DEMs to ascertain the ability of DEMs across resolutions to portray river-floodplain connectivity. Overall, this thesis will enhance our understanding of how to build intermediate scale hydrodynamic models in data-sparse

deltas and improve our knowledge of the impacts of DEM uncertainty on flood predictions, as well as providing a tool to simulate plausible versions of global DEMs.

To achieve these aims the following objectives and questions will be addressed:

Objective 1: Determine whether an intermediate hydrodynamic model at a regional scale can accurately represent flooding in a data-sparse delta

- Can an intermediate scale hydrodynamic model be built for a data-sparse delta using freely available data that accurately represents flooding?
- What aspects of the flood model structure and data are most important for inundation prediction?

Objective 2: Assess the implications of simulating global DEMs for flood inundation studies

- What is the spatial error structure of the MERIT and SRTM DEMs in floodplains, and how does the spatial error structure vary between landcover types?
- How can plausible versions of MERIT and SRTM DEMs be simulated?
- What is the impact of using an ensemble of simulated DEMs to estimate flood extent compared to a deterministic prediction?

Objective 3: Identify and quantify river-floodplain connectivity of DEMs across resolutions

- Can river-floodplain connectivity be quantified?
- How does river-floodplain connectivity differ across DEM products and resolutions?
- Is the accurate representation of river-floodplain connectivity more important for smaller flood events?

The aims, objectives and research questions identified above will be explored within three results chapters. Work contained within these chapters has so far been published in 1

paper in an international peer-reviewed journal, with a freely available R Package created to disseminate the work (https://github.com/laurencehawker/DEMsimulation).

Results Chapter 1: An intermediate Scale Hydrodynamic Model of the Mekong Delta built using freely available data. In the first results chapter an intermediate scale hydrodynamic model of the Mekong Delta is built using freely available data. Analysis of what level of complexity is needed is carried out by varying the level of detail of channel width, depth and friction parameters. Following this an assessment of how different DEMs affect flood inundation prediction is carried out.

Results Chapter 2: Implications of Simulating Global Digital Elevation Models for Flood Inundation Studies. The second results chapter simulates plausible versions of the Shuttle Radar Topography Mission (SRTM) and Multi-Error-Removed-Improved-Terrain (MERIT) DEMs and assesses the impact of using an ensemble of DEMs on flood inundation prediction. The spatial error structure of SRTM and MERIT in 20 floodplain locations around the world are calculated, with these error relationships used with geostatistical techniques to implement simulation of statistically plausible DEMs. Flood models utilizing DEM ensembles are run for 2 locations with flood probability maps produced for each location. From this chapter a package in the R language was created whereby a user can simulate versions of SRTM or MERIT in floodplain locations.

Results Chapter 3: Measuring Floodplain Connectivity of DEMs. The final results chapter uses connected component analysis and patch statistics to quantify river-floodplain connectivity. A range of DEM products and scales are assessed to determine the ability of a DEM to represent river-floodplain connectivity. Moreover, river-floodplain connectivity is assessed for various water height scenarios to assess how the magnitude of the flood impacts river-floodplain connectivity. The developed technique is a rapid way to assess the ability of a DEM to be able to depict river-floodplain connectivity.

1.3 Thesis Structure

Following this introduction, Chapter 2 provides a general review of the literature concerning flooding and hydrodynamic models. More specific literature is then found within each

results chapter. Chapter 3 briefly describes the hydrodynamic model used in the thesis. Chapters 4-6 contain the three results sections. A synthesis of the key findings and the conclusions of the thesis are outlined in Chapter 7, followed by a bibliography in Chapter 8.

1.4 Peer Reviewed Work

Material in this thesis has been presented in peer-reviewed journals and at academic conferences. All of which are my own work and are detailed below.

1.4.1 Peer-Reviewed Publications (Published, In Review and In Preparation)

- Hawker, L., Rougier, J., Neal, J. C., Bates, P. D., Archer, L., & Yamazaki, D. (2018). Implications of Simulating Global Digital Elevation Models for Flood Inundation Studies. *Water Resources Research.* 54. https://doi.org/10.1029/2018WR023279
- Hawker, L., Bates, P. D., Neal, J. C., & Rougier, J. (2018). Perspectives on Digital Elevation Model (DEM) Simulation for Flood Modeling in the Absence of a High-Accuracy Open Access Global DEM. *Frontiers in Earth Sciences*. 6:233. doi: 10.3389/feart.2018.00233
- Hawker, L., Bates, P. D., & Neal, J. C. (n.d.). Flood Modelling in data-sparse deltas – the case of the Mekong Delta. *Hydrological Processes* (*In Preparation)*.
- Hawker, L., Bates, P. D., & Neal, J. C. (n.d.). Measuring Floodplain Connectivity of DEMs. *In Preparation*.

1.4.2 Conference Presentations

- Hawker, L., Rougier, J., Neal, J. C., Bates, P. D. & Yamazaki, D. (2018). Simulating DEMs for flood models. Global Flood Partnership, Delft, Netherlands: Poster Presentation.
- Hawker, L., Rougier, J., Neal, J. C., & Bates, P. D. (2018a). Simulating candidate DEMs for flood inundation studies. European Geophysical Union, Vienna, Austria: Poster Presentation.

- Hawker, L., Rougier, J., Neal, J. C., & Bates, P. D. (2018b). Analysing semi-variograms for floodplains to generate candidates of the true DEM for flood inundation studies. European Geophysical Union, Vienna, Austria: Oral Presentation.
- Hawker, L., Rougier, J., Neal, J. C., & Bates, P. D. (2017). Assessing uncertainty in SRTM elevations for global flood modelling. American Geophysical Union, New Orleans, LA: Oral Presentation.
- Hawker, L., Bates, P. D., & Neal, J. C. (2017a). An intermediate scale flood inundation model of the Mekong Delta. UK Young Coastal Scientists: Oral Presentation.
- Hawker, L., Bates, P. D., & Neal, J. C. (2017b). Flood inundation Modeling in Data Sparse Deltas. European Geophysical Union, Vienna, Austria: Poster Presentation.
- Hawker, L., Bates, P. D., & Neal, J. C. (2017c). How significant is irrigation for flood inundation Modelling in deltas? Community Surface Dynamics Modelling System Annual Meeting, Boulder, CO: Poster Presentation.
- Hawker, L., Bates, P. D., & Neal, J. C. (2017d). Including irrigation in flood inundation Modelling – An initial exploration of the Mekong Delta. Poster. Japanese Geophysical Union, Chiba, Japan: Poster Presentation.
- Hawker, L., Bates, P. D., & Neal, J. C. (2017e). Flood inundation modelling in data sparse deltas – The case of the Mekong Delta. International Conference Flood Management: Poster Presentation.
- Hawker, L., Bates, P. D., & Neal, J. C. (2016). Modelling floodplain inundation of the Mekong Delta using a regional hydrodynamic model with a view to future scenarios. Japanese Geophysical Union, Chiba, Japan: Oral Presentation.

Chapter 2 Scientific Background

2.1 Introduction to Flooding

"Floods are 'acts of God,' but flood losses are largely acts of man."

Gilbert White (1945)

A flood is defined as the condition where river discharge exceeds bankfull limitations. In normal conditions rivers flow in well-defined channels, but at instances of extreme discharges, banks are overtopped and floodplains become inundated. This type of flooding is called fluvial flooding and is the type of flooding considered in this thesis. Other common types of flooding include pluvial flooding, which is caused by intense rainfall in urban areas that runs off the impervious surfaces, and coastal flooding, which is caused by coastal water inundated land through high tides and storm surges. Less common types of flooding are dam-break floods, groundwater flooding ice-jam floods and glacial outburst floods. Drivers of floods include heavy rainfall and/or storm surges. Often two or more extreme events can occur simultaneously or successfully to create so-called compound events (Wahl et al., 2015, Leonard et al., 2014). The definitions of the key components of a flood are outlined in Table 2-1.

Table 2-1 Definitions of the key components of a Flood

Component	Definition
Annual Flood	Maximum daily flow during a year
Bankfull Discharge	Discharge at which a river channel is full to capacity.
Flood Event	A series of flows that comprise of a progressive rise, culminating in a peak and then receding to a normal flow

Flood Extent	The areal extent of flood water on a floodplain
Flood Peak	Highest elevation reached by the flood waters during a flood event
Flood Stage	Elevation of the Water Surface
Return Period	Statistical occurrence of a flood of a particular magnitude at a location. E.g. A return period of 50 years means on *average* a flood of that magnitude occurs once every 50 years.

The aforementioned discussion of floods refers to the physical component of a flood, or in other words the flood hazard. A flood becomes damaging when assets and/or people become exposed, in what is commonly termed as exposure. The ability of the exposed to anticipate, cope with and resist the impact of the hazard is termed the vulnerability and is related to a complex nexus of political-institutional, economic and socio-cultural factors. These 3 factors combine to form flood risk which is defined as the probability that a flood of a given magnitude and given loss will occur within a given time span and is related in the following equation:

$$Flood\ Risk = Flood\ Hazard\ x\ Exposure\ x\ Vulnerability \quad (1)$$

Flooding is one of the most significant causes of economic losses and fatalities amongst natural hazards, with the number of loss events increasing (Figure 2-1). The seriousness of flooding should not be understated. In the past 2 decades, UNISDR (2015) estimate that a staggering 2.3 billion people have been affected by flooding, resulting in 157,000 fatalities. The greatest economic losses are generally found in higher-income countries where a relatively small number of large events can cause substantial damages. For example, in 2017 the hurricane trio of Harvey, Irma and Maria caused an estimated US$220 billion in damages out of the $US340 billion in total damages for all natural catastrophes for that year (MunichRE, 2018). Yet these events largely overshadowed the devastating floods in South Asia which caused an estimated 2,700 fatalities (MunichRE, 2018). In 2016 alone, flooding caused an estimated $56 billion worth of damage (MunichRE, 2016). Societies choose what

risk level to protect against with the notion of acceptable risk. Of course no risk is acceptable but is a combination of the costs and benefits (Kaplan and Garrick, 1981).

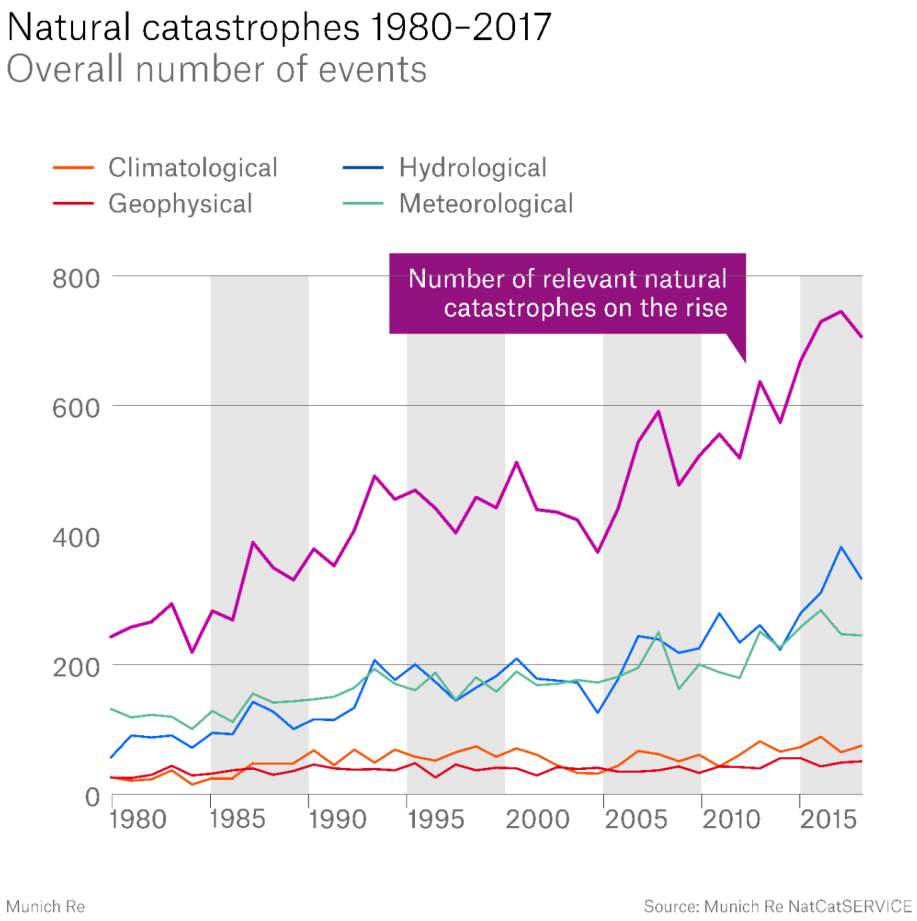

Figure 2-1 Loss Events Worldwide 1980-2017 from MunichRE (2018). Note the increasing number of hydrological (e.g. flooding) and meteorological hazards

Flood risk is expected to increase in the future for several reasons. The flood hazard is expected to increase in magnitude and frequency due to a warming climate (Hirabayashi et al., 2013, Dottori et al., 2018, Kundzewicz et al., 2014, Winsemius et al., 2015, Arnell et al., 2018, Arnell and Gosling, 2016). Furthermore, exposure to flooding is expected to increase as world population continues to increase, prompting humans to build in more at-risk areas due to land pressures and marginalization (Donner and Rodriguez, 2008, Douglas et al., 2008, Jongman et al., 2012). Thirdly, those that are most vulnerable to flooding are predicted to become disproportionally more affected by flooding in the future (Sayers et al., 2018). These factors have led authors to predict increased damages and fatalities from flooding in

the future (Hirabayashi et al., 2013, Dottori et al., 2018, Sayers et al., 2018, Winsemius et al., 2015, Wing et al., 2018, Alfieri et al., 2017), with Alfieri et al. (2017) for example reporting that even for an optimistic warming scenario of 1.5°C there will be more than a doubling of global flood risk compared to 1976-2005. Therefore, there is a clear need to effectively predict flooding to plan and manage the risk from flooding both in the current day and the future.

Hydrodynamic models have been a key tool to delineate current and future flood hazard (Wing et al., 2018, Sampson et al., 2015, Teng et al., 2017). They have been used in numerous flood-related applications including flood risk mapping (Wing et al., 2017), flood damage assessment (Merz et al., 2010), real-time flood forecasting (Barthélémy et al., 2018), flood related engineering (Gallegos et al., 2009) and water resource planning (Hanington et al., 2017). Yet by their very nature, hydrodynamic models are an approximation of reality and will always be incorrect even if the highest quality data is used (Beven et al., 2011). However, most parts of the world do not have hyper (<5m) or even high-resolution data (1-30m) data or a dense network of hydrologic measurements to drive hydrodynamic models, so model results are subject to substantial uncertainties. Furthermore, even state of the art hydrodynamic models can take a long amount of time for computation, especially at high resolutions meaning that even if high quality data is available a tradeoff needs to be made between model resolution and runtime. To be able to explore the many uncertainties in their predictions, modellers need to run hydrodynamic models multiple times which often results in models being run at a coarser resolution than the scale of the best available data. One key input into a hydrodynamic model is information on topography from a digital elevation model which has been found to be a key control on predicted flood extent (Horritt and Bates, 2002).

This chapter will outline the scientific background of how floods are modelled, before selecting a flood model and justifying why its selection was appropriate. It should be noted that each results chapter contain a considerable amount of scientific background that pertains to the topic of that chapter. For instance, results chapter 1 contains scientific background of large river deltas, threats to large river deltas, as well as a background of the Mekong Delta. Results Chapter 2 contains an overview of DEMs, their uncertainties and the geoscientists behind DEM simulation. Finally, results Chapter 3 contains the scientific

background of river-floodplain connectivity. This structure was selected to aid the reader in each chapter, creating a more modular document.

2.2 Modelling Flood Inundation

To effectively plan and manage flood risk, it is useful to predict which areas are at greatest threat to the flood hazard. The most common way to simulate and predict the flood hazard is to use a hydrodynamic model (Bates and De Roo, 2000, Neal et al., 2012a, Sampson et al., 2015). Hydrodynamic models can be operated at a range of scales and complexities, incorporating one, two or even three spatial dimensions. Outputs of hydrodynamic models are temporally distributed and give the water depth, velocity and areal extent. To this end, this section will give an overview of hydrodynamic models as well as other methods to evaluate flooding, before proceeding to justifying the choice behind the hydrodynamic model used for this thesis.

2.2.1 Hydrodynamic Models

A hydrodynamic model is computer code that simulates the movement of water using computational fluid dynamics theory. Another term for a hydrodynamic model is a hydraulic model which is also frequently used in the literature. Hydrodynamic models are applied to simulate fluvial, pluvial and coastal flooding. In fluvial applications, water is routed along a river channel, and when the river channel overtops the water is then routed onto the floodplain (Bates and De Roo, 2000). In pluvial applications, water is routed through typically urban areas and is driven by water originating from rainfall (Sampson et al., 2013) or point sources such as manholes (Leandro et al., 2009). In coastal applications, water from tidal oscillations or storm surges are routed up river channels or when water overtops coastal defenses (Bates et al., 2005b). Outputs of these hydrodynamic models are a map of the spatial extent of flood inundation along a time series which are in turn used by flood risk managers and planners to inform planning and risk mitigation strategies.

The main controls on a flood wave is the balance between gravitational forcing and friction (Bates, 2012), therefore topography and friction parameters are key in controlling flood predictions. Although water flows in 3 dimensions, in hydrodynamic models the

representation of flow can be either in one (1D), two (2D) or three (3D) dimensions, with 1D models being the least complex and 3D models being the most complex and computationally demanding. A modeler must make a tradeoff between available data, computational resources available and expertise. Bates and De Roo (2000) nicely sum up the choice of model complexity when they note that "the best model will be the simplest one that provides the information required by the user whilst reasonably fitting the available data".

Table 2-2 Types of Hydrodynamic Models. Adapted from Pender and Neelz (2007)

Type	Description	Computation Time	Software Example
0D	No physical laws included in simulations	Seconds	ArcGIS
1D	Solution of 1D Saint-Venant equations	Minutes	HEC-RAS; MIKE 11
1D+	1D plus flood storage cell for floodplain flow	Minutes to Hours	HEC-RAS; MIKE 11
1D/2D	1D for river channel flow and 2D for floodplain flow	Minutes to Hours	LISFLOOD-FP; MIKE FLOOD; SOBEK; TUFLOW
2D	Solution of 2D shallow water equation	Hours to Days	CaMa-Flood; LISFLOOD-FP; MIKE 21 TELEMAC 2D
2D+	2D plus a solution for vertical velocities using continuity only	Days	TELEMAC 3D
3D	Solution of 3D Navier Stokes Equations	Days	Delft 3D

2.2.2 Flow in Hydrodynamic models

In hydrodynamic models, water flow is calculated by mathematical equations known as the shallow water equations (SWEs). The SWEs are a set of equations derived from the Navier-Stokes equations that in turn are derived from Newton's second law of motion. These

equations are used in a variety of applications in computational fluid dynamics such as climate modeling and aerodynamics. Different SWEs are applied to calculate flow depending if the flow is steady (uniform) or unsteady.

2.2.2.1 Steady Flow in Open Channels

Steady flow requires the properties of flow (e.g. water depth and velocity) within an open channel to be unvarying in time (Chaudhry, 2007). Uniform flow is similar as it is characterized by a constant mean velocity and constant water depth along the direction of flow for a given length of channel (Brandimarte, 2012). For steady/uniform flow to occur, the discharge, bed slope and Manning's roughness must be constant. Steady and uniform flows are represented using either the Chezy or Manning's equations. The Chezy equation calculates the mean velocity by multiplying the square root of hydraulic radius R and slope S with a coefficient known as the Chezy coefficient C that relates channel roughness with hydraulic radius.

$$V = C\sqrt{RC} \tag{2}$$

Similarly, Manning's equation relates mean velocity to Manning's roughness coefficient n, the hydraulic radius R and the bed slope.

$$V = \frac{1}{n} R^{\frac{2}{3}} S^{\frac{1}{2}} \tag{3}$$

To calculate discharge Q, these equations can be combined with cross sectional area of a channel A.

$$V = AV = A\frac{1}{n} R^{\frac{2}{3}} S^{\frac{1}{2}} \tag{4}$$

However, the complexity of nature often makes the assumptions for these steady flow equations too simplistic and thus hydrodynamic models tend to instead represent flow with equations describing unsteady flow.

2.2.2.2 Unsteady Flow in Open Channels

Flows within natural systems are inherently unsteady as the conditions of flow very in time and are non-uniform in space as velocity and depth varies. To describe unsteady flows, the Navier-Stokes equations describe flow through continuity (conservation of mass) and momentum (conservation of energy). Based on several assumptions (e.g. fixed channel boundaries), the Navier-Stokes equations can be simplified to what are known as the Saint-Venant Equations. The simplest spatial representation of flow in hydrodynamic models is in 1D and involves solving the 1D Saint Venant equations, or a simplification of these, which are in the following form:

$$Continuity = \frac{\delta A}{\delta x} + \frac{\delta Q}{\delta x} = 0 \tag{5}$$

$$Momentum = \underbrace{\frac{\delta Q}{\delta t}}_{Accleration} + \underbrace{\frac{\delta}{\delta x}\left[\frac{Q^2}{A}\right]}_{Advection} + \underbrace{\frac{gA\delta(h+z)}{\delta x}}_{Water\ Slope} + \underbrace{\frac{gn^2Q^2}{R^{\frac{4}{3}}A}}_{Friction\ Slope} = 0 \tag{6}$$

Where A is the cross-sectional area of the channel, x is the distance in the x Cartesian direction and Q is the discharge. In the momentum equation, the additional terms are z (bed elevation), R (hydraulic radius), g (acceleration due to gravity) and n (Manning's coefficient of Friction). The degrees of complexity can be split into the following 4 categories: Kinematic, Diffusive, Inertial and Fully Dynamic. Kinematic models are the simplest and only contain the friction slope term. Diffusive models contain the friction slope and water slope. Inertial models contain the friction slope, water slope and local acceleration term. Finally, a fully dynamic model contains all the terms. In its 2D formulation, the Saint-Venant have the extra dimension y and are computationally more expensive to solve. Flows can also be solved in 3D but this is often deemed unnecessarily complex (Bates and De Roo, 2000). However, in situations when vertical turbulence, vortices and spiral flows are important (e.g. levee breaches, dam breaks), 3D models may be necessary. These equations have no analytical solution but can be solved using numerical techniques. Developers have varied the degree of complexity by removing some components within the full Saint-Venant momentum equations.

2.2.2.3 Types of Numerical Solvers

SWEs are solved differently depending on how the equations are discretized in time and space, with the common distinction between explicit and implicit methods (Popescu, 2012). For explicit methods, St Venant equations are solved for every point within the model domain at a particular time. At the next timestep, information from the previous timestep is taken to solve the St Venant equations again at every point. The model follows this pattern until completion. However, if the timestep is too large, instabilities can occur, allowing water to traverse through a cell in a timestep. Conversely, if the timestep is too small, the model runtime will be prohibitively long. To obtain a suitable timestep to avoid instabilities, the Courant Friedrichs Lewy (CFL) equation can be used and can be written as:

$$\frac{tc}{x} < 1 \tag{7}$$

Where t is the timestep, c is the velocity of the flood wave and x is the spatial resolution. Setting a CFL threshold very close to 1 runs the risk of instabilities arising, so modellers typically set the CFL threshold slightly below 1. In the CFL equation the timestep is related to spatial resolution, and subsequently scales. In other words, the smaller the spatial resolution, the smaller the distance the flood wave can travel before traversing two grid cells (which causes instabilities), thus the timestep must reduce to insure this does not occur. Therefore, in hyper and high-resolution models, the timestep becomes very small.

Implicit methods use information from both the previous and current timestep to perform calculations. As a result, implicit methods are always stable and thus do not require the CFL equation. However, implicit methods come at a cost that they are complex to step-up and the computation time is substantially larger per timestep compared to explicit methods (Popescu, 2012). If the timestep is too long however, the accuracy of the solution can degrade.

Whilst implicit and explicit methods describe how SWEs are solved in time, methods are needed to specify how they are solved in space. Two common methods to describe how these equations are solved in space are to use either finite difference or finite volume

approaches (Hervouet, 2007, Di Baldassarre, 2012a). In finite difference methods, calculations are made at multiple points in the model domain based on how the points relation to nearby points. The finite volume approach builds on this with cells having volumes, with the associated value of a cell assigned to the centre of each cell. Finite element is similar to finite volume difference in that the model domain is split up into a number of elements, with the drawback that the mathematical methods to produce solutions are computationally expensive (Néelz and Pender, 2013). Finite volume, finite element and finite difference can be used in unstructured grids (e.g. TELEMAC, Galland et al. (1991)) allowing cells in a model to vary in size which is particularly useful in areas of complex topography where cell size can be decreased in areas of complex topographies but increased in less complex topography. Using structured grids is substantially computationally cheaper than running unstructured grids (Horritt and Bates, 2001a). Furthermore, many input datasets (e.g. Digital Elevation Models) are available in structured grids, making setting up models based on finite difference methods less complex.

2.2.3 Data Requirements for Hydrodynamic Models

In essence, hydrodynamic models describe how water flows through a landscape. Therefore, the principle data requirements for hydrodynamic models are data describing the topography of the landscape, how much water is flowing in and out of the model, and the friction acting against the flow of water. Additionally, some hydrodynamic models may require data on channel geometry and other factors such as infiltration. The more complex the hydrodynamic model the more data is required, with general data requirements and outputs by hydrodynamic model type outlined in Table 2-3. Therefore, even if a more complex hydrodynamic is available, a modeler could be restricted by data availability. On the contrary, a modeler may have a wealth of data but has a lack of experience or the computational time required for simulations.

Table 2-3 Input and output data by type of hydrodynamic model. Adapted from Di Baldassarre (2012a)

Type	Input Data	Output

0D	DEM; Upstream water level; Downstream water level	Inundation extent and water depth
1D	Surveyed cross sections of channel and floodplain; Upstream discharge hydrographs; Downstream stage hydrographs	Water Depth & average velocity at each cross section; Inundation extent by intersecting predicted water depths with DEM; Downstream outflow hydrograph
1D+	As 1D models	As 1D Models
1D/2D	DEM; Upstream discharge hydrographs; Downstream stage hydrographs	Inundation Extent; Water Depths; Downstream outflow hydrographs
2D	DEM; Upstream discharge hydrographs; Downstream stage hydrographs	Inundation Extent; Water Depths; Downstream outflow hydrographs; Depth averaged velocities at each computational node
2D+	DEM; Upstream discharge hydrographs; Downstream stage hydrographs; Inlet velocity distribution	Inundation Extent; Water Depths; Downstream outflow hydrographs; Velocity vector at each computational cell
3D	DEM; Upstream discharge hydrographs; Downstream stage hydrographs; Inlet velocity distribution and turbulent kinetic energy distribution	Inundation Extent; Water Depths; Downstream outflow hydrographs; Velocity vector and kinetic energy at each computational cell

2.2.3.1 Topography

One of the key controls on predicted inundation extent is topography (Bates and De Roo, 2000). Small errors in topography can have an especially large influence on flood predictions due to the low gradients associated with floodplains. The typical topography input into a hydrodynamic model is a gridded representation of elevation called a digital elevation model (DEM). A DEM can be created from ground surveys, digitizing existing hardcopy topographic maps or by remote sensing techniques. DEM's are now predominantly created using remote sensing techniques with Smith and Clark (2005) observing the benefits that a large spatial area can be mapped by fewer people at a lower cost. Remotely sensing techniques include photogrammetry (Coveney and Roberts, 2017, Uysal et al., 2015), airborne and spaceborne Interferometric Synthetic Aperture Radar (InSAR) and Light

Detection And Ranging (LiDAR). Spaceborne DEMs (e.g. Shuttle Radar Topography Mission (SRTM) Farr et al. (2007)) are of high/intermediate scale, whilst photogrammetry and LiDAR derived DEMs are of hyper scale (Table 1-1). Hyper resolution DEMs are rarely available, with approximately 0.005% of the earth's land area having free LiDAR data. Therefore, for the vast majority of the world (and assuming little to no funds are available to acquire a hyper scale DEM), the best source of topographic information is from global DEM's (Table 2-4).

Table 2-4 Global DEM Products

	Dataset	Coverage	Acquisition Years	Sensor	Wavelength	Resolution (m)	Vertical Accuracy	Reference
Free Global DEMs	ALOS AW3D30	82°S - 82°N	2006-2011	Optical	0.52-0.77um	30	4.4m (RMSE)[1]	Tadono et al. (2014)
	ASTER GDEM	83°S - 83°N	2000-2011	Optical	0.78-0.86	30	17m (95% conf.)[2]	Tachikawa et al. (2011a)
	GMTED2010	Entire Earth	Completed 2010	Derived from 11 sources of elevation information		250,500,1000	26m (RMSE)[3]	Danielson and Gesch (2011)
	SRTM	56°S - 60°N	2000	SAR C Band	5.66cm	30,90	6m (MAE)[4]	Farr et al. (2007)
	TanDEM-X 90	Entire Earth	2010-2015	SAR X Band	3.1cm	30,90	Unknown	Rizzoli et al. (2017)
Error Reduced Versions of SRTM	EarthEnv	60°S - 83°N	ASTER & SRTM			90	4.15m (RMSE)[5]	Robinson et al. (2014)
	NASADEM		Expected release late 2018					Crippen et al. (2016)
	MERIT	Entire Earth	AW3D30, SRTM & Viewfinder Panorama			90	5m (LE90)[6]	Yamazaki et al. (2017)
	No Name		Same as SRTM			90	5.9m (RMSE)[7]	O'Loughlin et al. (2016b)
	No Name		Same as SRTM			90	1m reduction in RMSE[8]	Zhao et al. (2018)
	Viewfinder Panorama	Entire Earth	ASTER, SRTM & Other Sources			90	Not Reported	de Ferranti (2014)
Commercial Global DEMs	ALOS AW3D	82°S - 82°N	2006-2011	Optical	0.52-0.77um	5	2.7m (RMSE)[9]	Takaku and Tadono (2017)
	PlanetDEM 30 Plus	Entire Earth	Same as SRTM			30	Not reported	Planet (2017)
	NEXTMap World 10	Entire Earth	Not Reported			10	10m (LE95)[10]	InterMap (2018)
	WorldDEM	Entire Earth	2010-2015	SAR X Band	3.1cm	12	<1.4m (RMSE)[11]	Rizzoli et al. (2017)

N.B. Older Global DEMs ACE GDEM (Berry et al., 2000) and GTOPO30 (Gesch et al., 1999) were not included in the table as these products have been superseded by more recent GDEMs. 1) Tadono et al. (2016) 2) Tachikawa et al. (2011b) 3) Danielson and Gesch (2011)

4) Rodriguez et al. (2006) 5) Robinson et al. (2014) 6) Yamazaki et al. (2017) 7) O'Loughlin et al. (2016b) 8) Zhao et al. (2018) 9) Takaku et al. (2016) 10) InterMap (2018) 11) Wessel et al. (2018)

Despite the recognized importance of topography on flood predictions, uncertainty in flood predictions from uncertain topography has been largely overlooked, with studies typically focusing instead of other hydraulic parameters such as friction (Wechsler, 2007). The reason behind this is twofold. First, there is a perceived lack of DEM products (even though this argument is becoming weaker as evidenced by the number of DEM products outlined in Table 2-4), so flood studies typically take a single DEM and assume this to be the best available source of topographic information. The practice is especially prevalent in data-sparse regions, where a perceived lack of DEM products dictates that only a single DEM is used, with this most commonly being SRTM (Yan et al., 2015b). So, whilst studies may vary other parameters (e.g. friction), they rarely vary DEM products. Secondly, for most locations the best source of topographic information is at 90m so there is limited scope to vary model resolution whilst still obtaining useful results as coarsening the resolution too greatly result in important floodplain topography being 'lost'. Studies that do use multiple DEMs either resample DEMs to a coarser resolution to explore the effect of resampling strategies and/or scale (Horritt and Bates, 2001a, Fewtrell et al., 2011, Neal et al., 2009b, Savage et al., 2016a, Komi et al., 2017, Saksena and Merwade, 2015), or compare flood extents using different DEM products (Li and Wong, 2010, Jarihani et al., 2015, Bhuyian and Kalyanapu, 2018). See Table 2-5 for an overview of studies that have assessed the impact of topographic uncertainty on flood predictions. Usually, the quality of flood predictions increases as DEM resolution increases, but there is often a point where the increase in flood prediction quality increases negligibly and is not worth the additional computational power. For example, Savage et al. (2016b) conclude that models with a resolution finer than 50m offered little gain in flood prediction quality for a hydrodynamic model of the Imera basin, Sicily. Conversely, the same authors also found that flood prediction quality deteriorated markedly at resolutions coarser than 100m. Higher resolution DEMs are more important when modelling urban environments (Fewtrell et al., 2008) so buildings can be captured. On the other hand, too much detail can induce spuriously precise results which does not represent the uncertainties in making flood predictions (Savage et al., 2016b, Dottori et al., 2013).

Table 2-5 Effect of DEM resolution and product on flood inundation predictions

Reference	Location	DEM	Resolutions	Model	Main Finding
Horritt and Bates (2001a)	River Severn	LiDAR	10,20,50,100,250,500,1000	LISFLOOD-FP	Below 100m resolution model performance similar. For one model 250m resolution best
Haile and Rientjes (2005)	Tegucigalpa, Honduras	LiDAR	1.5,4.5,7.5,15	SOBEK	Large differences in predicted flood extent. Variations occur with DEM re-sampling techniques
Wilson and Atkinson (2005)	River Nene, UK	PROFILE Contour DEM, DGPS	30	LISFLOOD-FP	100 versions of DEM were simulated using Sequential Gaussian simulation. Uncertainty in predicted inundation extent greatest where elevation gradients were smallest
Yu and Lane (2006)	Tadcaster, UK	LiDAR	4,8,16,32	JFLOW (Similar)	Small changes in resolution can have considerable effects. Inundation affected by lack of connectivity in coarser resolutions which in part can be compensated with by wetting and roughness parameters
Sanders (2007)	Santa Clara River near Castaic Junction	LiDAR, IfSAR, NED, SRTM	3,10,30,60,90	BreZo (2D)	LiDAR is the best source of terrain data, with its ability to detect bare earth important. NED DEMs flood zones 25% smaller than other DEMs. Little difference predicted in flood predictions between SRTM at 30 and 90m
Fewtrell et al. (2008)	Greenfield, Glasgow	LiDAR	2,4,8,16	LISFLOOD-FP	For urban areas representation of buildings important so finer resolution required. Response of Manning's friction coefficient to model resolution is non-stationary
Li and Wong (2010)	Kansas River	LiDAR, NED, SRTM	2,10,30	MicroDEM	LiDAR and NED similar. SRTM noticeably different, with flood prediction fragmented. DEM source more important than resolution for flood extent
Fewtrell et al. (2011)	Alchester, UK	LiDAR (Terrestrial)	0.5,1,2,5	LISFLOOD-FP	Step change in performance between 2m and 5m grid resolution due to degradation of road network and camber representation
Manfreda et al. (2011)	River Arno, Italy	ASTER GDEM, SRTM, Local DEM	20,40,60,80,100, 120,140,160,180, 260,360,720	0D Method	Best result at 100m. SRTM offered best result. Only shows geomorphic characteristics of a floodplain.
Neal et al. (2011)	Tewkesbury, UK	LiDAR	2,10,20,40	LISFLOOD-FP	Greatest loss of accuracy between 10m or 20m. Best accuracy at 2m. Finest resolutions could simulate inundation dynamics best. Valley filling flow magnitudes similar all resolutions
Yu and Lane (2011)	River Wharfe, UK	LiDAR	4,8,16,32	FloodMap	Using subgrid information in coarse meshes improved model performance but improvement only relatively small. High resolution features (walls, buildings) are important

Reference	Location	DEM	Resolutions	Model	Main Finding
Sampson et al. (2012)	Alchester, UK	LiDAR (Airborne & Terrestrial)	0.1,1	LISFLOOD-FP; ISIS-FAST	Bigger difference between DEM source than resolution
Wang et al. (2012)	South Tibet	ASTER GDEM, SRTM, DEM from aerial photography	90	HEC-RAS	ASTER 2.2% smaller and SRTM 6.8% larger inundation extent compared to high resolution DEM
Ozdemir et al. (2013)	Alchester, UK	LiDAR (Terrestrial)	0.1,0.5,1	LISFLOOD-FP	Loss of hydraulic connectivity if micro terrain features not included
Jarihani et al. (2015)	Thomson River, Australia	ASTER GDEM, SRTM	30,60,90,120,250,500,1000,2000	TUFLOW 2D	Model Performance noticeably worsened after 120-250m. SRTM better than ASTER GDEM
Saksena and Merwade (2015)	6 Stream reaches in USA	LiDAR, NED, SRTM	1,3,6,30,90	HEC-RAS	Mean water surface elevation has a strong positive linear relationship with grid size. Predicted flood extent increases with coarser DEM resolutions. DEM source important, as LiDAR derived DEM at 30m gave better prediction than NED at 30m
Ali (2016)	Kigali, Rwanda	ASTER GDEM, SRTM, DEM from aerial photography	5,10,20,30	SOBEK	DTM essential to represent urban flooding as ASTER and SRTM were found to be inadequate without correction. Models above 15m began to show significant inaccuracies
Savage et al. (2016b)	Imera Basin, Sicily	LiDAR	10,20,50,100,200,250,300,350,400,450,500	LISFLOOD-FP	Model performance deteriorates at resolutions coarser than 50m. Below 50m little gain in performance. Doubling model resolution lengthens computation rime by order of magnitude
Komi et al. (2017)	Oti River, West Africa	SRTM	30,60,120,240,480,960	LISFLOOD-FP	Best index of fix at 480m. Worst performance at 30m. Local scale noise the likely reason for worse performance. Noise smoothed in coarsening DEM.
Bhuyian and Kalyanapu (2018)	American River	ASTER, LiDAR,NED, SRTM	3,10,30,90	HEC-RAS	ASTER & SRTM overestimated inundated areas >4x compared to LiDAR and NED. Low hydraulic connectivity in ASTER. 30m Resolution gave the lowest errors.

2.2.3.2 Boundary Conditions

The amount of water entering a model is described by the upstream boundary condition (typically from a gauge), whilst the amount of water exiting the model is described by the downstream boundary condition. In a fluvial setting, upstream boundary conditions are described by hydrographs, whilst for coastal applications tidal gauges describe boundary conditions and for pluvial applications point sources (e.g. burst water main) or direct rain on grid are used. For the downstream boundary, the water stage, flow or slope is defined to determine how much water leaves the model domain, and can be informed by a water stage reading. For fluvial applications on which this thesis focuses, boundary condition uncertainties arise from uncertainties in the discharge measurements and the water heights on which the downstream boundary is based. Discharge is commonly estimated by first measuring the water stage and then applying a rating curve. Measuring the water stage and discharge on multiple occasions at the gauge location and subsequently determining the relationship between the two are used to derive rating curves. This approach is favoured as one can easily estimate the discharge just by measuring the water level. However, for large floods a number of uncertainties occur from the measurement of the water level, the cross sectional area of the channel (especially if flow goes out of bank), and the extrapolation of the rating curve (Di Baldassarre and Montanari, 2009, Domeneghetti et al., 2012). Extreme events can also destroy gauging equipment so even if a location is normally gauged it may not be in an actual flood event. In a comprehensive literature review, McMillan et al. (2012) suggests discharge uncertainties of between 10-20% for medium to high flows and approximately 40% when flow goes out of bank. As a result, studies have tested the sensitivity of flood predictions to boundary conditions by varying the upstream and downstream boundary conditions (Pappenberger et al., 2006, Apel et al., 2008, Domeneghetti et al., 2013, Pappenberger et al., 2008).

2.2.3.3 Friction

The friction term is typically described by Manning's roughness coefficient (n) and varies by surface. A larger Manning's roughness value means a greater frictional force acts upon the

flow of water. Values of Manning's *n* are dependent on the roughness of a surface and consequently vary by channel bed material and land use type. Typical values of Manning's *n* can be found in Chow (1959). Friction parameters are usually lumped into two separate parameters to describe the channel friction and the floodplain friction, with floodplain friction typically having higher values of Manning's *n* (Horritt and Bates, 2001a, Aronica et al., 2002, Horritt et al., 2007). In reality, Manning's *n* varies in time and space (Di Baldassarre, 2012b), so some attempts have been made to parameterize further by splitting channels into sections (Hall et al., 2005), deriving distributed friction values from remote sensing (Schumann et al., 2007, Wood et al., 2016, Tarpanelli et al., 2013), classifying by floodplain land-use type (Wilson and Atkinson, 2007, Mtamba et al., 2015, Afshari et al., 2018) or floodplain characteristics (Manh et al., 2014). Whilst friction is a physically based characteristic that can be measured, values vary in time and space and are scale dependent (Horritt et al., 2007). Therefore, friction parameters can be classed as effective parameters during calibration in that they can be calibrated to make up for other errors from boundary conditions, topography and model structure (Di Baldassarre, 2012b, Bates et al., 2005a). Some may quaff at such a practice as if the model cannot produce reality with physically plausible values then it is evidence that the model is wrong (Cunge, 2003). This sentiment may be correct if all data and model structure are error free, and the friction values specified can correctly represent the momentum losses, but such is the complexity of nature that this is not the case. Additionally, it should be noted that the purpose of a hydrodynamic model for flood prediction is to correctly predict water depths and flood extent, and not friction values(Di Baldassarre, 2012b).

Being an effective parameter makes estimating *a priori* a distribution of values difficult, and thus published values (e.g. Chow (1959)) should be treated at best as a guide to a likely range (Horritt et al., 2007). Therefore, friction parameters are frequently altered to perform sensitivity analysis, usually with Manning's *n* values kept within physically realistic ranges. By treating Manning's *n* as an uncertain parameter, hydrodynamic models have been calibrated to a specific flood event by comparing model output to an observation of a recorded event (Di Baldassarre, 2012b). Once a hydrodynamic has been suitably calibrated to an observed event, the hydrodynamic model has been shown to be effective in making

flood predictions (Horritt and Bates, 2002, Bates et al., 2004). However, there is often some degree of equifinality as multiple combinations of model parameters often produce very similar levels of performance (Aronica et al., 2002). Furthermore, if model performance is sharply higher for a narrow region of parameters, then calibrating a model for the given flood event can cause the hydrodynamic model to be over-conditioned for the given flood event. (Hunter et al., 2006). In other words, if a hydrodynamic model can only model a given event for a very specific range of optimum parameter values, it is possible that for a different event the optimum parameter set would be different, and thus the model performance would be sub-optimum. This case is prevalent when poor observational, or 'disinformative' data is used to calibrate a model (Beven and Westerberg, 2011) as modelers can become overconfident in model performance but in reality the model is only matching poor, erroneous data. Therefore, the model would be making a poor prediction in reality, which could be particularly problematic if acted upon for flood management. Whilst calibrating hydrodynamic models with Manning's n is popular, it is clear it can have a substantial influence on model outputs and should be carefully considered in the calibration process.

2.2.3.4 Channel Geometry

For many rivers there is a lack of information on channel geometry as bathymetric surveys are very costly and time-consuming. However, 2D models require information on river channel bathymetry. Therefore, approximations of channel geometry have to be made. It is common to assume the channel shape is rectangular (e.g. Bates and De Roo (2000)). Whilst this assumption is reasonable, there is clearly enough variation in nature that means this assumption is too basic. As a result, studies have investigated model sensitivity to varying channel shape and have found that calibrating depth and/or channel shape may be preferable to assuming a rectangular shape and calibrating friction alone (Neal et al., 2015). Further uncertainty comes from a lack of knowledge of river widths. Whilst river widths can be estimated manually from satellite images, this is time-consuming and cumbersome, and is only suitable for a small reach. An alternative is deriving river widths automatically based on satellite optical images (Landsat or Sentinel), with global databases available such as GWD-LR (Yamazaki et al., 2014a) or GRWL (Allen and Pavelsky, 2018), or automatic tools

such as RivaMap (Isikdogan et al., 2017).To date, little attention has been paid to hydrodynamic model sensitivity to uncertain width values.

Channel bathymetry remains a key unknown with no global dataset available (Bates, 2012). Estimating channel bathymetry from remote sensing has proved difficult as signals detectable from satellite sensors cannot penetrate far into the water surface. Therefore, a number of different methods have been proposed. Remotely sensed observations of water surface elevation and river width have been used to estimate bathymetry for several locations, but as of yet not on a global scale (Mersel et al., 2013). This has positive implications for the upcoming Surface Water and Ocean Topography (SWOT) mission that will provide a record of water surface height and river width. Moreover, synthetic SWOT outputs have been successfully used in a data assimilation approach with hydrodynamic models (Yoon et al., 2012, Durand et al., 2008). Alternatively, river bathymetry has been estimated from optical imagery and geostatistical techniques (Adnan and Atkinson, 2012, Legleiter and Overstreet, 2012). When available, hyper resolution LiDAR (Hilldale and Raff, 2008) or structure-from-motion photogrammetry (Javernick et al., 2014) have been used to estimate bathymetry, with the usefulness of these techniques only really relevant to the reach scale. Recently, Lee et al. (2018) applied a principal component geostatistical approach for bathymetry estimations using velocity observations through 2D SWE. Even when there are bathymetric measurements, these measurements are usually restricted to certain locations along a reach. Therefore, GIS techniques are applied, with the choice of interpolation technique found to give different river profiles (Merwade et al., 2008, Zhang et al., 2016). Several studies have investigated the impact of uncertain channel depth of flood prediction (Wong et al., 2015, Grimaldi et al., 2018, Cook and Merwade, 2009, Neal et al., 2012a). In essence the channel geometry is intrinsically linked to the capacity of the channel and is thus directly related to the bankfull discharge. The relationships between channel geometry and channel width, depth, velocity and discharge are described by the term 'hydraulic geometry' (Leopold and Maddock, 1953)

2.2.4 0D Models

0D models do not consider any physical processes in flood inundation and are based on the most simple hydraulic principles (Pender, 2006). They are orders of magnitude quicker to run than hydrodynamic models and can be useful for a broad-scale assessment of flood extents and depths (Pender, 2006, Teng et al., 2017). The so called 'bathtub method' is one such example of a 0D model whereby a DEM is intersected by water stage planes to delineate the areal extent of a flood (Figure 2-2), with studies using such an approach using focused on coastal flooding (Leon et al., 2014, van de Sande et al., 2012). Alternatively, flood prone areas can be detected by calculating the topographic index from DEMs (Samela et al., 2015, Manfreda et al., 2011).

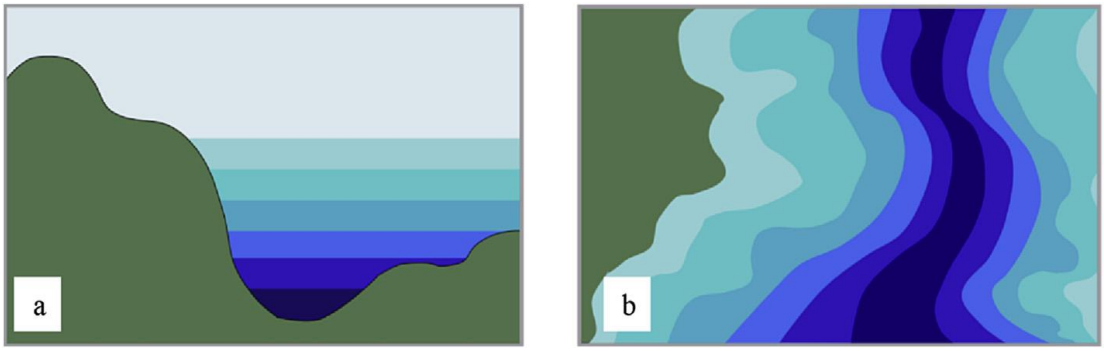

Figure 2-2 Bathub Method Schematic: a) Intersection of DEM with multiple water surfaces. b) Flood extent based on connectivity between the water planes. From Teng et al. (2017)

2.2.5 Empirical Methods

Historical catastrophic floods are often studied by geologic or historical clues left behind. For instance, during large floods slack-water deposits (sand and silt) accumulate rapidly as flood waters suspend sediment. Subsequently, when flow velocities drop, suspended sediment is abruptly deposited leaving a layer of deposits. By studying the stratigraphy, Sheffer et al. (2003) documented historical flooding in the Ardeche river. Geochemical analysis of floodplain deposits can further add to the record (Berner et al., 2012). Alternatively, historic records such as city accounts (Glaser and Stangl, 2001), etchings (Herget and Meurs, 2010), flood marks, legal documents (Kiss, 2009), narratives (Brázdil et al., 2006), newspapers (Guzzetti et al., 1994), photographs (Smith et al., 2011), songs (Brázdil et al., 2006), taxation records (Brázdil et al., 2014) and weather recordings (Brázdil et al.,

2006) have be used to construct historic flood records. Whilst interesting, the usefulness of this information to modern planners could be seen to be limited as society and river geometry has changed beyond recognition to the historic times when these floods were modelled. Nevertheless, such information is valuable to inform about the potential flood hazard.

2.2.6 What type is best?

When discussing model selection, the famous quote of statistician George Box is often cited, where he noted "All models are wrong, but some are useful". Whilst true, models can be ranked as being useful, partially useful and completely useless for their intended application (Burnham and Anderson, 2002). The art of modeling is to choose the correct model that will achieve the goal of the task. So, for a flood model application, a modeler should consider that their main task is to provide a reliable prediction of flood inundation. All other details are unnecessary. A useful way to conceptualize this tradeoff is the principle of parsimony as schematized by Box and Jenkins (1970) in Figure 2-3. In the principle of parsimony, as the model complexity increases, the bias tends to decrease, but the uncertainty tends to increase. This idea is also known as Occam's razor that states that all unnecessary detail should be removed. Therefore, the task of the modeler is to build a suitable model that is a trade-off between bias and uncertainty – or in other words to build a parsimonious model. unparsimonious models can range from models that are not complex enough to represent the dominant process, to models that are unnecessarily complex in that by adding additional parameters a model can fit almost any data and thus such a model might make poor predictions as the parameterization will be affected by the relatively high uncertainty (Di Baldassarre, 2012a).

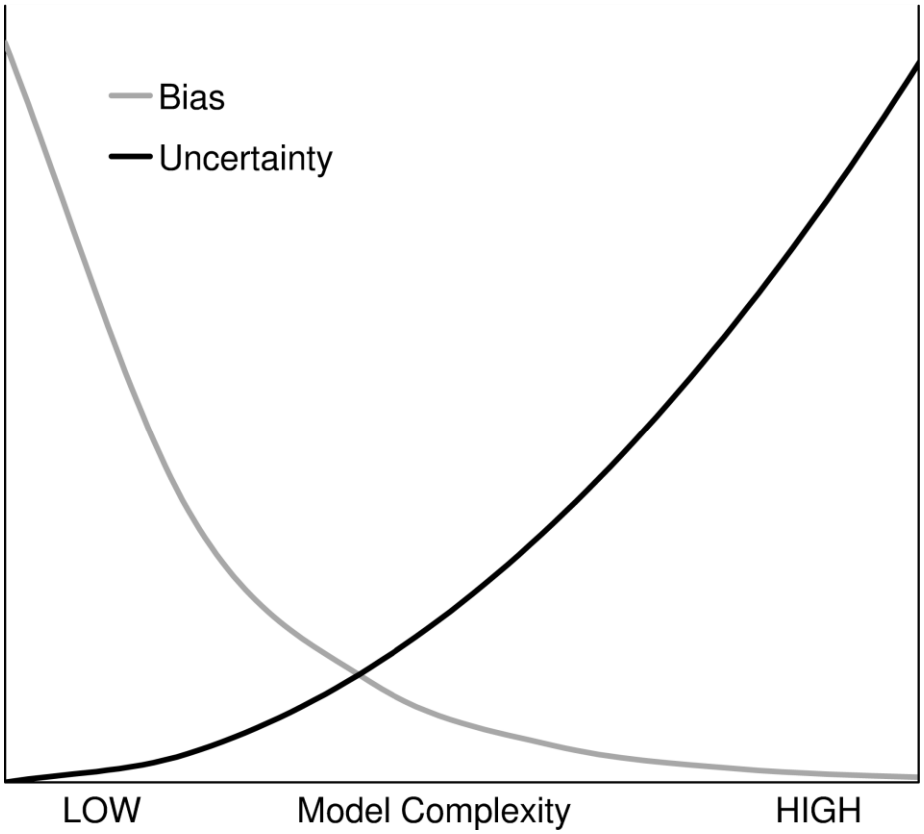

Figure 2-3 Principle of Parismony. A concept of trade-off between bias (grey) and uncertainty (black) in model complexity. From Di Baldassarre (2012a)

Before choosing a suitable hydrodynamic model, the modeler should make 4 main considerations:

- What are the dominant processes controlling flood inundation?
- What data are available?
- What are the computational resources available?
- When do the results need to be available?

First the modeler should assess the likely flood inundation processes. For instance, if one is tasked with modeler a reach where flooding is controlled by topographic discontinuities (e.g. manmade embankments), a 1D model would be principally suited. Taking another example, if the location under consideration is a large floodplain where floodplain topography is a key control on flood extent, then a 2D model is likely to be most appropriate (Di Baldassarre, 2012a).

Second the modeler must consider the data available. Models are only as good as the data used to calibrate and verify them (Abbot, 1979, Beven and Westerberg, 2011). Indeed, including too much detail can be potentially misleading as detail can breed overconfidence in results (Dottori et al., 2013). As an increasing amount of high-resolution data becomes available, there is a danger that a reductionist approach can be taken where modelers become fixated with higher resolution and more complexity but miss the added uncertainty that this brings (refer to Figure 2-3). However, if better data is needed to capture the correct processes, a modeler should do their upmost to obtain this additional information if time and money allows (though rarely the case). Or at least a modeler should evaluate the epistemic uncertainties associated with the data, elicit information about uncertainty from experts and efficiently audit their workflow so the assumptions made are clear (Beven et al., 2018)

Thirdly, the modeler should consider the computational resources available. It is unsuitable to choose a complex model that will take an exorbitant amount of time or will simply not work on the machine at hand. Equally, if the results of a project are to be disseminated and used by those not primarily trained as a hydrodynamic model, it is important to choose a model that will be easily understandable for the intended user. Additionally, it is beneficial to choose a model that is being continuously developed so that advancements in computational architecture can be exploited to maximize efficiency. If the model is intended for sensitivity analysis or to produce flood probability maps, a lower complexity model is needed that allows multiple simulations. Model resolution can have a large impact on simulation time, with Savage et al. (2016b) finding that simulation time increases by an order of magnitude by halving the model resolution.

Lastly, a time consideration should be made. If a project has a deadline in 6 months, it is unwise to choose a model that will take weeks to months to run, especially with the additional time needed to set up the model. Also, the time constraints relating to the applications should be considered. For instance, flood forecasting requires fast models.

All in all, there is no one best type of model. The choice of model is dependent on the application, data available, computational resources and time available. However, wherever

possible the best model will be the simplest one that gives the required information whilst reasonably fitting the data (Bates and De Roo, 2000).

2.3 Hydrodynamic Model Choice

2.3.1 Model Requirements

For the requirements of this thesis a hydrodynamic model must fulfill the following criteria:

- Computationally efficient enough to run multiple simulations at a regional scale at an intermediate resolution
- Few data requirements (i.e. suitable for a data-sparse location)
- Ability to represent flood inundation over a large floodplain
- Ability to represent backwater effect
- Access to source code

The intended focus area of this thesis – the Mekong Delta – is an extremely large area. A trade-off is needed between model complexity and resolution, so the model can capture the correct processes but can in turn be run multiple times. As flood inundation spreads over topography, it is necessary to simulate flow over the complex topography of the floodplain so a 2D model is most appropriate. A 1D model would be inappropriate as it would be too simple to resolve the complex floodplain topography. Conversely, a 3D model would be far too computationally expensive and would not have the required data to make the flood predictions effective. Additionally, the model should take in the order of minutes to hours to compute to allow for a suitable exploration of the complexity needed in a timely manner. Moreover, the hydrodynamic model must be able to run at different resolutions to be able to investigate the effects of scale. The model should be able to represent backwater effects that have a strong influence in the Mekong Delta, both from the coastal area and the Tonle Sap lake. Lastly, it is beneficial to have access to the source code to make any changes. As a result, we choose to use the LISFLOOD-FP hydrodynamic model, which will be briefly discussed below.

2.3.2 LISFLOOD-FP

A model that satisfies the aforementioned criteria is LISFLOOD-FP (Bates et al., 2010). The model has been continually improved since its inception in 2000 (Neal et al., 2018), with its computational efficiency and ability to utilize high performance computing a particular advantage when performing multiple simulations. LISFLOOD-FP has performed well when tested against a range of academic and commercial hydrodynamic models in both rural and urban settings and across a range of scales (Horritt and Bates, 2001a, Horritt and Bates, 2002, Hunter et al., 2008, Bates et al., 2010, Neal et al., 2012b, Néelz and Pender, 2013). For example, when comparing the diffusive, inertial and full 2D shallow water equations of LISFLOOD-FP, (Neal et al., 2012b) found that the inertial model only had small differences in model predictions when compared to the fully dynamic 2D models for sub-critical flow. The model has been applied to fluvial (Neal et al., 2012a, Horritt and Bates, 2001a), pluvial (Fewtrell et al., 2008, Neal et al., 2009b, Fewtrell et al., 2011, de Almeida et al., 2012) and coastal flooding (Lewis et al., 2013, Purvis et al., 2008, Bates et al., 2005b, Quinn et al., 2013) across a range of scales from hyper resolution (Fewtrell et al., 2011, Sampson et al., 2012), to high (Horritt and Bates, 2001a, Wing et al., 2017, Ettritch et al., 2018) and to intermediate scales (Neal et al., 2012a, Komi et al., 2017, Schumann et al., 2013, Wilson et al., 2007, Sanyal et al., 2013, Biancamaria et al., 2009, Lewis et al., 2013, Altenau et al., 2017). Recently, LISFLOOD-FP has been used to create a global flood model (Sampson et al., 2015) currently run by Fathom Global Ltd. Consequently, LISFLOOD-FP has been found to accurately simulate flooding in a computationally efficient manner and is thus appropriate for this thesis. Other models could be used, but doing so would produce similar results, and at the expense of time in setting them up. It is expected that any conclusions reached in this thesis would be transferable to other hydrodynamic models.

2.3.2.1 LISFLOOD-FP – A Brief Model History and Description

LISFLOOD-FP was first presented by Bates and De Roo (2000). The published model development of LISFLOOD-FP can be found in Table 2-6. The premise behind LISFLOOD-FP was to create a simple as possible model that could be used with the ever-increasing number of high-resolution DEMs. This involved representing the channel in 1D to simulate the propagation of the flood wave, and the floodplain in 2D to enable the simulation of

floodplain water depths and subsequent inundation extent (Bates and De Roo, 2000). In the original version of LISFLOOD-FP, channel flow was calculated using a kinematic wave model which simplifies the St Venant momentum equation by eliminating the local acceleration, convective acceleration and pressure terms. Each channel cell has a value for cross-sectional area, bed elevation and friction, with the assumption of a wide and shallow rectangular channel shape which means the wetted perimeter can be approximated as the channel width. Channel flow was solved using implicit scheme. Once the bankfull depth of the channel is exceeded, water is routed onto the adjacent floodplain pixels. The volume of water flowing into the floodplain pixels is calculated at each time step from the 4 neighboring cells (upstream, downstream, left, right), with the flowrate also calculated using Manning's equation. Floodplain flow is then approximated as a 2D diffusion wave, where flow is calculated using an explicit scheme after the water depths has been updated. Each floodplain pixel are treated as individual storage volumes, with the flow between them calculated using the Manning's equation based on the free surface slope between floodplain pixels (Horritt and Bates, 2001a). Hence each floodplain pixel must also have a Manning's friction value with the elevation of the floodplain cell derived from the DEM. In the original scheme presented in Bates and De Roo (2000), the channel was represented as a set of pixels running through the computational grid, where water depth is calculated using the channel flow rather than the floodplain flow scheme (Horritt and Bates, 2001a). This created a scaling issue, whereby the channel width was included as a parameter, with this width likely being different from the floodplain grid size. For large pixel sizes this causes a discrepancy whereby the channel occupies a much larger area of the floodplain than necessary. As a result, a slightly different scheme was implemented whereby the channel occupies no floodplain pixels, but instead the channel overlays the floodplain pixels with flow interaction between the overlying pixels calculated using Manning's equation (Horritt and Bates, 2001a). The initial versions of LISFLOOD-FP was found to perform well with other academic and commercial models (Horritt and Bates, 2001b, Horritt and Bates, 2002), whilst the computational efficiency made Monte Carlo simulations possible (Aronica et al., 2002) and simulations in large domains (Horritt and Bates, 2001a).

Table 2-6 Published model development of LISFLOOD-FP

Year	Development	Reference
2000	LISFLOOD-FP First Presented. 1D Channel, 2D Floodplain	Bates and De Roo (2000)
2005	Adaptive timestep scheme implemented	Hunter et al. (2005)
2009	OpenMP Parallelisation	Neal et al. (2009a)
2010	Inertial formulation of shallow water equations.	Bates et al. (2010)
2012	q-centered numerical scheme implemented	de Almeida et al. (2012)
2012	Subgrid scheme implemented	Neal et al. (2012a)
2013	Rainfall Routing Scheme	Sampson et al. (2013)
2015	Parameterisation of Channel shape	Neal et al. (2015)
2018	Further optimisation (parallelisation, wet/dry cell marking, data access, vectorisation)	Neal et al (2018)

Since the initial release of LISFLOOD-FP there have been numerous developments. For instance, Hunter et al. (2005) introduced a diffusive wave version of LISFLOOD-FP with an adaptive timestep. This was designed to overcome the limitation of a fixed timestep in the initial model. If the model timestep was too large, water was found to traverse through a whole cell during one timestep leading to a chequerboard oscillation where the model becomes unstable with large flows transferred into a cell in one timestep which then all flows back in the next timestep (Hunter et al., 2005). One solution is to use a flow limiter to replace the calculated floodplain flow. The flow limiter is a function of grid size and model timestep as opposed to floodplain friction, thus floodplain flow became insensitive to Manning's friction for the floodplain. To resolve this, Hunter et al. (2005) introduced an optimal adaptive timestep determined by the CFL condition for model stability which allowed the model timestep to become temporally variable. Although the adaptive timestep made better flood predictions than the fixed time step model, with improvements particularly in the wetting and drying of the floodplain, Hunter et al. (2006) found that simulation time was typically 6x more than the fixed timestep model. The reasons behind this behavior are twofold. First, the optimum timestep reduces quadratically with decreasing grid size, which leads to simulation times 2-10x greater for resolutions between 25-100m. Secondly, the optimum timestep is linked to water surface slope, so when the flow rate (and thus the water surface slope) reduced to zero so did the timestep (Bates et al., 2010). As a result, most diffusive models with the adaptive scheme took longer to run than fully dynamic 2D models (Hunter et al., 2008) In addition, acceptable parameter sets occurred over a broader parameter space for the adaptive scheme compared to the fixed

timestep scheme suggesting the adaptive scheme may be easier to calibrate (Hunter et al., 2006).

The next major development in LISFLOOD-FP combatted the high computation cost of running the adaptive scheme by incorporating local inertial terms (Bates et al., 2010). The study of Hunter et al. (2008) identified that the lack of mass and inertia was the key reason behind the strict time step control. Taking the momentum equation from SWE, Bates et al. (2010) drops the advection term, as floodplain flow advection was found to be relatively unimportant (Hunter et al., 2007), but keeps the acceleration term. By including the acceleration term, water now has mass, and is therefore less likely to generate rapid reversals in flow that can lead to a chequerboard oscillation effect (Bates et al., 2010). Therefore, the continuity equation which describes the change in water height for a given cell for this formulation of LISFLOOD-FP is described by:

$$h_{i,j}^{t+\Delta t} = h_{i,j}^{t} + \Delta t \frac{Q_{x\, i-\frac{1}{2},j}^{t+\Delta t} - Q_{x\, i+\frac{1}{2},j}^{t+\Delta t} + Q_{y\, i,j-\frac{1}{2}}^{t+\Delta t} - Q_{y\, i,j+\frac{1}{2}}^{t+\Delta t}}{A_{i,j}} \quad (8)$$

where h is water depth (m) at the center of a cell, i and j are the spatial indices of the cell in the x and y Cartesian directions respectively, t is the current time (s), Δt is the timestep, $t + \Delta t$ is the time at the next timestep, Q is the flow (m^3s^{-1}) between two cells and A is the water surface area in a cell (m^2). To calculate the water flow between cells, the momentum equation for this formulation of LISFLOOD-FP becomes:

$$Q_{i+\frac{1}{2}}^{t+\Delta t} = \frac{q_{i+\frac{1}{2}}^{t} - g h_{flow}^{t} \Delta t\, S_{i+\frac{1}{2}}^{t}}{\left(1 + \frac{g \Delta t n^2 |q^t|}{\left(h_{flow}^{t}\right)^{\frac{7}{3}}}\right)} \Delta x \quad (9)$$

where Δx is cell resolution (m), q^t is the flow from the previous timestep Q^t divided by cell resolution Δx, g is acceleration due to gravity (ms^{-1}), n is the Manning's coefficient of roughness ($sm^{1/3}$) , S is the water surface slope and h_{flow}^{t} is the depth that water can flow

through between cells, and is calculated as the difference between the highest bed elevation and the highest water surface between two cells (m).

Whilst the CFL condition can be used to identify an appropriate timestep, it is not sufficient to ensure model stability as the assumption of a small amplitude in calculating the wave celerity is not always valid and because the friction term is included (Bates et al., 2010). To ensure model stability, Bates et al. (2010) introduced a coefficient α in the following equation to calculate maximum timestep t_{max}

$$t_{max} = \alpha \frac{x}{\sqrt{g h_t}} \tag{10}$$

Where x is the cell width and the remaining terms described previously. The coefficient term α has a range between 0.2-0.7. The new formulation allows the stable timestep to scale with $1/\Delta x$ rather than $1/\Delta x^2$ in the diffusive cell code. As a result, stable maximum timesteps increased between 1-3 orders of magnitude. In testing the new formulation, Bates et al. (2010) report a maximum speed up of 1120x over the diffusive storage model, although this was dependent of water surface gradient and model resolution. The RMSE difference between the new formulation of Bates et al. (2010) was only 1cm compared to the scheme of Hunter et al. (2005). Some instabilities occurred when low floodplain friction values were used that can be especially prevalent in urban environments Bates et al. (2010). By introducing numerical diffusion from a q-centered numerical scheme, de Almeida et al. (2012) enhanced stability at a negligible additional computational cost compared to the formulation of Bates et al. (2010).

The next major development to LISFLOOD-FP has been the inclusion of a sub-grid scheme by Neal et al. (2012a). In the sub-grid scheme, any size channel below grid resolution can be represented. This development is important for intermediate scale models as for model resolutions >100m the grid size imposed an increasingly severe restriction on the simulation of channelized flow (Altenau et al., 2017). Channel flow is calculated by a 1D interpretation of the 2D scheme presented by Bates et al. (2010) with two additional variables of channel bed elevations and channel widths. Unlike previous versions of LISFLOOD-FP, the sub-grid scheme does not assume a rectangular channel where the hydraulic radius is approximated

by the flow depth. This is because the subgrid model could be required to simulate small, narrow and deep channels, so the formulation was changed to define the hydraulic radius as the area of flow between cells divided by the wetted perimeter (which is defined by the cannel width and water depth). Neal et al. (2012a) note that this formulation can suffer instability issues in situations where large channels flow into small channels. In the subgrid formulation the momentum equation becomes:

$$Q_c^{t+\Delta t} = \frac{Q_c^t - gA_{c,flow}^t \, \Delta t \, S_c^t}{(1 + g\Delta t n^2 |Q_c^t| / [(R_{c,flow}^t)^{\frac{4}{3}} A_{c,flow}^t])} \tag{11}$$

Where Q_c^t is flow, $A_{c,flow}^t$ is the area of the flow between cells and $R_{c,flow}^t$ is the hydraulic radius. To obtain the hydraulic radius, the width of flow at each edge is calculated by:

$$w_{c,flow} = \min(w_{c,i}, w_{c,i+1}) \tag{12}$$

Where w_c is the channel width. Channel flow area is then calculated based on the depth of flow:

$$A_{c,flow}^t = w_{c,flow} \, h_{c,flow}^t \tag{13}$$

Finally, hydraulic radius is defined as:

$$R_c^t = \frac{A_{c,flow}^t}{w_c + 2h_{c,flow}^t} \tag{14}$$

However, for many rivers, information on the channel bed elevation is not available. Therefore, Neal et al. (2012a) use hydraulic geometry (Leopold and Maddock, 1953) to estimate channel depth based on applying a coefficient and fractional exponent to river width. This makes the sub-grid version of LISFLOOD-FP particularly useful in large data-sparse floodplains. A schematic diagram of the different types of model is given in Figure 2-4.

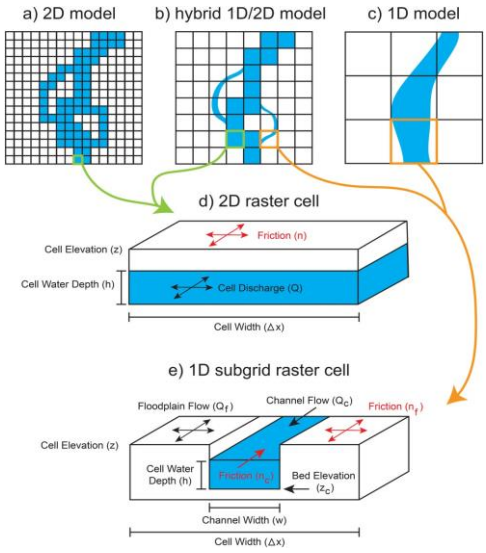

Figure 2-4 Conceptual diagram of types of hydrodynamic models (a) 2-D channel flow model, (b) hybrid 1-D/2-D channel flow model, (c) 1-D channel flow model, (d) 2-D raster cell with relevant variables, and (e) 1-D subgrid raster cell with relevant variables. Courtesy of Altenau et al. (2017)

Other LISFLOOD-FP developments have included a rainfall routing scheme (Sampson et al., 2013), parameterizing channel shape (Neal et al., 2015) and optimization of the code through parallelization (Neal et al., 2009a) , tracking of wet/dry cells, data access efficiency and vectorization (Neal et al., 2018). The latest optimization work yielded performance improvements of between 4.2x and 8.4x faster on a single core machine, and 34-60x faster on a 16 core machine (Neal et al., 2018). LISFLOOD-FP has also been coupled to the CAESAR landscape evolution model (Coulthard et al., 2013) and to a global hydrological model (PCR-GLOBWB) through the GLOFRIM project (Hoch et al., 2017). Continuing development of LISFLOOD-FP is ongoing.

2.4 Summary

This chapter has outlined flooding, how floods are modelled and a discussion of the choice of LISFLOOD-FP for the hydrodynamic model used in this thesis. Further discussion of DEMs, their uncertainty, geostatistics and river floodplain connectivity are described in further detail in subsequent chapters.

Chapter 3 An Intermediate Scale Hydrodynamic Model of the Mekong Delta built using freely available data

Paper in Preparation

3.1 Preface

This first results chapter consists of work currently under preparation for submission. All simulations, analysis, writing and figures were completed by the lead author with advice from Paul Bates and Jeffrey Neal. Flow estimates of the Tonle Sap were provided by Matti Kummu of Aalto University. Detailed channel information was provided by the WISDOM Project through Claudia Kuenzer of the German Aerospace Center. Satellite Imagery to estimate flood extent was provided by Akihiko Kotera of Kobe University. Matthew Lewis of Bangor University provided guidance on using the FES2014 data.

3.2 Context

As the main aim of this thesis was to further our understanding of how uncertainty of topography impacts flood inundation predictions in data-sparse environments, a pre-requisite was to build a hydrodynamic model that can be used as a tool to determine how uncertain data propagate into flood predictions. An intermediate scale (540 m) was chosen (see Table 1-1) to allow for a suitable computation time for Monte Carlo simulations. A data-sparse river delta (Mekong) was chosen as a test case for two reasons – 1) River deltas have a high flood risk but are not modelled at the intermediate scale despite the obvious need. 2) A hydrodynamic model at an intermediate scale of such an environment does not presently exist and fits within the local to global scale models that currently exist for the delta. This chapter will investigate the level of detail needed to make accurate flood predictions in a data-sparse river delta environment and will provide guidance on how a hydrodynamic

model should be built at an intermediate scale which could be utilised in other less studied deltas. An intermediate scale model is suitable for data-sparse deltas for three reasons. 1) A lack of data to calibrate and validate the model; so even if a high-resolution model could be built, data is often not available to evaluate it. 2) Multiple scenarios can be run to explore uncertainties in the model structure and parameterization. 3) High-resolution can provide a false level of confidence in results, pushing modelers to a deterministic mapping approach which has the danger of missing some at-risk areas. At a practical level, flood risk management requires a map of potentially flooded areas, and for that to be readable high-resolution model results often have to be aggregated to a coarser scale, thus negating the need for high-resolution models (Dottori et al., 2013). The key question remains as to whether an intermediate scale model can accurately simulate flooding. To this end this chapter will aim to address this question.

3.3 Introduction

River deltas are highly dynamic, low topographic slope areas that form when a river deposits sediment into a standing body of water. In the context of this work, a delta is considered the 'seaward area of a river valley after the main stem of a river splits into distributary channels (Syvitski and Saito, 2007). River deltas are among the most productive and economically important ecosystems in the world, acting as a hotspot for biological productivity, a home to an estimated 600 million people and an area of high agricultural productivity (Day et al., 2016, Passalacqua, 2017). Yet, river deltas are also one of the most threatened global ecosystems, primarily because of human activities. Recently, there has been a growth in population in river deltas with much of this increase in growth concentrated in deltaic mega cities, heralding a shift from economies dominated by agriculture towards economies increasingly reliant on manufacturing and export processes (Syvitski et al., 2009, Seto, 2011, Day et al., 2016). Yet, river deltas form one of the most flood prone areas in the world, and this is widely expected to increase in the future as a result of sea level rise, subsidence and precipitation increases (Syvitski et al., 2009, Hallegatte et al., 2013).

Despite this, flood models focused on river deltas are scarce. Studies exist in developed countries, such as in the Rhine Delta (Klerk et al., 2015), and in developing countries studies mainly focus on the Mekong Delta (see Table 3-2) and the Ganges-Brahmaputra (Karim and Mimura, 2008, Lewis et al., 2013, Ikeuchi et al., 2017, Ikeuchi et al., 2015). River deltas in developing countries have a high flood risk (Syvitski et al., 2009, Ericson et al., 2006), and tend to be characterized by a lack of data, making flood modelling in these regions challenging. Data sparse deltas can be modelled with coarse scale models based on open data, but these have been found to perform poorly (considered models that correctly predict <50% of observed flooding) in these areas (Trigg et al., 2016). Yet, coarse and intermediate scale models are important as they do not rely on detailed data so can be applied to data-sparse regions and are computationally efficient such that Monte Carlo methods can be applied. Recently, Ikeuchi et al. (2017) devised a method that can be used across multiple deltas by downscaling results from the global CaMa-Flood which is run at 0.1° (approximately 10 km at the equator) and coupling it with the Global Tide and Surge Reanalysis (GTSR) dataset. Whilst valuable, the coarse resolution of the global model makes accurate simulations of inundation extent difficult as the model resolution is too coarse to resolve floodplain features that control the flood inundation. With the need to better understand the flood risk in deltas, an approach is needed whereby open data can be utilised to build a flood model at an appropriate scale to give accurate results. Hydrodynamic models at the coarse scale (>1 km) cannot represent the key floodplain features that control flood inundation and, in turn, almost all the world's deltas do not have the topographic data to model at the hyper resolution scale (<30 m). Therefore, we are left with the choice to model at the high-resolution scale (30-270 m) or the intermediate scale (270-1000 m). Whilst topographic data are available globally through the Shuttle Radar Topography Mission (SRTM) DEM at 90 m, data are noisy at that resolution with a random height error of approximately 6m which is above the height of a typical flood wave amplitude (4-6 m). However, by coarsening the DEM to intermediate scales, the random height error drops to ~10% of the flood wave amplitude (~0.6 m random height error at 1 km). Whilst not perfect, modelling at the intermediate scale provides a compromise between vertical noise, resolution and computational resources. Previous studies in the Amazon (Wilson et al., 2007) and Niger (Neal et al., 2012a) have found that this approach produces

acceptably accurate results. Thus, in this thesis the aim is to address whether an intermediate scale can produce acceptably accurate results on a large river-delta environment. To this end, this chapter sets out to address the following questions:

- Can an intermediate scale hydrodynamic model be built for a data-sparse delta using freely available data that accurately represents flooding?
- What aspects of the flood model structure and data are most important to inundation prediction?

For this study, the Mekong Delta is selected as a study site. This is justified as the delta can be considered as being data-sparse and experiences the threats and challenges that many of the world's large deltas experience, thus, can be considered a typical heavily populated large delta. These threats include sea-level rise (Wassmann et al., 2004), salinity intrusion (Smajgl et al., 2015), shoreline retreat (Anthony et al., 2015), subsidence (Erban et al., 2014, Minderhoud et al., 2017), tidal deformation (Nhan, 2016) and upstream damming (Räsänen et al., 2017) . Secondly, there has been a range of flood inundation studies in the Mekong Delta ranging from coarse resolution global type models to high resolution models that rely on bespoke data (Table 3-2) , so the intermediate scale model developed in this chapter positions itself between these models on the complexity scale, allowing for comparison between the approaches.

3.3.1 Challenges in River Deltas

River deltas are facing a host of key challenges. Upstream damming is starving sediment supply (Giosan, 2014, Kondolf et al., 2014), which is also important in providing nutrients for agriculture. In some deltas, the demand for building material has driven channel bed mining (Brunier et al., 2014). Anthropogenically built channels linking irrigated paddies, are becoming more prevalent, posing management challenges. An increase in demand for groundwater and hydrocarbons has led to increased extraction and, thus, subsidence that can outpace sea-level rise by one to two orders of magnitude (Syvitski et al., 2009, Higgins, 2016). Aquaculture contributes to this water demand, and is becoming increasingly widespread (Ottinger et al., 2016). At the coast, mangroves are being depleted in many

areas, despite widespread recognition of their ability in attenuating storm surges (Zhang et al., 2012, Quartel et al., 2007, Horstman et al., 2014). Salt-water intrusion is increasingly becoming a problem in some deltas, damaging crops (Smajgl et al., 2015). With the reduced sediment supply, coastal erosion is more prevalent (Besset et al., 2016). Lastly, storm surges can be catastrophic for deltas, as demonstrated by Cyclone Nargis and Hurricane Katrina devastating the Irrawaddy and Mississippi deltas respectively. To survive, deltas need to be in equilibrium – or in other words enough sediment needs to come in to replenish the eroded material. Yet this is increasingly not the case, with deltas effectively sinking making them more susceptible to flooding. For example, Syvitski et al. (2009) conservatively estimated a 50% increase in deltaic areas vulnerable to flooding by the end of the 21st century.

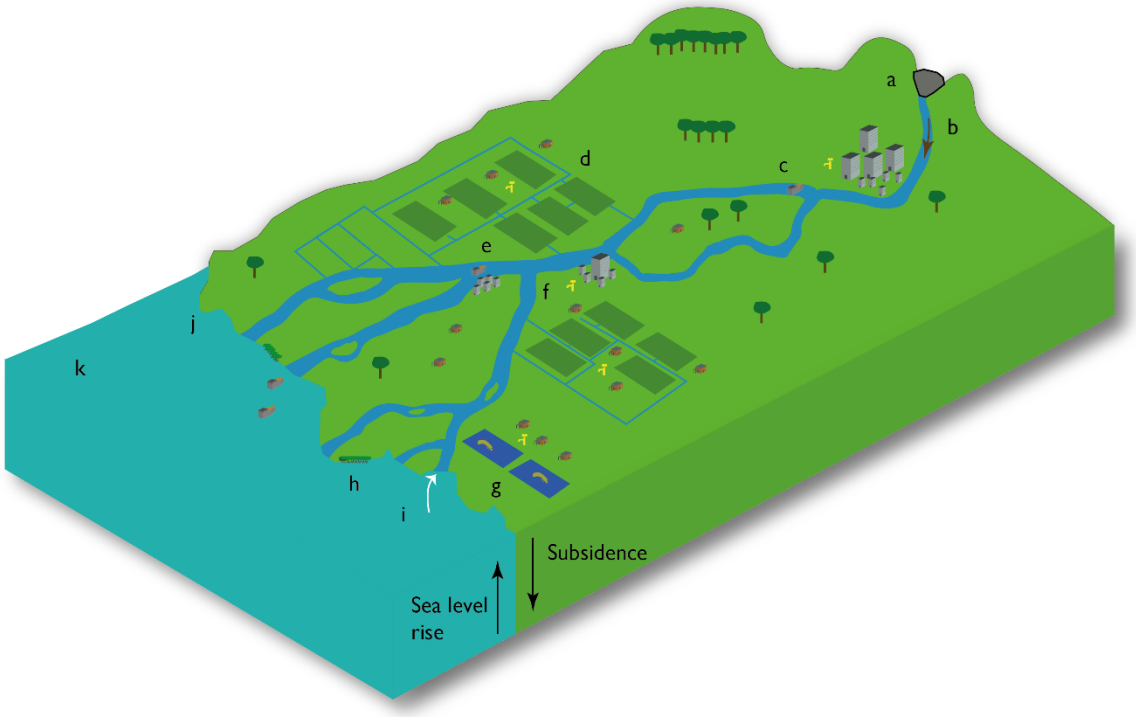

Figure 3-1 Threats & Challenges to Deltas: a) Upstream Damming; b) Reduced Sediment Delivery; c) River channel bed mining; d) Anthropogenically built channels; e) Irrigation; f) Groundwater & hydrocarbon extraction; g) Aquaculture; h) Mangrove Depletion; i) Salt-water Intrusion; j) Coastal Erosion; k) Storm Surges

3.4 Study Site

The Mekong Delta is considered the world's third largest by area (Coleman and Huh, 2004) with the Vietnamese part home to almost 20 million people (Szabo et al., 2016) and the Cambodian part home to around 10 million people. Despite falling fertility and relatively high out migration, population has continued to grow, particularly in urban centres such as Can Tho city (Dun, 2011). The region is biodiverse (Campbell, 2012) and plays a crucial role in regional food security, supplying 50% of Vietnam's food, 90% of Vietnam's rice and 60% of Vietnam's fish, with the region is known colloquially as the rice bowl of Vietnam (Anthony et al., 2015, Käkönen, 2008). Two monsoonal systems, the southwest Indian Monsoon and the northwest Pacific Monsoon, cause two distinct seasons within the Delta: A dry season from December to the end of April, and a wet season from May to November (Hung et al., 2012). The mean discharge of the Mekong at the Kratie gauge to the North of the delta is 14,500 m^3/s (MRC, 2010b), with approximately 85% of river discharge in the wet season and the remaining 15% in the dry season (Le et al., 2007).

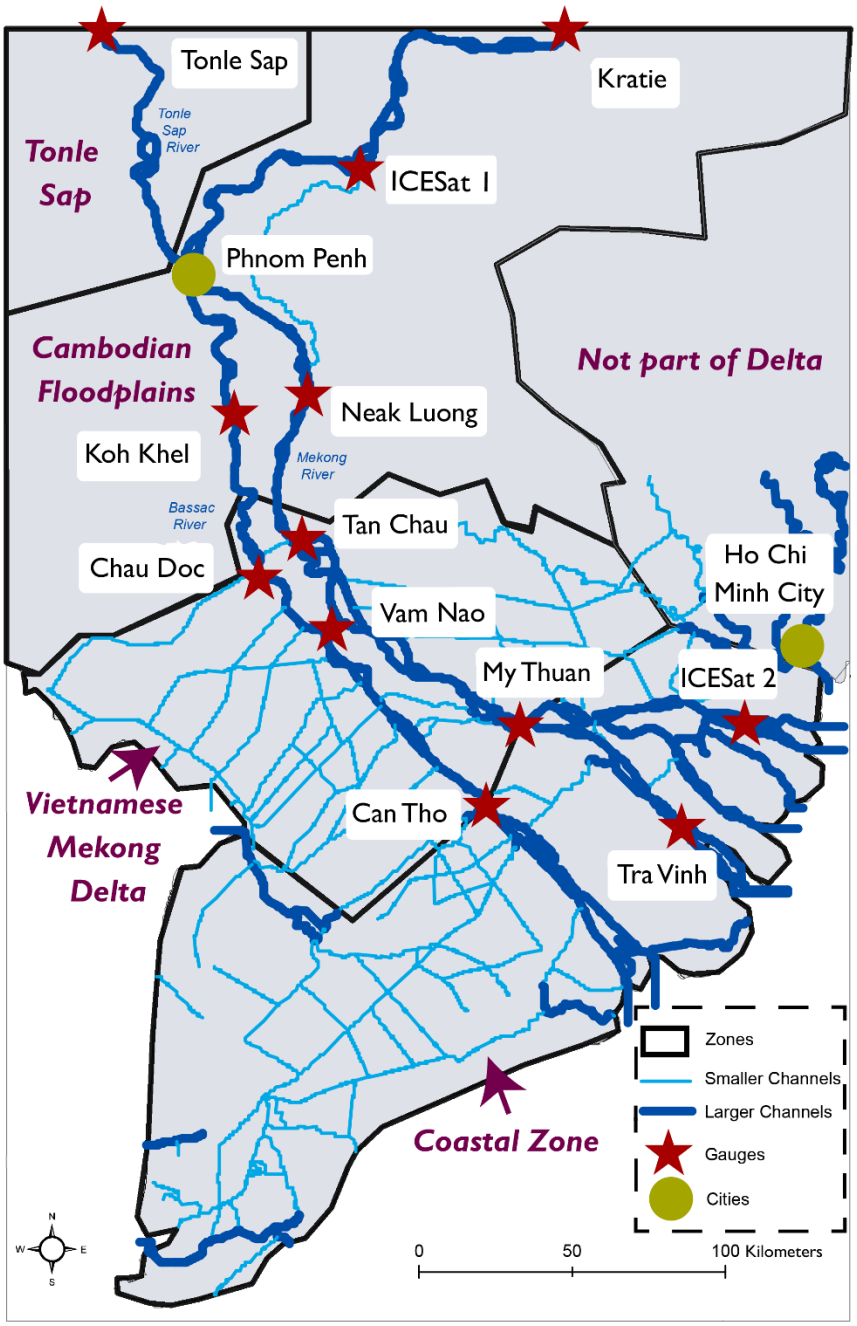

Figure 3-2 Map of Study Domain. The study site was defined using the delta definition of Syvitski & Saito (2007) but extended to encompass Tonle Sap Lake and the Kratie river gauge. Zones are delineated in black and are referred to throughout the text. Dark blue refers to the main channels of the Mekong Delta and lighter blue channels depict the smaller channels included in most of the models (far more smaller channels exist in reality). Gauges used to calibrate and validate the model are shown by red stars and the two major cities in the region are shown by yellow circles.

The development of the Mekong Delta can be traced back to the French Colonial rule (1887-1954), when French dredgers opened up the Mekong wetlands by digging hundreds of kilometres of canals (van Staveren et al., 2018, Biggs, 2010). This opened up the sparsely populated wetlands for agriculture and settlement, consequently resulting in the relocation of tens of thousands of farmers from the north of Vietnam (Janssen, 2015). The dredged material was subsequently used to construct dikes. The 1970s saw a shift from flood avoidance and adaptation to flood control with the construction of so-called 'August dikes' which allowed inundation of rice fields in August (Howie, 2011). The 'doi moi' policy reforms of 1986 heralded a shift towards the intensification of rice cultivation under relatively flood free conditions, resulting in the Vietnamese government heightening the dike network. This has continued further, especially in the northern provinces of the Vietnamese Mekong Delta which have seen a large growth of high dikes in recent years (Tran et al., 2018b). However, the recent adoption of the Mekong Delta Plan (MDP) (Vietnam, 2013) has changed the development trajectory of the delta back towards a system with more flood control.

The Mekong main stem flows into the floodplains of southern Cambodia before splitting into 3 branches just to the north of Phnom Penh. These branches are the Bassac (Hau) River, the Mekong (Tien) River and the Tonle Sap River. The latter river links to the Tonle Sap Lake which plays a crucial role in the hydraulics of the area. As the Bassac and Mekong rivers flow into Vietnam, they briefly meet again at Vam Nao Island, before splitting out through the Mekong delta. The Bassac splits into three channels and the Mekong into five (formerly six) to flow out of eight outlets. The Mekong's Sino-Vietnamese name, Cuu Long, translates as the 'nine dragons', referring to the nine outlets (now eight) of the river (van Staveren et al., 2018).

The area under consideration in this chapter can be split into four areas: The Cambodian floodplains; Tonle Sap Lake; Vietnamese Mekong Delta (VMD) and the coastal zones. To the north of the domain, the Cambodian floodplains are a comparatively natural system with little human interference, despite a recent push to intensify the agricultural productivity of the area (Erban and Gorelick, 2016). During the flood season this region is largely inundated, and provides important flood attenuation (Fujii et al., 2003).

The Tonle Sap Lake forms the largest freshwater body in Southeast Asia. The importance of the lake is profound, acting as a natural flood reservoir which reduces flooding downstream in the wet season and providing dry season flow to the delta from September/October onwards (Kummu et al., 2014). During the wet season, 20% of the Mekong mainstream enters the lake, whilst in the dry season between October-March 20-50% of the discharge at the Chaktomuk confluence on the Mekong main stem comes from the Tonle Sap (Kummu et al., 2014). Possible future development of irrigation and hydropower, as well as climate change, is expected to bring considerable alterations to the flood pulse of the Tonle Sap (Kummu and Sarkkula, 2008).

The Vietnamese Mekong Delta is a highly complex, anthropogenically dominated region. At the Cambodian-Vietnamese border, approximately 80% of floodwater (20,500-25,500 $m^3 s^{-1}$) is carried in the Tien River at Tan Chau, whilst 20% (6500-7660 $m^3 s^{-1}$) is carried in the Hau river at Chau Doc (Tri, 2012). This 19,500 km^2 area has an estimated 91,000 km of channel network, compromising a plethora of channels, dikes, sluice gates and pumps (Manh et al., 2015). The floodplains in this area are highly compartmentalised, with areas ranging from 50-500ha (Manh et al., 2015). These compartments are mostly used for rice production, with flow controlled depending on flood magnitude and crop types/patterns.

Water levels within the region have altered in recent years because of upstream dams, flood prevention systems, subsidence and sea level rise (Cochrane et al., 2014, Fujihara et al., 2016, Dang et al., 2016, Duc Tran et al., 2018). Thus far, the impact of dams on water levels in the Mekong Delta has been limited, but with the major planned developments this could alter (Dang et al., 2016, Dang et al., 2018). In the northern Vietnamese Mekong Delta, particularly in An Giang province, flooding has been reduced by approximately 40% when comparing two hydrologically similar floods (2000 and 2011). As a result of less flooding in the northern part of the Vietnamese Mekong Delta, the flood wave has shifted downstream resulting in higher water levels and more flooding in the southern part of the Vietnamese Mekong Delta (Dang et al., 2016). In the future, scenarios of upstream damming, flood prevention strategies, rainfall changes, subsidence and sea level rise are expected to demonstrably alter the flow regime, presenting a considerable challenge for future planning (Dang et al., 2018,

Dang et al., 2016, Anh et al., 2018, Wassmann et al., 2004, Tri et al., 2013, Delgado et al., 2012, Takagi et al., 2016, Van et al., 2012)

The coastal area extends southwards from the Can Tho and My Thuan gauges towards the coast and encompasses the Cau Mau peninsula. Much of this area is below sea level. Tides in the region are a mixture of diurnal (Gulf of Thailand) and semi diurnal (South China Sea), with a high range of up to 4m in the South China Sea (Nguyen and Savenije, 2006, Hung et al., 2012). The rivers in this area are affected by tidal backwater influences, especially in the dry season with tidal influences evident in water levels more than 120 km inland (Fujihara et al., 2016). In areas closer to the coast, flood events are typically a mixture of high-water levels during the flood season, high tides and storm surges. Presently, storm surges are not a major source of flood hazard, even though Typhoon Linda's storm surge in 1997 produced the highest water level in some parts of the Mekong Delta for a 20 year period (Le et al., 2007). It was previously thought that storm surge awareness was low (<40% respondents knew what a storm surge was) (Takagi et al., 2013), but this has since been questioned (Anh et al., 2017). However, in the future storm surges are expected to increase for the Mekong Delta (Takagi et al., 2013), exasperated by expected sea level rise (Wassmann et al., 2004, Doyle et al., 2010). Information on coastal water levels are difficult to obtain for the region with a limited spatial and temporal coverage.

3.4.1 Threats to the Mekong Delta

The Mekong Delta experiences a host of threats aside from flooding as outlined in Table 3-1. These threats are intrinsically linked to flood hazards and highlight the dynamic nature of the delta. Social challenges are not highlighted here, but of course exist.

Table 3-1 Threats to the Mekong Delta

Challenge	Headline	References
Channel Bed Mining	Between 1998-2008 average deepening of channels 1.3m[1]	[1]Brunier et al. (2014)

Challenge	Headline	References
Mangrove Depletion	Average mangrove width 140m due to depletion[2].	[2]Phan et al. (2015); Nguyen et al. (2017)
Salinity Intrusion	Rice production will be affected and/or adaptation methods needed[3].	Wassmann et al. (2004); Renaud et al. (2015) ; [3]Smajgl et al. (2015); Kantoush et al. (2017)
Sea Level Rise	4mm/yr^{-1} [4]. By 2050, sea level rise is expected to be 30cm along the South Vietnamese coast[5]	[5]Smajgl et al. (2015); Dang et al. (2016); [4]Fujihara et al. (2016)
Shoreline Retreat	50% of 600km shoreline experiencing shoreline retreat between 2003-2012[6]	[6]Anthony et al. (2015); Besset et al. (2016)
Subsidence	Subsidence rates due to groundwater pumping of ~1-4cm/yr^{-1}. Thus by 2050, land subsidence could be ~0.88m (0.35-1.4m)[7]	[7]Erban et al. (2014); Erban and Gorelick (2016); Minderhoud et al. (2017); Minderhoud et al. (2018)
Tidal Deformation	Maximum tidal water levels and tidal amplitude are increasing quicker than sea level alone as the tides themselves are deformed by sea-level rise[8].	[8]Nhan (2016)
Upstream Damming	Under a definite build scenario, there will be a 51% reduction in sediment to the delta, and a 96% reduction if all planned dams are built[9].	Kummu and Sarkkula (2008); Grumbine and Xu (2011); MRC (2011a); Lauri et al. (2012); Orr et al. (2012); Piman et al. (2013); Arias et al. (2014); Cochrane et al. (2014); Lu et al. (2014); [9]Kondolf et al. (2014); Manh et al. (2015), Rubin et al. (2015); Räsänen et al. (2017); Dang et al. (2018)

Dang et al. (2018) investigated future hydrological alterations based on several threats. The authors concluded that the Cambodian floodplains would be most affected by upstream damming. The Vietnamese Mekong Delta would be most affected by water infrastructure in

the wet season and sea level rise in the dry season, with planned canal widening found to make little difference to the flood depth. In the coastal regions, land subsidence and sea level rise are predicted to have the greatest impact. It should be noted that the Mekong Delta is a highly dynamic system (Le et al., 2018) that has rapidly changed in the past 2 decades making understanding the threats and challenges extremely challenging.

3.4.2 Flooding in the Mekong Delta

Flooding in the delta occurs annually. Nguyen et al. (2007) estimated that 2.5 million people in the VMD live in areas affected by deep flood water (up to 3 metres) and 3 million in areas affected by medium flooding (up to 1.5 metres). However, too much flooding causes damage to crops and infrastructure, as well as fatalities. Causalities occur either as the flood hits or as people are living for several weeks on water, epidemic diseases (such as marsh fever, dengue and diarrhoea) spreads and threatens the most vulnerable (Nguyen et al., 2007). The most severe recent flood occurred in 2000, causing an estimated 500 fatalities and US$500 million worth of damage (Hien et al., 2005, Chinh et al., 2016). Yet this flood only had an estimated return period of one in 20 years (Le et al., 2007). Consequently, the Vietnamese government embarked on a major flood defence project, particularly focused in the north of the VMD. Other, 'living with flood' strategies have been applied, including moving households from flood prone areas to safe locations and diversifying crops to reduce potential losses (Chinh et al., 2016). The effects of the flood defence projects were noted by Dang et al. (2016) as the 2011 flood was hydrologically similar, but considerably less inundation occurred in some regions. Other damaging floods with costs over $US 50 million occurred in 1991, 1994, 1995, 1996, 2001, 2002 and 2011 (Chinh et al., 2016). Flood relief and disaster recovery are implemented by Vietnamese political and social organisations as well as some international organisations. Government efforts tend to focus on recovering public infrastructure, with support for affected households being very limited (Garschagen, 2013), with no flood insurance in the area (Chinh et al., 2016).

However, benefits of small to medium scale flooding outweighs the disadvantages, and are indeed welcome (Duc Tran et al., 2018). Small and medium scale floods bring supplies of fertile sediment and fish which are pivotal for those who rely on agriculture for their

livelihoods (Käkönen, 2008, Hung et al., 2012). These floods are known as the 'beautiful' floods (Nguyen et al., 2007). It is estimated that approximately 160 million tons of fluvial sediment is deposited annually by seasonal floods (Tri et al., 2013, Marchand et al., 2014). In addition, small and medium scale flooding improves soil fertility by flushing fields, reducing harmful toxins and salinity (Nguyen et al., 2007, Hung et al., 2012). With increased intensification of rice cultivation and a shift towards triple cropping (Kontgis et al., 2015, Nguyen et al., 2016), dike height has increased meaning fields are no longer flushed naturally (Duc Tran et al., 2018). The recently endorsed Mekong Delta Plan [MDP] (Vietnam, 2013) recognizes the environmental sustainability challenges of the high dikes associated with triple rice cropping and proposes a shift back towards controlled flooding, thus the contesting policy of flood prevention that has dominated the last several decades. With reference to the '9 dragons' popular name of the Mekong, van Staveren et al. (2018) calls this encouraged seasonal flooding as the 'tenth dragon'. Yet, despite rules stating that 8 crops should be grown within 3 years (the so called 3-3-2 cycle), allowing for recovery of the paddy system, this is largely ignored as the economic benefits outweigh the costs (Chapman et al., 2016, Tran and Weger, 2017, Tran et al., 2018b). This triple rice cropping system has increased the reliance on fertilisers and pesticides (Howie, 2011) and reduced the importance of the 'beautiful' flood. In general farmers feel less connected to the natural regime, with the intensification of rice cultivation being recognized as the main reason why ecosystem services has reduced (Berg et al., 2017). This situation could potentially change with Tran et al. (2018a) concluding that the long-term economic benefits are only marginally improved compared to sticking with double cropping, and that alternative farming methods/diversification can offer greater economic benefits. Additionally, farmers are concerned with environmental sustainability, but the stable rice market and lack of promotion of other farming methods makes a shift towards controlled flooding difficult (Tran et al., 2018b).

Awareness of a positive perception of flooding is useful when considering flood inundation modelling as the general discourse around the subject portrays flooding as being negative or even catastrophic. If flooding is welcomed, consideration of what constitutes 'good' and 'bad' flooding is an important question when communicating the risk to the users. Indeed, it

is a paradox to the general conception of flood risk, with small scale and regular flooding potentially enhancing economic wellbeing and safety.

3.4.3 Flood Models in the Mekong Delta

Despite the relative lack of data, there are several flood inundation models of the Mekong Delta across a range of scales and complexities. Table 3-2 provides details of flood inundation models in the Mekong Delta, with Table 2-2 in section 2.2.2 reminding the reader of the model types. However, many of the models are very detailed and use non-freely available data. Whilst this is valuable, it is difficult to easily reproduce for other data-sparse deltas. Most of the models use a 1D river channel representation plus a storage cell representation of floodplain areas, with only the Apel et al. (2016) study using a 2D modelling approach like this study. However, the Apel et al. (2016) 2D model is only for Can Tho city and utilises a bespoke '1D plus storage cell' model developed by Dung et al. (2011) as a boundary condition. All these studies, except Yamazaki et al. (2014b) rely on some non-freely available data. Additionally, none of the models use the Multi Error Removed Improved Terrain (MERIT) DEM, with elevation errors in this data source shown to be noticeably reduced in the Mekong Delta (Yamazaki et al., 2017). In addition, the models outlined in Table 3-2 do not always include a tidal downstream boundary condition. Therefore, the intermediate scale (540 m) LISFLOOD-FP subgrid model built in this chapter fills an important gap within the suite of Mekong Delta models, as it is a 2D model across the whole delta which has a computation time that allows for scenario analysis but has sufficient complexity to simulate comparatively detailed patterns of flood inundation.

Table 3-2 Flood Models in the Mekong Delta

Study	Simulation Period	Type	Resolution	Study Extent	Data Used
Zanobetti et al. (1970)	Not Specified	1D channel and storage units	300 meshes	Cambodia and Vietnam	Field Studies
Khue (1986)	1996 in Wassmann et al. (2004)	1D channel and storage units	1,505 nodes and 555 storage cells	Cambodia and Vietnam	Water level and discharge from gauges. Rainfall and Evaporation.
Dutta et al. (2007)	01/07/2002 – 31/10/2002	1D channel and storage units	1km	Cambodian Floodplain	Largely from Mekong River Commission (MRC). Freely available.
Le et al. (2007)	01/06/2002 – 31/12/2002	1D channel and storage units	100m	Cambodia and Vietnam	Gauge information from Mekong River Commission (MRC but dike/sluice information not freely available.

Study	Simulation Period	Type	Resolution	Study Extent	Data Used
Hoa et al. (2008)	01/07/2000 – 30/11/2000 & 01/07/2001 – 30/11/2001	1D channel and storage units	100m	Cambodia and Vietnam	Gauge information from Mekong River Commission (MRC) but dike/sluice information not freely available.
Dung et al. (2011)	01/06/2008 – 31/12/2008	Quasi 1D/2D model based on MIKE 11	Compartments and branches used for floodplain	Cambodia and Vietnam	Mekong River Commission (MRC) and Shuttle Radar Topography Mission (SRTM) data (Freely available). Some additional weir/dike information (Not freely available).
Duong et al. (2014)	2000 & 2011	Quasi 1D/2D model based on MIKE 11	Compartments and branches used for floodplain	Cambodia and Vietnam	Same as Dung et al. (2011)
Manh et al. (2014)	2009 - 2011	Quasi 1D/2D model based on MIKE 11 coupled with sediment transport model	Compartments and branches used for floodplain	Cambodia and Vietnam	Same as Dung et al. (2011) but 11 zones used instead for zonation of parameters.

Study	Simulation Period	Type	Resolution	Study Extent	Data Used
Yamazaki et al. (2014b)	01/05/2001 – 30/04/2002	1D+ Global hydrodynamic model (CaMa Flood)	10km	Cambodia and Vietnam	Mekong River Commission (MRC) and Global Width Database for Large Rivers (GWD-LR) (Freely Available)
Apel et al. (2016)	26/09/2011 – 02/10/2011 & 24/10/2011 – 31/09/2011	1D channel and storage units model fed boundary to 2D model for Can Tho	15m	Can Tho city	Mekong River Commission (MRC) and WISDOM Project data (Freely available). 5 and 15m DEM (Not freely available)
Triet et al. (2017)	2000 & 2011 floods	Quasi 1D/2D model based on MIKE 11	Compartments and branches used for floodplain	Cambodia and Vietnam	Mekong River Commission (freely available) Other gauge data from Southern Regional Hydro-Meteorology Center of Vietnam (SRHMC). Dike information from Southern Institute of Water Resources research (SIWRR) and LIDAR DEM from Ministry of Natural Resources and Environment of Vietnam (MONRE). Not freely available

Study	Simulation Period	Type	Resolution	Study Extent	Data Used
Dang et al. (2018)	2000 and future scenarios	Quasi 1D/2D model based on MIKE 11	Compartments and branches used for floodplain	Cambodia and Vietnam	Based on Dung et al. (2011) model with 6 future scenarios.
Duc Tran et al. (2018)	2011 & 2013	Quasi 1D/2D model based on MIKE 11	Compartments and branches used for floodplain	Cambodia and Vietnam	Based on Dung et al. (2011) model with updated dike information from SIWRR. SRTM used for DEM
Ngo et al. (2018)	2000-2002;2011	1D SWMM Model	37 Nodes and 40 Links	Can Tho City	Gauge information from Mekong River Commission (MRC)

3.5 Methodology

An intermediate scale hydrodynamic model that will run multiple simulations requires a computationally efficient numerical scheme and a model structure that does not rely on detailed field data being available. The coastal nature of the domain also dictates that the model must be able to simulate backwater effects and bifurcations.

3.5.1 Choice of Model

Based on the aforementioned required model specifications, the raster-based hydrodynamic model LISFLOOD-FP version 6.3 (Neal et al., 2012a) was chosen. Alternative 2D models such as TUFLOW or Mike 21 could have been used, but LISFLOOD-FP was chosen as 2D models generally produce similar results if set up in a controlled way (Hunter et al., 2008, Neal et al., 2012b), with LISFLOOD-FP being particularly attractive owing to its speed and having access to the source code. In this version of LISFLOOD-FP the river channel and floodplain flow are represented using the local inertia approximation of the 1D Saint-Venant equations. The subgrid version of LISFLOOD-FP implements a sub-grid scheme for channel flow, so channels below model resolution can be represented in an efficient manner. In a regional scale deltaic context this is especially useful as the domain size means that a relatively coarse (>100 m) model resolution can be used whilst still representing the complex network of smaller channels that cross the study area. In a study on the Niger Delta, Neal et al. (2012a) found that including subgrid channels in the floodplain increased model accuracy when compared to a model without channels (2D), a model without a floodplain (1D) and a model of the main channels and floodplain (1D/2D). Therefore, a sub-grid model can represent river-connectivity provided by smaller channels at an intermediate scale, with these smaller channels being prevalent in deltaic environments. Furthermore, the model can simulate backwater effects which can be important when high river flows interact with high tides, compounding the flood hazard. In previous studies, LISFLOOD-FP has been found to become unstable at low Manning's Friction values (less than 0.01), or under supercritical flow conditions (Bates et al., 2010, de Almeida et al., 2012), but these conditions are not present in a deltaic environment. Lastly, LISFLOOD-FP is computationally efficient,

with recent optimization of the code reporting a 4-8x performance increase for a single core and 34-60x when combined on 16 cores compared to a single core model, with performance comparing favorably to other commercial models (Neal et al., 2018).

LISFLOOD-FP simulations of large-scale floodplains have been conducted in several regions the Amazon (Wilson et al., 2007, Baugh et al., 2013), Damador (Sanyal et al., 2013), Logone (Fernández et al., 2016), Gambia (Ettritch et al., 2018), Ob (Biancamaria et al., 2009), Oti (Komi et al., 2017), Niger (Neal et al., 2012a) and Zambezi (Schumann et al., 2013). Recently LISFLOOD-FP has been applied at a global scale (Sampson et al., 2015). However, there has yet to be a study that specifically examines the sub-grid model's performance in a large coastal delta that is subject to substantial anthropogenic influences.

Because of the above, the choice of LISFLOOD-FP is justified. The model does not rely on detailed inputs making it appropriate for data-sparse environments, and the computational efficiency allows for Monte Carlo simulations.

3.5.2 Model Setup

The core inputs for the model are topography, upstream and downstream boundary conditions (discharge upstream, stage downstream), channel width and channel and floodplain roughness parameters. Optional inputs include channel bathymetry, evaporation, precipitation and channel shape where such data are available. When bathymetry is not known, approximations can be made using hydraulic geometry theory (Leopold and Maddock, 1953), based on empirical relationships between remotely sensed river widths and bank height.

3.5.2.1 Topography

Topography is a crucial factor in the estimation of flood extent (Horritt and Bates, 2002). Digital Elevation Models (DEM) provide a gridded representation of topography and are frequently used in geoscience models. From previous studies, we know that the quality of the DEM affects the quality of flood estimates, with higher resolution DEMs typically giving more accurate flood estimates (Horritt and Bates, 2001a, Fewtrell et al., 2008, Neal et al., 2009b, Fewtrell et al., 2011, Jarihani et al., 2015, Savage et al., 2016a, Savage et al., 2016b).

However, this comes at a computational cost with Savage et al. (2016b) noting that halving the model resolution in LISFLOOD-FP increases the simulation time by an order of magnitude. The use of a high-resolution DEM (<30m) is also restricted by data availability. High resolution DEMs, most commonly created using LIDAR technology, are rarely freely available and are largely confined to developing countries.

From previous flood studies in the Mekong Delta (Apel et al., 2016, Triet et al., 2017), we know that LIDAR data exists for the Vietnamese part of the delta. However, this LIDAR data were not freely accessible. Late into the project, LIDAR data for An Giang province was acquired, which allowed for multiple DEMs to be used in the model build (LIDAR, MERIT, SRTM) and subsequently for the analysis of how different DEM products impact flood predictions. Concurrently, a field campaign in September 2017 to Cambodia and Vietnam was completed as part of an expedition led by the University of Hull and the university of Southampton in the UK. As part of the field campaign ground observations of elevation were collected using a Leica GNSS receiver which were then used to assess the accuracy of the global DEM products (MERIT & SRTM).

As a result of the limited access to hyper-scale/high-resolution LIDAR data, an open-access global DEM is needed. Even if the all the available LIDAR data were obtained, it remains to be seen how the LIDAR data would have been integrated with other DEMs as Cambodia does not have any LIDAR data as far as the authors are aware. The Shuttle Radar Topography Mission (SRTM) is the most widely used global DEM, covering 99.97% of the Earth's land surface between 56°S and 60°N at resolutions of 3 arc seconds (≈90 m) and more recently at 1 arc second (≈30 m) (Rabus et al., 2003, Farr et al., 2007). Various versions of SRTM exist, with the CGIAR-CSI developed void filled version (Jarvis et al., 2008) the most widely used. Other freely available DEMs include the Advanced Spaceborne Thermal Emission Radiometer at 90 m resolution (ASTER) (Abrams, 2000), and the Advanced Land Observing Satellite (ALOS AW3D30) (Takaku and Tadono, 2017) at 30 m resolution. The recent DLR (German Space Center) TanDEM-X global DEM at 12.5 m resolution has potential to give more accurate flood estimates (Archer et al., 2018), but is only available for educational purposes via a lengthy application, with the area to be requested smaller than the study area being considered here. Despite being acquired in 2000, the SRTM DEM is still

the most popular global DEM because of its better accessibility, feature resolution and vertical accuracy and a smaller number of artefacts and noise compared to alternative global DEMs (Jing et al., 2014, Rexer and Hirt, 2014, Jarihani et al., 2015, Sampson et al., 2016, Hu et al., 2017) . As a result, the CGIAR-CSI developed void filled version SRTM DEM was used in this study.

Even though SRTM is widely used, there are numerous critical issues. Sampson et al. (2016) highlight five issues of these: 1) poor vertical accuracy due to noise (see Rodriguez et al., 2006 for detail); 2) difficulty in resolving a bare-earth DEM due to radar reflection from the top of the vegetation canopy and within it; 3) large positive elevation biases in urban areas due to the inability to resolve street-scale features, often resulting in urban areas unrealistically not flooding; 4) systematic errors relating to instrument pitch and yaw resulting in "striping"; 5) inability to resolve bathymetry of water bodies due to radar reflection. As a result, numerous efforts have been made to correct errors, such as void filling (Jarvis et al., 2008), hydrological correction (Lehner et al., 2008) and the removal of vegetation bias (Baugh et al., 2013, O'Loughlin et al., 2016b, Zhao et al., 2018, Pinel et al., 2015). Absolute bias in floodplains is relatively low, with the majority of error being random error which has been found to be approximately 6 m for SRTM data (Rodriguez et al., 2006).

This chapter also uses a recently released multiple error removed version of the Shuttle Radar Topography Mission (SRTM) called the Multi-Error-Removed-Improved-Terrain (MERIT DEM) (Yamazaki et al., 2017). In the MERIT DEM, errors have been reduced by separating absolute bias, stripe noise, speckle noise and vegetation bias with the most noticeable improvements in accuracy reported in flat regions (Yamazaki et al., 2017). With fewer artefacts (Hirt, 2018) and a better performance in flood models compared to SRTM (Chen et al., 2018), the MERIT DEM is to date the most effective global DEM correction. With the MERIT DEM being comparatively new, few flood studies have used it, thus, to test the impact of reduced errors, it is included in this study. It should also be noted the MERIT does not currently correct for urban biases, nor does it consider bathymetry.

3.5.2.2 Choice of model resolution

Many modellers tend to focus on the nominal resolution of the DEM, but the vertical accuracy is of greater importance to flood modelling (Sampson et al., 2016). Numerous studies have found that model performance improves with increasing resolution but this plateaus when a certain resolution is reached (Horritt and Bates, 2001a, Fewtrell et al., 2008, Savage et al., 2016b). For LISFLOOD-FP, halving the model resolution increases the computational run time by an order of magnitude (Savage et al., 2016b), so a trade-off between resolution, vertical accuracy and run time is needed. This is especially important when multiple models are being run for probabilistic flood predictions or future scenario analysis.

Floods are essentially a shallow water flow, meaning vertical noise within a DEM alters the flood dynamics as noisy pixels act as blockages or sinks. To reduce random noise in the DEM, the grid size can be resampled to a coarser resolution. By aggregating, elevation errors cancel out to some extent with the assumption of random noise. The standard deviation of the SRTM error is unknown for the Mekong Delta. Rodriguez et al (2006) found elevation errors to be 4.68 m for Africa, and Yamazaki et al (2017) a value of 5 m for flat areas, so we will assume an error of 5 m for this study. Assuming errors are normally distributed, the sampling error in the aggregated cell will decrease based on $1/\sqrt{N}$, where N is the number of observations. In reality, the error in the DEM sample will not have a zero mean, be normally distributed or be spatially uncorrelated, meaning this approach will underestimate the error in the DEM. Nevertheless, it can be a useful guide when choosing a resolution. To obtain a difference of less than 1m between two aggregated blocks with a probability of 95%, Neal et al (2012) aggregated 100 SRTM pixels giving a model resolution of 900 m (10x10 90 m pixels) for their study of the Niger Delta. As computational power has increased since the Neal et al (2012) study, so a model resolution of 540 m is used in this study (i.e. 6x6 SRTM cells). The standard deviation of errors reduces to 0.83 m for this aggregation block size under the best-case scenario of random normal errors. Typical small scale-scale floodplain features that control inundation in the delta are embankments that are in the order of 1-3 m in height, thus the standard deviation of errors for a 540 m block at 0.83 m is appropriate. Yet the floodplain topography is spatially complex, especially in the Vietnamese part of the

Delta where embankments border the dense network of channels, thus a coarser resolution is inappropriate as the spatial complexity would be lost. This trade-off allows for an appropriate model run time and minimizes the loss of small-scale features.

3.5.2.3 Upstream Boundary

Daily inflows for the main stem were available from the Kratie gauging station, available from the Mekong River Commission (hereafter known as MRC). Due to the importance of the Tonle Sap Lake on the regional hydrodynamics, the model also needs inflows and outflows from the Tonle Sap Lake. A reliable long-standing record of flow does not exist for the Tonle Sap River, so flow estimates from a detailed water balance model of the Tonle Sap Lake developed by Kummu et al. (2014) were used. The water balance model of the Tonle Sap Lake of Kummu et al. (2014) was constructed using measured data and compared well with simulation results.

3.5.2.4 Downstream Boundary

Tidal heights at each Mekong outlet were used as downstream boundary conditions for the model and are estimated using harmonic analysis. First, 18 constituents covering both diurnal and semi-diurnal constituents were extracted from the FES2014 global tide model (Carrere et al., 2015), and then processed through the T-Tide package in Matlab (Pawlowicz et al., 2002). A selection of 18 constituents were made to cover the main tidal signals. The result is tidal height estimates on a 1/16° grid at every 15 minutes. The closest grid to an outlet is assigned to that outlet (Figure 3-3). This technique provides hindcast and future tide predictions and thus is applicable to a wide range of flood modelling applications where detailed data are unavailable.

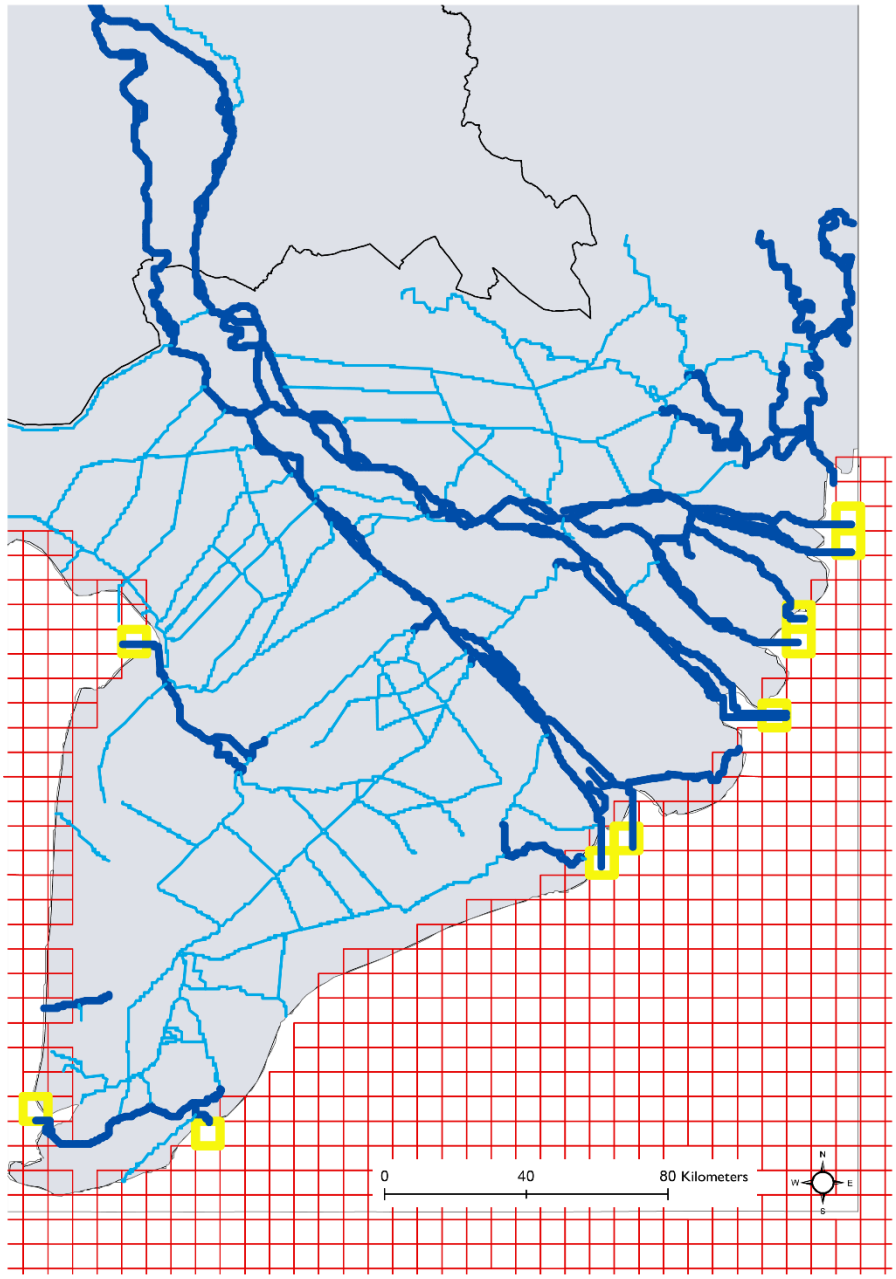

Figure 3-3 FES2014 Global Tide Model cells (red) and selected cells that overlap outlets (yellow)

3.5.2.5 Channel Widths

Today, several global river width databases and tools are available (Andreadis et al., 2013, Yamazaki et al., 2014a, Pavelsky and Smith, 2008, Allen and Pavelsky, 2018). These products

are either based on hydraulic geometry relationships (Andreadis et al., 2013) or satellite image processing techniques (Pavelsky and Smith, 2008, Yamazaki et al., 2014a). For this study, the GWD-LR database of Yamazaki et al. (2014a) was used. The GWD-LR product is derived from Landsat imagery and flow direction maps based on the SRTM Water Bodies and the HYDROSHEDS flow direction map. The code of GWD-LR was edited to reduce the island threshold value, thus allowing for channels that flow around islands to be delineated. Otherwise, branching of the river is not represented, with the channel appearing to go right through an island. The output was processed to ensure connectivity and then converted to a kml file to visually inspect and edit within Google Earth™. The limitation of this product is that the minimum channel width detected was 170 m, so only a limited number of channels outside the main stem were detected. To supplement this product we gained additional channel data from the WISDOM project, which consists of shapefiles of width and depth values for surveyed channels of >20 m in the Vietnamese Mekong Delta (WISDOM, 2016). Even with this additional dataset, some channels are still missing. The importance of including smaller channels in the flood estimates is unknown and, thus, was tested in this study.

3.5.2.6 Channel Bathymetry

Bathymetry data exist for the main stem for the years 1998 and 2008 and were supplied by the MRC. This consists of cross section surveys with points at approximately every 100 m. Approximately 250 m separate each cross-sectional survey. Uncertainty in the data comes from the lack of consensus about converting the vertical datum used (Ha Tien 1960) to the vertical datum of SRTM (EGM96). The 1998 dataset covers the mainstem of the whole domain but not the Bassac from Phnom Penh to Vam Nao (see Figure 3-2 for a reminder of locations), whilst the 2008 dataset covers a limited area of the Vietnamese main stem. The average elevation from the cross-sectional survey was taken as the bed elevation value for the channel pixels within the hydrodynamic model. This negates the impact of pits in the channel. When bed elevations were not known, they were linearly interpolated based on nearby channel slopes. Yet, for most data-sparse deltas, no bathymetry information was available, so model performance assuming no prior knowledge of bathymetry was also tested. This was investigated to determine how much influence bathymetry data had on

model performance. Previous studies have used bankfull discharge to estimate channel depth with Manning's equation (Andreadis et al., 2013) (equations 15,16)

$$Q_{bf} = \frac{1}{n} h^{\frac{5}{3}} \sqrt{S} W \tag{15}$$

Where Q_{bf} = bankfull discharge; n = Manning's channel roughness coefficient; h = channel depth; S = Water surface slope; W = width

To calculate channel depth, the values of the roughness coefficient, slope and width will remain the same for each channel pixel within a reach throughout the duration of the simulation. The roughness coefficient is estimated based on the best value from the All Bathymetry + Width model (Table 3-4) and the width is already known from the GWD-LR database and WISDOM project dataset. Water surface slope can be estimated from the slope of the DEM, satellite radar altimetry data or from gauges. As the study area has several water height gauges, slope is estimated by interpolating water surface heights between them. This can be supplemented with altimetry data such as ICESat (O'Loughlin et al., 2016a). Thus, the only varying parameter is the value of bankfull discharge. In general, bankfull discharge is considered to be a flow with a return period between 1 and 2.5 years for natural stable rivers (Andreadis et al., 2013, Pickup and Warner, 1976). Flooding occurs annually in the Mekong Delta, so the mean annual flow is used as a base bankfull discharge estimate. Typically, a more extreme flow is used, but as the delta floods for several months a year a lower value (in this case the mean annual flow) is used as the maximum annual flow would be an overestimation of the bankfull discharge. Subsequently, the mean annual flow (which is known as scale=1 in this chapter) is scaled to give a range of bankfull discharge values. Using the annual mean discharge is justified as the system floods for a prolonged period annually unlike most typical rivers. Bankfull discharge is assigned to each channel pixel based on the gauges along the reach associated with a gauge.

$$h = \frac{nQ_{bf}}{(\sqrt{S}W)^{\frac{3}{5}}} \tag{16}$$

An additional complication in a deltaic environment are bifurcations and flows around islands, so the discharge needs to be split otherwise an unrealistic depth value is assigned to the narrowing channels. To split the Q_{bf}, bifurcation points along the river network are identified. The widths of the two splitting channels are extracted, added together and then the percentage of this total for each channel calculated. Based on these percentages, the Q_{bf} is split. Using this technique, a set of river bathymetry estimates are generated.

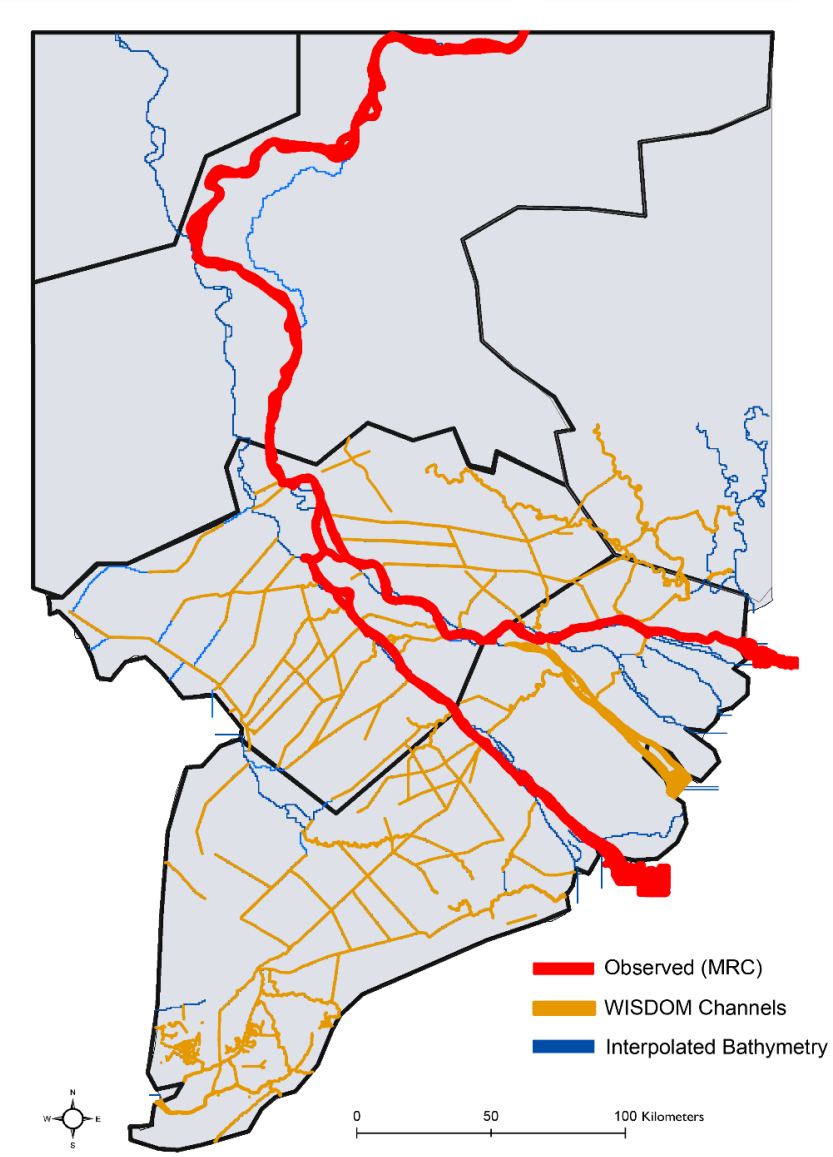

Figure 3-4 Bathymetry Data Coverage

3.5.3 Banks

To estimate channel bed elevation using the above technique, bank heights were required. This was achieved by using the river widths extracted from the GWD-LR database as a water mask and finding SRTM elevations on the outer edges of the channel. Due to the noise even in a vegetation smoothed DEM, these elevations must be smoothed to reduce errors in the bank heights used in the model. With the low gradient of the delta, a large smoothing window could be used following the principles discussed by Neal et al. (2012a) as the gradient of the delta is considerably less than the vertical error in the SRTM data. A 5 km window was chosen, so bank heights were estimated based on an average of SRTM elevations within the 5 km window.

3.5.3.1 Evaporation & Precipitation

For simplicity, uniform evaporation and precipitation rate were used. Several precipitation and evaporation measurements are available from the Mekong River Commission, but the data are largely incomplete. However, the meteorological station at Chau Doc has a complete record for the period required, so values from here were chosen as a representative rate. When local data are unavailable, global precipitation and evaporation products can be used.

3.5.4 Experimental Design

An initial benchmark model (called All Bathymetry + Width) was built using all available data at a resolution of 540 m. The All Bathymetry + Width model contained 375,472 cells, covering an area of 90,000 km^2. Of these cells, there were 13577 subgrid channel cells for the All Bathymetry + Width model, totaling over 7,300 km of river network. For the model variations with less channel detail, this figure was less. The All Bathymetry + Width model took 78 minutes per simulation year on a quad core 3.6 GHz Intel i7-4790 processor. Simulations were run for a 7-year period from 1 January 2001 to 31st December 2007. A sensitivity analysis on the All Bathymetry + Width model was then carried out by varying channel and floodplain friction values. These friction parameters can be estimated prior to running the model, but the relatively cheap computation time of the model allows for a

sensitivity analysis to be implemented. In a more data rich environment, the friction parameters can be provided by field survey, but for this study this were unavailable, so the range of friction values were estimated based on previous modelling versions of LISFLOOD-FP (Bates and De Roo, 2000, Bates et al., 2010, Neal et al., 2012a), other Mekong studies (e.g. Dung et al. (2011)) and inspecting land use maps and satellite imagery. Models were run using parameter values and sampling intervals as set out in For the DEM comparison a separate hydrodynamic model was built of An Giang Province, Vietnam. The year 2001 was chosen for simulation as this year had a large amount of damages (US$200 million), with approximately 300,000 homes damaged (Chinh et al., 2016). Only a single year was selected in the interest of computation time. The An Giang Province hydrodynamic model was run using LIDAR, MERIT and SRTM data at 3 arc-second resolution. Additionally, a 1 arc-second (30 m) LIDAR model was run to act as a benchmark. Hydrographs from Chau Doc and Vam Nao were taken as the upstream boundary conditions, whilst the downstream water level was set as the height of the Long Xuyen gauge. Channel widths were from the GWD-LR database (Yamazaki et al., 2014a) and bathymetry from the Mekong River Commission as in the larger Mekong Delta model presented in this chapter. DEM accuracy assessment of MERIT and SRTM were carried out by collecting ground observations using the Leica GS10 GNSS receiver. In total, 881 points were taken near Kampong Cham, Cambodia and Can Tho, Vietnam.

Table 3-3. The importance of having measured bathymetry in the model is tested by a collection of models known as Qbf Bathymetry + All Width which were constructed by scaling the bankfull discharge estimates (Table 3-3). To assess the importance of missing channels, additional channel detail provided by the WISDOM project was stripped away, based on intervals selected from the histogram of channel widths, with this model known as All Bathymetry + Reduced Channel Detail. Details of all the models are outlined in Table 3-4. Analysis of flood extent was analysed for three calendar years which were classified as climatologically wet, normal and dry (Table 3-5), to assess model performance for different severity of flooding. For the DEM comparison a separate hydrodynamic model was built of An Giang Province, Vietnam. The year 2001 was chosen for simulation as this year had a

large amount of damages (US$200 million), with approximately 300,000 homes damaged (Chinh et al., 2016). Only a single year was selected in the interest of computation time. The An Giang Province hydrodynamic model was run using LIDAR, MERIT and SRTM data at 3 arc-second resolution. Additionally, a 1 arc-second (30 m) LIDAR model was run to act as a benchmark. Hydrographs from Chau Doc and Vam Nao were taken as the upstream boundary conditions, whilst the downstream water level was set as the height of the Long Xuyen gauge. Channel widths were from the GWD-LR database (Yamazaki et al., 2014a) and bathymetry from the Mekong River Commission as in the larger Mekong Delta model presented in this chapter. DEM accuracy assessment of MERIT and SRTM were carried out by collecting ground observations using the Leica GS10 GNSS receiver. In total, 881 points were taken near Kampong Cham, Cambodia and Can Tho, Vietnam.

Table 3-3 Ranges of model parameters and calibration sampling intervals

Table 3-3 Ranges of model parameters and calibration sampling intervals

	Minimum	Maximum	Sampling Interval
Floodplain Friction	0.02	0.10	0.0050
Channel Friction	0.02	0.10	0.0025
Width Threshold	25	150	25
Qbf scaling	1	5	0.5

Table 3-4 Model Variants

Variant name	Floodplain Friction	Channel Friction	Channel Width	Channel Bathymetry	Number of models

All Bathymetry+ Width	Range from *For* the DEM comparison a separate hydrodynamic model was built of An Giang Province, Vietnam. The year 2001 was chosen for simulation as this year had a large amount of damages (US$200 million), with approximately 300,000 homes damaged (Chinh et al., 2016). Only a single year was selected in the interest of computation time. The An Giang Province hydrodynamic model was run using LIDAR, MERIT and SRTM data at 3 arc-second resolution. Additionally, a 1 arc-second (30 m) LIDAR model was run to act as a benchmark. Hydrographs from Chau Doc and Vam Nao	Range from *For* the DEM comparison a separate hydrodynamic model was built of An Giang Province, Vietnam. The year 2001 was chosen for simulation as this year had a large amount of damages (US$200 million), with approximately 300,000 homes damaged (Chinh et al., 2016). Only a single year was selected in the interest of computation time. The An Giang Province hydrodynamic model was run using LIDAR, MERIT and SRTM data at 3 arc-second resolution. Additionally, a 1 arc-second (30 m) LIDAR model was run to act as a benchmark. Hydrographs from Chau Doc	All available measured widths (GWD-LR & WISDOM datasets)	All available measured bathymetry. Missing values linearly interpolated	561

were taken as the upstream boundary conditions, whilst the downstream water level was set as the height of the Long Xuyen gauge. Channel widths were from the GWD-LR database (Yamazaki et al., 2014a) and bathymetry from the Mekong River Commission as in the larger Mekong Delta model presented in this chapter. DEM accuracy assessment of MERIT and SRTM were carried out by collecting ground observations using the Leica GS10 GNSS receiver. In total, 881 points were taken near Kampong Cham, Cambodia and Can Tho, Vietnam.

and Vam Nao were taken as the upstream boundary conditions, whilst the downstream water level was set as the height of the Long Xuyen gauge. Channel widths were from the GWD-LR database (Yamazaki et al., 2014a) and bathymetry from the Mekong River Commission as in the larger Mekong Delta model presented in this chapter. DEM accuracy assessment of MERIT and SRTM were carried out by collecting ground observations using the Leica GS10 GNSS receiver. In total, 881 points were taken near Kampong Cham, Cambodia and

Can Tho,

Vietnam.

Table 3-3

Table 3-3

Qbf Bathymetry + All Width	Best from All Bathymetry + Width model	Range from Table 3-3	All available measured widths	Estimated using Manning's Qbf technique. Scaled as outlined in *For* the DEM comparison a separate hydrodynamic model was built of An Giang Province, Vietnam. The year 2001 was chosen for simulation as this year had a large amount of damages (US$200 million), with approximately 300,000 homes damaged (Chinh et al., 2016). Only a single year was selected in the interest of computation time. The An Giang Province hydrodynamic model was run using LIDAR, MERIT and SRTM data at 3 arc-second resolution. Additionally, a 1 arc-second (30 m) LIDAR model was run to act as a benchmark.	330

Hydrographs from Chau Doc and Vam Nao were taken as the upstream boundary conditions, whilst the downstream water level was set as the height of the Long Xuyen gauge. Channel widths were from the GWD-LR database (Yamazaki et al., 2014a) and bathymetry from the Mekong River Commission as in the larger Mekong Delta model presented in this chapter. DEM accuracy assessment of MERIT and SRTM were carried out by collecting ground observations using the Leica GS10 GNSS receiver. In total, 881 points were taken near Kampong Cham, Cambodia and

Can Tho,

Vietnam.

Table 3-3

All Bathymetry + Reduced Channel Detail	Best from All Bathymetry + Width model	Range from *For* the DEM comparison a separate hydrodynamic model was built of An Giang Province, Vietnam. The year 2001 was chosen for simulation as this year had a large amount of damages (US$200 million), with approximately 300,000 homes damaged (Chinh et al., 2016). Only a single year was selected in the interest of computation time. The An Giang Province hydrodynamic model was run using LIDAR, MERIT and SRTM data at 3 arc-second resolution. Additionally, a 1 arc-second (30 m) LIDAR model was run to act as a benchmark. Hydrographs from Chau Doc	Width detail stripped away based on thresholds in *For* the DEM comparison a separate hydrodynamic model was built of An Giang Province, Vietnam. The year 2001 was chosen for simulation as this year had a large amount of damages (US$200 million), with approximately 300,000 homes damaged (Chinh et al., 2016). Only a single year was selected in the interest of computation time. The An Giang Province hydrodynamic model was run using LIDAR, MERIT and SRTM data at 3 arc-second resolution. Additionally, a 1 arc-second (30 m) LIDAR model was run to act as a	All available measured bathymetry. Missing values linearly interpolated	198

and Vam Nao were taken as the upstream boundary conditions, whilst the downstream water level was set as the height of the Long Xuyen gauge. Channel widths were from the GWD-LR database (Yamazaki et al., 2014a) and bathymetry from the Mekong River Commission as in the larger Mekong Delta model presented in this chapter. DEM accuracy assessment of MERIT and SRTM were carried out by collecting ground observations using the Leica GS10 GNSS receiver. In total, 881 points were taken near Kampong Cham, Cambodia and	benchmark. Hydrographs from Chau Doc and Vam Nao were taken as the upstream boundary conditions, whilst the downstream water level was set as the height of the Long Xuyen gauge. Channel widths were from the GWD-LR database (Yamazaki et al., 2014a) and bathymetry from the Mekong River Commission as in the larger Mekong Delta model presented in this chapter. DEM accuracy assessment of MERIT and SRTM were carried out by collecting ground observations using the Leica GS10 GNSS receiver. In total, 881 points were taken near Kampong Cham, Cambodia and

Can Tho, Vietnam.	Can Tho, Vietnam.
Table 3-3	Table 3-3

Table 3-5 Flood Extent Validation Period

Start Date	End Date	Description
20/07/2001	03/12/2001	Wet
01/05/2004	02/12/2004	Dry
10/06/2007	03/12/2007	Normal

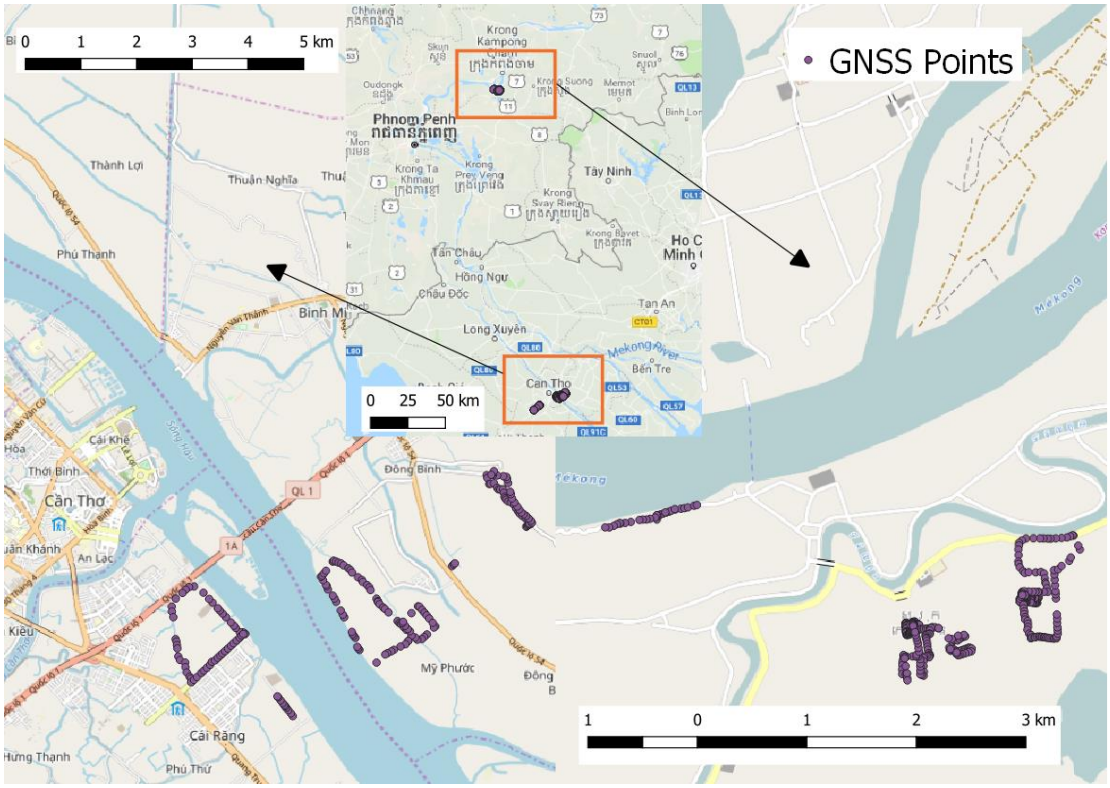

Figure 3-5 Elevation ground measurements using a Leica GS10 GNSS receiver (purple dots) for Can Tho, Vietnam (left) and Kampong Cham, Cambodia (right)

Figure 3-6 Surveying near Kampong Cham, Cambodia

3.5.5 Model Validation

An essential component of hydrodynamic model evaluation is the ability to validate the predictions against previous recorded measurements. In this chapter, a variety of local and global data were used to do this that are outlined below.

3.5.5.1 Observed Gauge Measurements

Daily records for four discharge gauges (Can Tho, Chau Doc, My Thuan and Vam Nao) and five water level gauges (Can Tho, Koh Khel, Tau Chau, Tra Vinh and Vam Nao) were used for validation (Figure 3-2). These gauges are maintained by the Mekong River Commission (MRC), with data available from their website. Gauge discharge errors are not reported. These gauges have been used in other Mekong models (Table 3-2) with no mention of errors.

3.5.5.2 Remotely Sensed Gauge Measurements

The gauge data has a limited spatial coverage, so to validate the model at additional spatial locations remotely sensed virtual gauges were derived. Snapshots of river water heights were used from the ICESat derived water surface heights dataset by O'Loughlin et al. (2016a). This database contains over 0.5 million quality checked transect averaged water surface heights from 2003-2009, with vertical accuracy of ~10 cm mean absolute error comparing favourably to other altimetry data such as from Envisat (mean absolute error ~28 cm) (O'Loughlin et al., 2016a). Whilst, ICESat derived water heights are a useful tool to broaden spatial coverage of validation, the record is temporally sparse and limited to a relatively short period.

3.5.5.3 Flood Extent

Surveyed flood extents exist for the Mekong Delta (Ling et al., 2015, Chinh et al., 2016) but these are limited in spatial and temporal coverage so are not appropriate for a study area of this size. For a study area of the Mekong Delta, flood extent measured by remote sensing is appropriate as it covers a large area. Remote sensing of flooding can be based on either optical or SAR (Synthetic Aperture Radar) imagery. SAR works by beaming a signal to the Earth's surface and recording the backscattered signal at a receiving unit. The major advantage of SAR is that it can penetrate clouds that commonly exist during flood events

and work day or night, so it is the preferred method for flood inundation mapping (Di Baldassarre et al., 2011, Matgen et al., 2007). Several studies have delineated flood extent in the Mekong Delta using optical (from the Moderate Resolution Imaging Spectrometer (MODIS) sensor) and SAR (from ENVISAT-ASAR-WSM) imagery. Details of the mapped flooding in the Mekong Delta are found in Table 3-6. In general, flood maps of Mekong Delta generated by remote sensing have been reported to underestimate flooding, particularly in urban and heavily vegetated areas (Table 3-6) (Kuenzer et al., 2013). The MODIS record provided by Dr Kotera was used as it covered the period simulated in this chapter in its entirety. In Kuenzer et al. (2015), MODIS based flood inundation mapping of deltas was reported to have an accuracy of between 79-99%, with errors mostly occurring at water boundaries. Furthermore, rice paddies are often classified as flooded, which is the reality, but one could question whether these should be included for validation purposes as these rice paddies are deliberately flooded and can have a shallow water depth. To be used to calculate skill scores, the MODIS data needed to be resampled to 540 m, which was carried out using bilinear resampling. There was relatively little difference in scale between MODIS resolution (250 m) and model resolution (540 m), so the error introduced to the resampled MODIS data by interpolation was likely to be minimal.

Table 3-6 Remotely Sensed Flood Inundation Extent of the Mekong Delta

Satellite	Time Frame	Resolution	Limitations	Author(s)
MODIS	2000-2005 8-day composite	500m	Separating 'mixed' pixels from water pixels a challenge	Sakamoto et al. (2007)

Satellite	Time Frame	Resolution	Limitations	Author(s)
MODIS	2013	250m	Water Bodies below resolution not detected. Sediment rich water not detected as water bodies. Detection accuracy could be improved by including more bands. Results in underestimation of water surface.	Kuenzer et al. (2015)
MODIS	2000-2015 8-day composite	250m	Separating 'mixed' pixels from water pixels a challenge. Will not penetrate through vegetation In Chao Phraya, Thailand, flood overestimated.	Data supplied by Dr Akihiko Kotera using technique from Sakamoto et al. (2007) Related papers - (Kotera et al., 2016)
ENVISAT-ASAR-WSM	2007-2011 Repetition Rate 35 days	150m	Poor detection of flooded areas under vegetation. Particularly a problem for mangrove areas and overgrown banks. When there are multiple surfaces within a cell, the returned signal is too 'bright' for the flood detection algorithm, thus some cells that are partially flooded go un-detected. Urban areas often appear never flooded.	Kuenzer et al. (2013)

3.6 Results

In total, 1,079 models were run with model performance assessed by comparing to four discharge gauges, five stage gauges, ICESat records and MODIS. Performance metrics used are root mean square error (RMSE), Nash-Sutcliffe efficiency (Nash and Sutcliffe, 1970), and Critical Success Index (CSI).

3.6.1 Simulation of Water Level & Discharge

Water levels were evaluated using five gauges and ICESat data. The RMSE range for the gauges was between 0.436 m and 0.889 m for the most detailed model (All Bathymetry + Width) (Table 3-7 & Table 3-8). These RMSE values compare well the error from random noise in the DEM that is 0.83 m for the 540 m resolution that the models are run at. Results from the sensitivity analysis indicate that model performance is best (by RMSE and NSE scores) at lower friction values, and that water level is barely sensitive to the floodplain friction parameter. The ICESat results provide a further useful validation dataset even though the number of observed points is limited. There is very good agreement with ICESat 1 Stage point. However, for ICESat 2 Stage point there are several potentially erroneous points, which could be due to the ICESat signal deflecting off boats.

Table 3-7 Optimal RMSE values for the All Bathymetry + Width model with associated Manning's friction values for 2001-2007.

	Overall	Kok Khel	Tan Chau	Vam Nao	Can Tho	Tra Vinh
RMSE (m)	0.688	0.678	0.889	0.641	0.436	0.805
Floodplain *n*	0.020	0.020	0.020	0.020	0.100	0.020
Channel *n*	0.020	0.035	0.020	0.020	0.020	0.020

Table 3-8 Optimal RMSE values for the All Bathymetry + Width model with associated Manning's friction values for 2001-2007 when only considering flows above the annual median

	Overall	Kok Khel	Tan Chau	Vam Nao	Can Tho	Tra Vinh
RMSE (m)	0.608	0.493	1.211	0.608	0.353	0.668
Floodplain *n*	0.020	0.020	0.020	0.020	0.100	0.020
Channel *n*	0.020	0.035	0.020	0.020	0.025	0.060

Table 3-9 Optimal NSE values for the All Bathymetry + Width model with associated Manning's friction values for 2001-2007

	Overall	Chau Doc	My Thuan	Vam Nao	Can Tho
NSE	0.627	0.746	0.493	0.904	0.459
Floodplain *n*	0.095	0.100	0.095	0.040	0.020
Channel *n*	0.035	0.035	0.040	0.027	0.035

Discharge results had a higher NSE score (1 corresponds to perfect match) at the upstream gauges. This is primarily due to the difficulty of accurately simulating the backwater effect from the tides due to the lack of bathymetry data. Additionally, by moving downstream more bifurcations are present. There is a lack of knowledge about how flows split at these bifurcations due to a lack of detailed data, with these errors propagating by moving downstream. Like the water level, discharge is not sensitive to the floodplain friction parameter, with optimum model performance between 0.027 – 0.040, which is typical for agricultural floodplains.

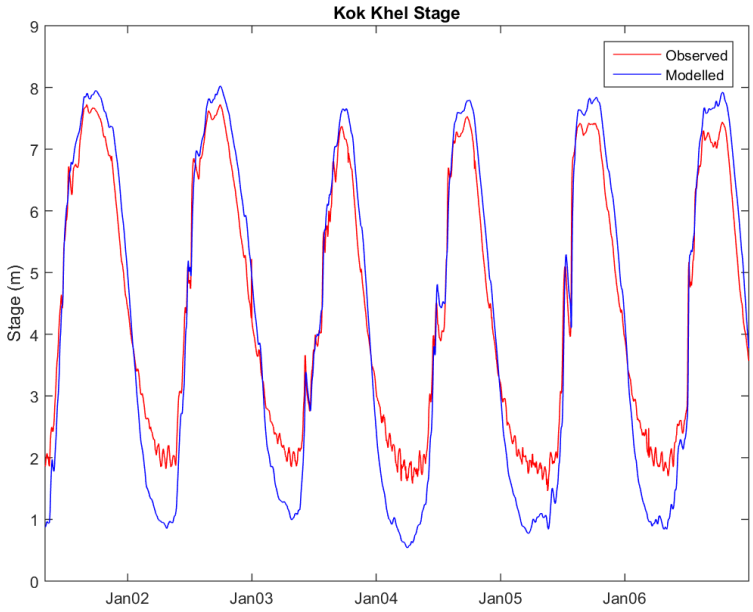

Figure 3-7 Daily observed and simulated water level for Koh Khel for 2001-2007 for best performing All Bathymetry + Width model. Observed water level in red and simulated water level in blue.

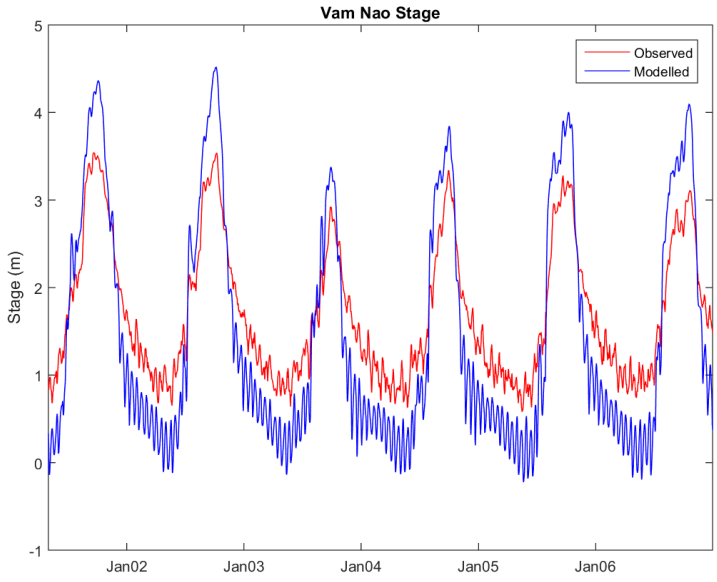

Figure 3-8 Daily observed and simulated water level for Vam Nao for 2001-2007 for best performing All Bathymetry + Width model. Observed water level in red and simulated water level in blue.

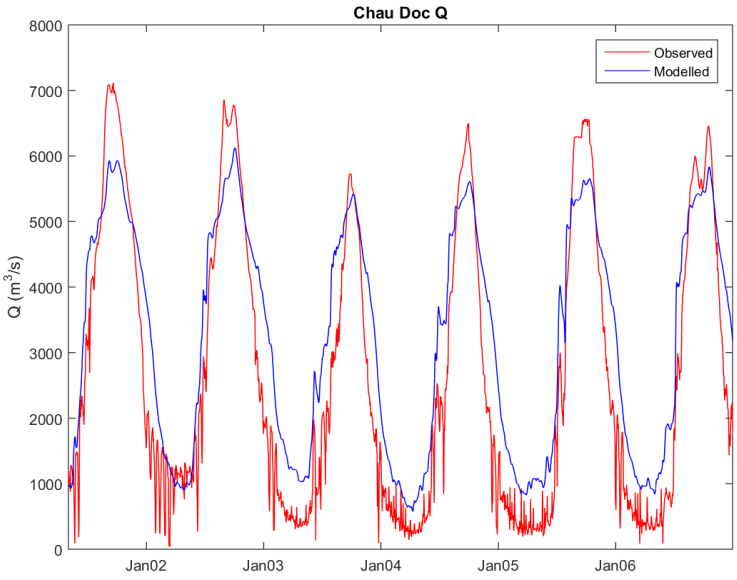

Figure 3-9 Daily discharge at Chau Doc for best performing for best performing All Bathymetry + Width model. Observed water level in red and simulated water level in blue.

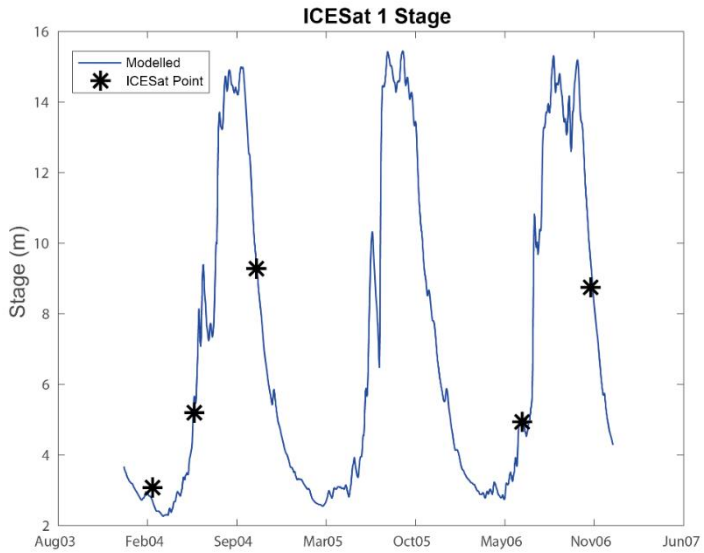

Figure 3-10 Simulated daily water level for best performing All Bathymetry + Width model at ICESat point 1 (see Figure 3-2 for location). Observations from the ICESat satellite are shown by the black marker and the daily simulated water level is shown by the blue line.

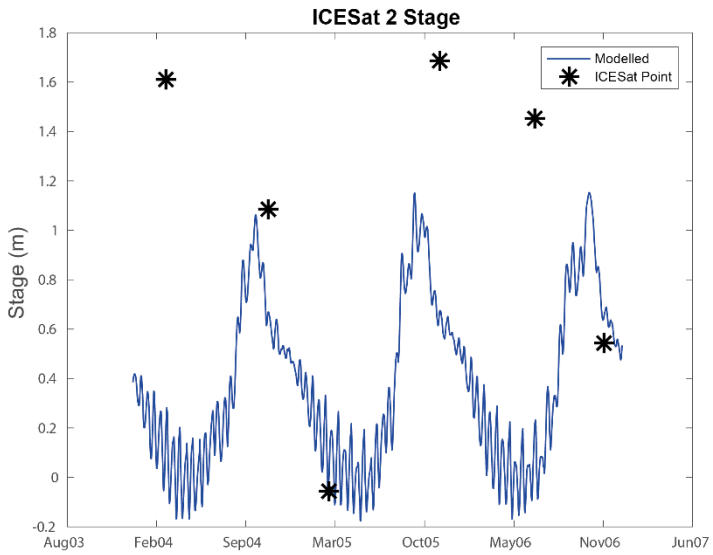

Figure 3-11 Simulated daily water level for best performing All Bathymetry + Width model at ICESat point 2 (see Figure 3-2 for location). Observations from the ICESat satellite are shown by the black marker and the daily simulated water level is shown by the blue line.

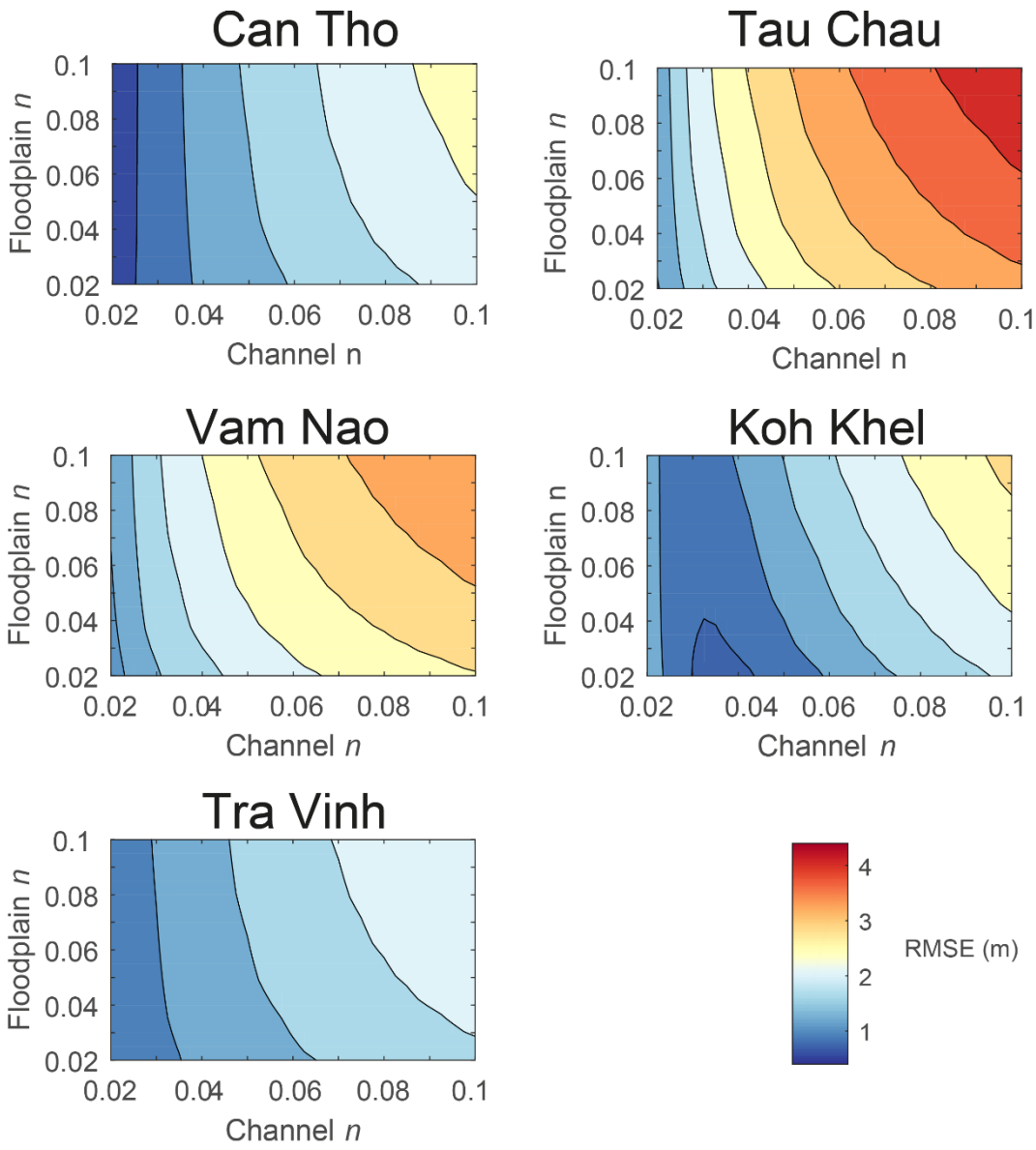

Figure 3-12 Sensitivity of RMSE values to Manning's friction parameters for All Bathymetry + Width model. Blue indicates lower RMSE values, whilst red indicates higher RMSE values. The most accurate models are those in blue, especially those in dark blue.

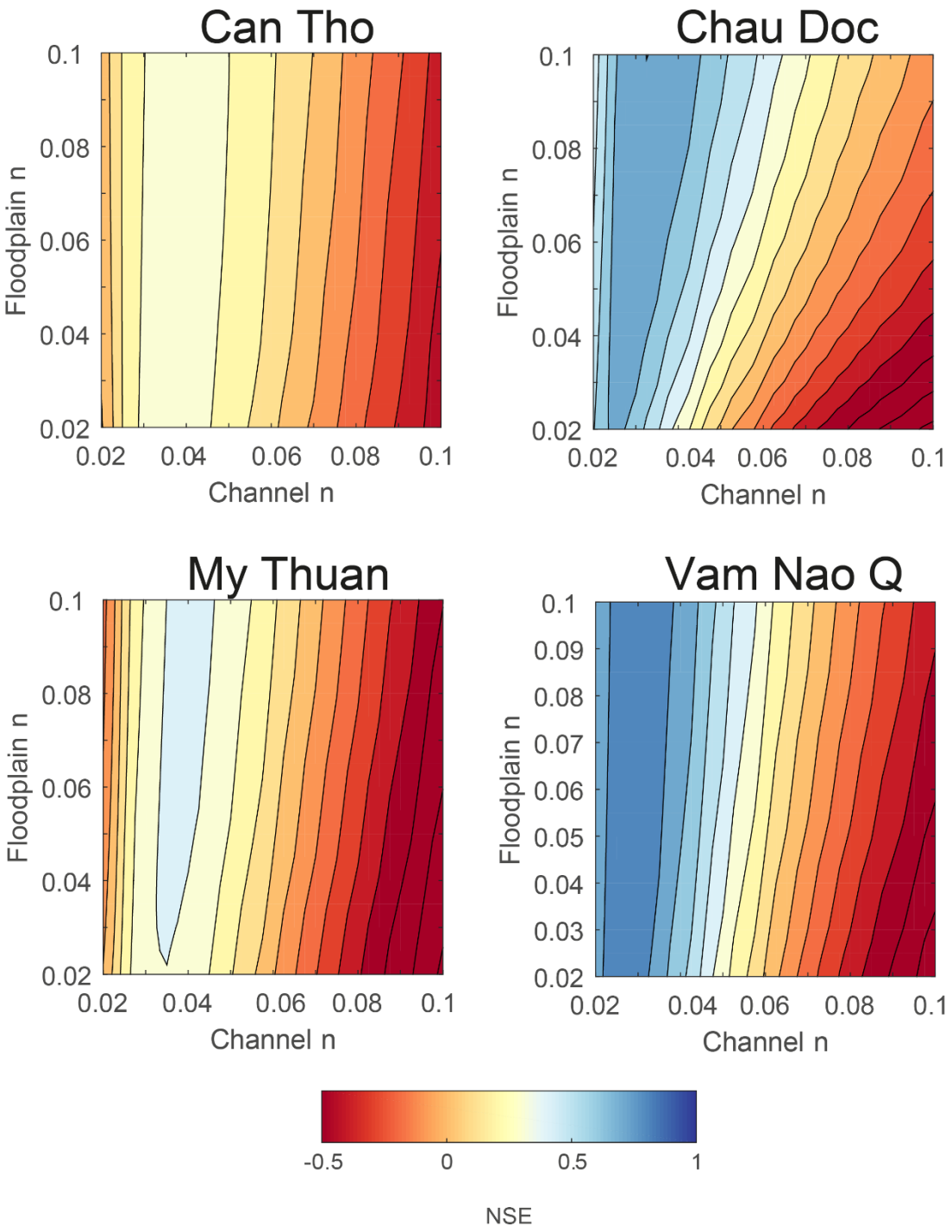

Figure 3-13 Sensitivity of NSE scores to Manning's friction parameters for All Bathymetry + Width mode. Blue indicate NSE values closer to 1 (with 1 corresponding to a perfect match between simulated discharge and observed discharge). Red corresponds with a poor match between simulated and observed discharge. The most accurate models are those in blue, especially those in dark blue

There is no clear optimum set of friction parameters for the All Bathymetry + Width model. However, the All Bathymetry + Width model is more sensitive to channel friction than floodplain friction. For the All Bathymetry + Width model, best results for water level (lowest RMSE value) are realized when channel friction is minimised, but for discharge the best results (NSE value closest to 1) were between Manning's friction values of 0.027 – 0.040. Clean, earthen channels typically have a channel friction of 0.02, with natural streams ranging up to 0.035 (Chow, 1959). Parts of the system have been heavily managed, thus reducing channel friction, whilst the heavily vegetated channels with higher friction values (>0.04) are typically smaller channels which are mostly excluded from the model. Therefore, optimum model results align with physically realistic values. The All Bathymetry + Width model had NSE values closer to 1 for higher floodplain friction values, whilst had marginally lower RMSE values for water level at lower floodplain friction values. Manning's friction values above 0.075 are considered unrealistic for the floodplains in the Mekong Delta as Manning's values for agricultural areas range between 0.030-0.040 for cultivated cropland, 0.050-0.100 for brush and approximately 0.100 for woodland (Chow, 1959). As most of the study site is cultivated, physically realistic Manning's friction values should be approximately around 0.030-0.040. When also considering the presence of mangroves, orchards and adjusting for the degree of irregularity and obstructions (Arcement and Schneider, 1989), physically realistic values are likely to be larger. Yet in calibration efforts, friction is an effective parameter that also compensates for other errors. Thus, the optimum values are not always what are expected (Horritt and Bates, 2002, Hunter et al., 2007, Savage et al., 2016a).

To proceed in the investigation of how much detail is needed to build an accurate flood model of the Mekong Delta, a set of Manning's friction values needed to be selected. There is no obvious set of values that work for all gauges from the sensitivity analysis. Therefore, a compromise was needed. For the channel, Manning's friction values of 0.0225 was selected as the optimum, with this value at the lower end of friction values for main channels (Chow, 1959). For the floodplain, a Manning's friction value of 0.050 was selected which falls within expected values of cultivated areas mixed with trees and adjusting for obstacles and/or

irregularities (Chow, 1959, Arcement and Schneider, 1989). The selected Manning's friction values are similar for channels compared to those used in the study of Manh et al. (2014), who used 10 zones to assign friction values. However, the floodplain friction values selected as the optimum for the All Bathymetry + Width model (0.050) are considerably larger than the values used by Manh et al. (2014) (0.018 and 0.036) which could be considered unrealistically low (and in fact lower than the channels). Both the channel and floodplain friction agree with values used in Dung et al. (2011).

3.6.2 Flood Extent

To assess model performance in predicting flood extent, the Critical Success Score (CSI) was calculated. CSI is a widely used metric that combines the hit rate, false alarms and miss rate to produce a combined score that penalises for both underprediction and overprediction (Horritt and Bates, 2001a, Sampson et al., 2015, Stephens et al., 2014).

$$Critical\ Success\ Index = \frac{A}{A + B + C} \tag{17}$$

Where A is the hit rate, B is false alarms and C is misses, with scores ranging from 0 (no match between model and observations) and 1 (perfect match between model and observation). The hit rate is the rate of correctly predicted inundated pixels, whilst the miss rate is the rate of pixels not flooded in the model but flooded in observations. The false alarm rate is the rate where the model predicts flooding, but the pixel is dry in the observations. To compute CSI, a binary Wet/dry map is needed. The threshold depth of water that is considered a flood is open to debate, so this study uses 3 values to assess whether this makes a difference to CSI values (Figure 3-14). Threshold depths of 0.1m (typically used), 0.5 m and 0.83 m are used. The value of 0.83 m is chosen as that is the random height error of the DEM at the 540 m resolution of this model. The MODIS imagery was resampled to the model resolution (540 m), with both model and MODIS images converted to a binary wet/dry to perform the calculations. For the 2001-2007 period for which the model was run, there were a total of 322 MODIS images to compare (Figure 3-14). CSI scores for different flood depth thresholds are plotted for the whole time-series of the model. Additionally, CSI and the False Alarm Ratio are plotted by month to distinguish the

performance of the model between the wet and dry season (Figure 3-15 & Figure 3-16). Lastly, CSI scores are calculated per pixel for 2001, 2004 and 2007 to delineate where the model is performing well or poorly (Figure 3-17 & Figure 3-18 & Figure 3-19).

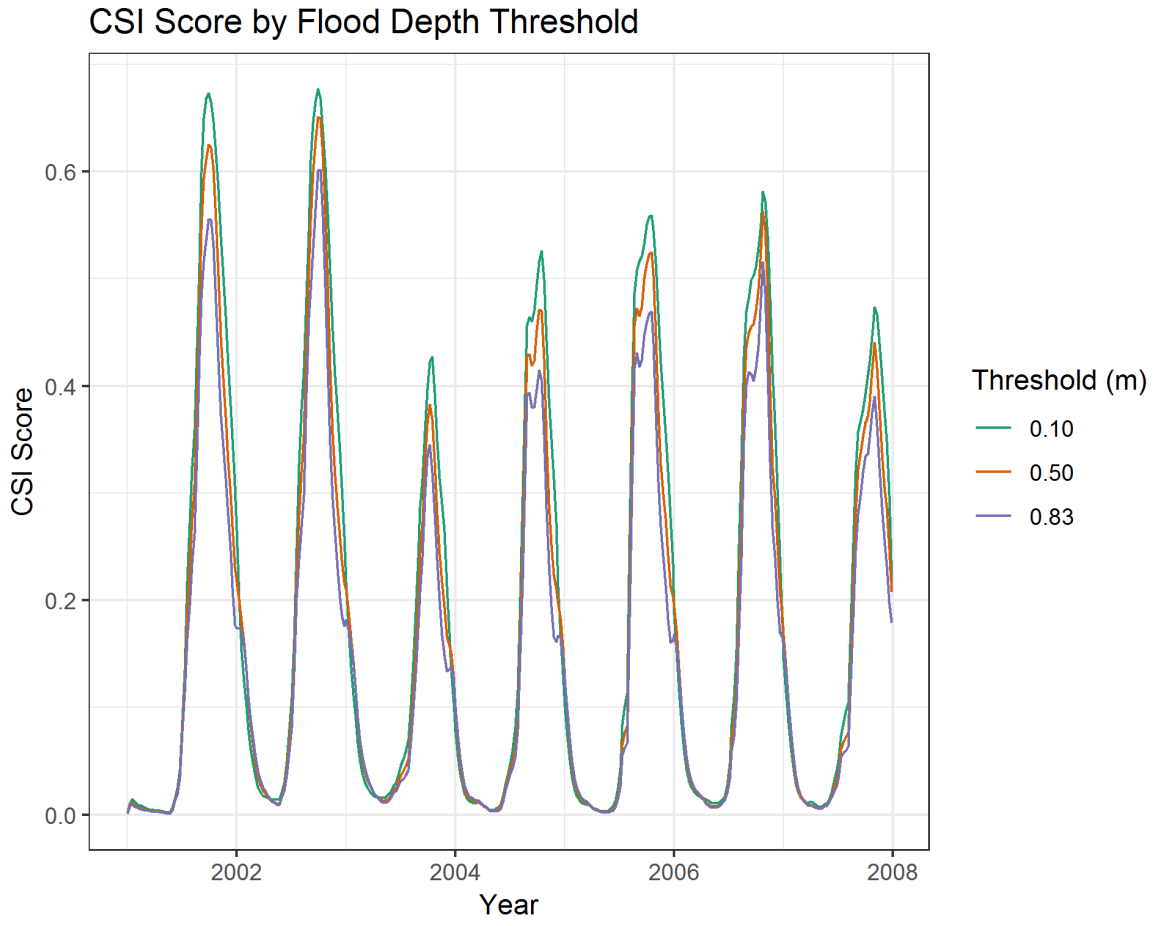

Figure 3-14 Critical Success Index (CSI) score by flood depth thresholds of 0.1 m, 0.5 m and 0.83 m for the All Bathymetry + Width model. CSI scores calculated over a 7-year period (2001-2007) at the time of the MODIS observations (approximately every 8 days; Total 322 images). A CSI score of 1 indicates a perfect match between simulated and observed flood extent, whilst a CSI score of 0 indicates no match between simulated and observed flood extent.

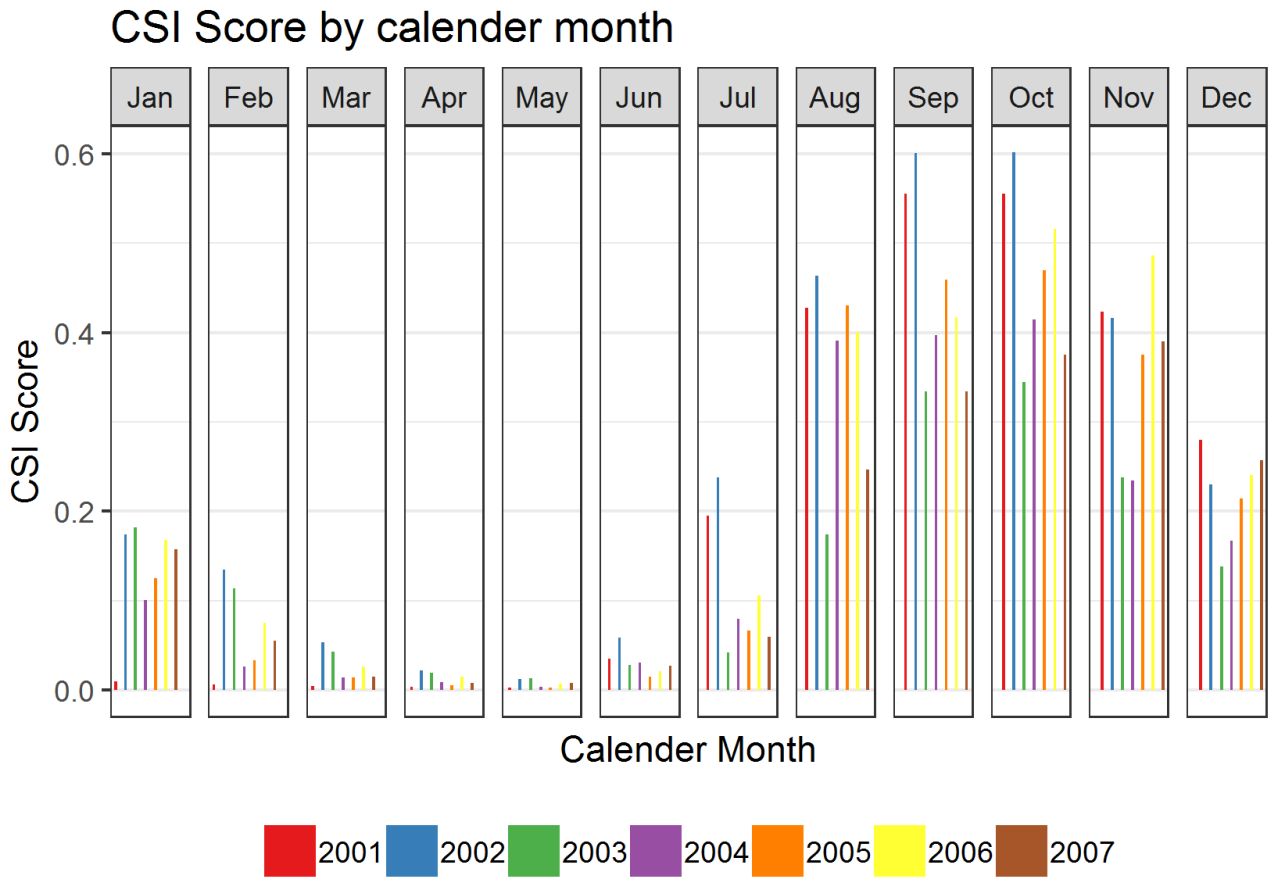

Figure 3-15 Maximum Critical Success Index (CSI) score per calendar month split by year for the All Bathymetry + Width model. A CSI score of 1 indicates a perfect match between simulated and observed flood extent, whilst a CSI score of 0 indicates no match between simulated and observed flood extent.

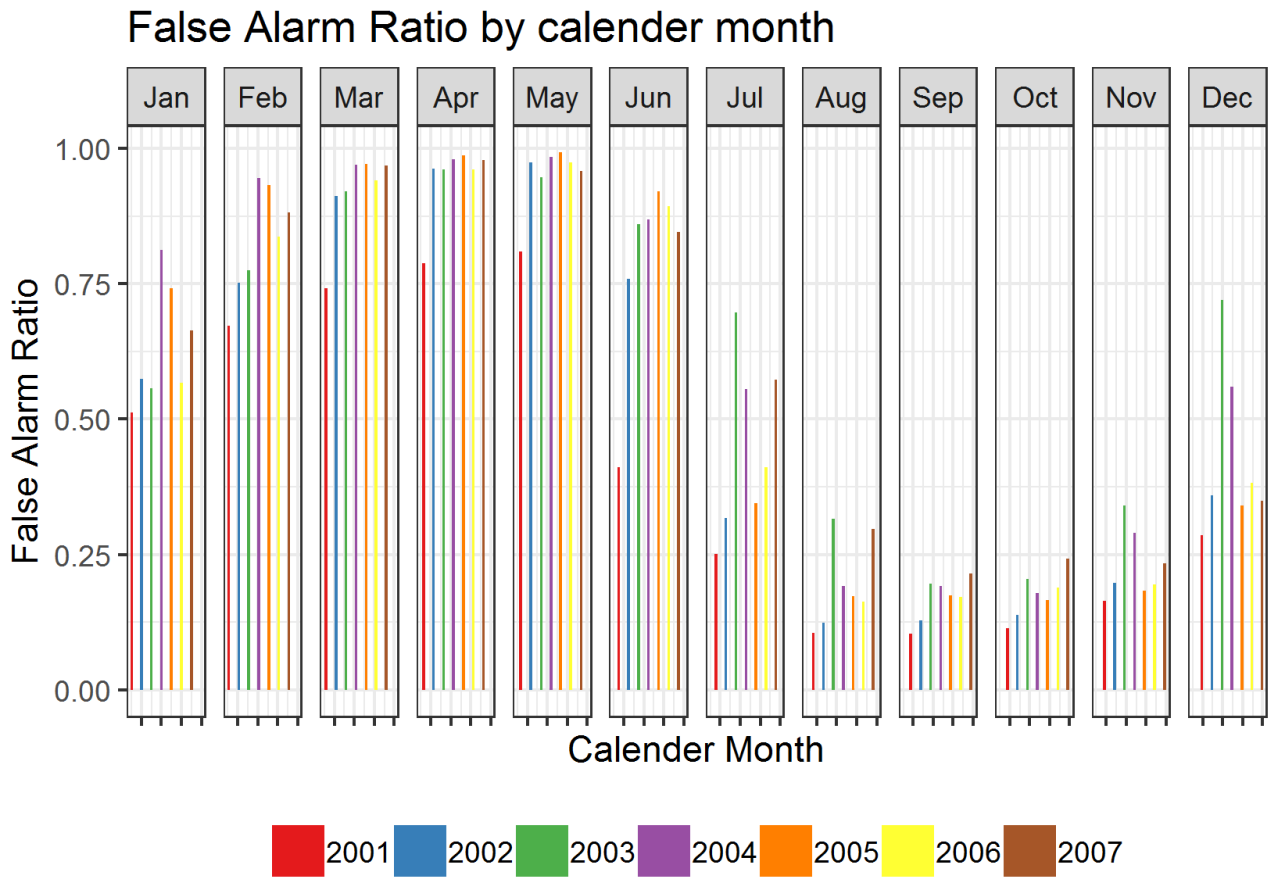

Figure 3-16 Maximum False Alarm Ratio score per calendar month split by year for the All Bathymetry + Width model. The false alarm ratio is the ratio of pixels predicted as wet in the model and dry in the observations. Maximum value of 1. Values of 1 suggest pixels predicted as wet in the model but dry in the observations.

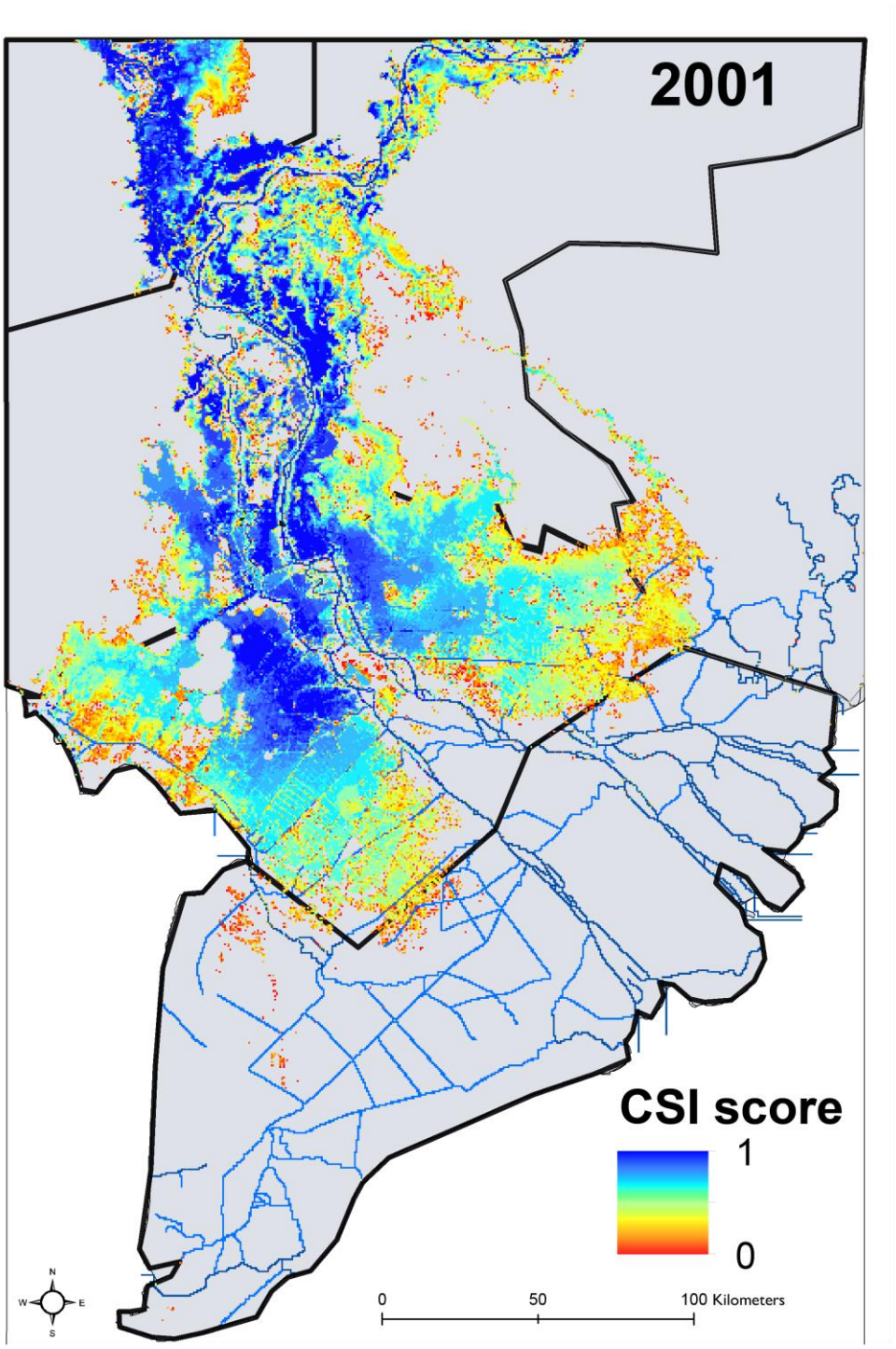

Figure 3-17 Critical Success Index (CSI) score per pixel for the All Bathymetry + Width model for 2001 which is considered a 'Wet' year.

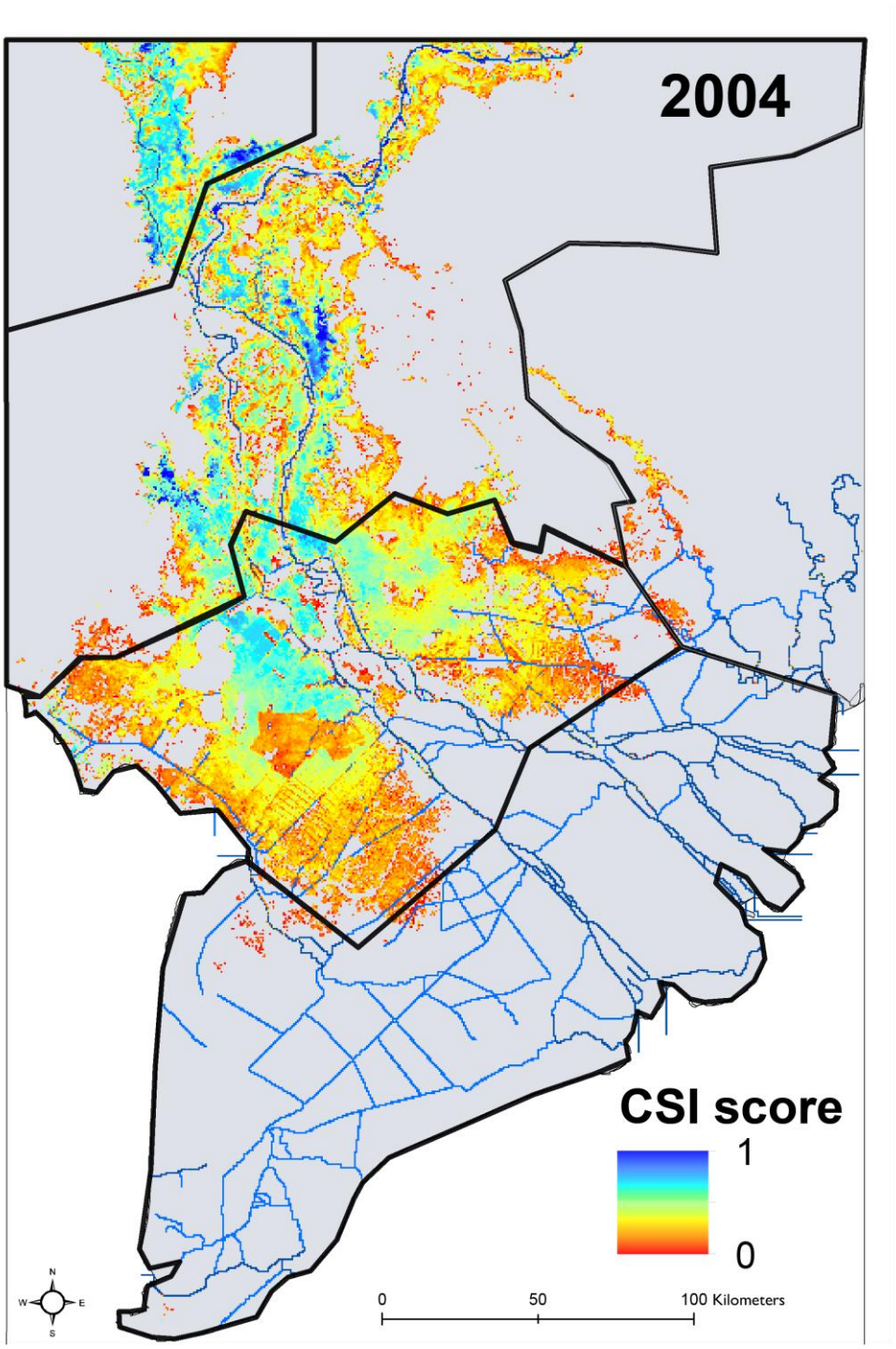

Figure 3-18 Critical Success Index (CSI) score per pixel for the All Bathymetry + Width model for 2004 which is considered a 'Dry' year.

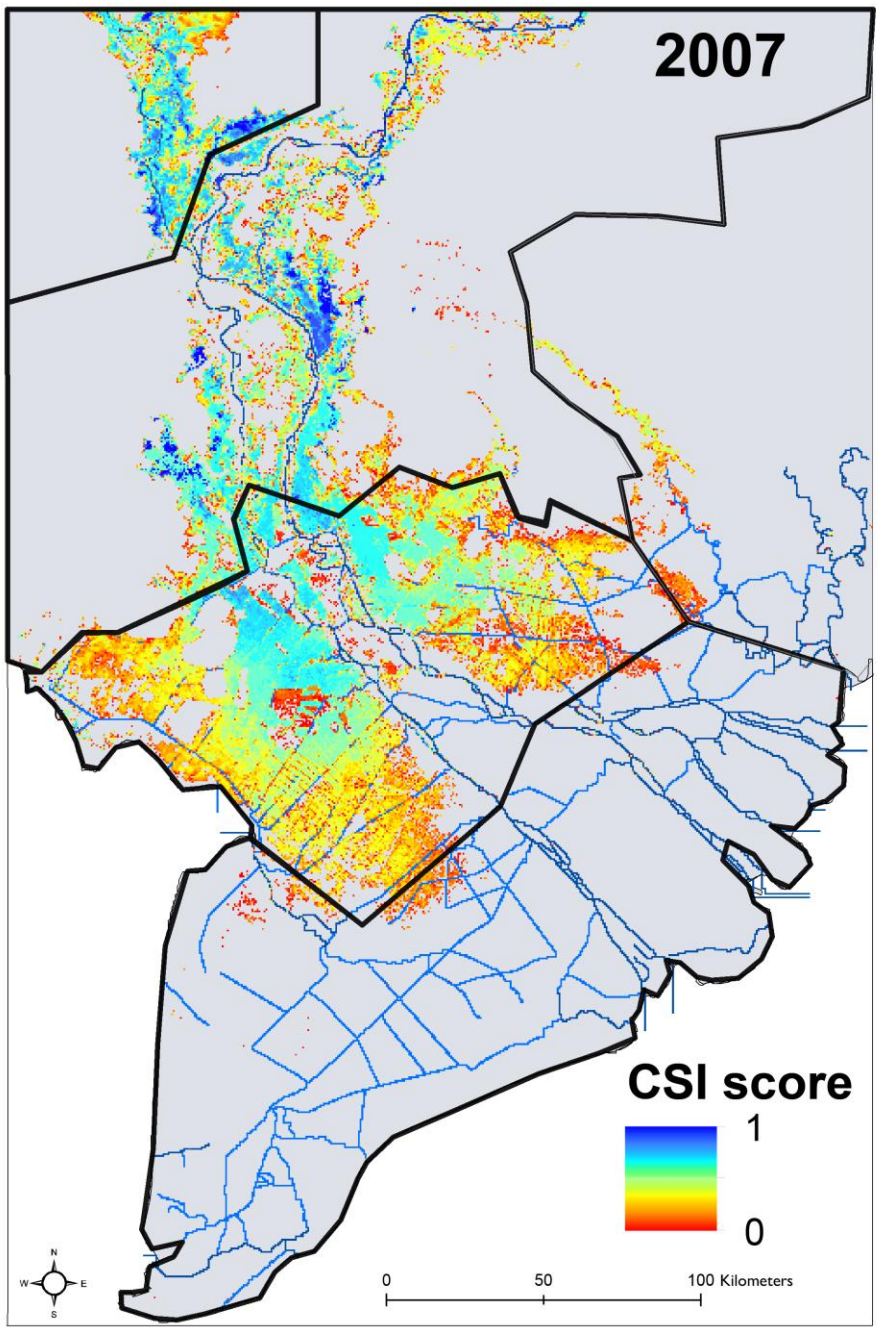

Figure 3-19 Critical Success Index (CSI) score per pixel for the All Bathymetry + Width model for 2007 which is considered a 'Normal' year.

In general, annual CSI scores shows the model has a good level of skill, with the known flooded areas largely flooding. The largest CSI score was in October 2002 (Figure 3-14) with a CSI Score of 0.62 (with 1 being a perfect match between model simulation and observation) for a flood depth threshold of 0.1 m. Another wet year, 2001, also performed well (Figure 3-17). The model performed worse when the years were dryer (Figure 3-18 & Figure 3-19). It was interesting to note that CSI scores are influenced by the flood depth threshold value, as for higher flood threshold depths, CSI scores decreased. If a flood depth threshold of DEM noise (0.83 m) is considered, best CSI scores drop to 0.60. The model performs well (blue) near the channels, with performance suffering the further away from the channels (red and yellow). The CSI scores compare favorably with those of the more detailed quasi 1D/2D model based on MIKE 11 (Dung et al., 2011) which have an approximate CSI score of 0.7 (personal communication Dr N Hung, October 2017). The LISFLOOD-FP model in this chapter over-predicted flood extent in some areas, particularly to the west of the domain and in the central coastal region. Dynamics were mostly resolved, with the simulated results flooding marginally too soon (~ 7 days). However, flooded areas were slow to dissipate, with flooded areas still visible in late December. In the MODIS imagery, the flood has receded by November, so the model fails to drain correctly. This is particularly prevalent in the far west of the domain and in the marshy areas of southern Cambodia. As a result, the CSI score is decreased.

From Figure 3-14 it is striking how CSI scores vary throughout the year. To explore this in more detail, CSI scores and False Alarm Ratio were plotted by month (Figure 3-15 & Figure 3-16). It is clear from Figure 3-15, that CSI scores are considerably greater in the wet season (May-November) compared to the dry season (December-April). Indeed, in the dry season, there is very little skill in the model with CSI values close to 0. Conversely, in the wettest months (September & October) the model has the largest CSI scores. Thus, the model has a certain amount of skill in predicting the largest floods. The reason for the low CSI scores in the dry season (and to a lesser extent the wet season) can be seen in Figure 3-16, which plots the False Alarm Ratio. The False Alarm Ratio refers to the ratio of total wet pixels that are incorrectly predicted as being flooded. In other words, a high False Alarm Ratio (maximum=1) indicates that a large number of pixels are being predicted as being flooded

where in fact they are not. Therefore, in the dry season in particular, the model in this Chapter has a large number of predicted flooded pixels which are not flooded in reality. These pixels would give a 'false alarm'. The reason why there is such a high False Alarm Ratio is due to the models inability to dewater in the dry season. This is in spite of evaporation. It is very likely that the lack of dewatering is due to not respecting the river-floodplain connectivity at lower water heights where negative relief forms and smaller channels are dominant. The problem of dewatering has also been reported in other intermediate scale models (Wilson et al., 2007) and high resolution models (Neal et al., 2011), with the loss of topographic features and non-representation of smaller channels attributed to a lack of dewatering. The lack of dewatering may also be due to an incorrect downstream boundary which is not allowing water to flow into the ocean as much as it should. The misrepresentation of river-floodplain connectivity is likely to be a by-product the DEM being unable to represent the micro-topography and negative relief features that control river-floodplain connectivity at lower flood levels. One possible reason is the aggregation of the DEM to 540 m. However, even at high resolution scale, Trigg et al. (2012) found that SRTM at 90 m missed 96% of channels in the middle reach of the Amazon which greatly restricted the modelled river-floodplain connectivity. The ability of the subgrid model to include smaller channels does somewhat negate the ability of SRTM to represent small channels, but it cannot help with the missed micro-topography or negative relief forms. It should also be noted that there is some uncertainty with the MODIS imagery. Despite these limitations, the model does well in the periods of the highest flood, so does have some use in predicting the most damaging flood hazard.

3.6.3 DEM Comparison

3.6.3.1 Accuracy of MERIT & SRTM DEMs

To calculate the error in MERIT/SRTM the GNSS points were first resampled to the grid of MERIT/SRTM. This resulted in 222 cells filled with GNSS measurements which are taken as observational data. For some MERIT/SRTM pixels there were more than 1 GNSS point, so when this occurred the values of all GNSS elevations were averaged. To visualize the data, flat violin plots were plotted alongside the points and overlaid with a histogram (Figure 3-20**Error! Reference source not found.**). The distribution of errors in the MERIT DEM are

noticeably narrower than that of SRTM. Additionally, error statistics were calculated (Table 3-4**Error! Reference source not found.**). If a normal distribution is assumed, error statistics of mean error (ME), standard deviation (STD), and root mean square error (RMSE) can be applied. Furthermore, robust accuracy measurements for non-normal distributions are considered as DEM error is not always normal (Höhle and Höhle, 2009). These robust accuracy measurements are median absolute distribution (MAD), normalized median absolute deviation (NMAD) and absolute deviation at the 90% quantile (LE90). The paper of Höhle and Höhle (2009) provides an excellent overview of using the aforementioned accuracy measurements. The NMAD can be regarded as an estimate for the standard deviation for heavy tail distributions. If the distribution was normal the STD would be the same as NMAD which is not the case. All the error statistics are larger for SRTM, thus for the simple DEM accuracy experiment carried out in this chapter, MERIT is considerably more accurate.

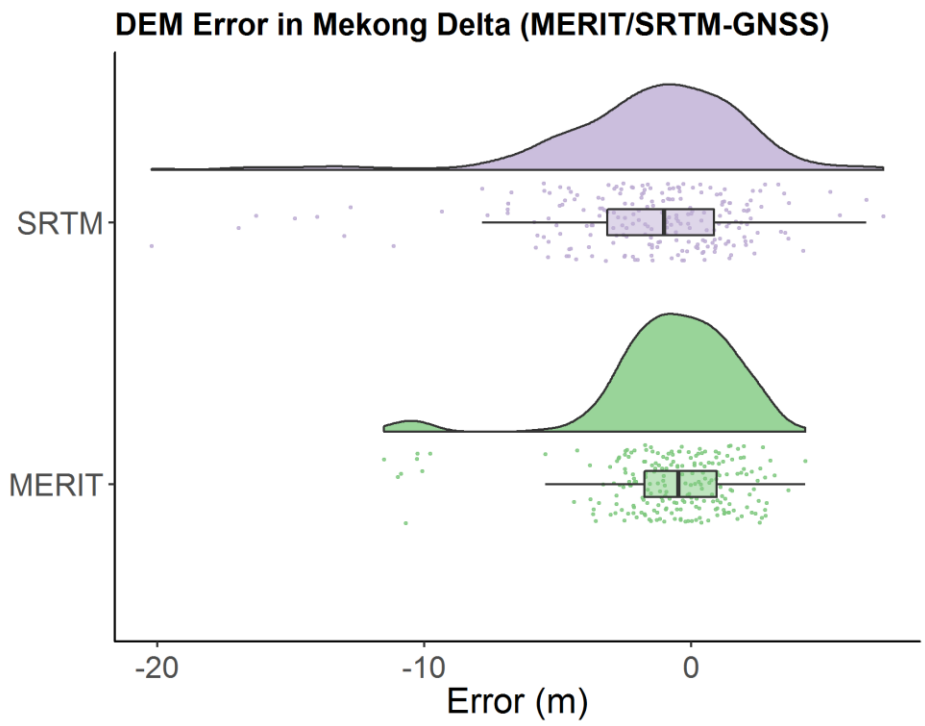

Figure 3-20 DEM Error in the Mekong Delta for SRTM and MERIT. The plot shows the distribution of errors for GNSS points resampled to the MERIT/SRTM grid. In total 222 points are assessed from 881 raw GNSS readings. MERIT = Multi-Error-Removed-Improved-Terrain. SRTM = Shuttle Radar Topography Mission

Table 3-4 Error Statistics for MERIT and SRTM DEMs measured against GNSS points

DEM	ME (m)	STD (m)	RMSE (m)	MAD (m)	NMAD (m)	LE90 (m)
MERIT	-0.72	2.59	2.68	2.06	3.05	1.98
SRTM	-1.60	3.79	4.10	2.83	4.20	2.09

3.6.3.2 Different DEMs and Flood Predictions

Manning's friction parameters (Chow, 1959) were set as 0.03 for the channel and 0.05 for the floodplain, which are both realistic and performed well in the larger Mekong flood model presented in this chapter. The maximum inundation water depths are presented in Figure 3-21**Error! Reference source not found.**.

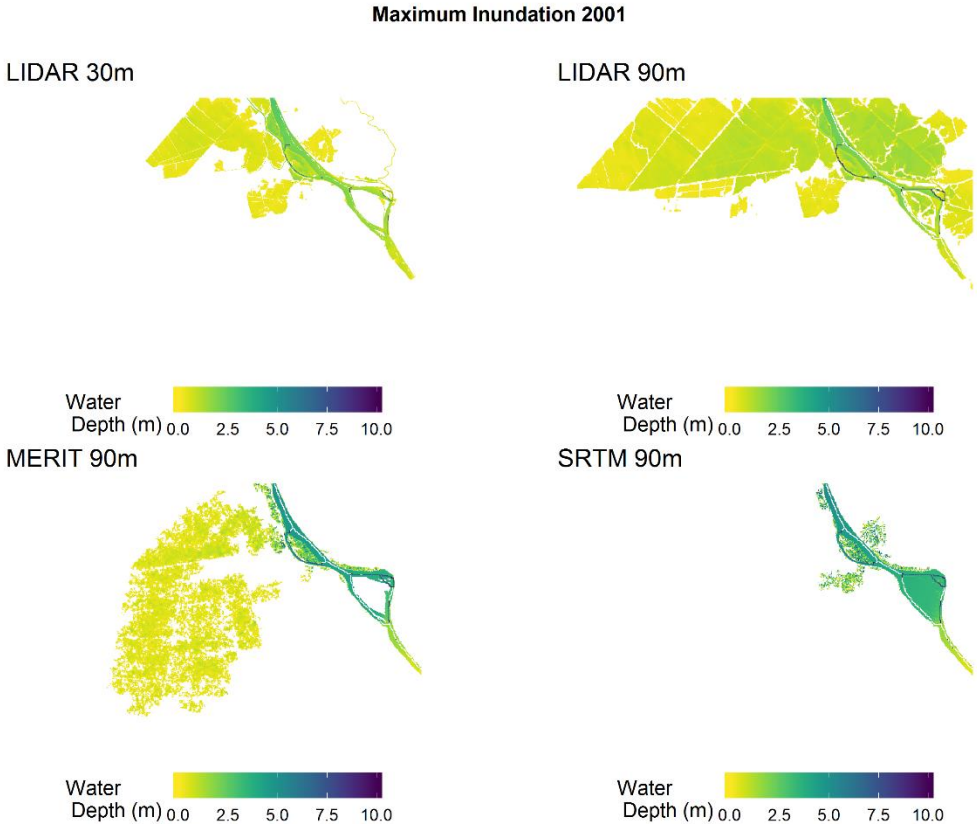

Figure 3-21 Maximum Flood Inundation for 2001 for four DEMs in An Giang Province, Vietnam. LIDAR = Light Detection and Ranging. MERIT = Multi-Error-Removed-Improved-Terrain. SRTM = Shuttle Radar Topography Mission

It is obvious from **Error! Reference source not found.** that the DEM has a large control on predicted maximum inundation. There is a notable difference in flood predictions between resolutions (LIDAR 30 m and LIDAR 90 m) which corroborates with other studies investigating the impacts of resolution on predicted flood extents (Horritt and Bates, 2002, Savage et al., 2016b). A less well-researched finding is that there is a stark difference in flood extents for the same resolution (90 m). The SRTM considerably underpredicts flood extent (compared to the LIDAR 30 m model), whilst the MERIT 90 m and LIDAR 90 m have noticeable differences to the LIDAR 30 m model. This finding poses the question that when a single DEM is used whether the results can be trusted, especially when that DEM is a global DEM product such as MERIT or SRTM. Many studies focus on the effects of other hydrological parameters on model results, with topography largely ignored despite the recognized impact it has on flood predictions (Wechsler, 2007).

3.6.4 Bathymetry from Bankfull Discharge Measurements

To test the importance of bathymetry on model results, the model was run again with the nine versions of bathymetry based on scaling the Q_{bf} values. As the model was found to be insensitive to floodplain friction, the floodplain friction value was set to 0.050 to minimize the number of model runs. The friction values for the channel were altered based on the range outlined in Table 3-3. RMSE's were computed at each gauge for each bathymetry variation.

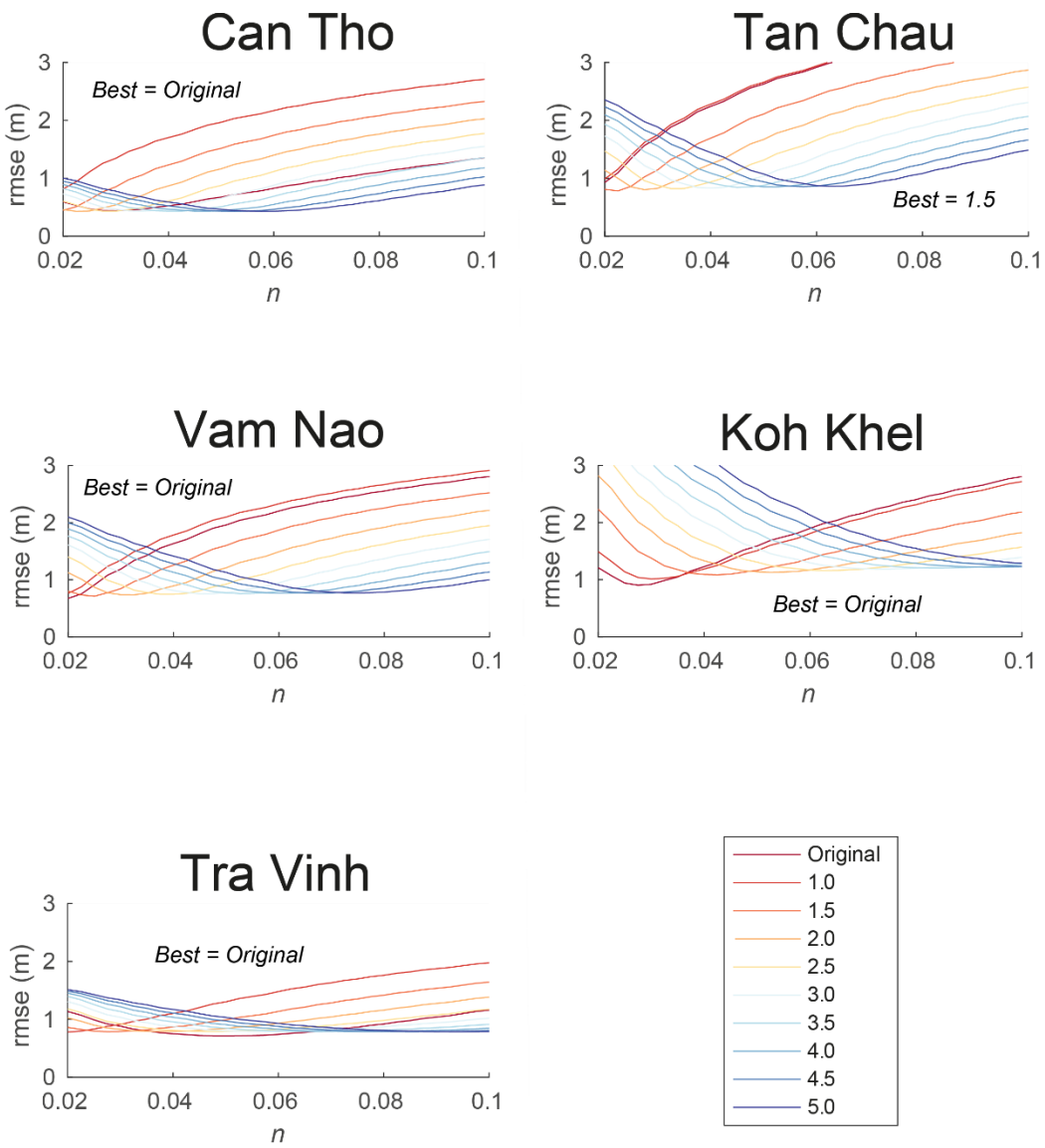

Figure 3-22 RMSE Values using the different bed variations. Numbers in the lower right refer to Q_{bf} scaling factor.

Unsurprisingly, the best bathymetry profile is the known bathymetry. However, the Q_{bf} technique did offer a good alternative when bathymetry data are not available. For Tan Chau, the Q_{bf} 1.5 profile has the smallest RMSE value for water level. Bathymetry Q_{bf} profiles of <1.5 perform similarly to the original bathymetry profile, albeit with smaller RMSE values at larger channel friction values. When Q_{bf} >3.0, RMSE scores are generally only marginally larger, but channel friction values are unrealistically large. Therefore, if bathymetry information is not known, using a scaling range of 1-2 for Q_{bf} to generate bathymetry profiles gives similar results compared to the known bathymetry for realistic channel friction values.

3.6.5 Channel Detail

To assess the importance of channel detail on model results, six variations of channel masks (All Bathymetry + Reduced Channel Detail) were produced based on thresholds outlined in Table 3-3. Each model variation was run across the range of channel friction values, with floodplain friction set at 0.050. The inundation extent changed most notably when channels below 25 m were excluded, especially in the Cau Mau Peninsula to the south west of the delta (Figure 3-23). The model with the greatest channel detail (25 m width threshold) had the least amount of flooding in terms of area. As less channels are included as the width threshold increases, the amount of flooded area increases. The range of values for total

flooded area range from 24457 km² for model with all channels above a width of 25 m included, to 27578 km² for the model that contains channels only above 150 m (Table 3-11).

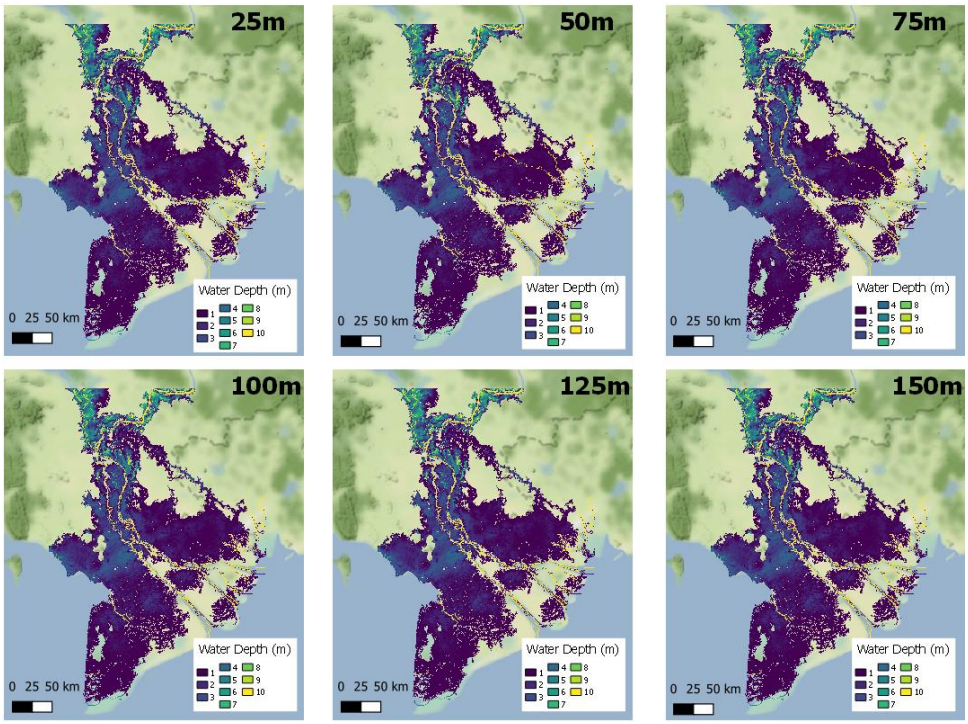

Figure 3-23 Maximum flood inundation for 2004 for different levels of channel detail. The channel width threshold is given in the top right of each map. Flood depth is shown on a scale from blue (shallowest) to yellow (deepest).

Table 3-11 Total Maximum Flooded Area for All Bathymetry + Reduced Channel Detail models for 2004

Width Threshold	Flooded Area (km²)
25m	24457
50m	26167
75m	26346

100m	27335
125m	27331
150m	27578

3.6.6 Downstream Boundary Estimates

The quality of tide height estimates from the harmonic analysis of FES2014 data used in this chapter was assessed against the Vam Kenh tidal gauge (Figure 3-24 & Figure 3-25). Unfortunately, only records from 2011 were available for the Vam Kenh tidal gauge. Modelled values were in general underestimated at the beginning and end of the calendar year and overestimated in the middle of the year. However, the peak of the flood season (September – November) was generally well estimated. An analysis for the whole of 2011, found an RMSE of 0.37 m.

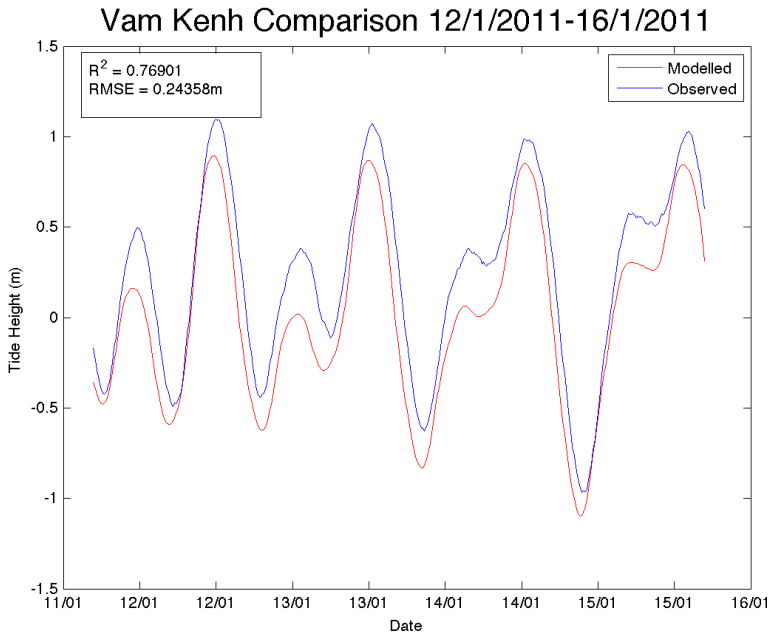

Figure 3-24 Comparison of tide height estimates from harmonic analysis using FES2014 (red line) and observed measurements at Vam Kenh (blue line) for a 5 day period in January 2011. R^2 and RMSE values are given in the top left corner

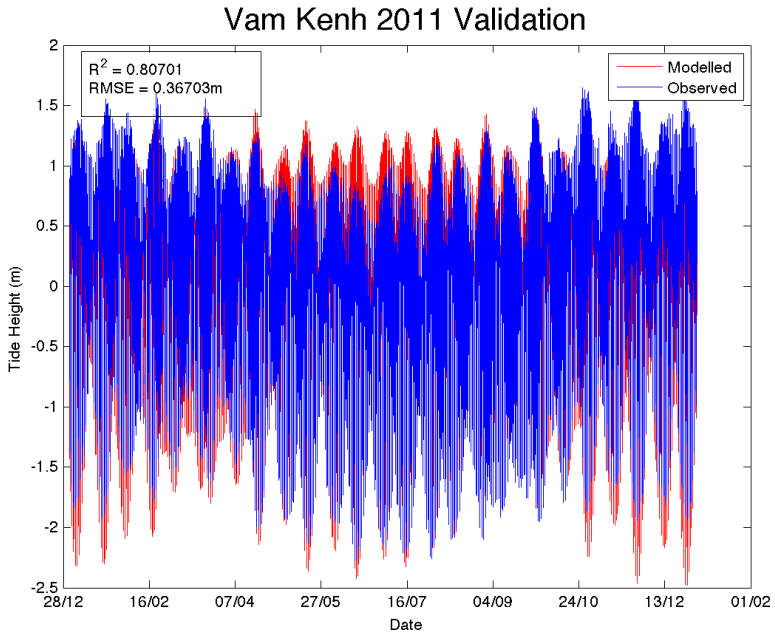

Figure 3-25 Comparison of tide height estimates from harmonic analysis using FES2014 (red line) and observed measurements at Vam Kenh (blue line) for 2011. R^2 and RMSE values are given in the top left corner

3.7 Discussion

To structure the discussion, each question set out in Section 3.3 is answered

3.7.1 Can an intermediate scale hydrodynamic model be built for a data-sparse delta using freely available data that accurately represents flooding?

To answer this question, it depends on the definition of "accurately" and the intended purpose. This model would be inappropriate for a small-scale engineering project, but it is more than suitable to delineate flooding at a sub-national level. RMSE scores are within the standard deviation of errors (0.83 m) for the aggregated DEM for three gauges and are very close to the other two. Inundation extent and dynamics are difficult to quantitatively evaluate using the traditional binary metrics due to the differing resolutions of the model and MODIS data and the uncertainty that surrounds the MODIS classification of wet pixels.

Qualitative assessment reveals that the areas of the Cambodian floodplains and the VMD near the Cambodian border flooded as expected. Quantitative assessment suggests that the model has a relatively high skill in the wettest months (largest CSI score 0.62), but a poor level of skill in the dryer months (CSI score close to 0). This model evaluation score compares to a CSI score of 0.7 for the MIKE11 based model of Dung et al (2011). Several areas to the west and in the central coastal region have overestimated flooding, as the model did not dewater correctly, but this is likely to be due to the lack of channel detail and the incorrect/missing micro topography. Therefore, a method to explore the impact of topographic uncertainty on flood predictions in data-sparse areas would be useful and one which will be explored in the following results chapter. The model developed in this chapter could be used to delineate the most at-risk areas for the more extreme events but will overestimate the flood extent and especially the length of flooding. The most appropriate use of this model for would be to identify the most at-risk areas and apply a more detailed dataset like that of several of the studies outlined in Table 3-2. Using more detailed topography and channel information, possibly with added information such as agricultural abstraction practices, would give more accurate and credible flood predictions. For scenario-based analysis of future flood predictions in the Mekong Delta (i.e. changing crop practices and climate change), the MIKE 11 based model of Dung et al (2011) is best with several studies already utilizing this work for scenario-based analysis (e.g. Triet et al, 2017). Yet, outside of the Mekong in other data-sparse deltas that have not had a detailed model built of them, the approach taken in this chapter may have some use in providing an initial estimate of flood hazard and how this may change in the future. Where possible, local information should be incorporated into the model. Equally, if model ensembles are required, the efficiency of model developed in this chapter allows for such analysis.

Therefore, an intermediate scale model built using freely available data can accurately simulate flooding in the wettest months in the highly complex, yet relatively data-sparse Mekong Delta. The next question is what data are important which will be needed so the model can be applied to other locations.

3.7.2 What aspects of the flood model structure and data are most important to inundation prediction?

To answer this question, important aspects of the data are discussed one-by-one, with an additional discussion of how hydrodynamic models can be improved in data-sparse deltas.

3.7.2.1 Channel Bathymetry

The lack of bathymetry data is the plight of many flood modelers working in data sparse areas. This research has indicated that although having bathymetry measurements is useful, it is not essential to accurately simulate flooding at this scale. The caveat to the bankfull discharge approach is the reliance on gauge data. This study used four gauges, but other study areas are likely to have less. Alternatively, discharge could be estimated by remote sensing, such as in the River Watch program (https://www.dartmouth.edu/~floods/AMSR-E%20Gaging%20Reaches/IndexMap.htm) . In this study context, appropriate Q_{bf} scaling, (with the scale of 1 equal to mean annual discharge) is found to produce the best RMSE and NSE scores between 1-2.5. Results suggest that if a single scaling factor is used to calculate the bathymetry based on a bankfull discharge, a scaling factor of 1.5x the mean of the annual flow gives the most accurate bathymetry estimates. If computational resources allow, a range of bankfull discharge estimates should be explored to test the sensitivity of flood predictions to different bathymetry estimates. It is worth noting that the bankfull discharge values are low compared to more traditional floodplains where bankfull discharge is assumed to occur every 1-2 years (Pickup and Warner, 1976). However, deltas typically flood annually (and for long durations), so taking a maximum discharge for every 1-2 years would lead to an overestimation of bathymetric depth.

3.7.2.2 Channel Detail

Intuitively, one would expect more cells to be flooded with less channels as the river network would have less capacity. This study found that including more channel detail resulted in less total flooded area. The analysis assessed maximum inundation which appears to be dominated by sheet flow at high water levels, thus suggesting that including smaller channels does not improve the river-floodplain connectivity at high water levels as

the river and floodplain are connected by sheet flow at high water levels. Yet, including smaller channels is important for lower water stage and dewatering of the floodplain as they act to connect the river and the floodplain, and thus should be included if possible. The inability of SRTM to represent river-floodplain connectivity (Trigg et al., 2012) means that these important processes are typically missed. Thus, in Chapter 5 an assessment of the ability of various DEMs to represent river-floodplain connectivity at a range of resolutions is carried out. Humans heavily control the smaller channels and those near the coast, so including them in a flood model that does not represent human controls may not be appropriate. Using just the GWD-LR database is acceptable, but if more detailed channels are available (particularly below 25 m), the modeller should aim to include them.

3.7.2.3 DEM

The recently released MERIT DEM (Yamazaki et al., 2017) was used over the more commonly used SRTM product. In their paper, Yamazaki et al. (2017) used the Mekong Delta as an example of how their error reduction method has improved the accuracy of the DEM, particularly in removing striping. Furthermore, 222 elevation observation points were collected in Cambodia and Vietnam using a GNSS receiver, with the results suggesting that MERIT is more accurate than SRTM in the region and, thus, further justifying the choice to use MERIT over SRTM. Using the MERIT DEM instead of SRTM improved flood extent results, noticeably along areas where striping was present in SRTM. Running the model at 540m resolution smoothed out much of the noise present in the DEM and allowed an appropriate runtime. The model could have been run at 90m but this would have taken considerably longer, with Savage et al. (2016b) noting that halving the model resolution increases the model runtime by an order of magnitude. Thus, using these findings, 90m resolution model would have taken approximately 3900 minutes (or 27 days) for a single simulation, or almost 80 years for all 1,079 models used in this chapter. Therefore, running at 90m would have been inappropriate for the number of simulations carried out in this chapter. Moreover, if a multi-delta experiment with various scenarios (e.g. climate change or dam scenarios) was carried out over such a long period (7 years), a resolution of 540m is more practical. Using a resolution of 540m, which is deemed here as intermediate, is an improvement on the previous versions of Mekong flood models that use global flood

models (e.g. CaMa-Flood (Yamazaki et al., 2014b)) but still allows for scenario based simulation. Finer scale models of the Mekong Delta (e.g. Can Tho city model of Apel et al. (2016)) use non-freely available topographic data (LIDAR), which is not only unavailable to all modellers but does not cover the whole delta. Furthermore, even if LIDAR data was available for the whole data, the computation time would be prohibitive and indeed unworkable if a scenario based stochastic approach was taken. Therefore, the model presented here at an intermediate scale is an appropriate tradeoff between available data, desired outputs and computation time, especially if an ensemble of models are to be run.

3.7.2.4 Friction Parameters

The model was found to be more sensitive to channel friction than floodplain friction. Optimum channel friction values for water elevation was found at low values (0.020) and for discharge at slightly higher (~0.035), all of which are within the realms of physical reality. For the floodplain, Manning's values of approximately 0.050 were found to give best model performance. The low computational cost of the model allowed for such a wide parameter space to be explored, but for other studies this could be reduced. A spatially uniform distribution of friction values was implemented in this study, but the model is capable of spatially distributing friction values both for the channel and floodplain. One could calibrate the model using zones of different friction much like the work of Dung et al. (2011) and Manh et al. (2014), but this was not done in this chapter as it would create a very large parameter space. Besides, particularly in Cambodia, the friction parameters fluctuate throughout the year as the flood disperses overbank, effectively creating a huge channel that is littered with vegetation.

3.7.2.5 Improvising Hydrodynamic Models in Data-Sparse Deltas – what is needed?

Despite the promising results, we believe that flood inundation modelling in data sparse deltas can be practically improved in four main ways: 1) Adding extra channel detail from remote sensing; 2) using additional DEM products; 3) separating deliberate flooding of rice paddies from damaging flooding; 4) adding levee information.

Extra channel detail, particularly below 50 m would help river-floodplain connectivity which is particularly prevalent in deltas. The recent launch of the Sentinel 2 satellite offers the possibility of generating a 10m water mask (Du et al., 2016b), whilst the Landsat TM, ETM+ and OLI images offers the possibility of generating 30m water masks as far back as 1984. Once a water mask has been delineated, river width extraction algorithms such as RivWidth (Pavelsky and Smith, 2008) or RivaMap (Isikdogan et al., 2017) can be used to estimate values.

Perhaps more importantly, additional DEM products should be investigated, owing to the relatively poor quality of MERIT/SRTM and the fact that these products were acquired in 2000 and thus could be considered outdated in the dynamic deltaic environment. The TanDEM-X DEM at 12.5m resolution (Rizzoli et al., 2017) could be one such DEM to investigate, but it has suffered from numerous delays and is only available for a limited number of educational purposes free of charge. Even if TanDEM-X at 12.5m were acquired, the whole of the delta would not be covered due to limitations of the number of DEM tiles that can be acquired. A further alternative is the NASADEM, which will be a reprocessed version of SRTM (NASA, 2017), but ultimately does still rely on SRTM acquired way back in 2000 and seems to be delayed. Additional recent DEMs such as a vegetation removed version of SRTM (Zhao et al., 2018) or CoastalDEM (Kulp and Strauss, 2018) could potentially be used, even though to date their availability is unclear. A further alternative is the idea of DEM simulation, whereby plausible versions of a DEM are simulated based on the spatial error structure. The idea of DEM simulation was fairly popular in in the 1990's and early 2000's (Holmes et al., 2000, Fisher, 1991, Goovaerts, 1997, Deutsch and Journel, 1998) but has faded out of fashion despite the wealth of DEM products and computational resources now available. More surprisingly is the fact that the technique has been seldomly used in flooding applications with only the study of Wilson and Atkinson (2005) using DEM simulation in fluvial flooding and a handful of simple coastal flooding applications (Leon et al., 2014, Fereshtehpour and Karamouz, 2018). Therefore, there is an opportunity to produce plausible DEMs at the resolution of a global DEM (e.g. MERIT at 90 m) allowing the possibility to explore the effects of topographic error at the minimum resolution of

topographic information available in a data-sparse location (i.e. resolution of a global DEM assuming no high-resolution LIDAR is available).

Thirdly, good and bad flooding needs to be separated so flood maps can be produced delineating more accurately the truly at-risk areas. Flooding generally is thought of as a negative phenomenon but for many in deltas it is essential to sustain their agricultural livelihoods. Delineation of good/bad flooding (otherwise thought of as deliberate and non-deliberate flooding) could be implemented by including an irrigation scheme. Taking the Mekong Delta as an example, remote sensing confirms the prevalence of irrigated rice paddies (Kontgis et al., 2015, Nguyen et al., 2016, Nguyen et al., 2015). Rice paddies have been found to demonstrably attenuate flooding (Masumoto et al., 2008, MRC, 2010a), but with the move towards triple rice cropping are becoming less frequently flooded. Water levels in paddies are controlled by sluice gates and pumps to the level required by the crop at the time in the crop cycle. From remote sensing paddies could appear flooded, but in fact are deliberately flooded to grow rice. Yet, if too much water is in a paddy, bad (or non-deliberate flooding) occurs. Delineating these deliberately and non-deliberately flooded paddies would be useful in gauging where the most negatively affected by flooding areas are as opposed to just wet areas. In addition, the presence of paddies suggest that irrigation channels are nearby as typically paddies are irrigated from river water (although increasingly groundwater is also used). A schematic of water balance in a paddy is given in Figure 3-26. Essentially to include such an irrigation scheme in a hydrodynamic model, one would need to obtain data on where the irrigated areas are, what the crop calendars are, and what water depths are needed at key points in the crop calendar. With evaporation and rainfall, water volume can be calculated based on paddy water demand. Global datasets are available for irrigated areas (GMIA; (Siebert et al., 2015)) and crop calendars (SACRA; (Kotsuki and Tanaka, 2015)), and should be supplemented by water depth guidelines for the crop in question. The water height at each model timestep would be updated and water either withdrawn or deposited back into the nearest river cell.

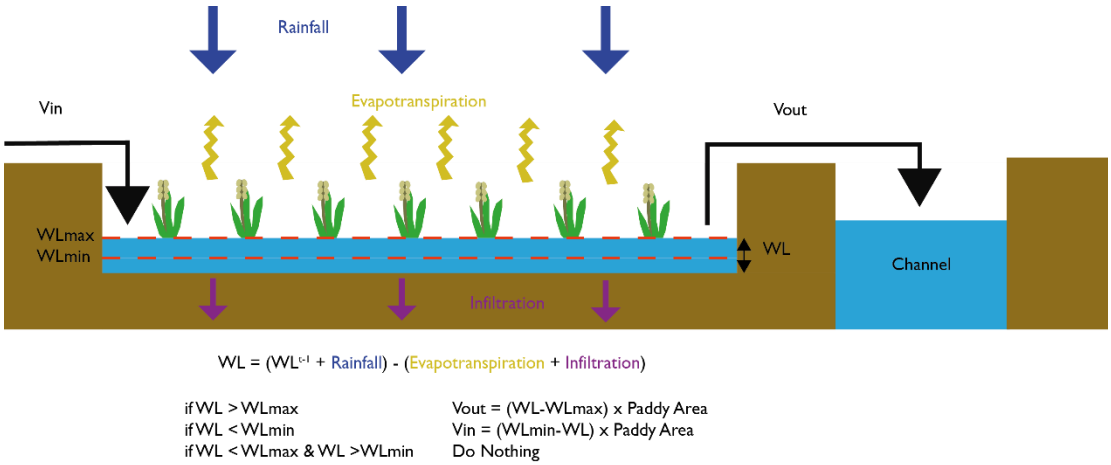

Figure 3-26 Schematic of the water balance for a paddy. WL refers to water level. Vin is volume in and Vout is volume out.

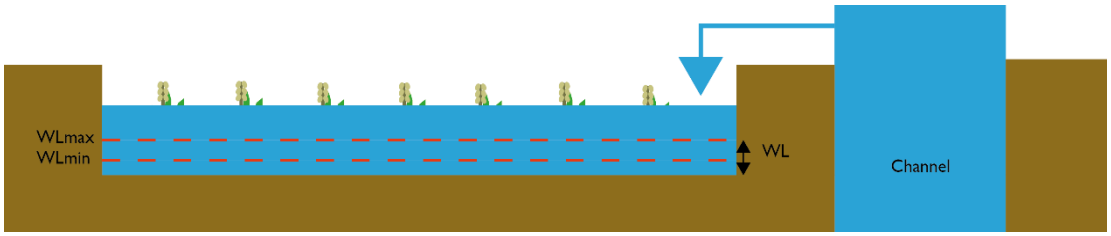

Figure 3-27 Paddy flooded so crops damaged but acting as flood attenuation. Considered negative flooding as crops damaged

Fourthly, including levee height information would be highly beneficial and remains one of the key challenges for all flood inundation studies on how best to capture this, especially over a large area. Whilst obtaining bathymetry data and a DEM with a low vertical error (e.g. LIDAR) is favoured, the practicality, cost and timeframe involved is prohibitive. It may be possible for a section of a delta, but not for a whole delta or multiple deltas, certainly within the next decade. Therefore, the four proposed improvements are a practical step in enhancing flood inundation modelling in data-sparse deltas.

3.8 Limitations

This study has some caveats. This chapter only assesses fluvial flooding, with the justification that the Mekong Delta has not suffered from major coastal flooding in the recent past. Yet, for other data-sparse deltas, this type of flooding is more pronounced. Coastal

flooding analysis of such data-sparse deltas is difficult to model with the MERIT/SRTM DEM due to the noise in the data being particularly prominent in coastal areas and the lack of forcing data. Furthermore, friction parameters were assumed to be uniform across the domain. Evaporation was included, but this was uniform and did not consider the transpiration component. Rainfall can be included in the model, but the noisy nature of the DEM resulted in routing problems, so was omitted. The biggest caveat however is the lack of detail about channels and dikes which the MIKE11 based model of Dung et al (2011) has. The model of Dung et al (2011) and the follow up studies have the ability to more accurately represent the important links between the river and the floodplain which are particularly important in deltas as evidenced by the stark difference in flood extents when using three different DEMs (LIDAR, MERIT and SRTM). The LISFLOOD-FP based model developed in this chapter simply cannot represent the river-floodplain connectivity adequately, which is likely to be due to the lack of channels and the inaccuracies of the DEM used. The model developed in this chapter suffers from the inability to dewater correctly, so although model evaluation metrics such as CSI are reasonably high in the wet season (0.62), they are very low in the dry season (close to 0) and, thus, the model shows very little skill in these periods.

3.9 Conclusions

This chapter presents an intermediate scale flood inundation model of the Mekong Delta built using freely available data and the LISFLOOD-FP subgrid model. A benchmark model, called the All Bathymetry + Width Model, was built using all freely available data. Sensitivity analysis was carried out on the All Bathymetry + Width Model by varying channel and floodplain friction parameters, resulting in 561 model variations. The All Bathymetry + Width Model showed a good level of skill with RMSE values across 5 gauges at 0.608m, NSE values of 0.627 across 4 gauges and a CSI score of 0.62. The model was also found to perform considerably better in wetter years and periods of high flow. Using the set of friction parameters found to work best for the All Bathymetry + Width Model (channel n 0.0225 and floodplain n 0.050) 2 further investigations were carried out to test the importance of knowing channel bathymetry and representing smaller channels not in the GWD-LR database, resulting in an additional 550+ model runs. Bathymetry was estimated based on bankfull discharge estimates and scaling these. Using only a global database of

river widths (GWD-LR) and estimating bathymetry using the bankfull discharge method yielded marginally worse results than the All Bathymetry + Width Model, indicating that a global type flood inundation model of the Mekong Delta that accurately depicts flooding can be built using freely available data. The model built in this chapter is the first 2D model of the Mekong Delta and fits in between the detailed models that need non-freely available data (e.g. LIDAR data) and coarse resolution global models. It is also the first to have estimated the downstream tidal boundary so comprehensively using harmonic analysis and the FES2014 dataset, allowing for some representation of the tidal backwater effect. Therefore, a flood model of any data-sparse delta could in theory be built using global datasets – MERIT/SRTM for the DEM; GWD-LR for channel widths; GRDC or local authorities for gauge information and FES2014 for downstream tidal boundaries, with bathymetry estimated using bankfull discharge. This leads to the possibility that other data-sparse deltas can be modelled in a similar manner to identify those areas at flood risk, paving the way for a much-needed analysis of flooding in these deltas which is not solely focused on coastal flooding. However, the model developed in this chapter in its current guise would be inappropriate for such analysis in the Mekong delta as the model does not dewater correctly leading to very poor skill (CSI score close to 0) in the dryer months. To improve flood modelling in data-sparse deltas, 4 additional pieces of data and/or model capabilities should be explored: 1) Adding extra channel detail; 2) Using additional and/or an ensemble of DEMs; 3) Adding an irrigation scheme to delineate good/bad flooding and include a human component and 4) Adding levee data. Yet, a key finding of this chapter is the stark difference in flood predictions by using different DEM products. The impact of DEM uncertainty has been rarely focused upon despite its recognized importance in flood predictions, especially in situations in data-sparse areas only global DEMs. Thus, the following results chapters will focus on DEM uncertainty and their impact on flood inundation prediction in data-sparse areas.

Chapter 4 Implications of Simulating Global Digital Elevation Models for Flood Inundation Studies

- Hawker, L., Rougier, J., Neal, J. C., Bates, P. D., Archer, L., & Yamazaki, D. (2018). Implications of Simulating Global Digital Elevation Models for Flood Inundation Studies. *Water Resources Research.* 54. https://doi.org/10.1029/2018WR023279
- Hawker, L., Bates, P. D., Neal, J. C., & Rougier, J. (2018). Perspectives on Digital Elevation Model (DEM) Simulation for Flood Modeling in the Absence of a High-Accuracy Open Access Global DEM. *Frontiers in Earth Sciences*. 6:233. doi: 10.3389/feart.2018.00233

4.1 Preface

This results chapter consists of papers that has been published in Water Resources Research and Frontiers in Earth Science. Simulations, analysis, writing and figures were completed by the lead author with advice and commenting of the manuscript from Paul Bates, Jeffrey Neal and Jonathan Rougier. The flood model of Ba, Fiji was kindly supplied by Leanne Archer. The MERIT DEM is the work of Dai Yamazaki and colleagues. Jonathan Rougier helped with the initial setup of the geostatistical code.

4.2 Context

The previous chapter built a regional scale 2D flood model of the Mekong Delta using freely available data. Inaccuracies in topography were suspected in having an influence on predicted inundation quality. Yet it was difficult to explore this source of uncertainty with a lack of: (a) high accuracy datasets for topography that could be used to assess errors in the MERIT DEM; and (b) knowledge of the spatial structure of these errors and (c) a method to simulate plausible DEM's suitable for flood modelling. Therefore, this chapter sets out to

simulate plausible versions of floodplains in global DEMs and test the impact of using ensembles of DEMs on predicted inundation extent.

4.3 Introduction

"People trust a map. It contains sharp lines, bright colours, and implies a great deal of effort by field staff, analysts and cartographers. Maps are a definitive statement , yet the world we commonly experience is far from definitive" (Davis and Keller, 1997b) p410

4.3.1 Digital Elevation Models

The first digital representation of terrain can be traced back to the 1950s and the pioneering work of Prof. Charles L Miller and colleagues at Massachusetts Institute of Technology who were tasked with expediting highway design by digital computation of photogrammetrically acquired terrain data. In each model, the X axis was aligned to the proposed direction of the highway and subsequently tied to the State Plane coordinate system using control points. Records of elevations were recorded by Kelsh plotters that were moved at regular intervals along the Y direction. This process was automated and several computer programmes were created where operators could interact with the data. All this was deployed on an IBM 650 computer which had a maximum storage capacity of just 2000 words. Despite the simple approach, this is widely recognised as the birth of digital representation of terrain (Doyle, 1978). Therefore, the earliest definition of a Digital Terrain Model given by Miller and Laflamme (1958) is 'a statistical representation of the continuous surface of the ground by a large number of selected points with known xyz coordinates in an arbitrary coordinate field'.

In the subsequent decades, the introduction of concepts such as a Digital Elevation Model (DEM) and Digital Surface Model (DSM) have created a confusing picture. We clarify these definitions in Table 4-1. For the remainder of this thesis we will focus on DEMs, especially as this is most relevant to flood models.

Table 4-1 Definitions of DEM, DTM and DSM

Product	Definition
Digital Elevation Model (DEM)	A numerical representation of the bare-earth surface arranged as a set of regularly spaced points on a Cartesian grid. Normally these grids are square and the elevations exclude buildings and vegetation, but variations do exist where these may not be the case. In other words, DEMs are any set of elevations measurements of the earth's surface that also record spatial proximity or spatial relationships between the elevation measurements, so a simple list of elevations does not constitute a DEM (Fisher and Tate, 2006). Land surface parameters are derived from the DEM.
Digital Terrain model (DTM)	All-encompassing original term to describe models of terrain elevation. A DTM is a synonym of a bare earth DEM (Maune, 2001).
Digital Surface Model (DSM)	The model represents the top of reflective surfaces such as buildings and vegetation (Maune, 2001). A good DSM should portray the surface adequately which could require high resolution as many surfaces (e.g urban areas) are highly complex.

DEMs are generated by first collecting elevation measurements from either: 1) Ground surveying techniques (e.g Global Positioning Units); 2) Existing hardcopy topographic maps; 3) Remote sensing (airborne lasers, airborne/satellite photogrammetry, airborne/satellite interferometry) (Nelson et al., 2009). These measurements are then processed to reduce errors, with further error propagation through the decisions made in the processing stage, such as the decisions made about treating unwanted depressions (Wilson, 2012). These set of points are then recorded onto a regular grid in Cartesian space – most commonly a square grid, and less frequently on a triangular or rectangular grid. By gridding the elevation points error is introduced through the interpolation process. Thus, for some very high-resolution applications a user may prefer to use the raw elevation data in point cloud format which is becoming increasingly available to the end-user. The DEM is subsequently interpreted and visualised before being used in a wide range of applications (Table 4-2).

Table 4-2 Examples of DEM Applications

Application	Reference
3D Visualisation	Zanchi et al. (2009)
Archaelogy	Menze et al. (2006)

Application	Reference
Climate Change Impact	Kramer et al. (2010)
Flood Models	Bates and De Roo (2000)
Forest Ecology	Simard et al. (2011)
Forest Fire	Hernández Encinas et al. (2007)
Geomorphology	Bailey et al. (2007)
Glaciology	Paul and Haeberli (2008)
Hydrology	Wise (2000)
Landscape Dynamics	Allen et al. (2013)
Planning Support	Aerts et al. (2003)
Pollution	Shamsudduha et al. (2008)
Seismology	Allen and Wald (2009)
Soil Mapping	Mulder et al. (2011)
Soil Redistribution	Claessens et al. (2005)
Solar Radiation	Reuter et al. (2005)
Species Dynamic Range Models	Schurr et al. (2012)
Urbanisation	Linard et al. (2013)
Valuation of landscape beauty	Schirpke et al. (2013)
Video Games/synthetic Terrains	Zhou et al. (2007)
Volcanology	Huggel et al. (2008)

4.4 DEM Error

"No Dataset is perfect. Each has its own limitations. Nevertheless, the temptation is to assume digital datasets are perfect" (Giles et al., 2010) p141

"Landscapes are not uncertain, but knowledge about them is" (Davis and Keller, 1997b) p432

To most the word *error* has an aura of negativity. It indicates that if more care was taken, a mistake could have been avoided (Taylor, 1997). The term also has monetary connotations with the colloquial term *costly error*. When referring to a DEM, we can consider the term *erro*r to refer to the departure of the measurement from the true value (Wechsler, 2007). Error is the part of *uncertainty* that is well defined (Oksanen, 2006). It is an irrefutable fact that errors are a part of spatial data and cannot be avoided (Wechsler, 2007, Gonga-Saholiariliva et al., 2011).

Error in the DEM can occur in both the horizontal (XY) and the vertical (Z) planes (Fisher and Tate, 2006). Typically, efforts have focussed on vertical errors as planimetric errors produces elevation errors but not vice-versa. Wise (2000) categorized vertical errors as systematic, blunders or random. Systematic errors occur in the DEM generation procedure and stem from processing techniques that can cause bias or artefacts. If this cause is known it can be removed or reduced (Wechsler, 2007). Blunders arise from human error (Wise, 2000) or equipment failure (Fisher and Tate, 2006) and are typically corrected if they are identified. Random errors occur in any system of measurement due to the wealth of measurement and operational tasks performed to create a DEM (Wise, 2000, Fisher and Tate, 2006), and remain even after known blunders and systematic errors are removed (Wechsler, 2007). Identifying random errors is challenging, with Lopez (1997) attempting it using principal component analysis. Blunders, systematic error and random error occur from 3 sources as identified by Wechsler (2007) and are (a) data error as a result of deficient spatial sampling or observations and age of data; (b) processing errors such as interpolation or numerical errors; and (c) measurement errors such as positional inaccuracy, faulty equipment or observer bias.

DEM error is most commonly quantified using the root mean square error (RMSE) statistic (Hunter and Goodchild, 1997, Fisher and Tate, 2006, Wechsler, 2007). Calculating this single global accuracy metric has its advantages as it is quick to calculate, easy to report and has been used widely in the literature (Carlisle, 2005). Yet, the disadvantage of such a global measure is widely discussed in the literature (Burrough and McDonnell, 1998, Wise, 2011, Wechsler, 2007, Carlisle, 2005, Kydriakidis et al., 1999, Zhang and Montgomery, 1994, Oksanen and Sarjakoski, 2006). Using such a global measure implies the error is aspatial, or in other words is the same across the entire area in question. By intuition we know this not to be the case and this will be discussed in detail in the next section as this idea is imperative to this work. Moreover, RMSE assumes that DEM errors are random and requires an assumption of normality, but in a number of studies this has been found not to be the case (Monckton, 1994, Fisher, 1998), with mean error being used instead by Fisher (1998). RMSE is also sensitive to larger errors. Error quantification metrics of DEMs have often been based on a small number of reference points. For example, Wechsler and Knoll (2006) report that

RMSE for a USGS 7.5 min DEM tile containing 161,355 data points was estimated using just 28 reference points. In later work, Wechsler (2007) uses an example of 120 million LIDAR points with a reported RMSE of 0.15 m which was calculated using just 174 ground survey points or 0.00014% of the data. With a normal distribution and a mean of 0 m, the standard deviation would range from -0.62 m to +0.62 m. Therefore, the vendor is stating that 95% of the data could deviate from the stated elevation by 0.15 m or less. Yet, 5% of the data could deviate by ±0.15 m to ±0.30 m and 1% (or 1.2 million points in this case) could deviate by ±0.30 m to ±0.62 m, leading Wechsler (2007) to conclude that the ability of the RMSE metric to represent the DEM accuracy is 'questionable'.

4.4.1 Spatial Error

In his 1970 paper, Waldo Tobler invoked what became known as *Tobler's First Law of Geography*, whereby he noted that "nearby things are more similar than distant things" Tobler (1970). Whilst this may appear to be a simple observation, it provides a useful theoretical framework when considering how error is related in space. First let us consider the scenario whereby the error in a DEM elevation pixel is spatially independent of its neighbour. In other words, the error in a pixel is uncorrelated to that of its neighbour. When considering error in relation to vegetation height, there is a general agreement that there is a positive bias in the errors, as with vegetation present the elevation is higher than the terrain. So, in general a pixel with a tree in it will likely have a larger error (or a larger positive bias) than a pixel containing a vegetation type with a much lower height (e.g grass). Similarly, a pixel with a steeper slope, or a particular aspect, typically has a larger error (positive or negative) than a flat surface. Taking this first scenario, and with our error assumptions laid out, the landscape would consist of a complete random selection of land cover and slope. From intuition, we know this to be completely unrealistic. A tree is likely to be next to another tree to form a forest. Grass is likely to be next to grass to form a field. A steep slope is likely to be next to another steep slope to form a mountain, and so on. Therefore, Tobler's First Law of Geography is a completely reasonable observation. Thus, we can consider the error in a DEM to be spatially dependent, or in geostatistical language, spatially autocorrelated. If we maximise the degree of spatial autocorrelation, all errors are perfectly correlated. Again, we know this to be unrealistic as this scenario would assume every pixel

to have the same characteristic (e.g vegetation height, slope, aspect) and the area to be small enough that the instrument errors (e.g striping) would not be present. Additionally, instrumentation used to sample the elevations tend to correlate errors in space independently, making this idealised scenario even more unrealistic. Perhaps if we consider a small area of a completely flat landscape this assumption would hold, but finding such a place on the highly heterogeneous Earth is impossible. Holmes et al. (2000) observes that the "global average error is small" but "local error values can be large, and also spatially autocorrelated". Consequently, we can deduce that the error in a DEM has some degree of spatial dependence.

4.4.2 Error Propagation

In the creation and utilisation of DEMs, uncertainty is introduced and perpetuates through four phases as schematised in Figure 4-1.

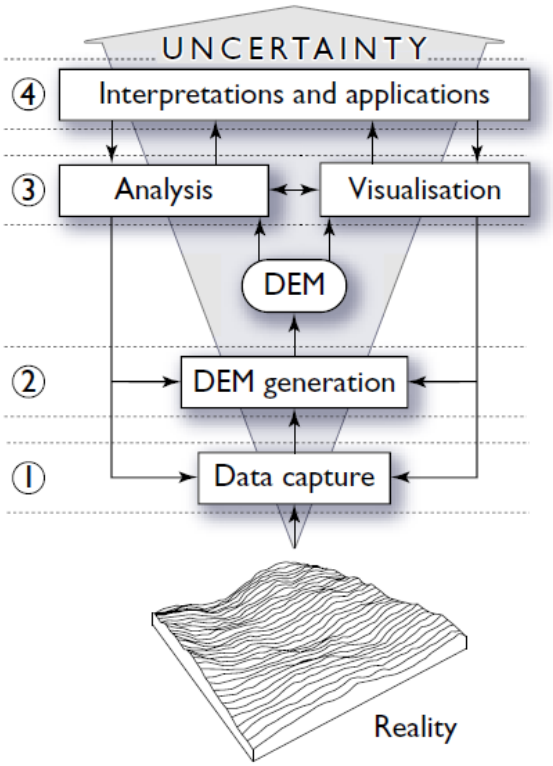

Figure 4-1 Process of constructing a Digital Elevation Model (DEM) and the propagation of uncertainty into the decision making (Oksanen (2006) modified from Hutchinson and Gallant (2000))

4.4.2.1 Data Capture

To create a DEM, one first needs to capture elevation data. In the past, the most prominent sources of elevation data were surface specific point elevation data (field surveys) and contour data derived from field surveys/point clouds. Nowadays, remote sensing is the favoured approach, with techniques ranging from photogrammetry, airborne and spaceborne interferometric Synthetic Aperture Radar (SAR) or LIght Detection And Ranging (LIDAR). Indeed, Smith and Clark (2005) note that the advent of remote sensing has meant that a larger area can be mapped by fewer people and at a diminishing cost.

4.4.2.1.1 Photogrammetry

Photogrammetry data are collected by attaching cameras to aircraft, with the more recent trend of using unmanned aerial vehicles (UAV) being used to generate DEMs at a low cost (Gonçalves and Henriques, 2015). In this technique, elevations are estimated using stereo-pairs of aerial photographs and so the process is largely suited to small landscapes (Hancock and Willgoose, 2001).

4.4.2.1.2 InSAR

InSAR (interferometric synthetic aperture radar) data utilises radar, often on satellite platforms, and takes advantage of the ability of the technology to extract continuous information over a large area without being restricted by clouds and night time that affects optical sensors. To collect the elevation data using SAR, the interferometric synthetic aperture radar (InSAR) technique is used which was first put into practice in the 1980's (Zebker and Goldstein, 1986). This technique is depicted in Figure 4-2. It involves two SAR satellites flying (ideally) in parallel tracks in slightly different directions and calculating the phase difference between the radar phases. Additionally, and now most commonly, two SAR antennas are placed on the same satellite as in SRTM. Radars can have different wavelengths (e.g X-band and C-band). For best results, the two SAR antennas should be operated simultaneously. In this particular setup, the primary antenna transmits and receives pulses, whilst the second antenna only receives. Using this setup has the advantage that an elevation is measured by antennas that are passing over a location very near (in temporal terms) to each other, reducing the impacts of changes in water vapour concentration and vegetation change that introduces phase errors when using repeat-pass

InSAR as for the latter the SAR instrument may pass over up to a month apart. The Shuttle Radar Topography Mission (SRTM) was the first single pass (two SAR antennas operated simultaneously) InSAR in space due to the high costs of using such a technique (Rabus et al., 2003).

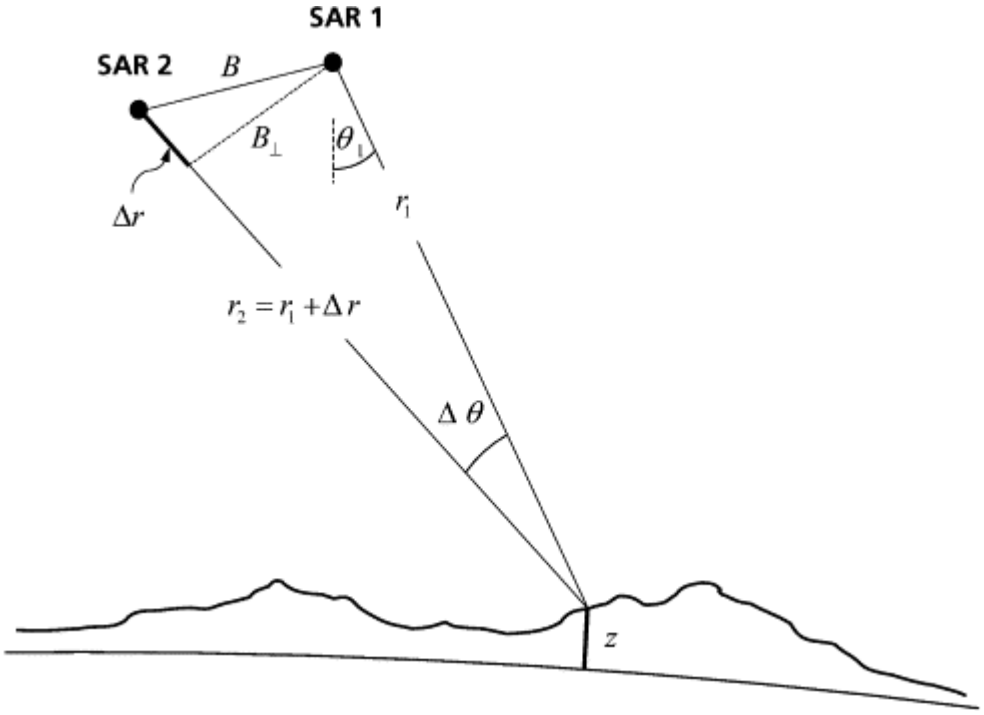

Figure 4-2 Across-track InSAR configuration. Courtesy of Rabus et al. (2003)

4.4.2.1.3 LIDAR

LIDAR data is collected by flying an aircraft over a landscape and emitting laser pulses to the surface which are subsequently reflected. The time taken for the laser pulse to be reflected back to the aircraft is measured, with the elevation subsequently calculated. This allows for a dense network of measurements to be collected over a large area very quickly. Pulsed laser beams are typically used to decipher multiple laser hits. Artefacts are then filtered to create either a DTM or DSM surface. For instance, in vegetated areas, the first return is assumed to be the canopy and the last the bare earth, thus vegetation height and a bare-surface can be inferred (Shan and Toth, 2008). Horizontal resolutions typically range between 0.5m-5m, with reported RMSE values typically less than 0.2m.

All these data sources have a form of error. For instance, GPS measurements, often seen as the gold standard for elevation measurements, are less accurate when the instrument's view to the sky is blocked by terrain and are limited to locations that are accessible (Carlisle, 2005). Contour data, produced from point cloud or field measurements, can be digitised, but this is subject to human error and the technique is known to undersample between contour points which is especially problematic in low-relief areas (Hutchinson and Gallant, 2000). Remotely sensed methods have the advantage of a broad spatial coverage, but are generally limited by sensors being unable to fully penetrate vegetation coverage and buildings, as well as issues related to instrument setup and terrain characteristics.

4.4.2.2 DEM Generation

Next the elevation data needs to be interpolated and gridded to create a DEM at a particular scale (Hutchinson and Gallant, 2000). Gridded products are generally favoured as they are compatible with other geophysical models that tend to work with grids (Wise, 2000). Numerous interpolation techniques exist, with four broad categories identified by Hutchinson and Gallant (2000) as triangulation; local surface patches and locally adaptive gridding. Indeed, by interpolating the error is intrinsically spatially dependent (Carlisle, 2005). Some of the most well-known interpolation methods are bilinear, inverse distance weighting, radial basis function, spline, local polynomial, ordinary kriging, universal kriging, multiquadratic radial basis function and regularized spline with tension (Wise, 2011, Chaplot et al., 2006, Mitas and Mitasova, 1999). The more traditional elevation data sources (points and contour lines) are spatially irregular and are processed with specific interpolation techniques to form triangulated irregular networks. Remotely sensed data are particularly conducive to the creation of regularly gridded DEMs, with gridding methods that have been adapted to filter out the noisy data (Hutchinson and Gallant, 2000). A multitude of empirical studies have investigated the effects of interpolation methods, usually by comparing interpolated surfaces to a higher accuracy reference surface or a subset of original points (Wise, 2000, Wise, 2011, Wise, 2007, Chaplot et al., 2006, Erdogan, 2009, Heritage et al., 2009, Desmet, 1997, Guo et al., 2010, Rees, 2000, Kidner, 2003, Bater and Coops, 2009). Several of these studies have also looked into the impact of spatial resolution in the interpolation process (Bater and Coops, 2009, Wise, 2011, Guo et al., 2010). Despite all

these studies there is no clear consensus on the best interpolation method (Fisher and Tate, 2006) . Errors in phase 2, or the DEM generation phase (see Figure 4-1), also occur with the choice of DEM approximation and the level of detail (e.g. mesh size or TIN density) (Oksanen, 2006). For some types of analysis it is necessary to further modify the DEM by removing erroneous depressions, also known as sinks or pits. Doing this is a 'necessary evil' for hydrologic analysis according to Burrough and McDonnell (1998), as one must be careful not to remove components that are real. Techniques to hydrologically condition the DEM include stream burning (Saunders, 1999), AGREE (Hellweger, 1997), ANUDEM (Hutchinson, 1989), outlet breaching (Martz and Garbrecht, 1999), iterative flow direction resolution (Kenny et al., 2008), Priority-Flood (Barnes et al., 2014) and TopologicalBreachBurn (Lindsay, 2016).

Phases 1 & 2 (DEM Capture and DEM Generation in Figure 4-1) are the input error in the DEM. When a DEM is produced by a user, perhaps for a bespoke study, the error in the data capture and processing is generally well understood and well-documented (Januchowski et al., 2010). This situation is now less common as users routinely acquire DEMs by purchasing or obtaining publicly available products. Yet these DEM vendors frequently do not supply adequate metadata on data collection and processing, leaving the user unsure of the uncertainty, and especially the spatial dependency of the uncertainty. This has led to calls from for DEM vendors to provide more detailed information (Kydriakidis et al., 1999, Wechsler, 2007).

4.4.2.3 Analysis & Visualisation

Phase 3 (Figure 4-1) constitutes the uncertainty introduced as part of the visualisation and analysis process. In other words, this phase (and subsequently phase 4) refers to the output from the DEM. Visualisation can be both a tool for identifying and communicating error. The most basic visualisation or errors are difference maps, or residual maps, but can also include graphs of summary statistics. Uncertainty introduced from DEM analysis refers to the propagation of errors into terrain parameters (e.g. slope, aspect etc). DEM users typically use these parameters in their analysis or models, so it is important to understand how error propagates to these parameters. Calculating these impacts is further complicated as often

there are different algorithms to calculate the same parameter (e.g. slope) (Wechsler, 2007). According to Thompson et al. (2001) several factors play an important role in the quality of the derived terrain parameters including terrain roughness and complexity, terrain modelling aspects (e.g. interpolation method), pixel size, vertical accuracy and the type of algorithm used. A wide body of literature has assessed these impacts by using strategies such as comparing terrain parameters calculated from a variety of DEM sources or by investigating the impact of different phase 2 processing techniques (e.g. interpolation or sink filling) on the terrain parameters. An example of the former is the work of Januchowski et al. (2010) who derive slope and aspect from five DEMs, with almost all DEMs providing overestimates of the parameters. Interestingly, they estimate a cost/accuracy ratio, suggesting that the relatively coarse SRTM (Shuttle Radar Topography Mission) provides the most appealing cost (cost of data and man hours to process)/accuracy ratio but this can alter depending on the threshold of accuracy required. The link between elevation error and slope has been well researched, with the largest errors in slope not necessarily corresponding to the largest errors in elevation (Holmes et al., 2000, Thompson et al., 2001, Januchowski et al., 2010, Gonga-Saholiariliva et al., 2011, Hunter and Goodchild, 1997, Carlisle, 2005, Fisher, 1998). Other terrain parameters are also assessed in conjunction with slope such as aspect (Goulden et al., 2016, Mashimbye et al., 2014, Januchowski et al., 2010), curvature (Wise, 2011), drainage basin area (Oksanen and Sarjakoski, 2005) and upslope contributing area (Wu et al., 2008). DEM resolution has been found to influence the quality of terrain parameters with higher resolutions generally giving more accurate terrain parameters, with the impact varying considerably across landforms (Kienzle, 2004, Deng et al., 2007, Chow and Hodgson, 2009, Sørensen and Seibert, 2007, Vaze et al., 2010, Wu et al., 2008, Zhang et al., 1999, Thompson et al., 2001, Thomas et al., 2017, Hancock, 2005, Shi et al., 2012). Differing interpolation techniques can seriously alter topographic parameters with curvature found to be particularly sensitive (Wise, 2011, Wise, 2007, Wise, 2000). The sink filling procedure has been found to seriously alter the spatial and statistical distributions of terrain parameters such as slope (Wechsler, 2000, Lindsay and Creed, 2005, Callow et al., 2007, Woodrow et al., 2016) as the elevation of the depression is raised (thus resulting in a larger positive bias in elevation) and consequently slope decreases. This brief overview of

the impact of DEM error on terrain parameters is far from exhaustive so the reader should consult the quoted references if additional information is required.

4.4.2.4 Interpretations & Applications

The last phase, phase 4, refers to the interpretations and applications derived from a DEM. In effect this is the impact DEM error has on a geoscientific model that utilises a DEM. For example, landslide hazard models usually calculate a factor of safety from the slope. As these models can rely on several terrain parameters, the uncertainty from the DEM has propagated through the phases as outlined in Figure 4-1. DEM resolution has been shown to impact model outputs for a wide range of geoscientific modelling applications including: landslide models (Claessens et al., 2005, Holmes et al., 2000), landscape models (Schoorl et al., 2000), the TOPMODEL hydrologic model (Wolock and Price, 1994, Zhang and Montgomery, 1994, Wise, 2007), the SWAT hydrologic model (Chaplot, 2005, Chaubey et al., 2005), the WEPP hydrologic model (Zhang et al., 2008), the HSPF model (Yang et al., 2014) and the LISFLOOD-FP hydrodynamic model (Savage et al., 2016b, Bates and De Roo, 2000, Horritt and Bates, 2001a). Yet, modellers often tend not to ask questions about model sensitivity to DEM derived parameters and instead focus on attributes such as hydrograph estimations and Manning's roughness coefficients (Wechsler, 2007).

What is not mentioned above is the uncertainty introduced by time. A landscape evolves, be it geomorphologically or more commonly with the help of humans, so one can be less certain about the accuracy of the DEM product as time goes on. It is unlikely one would use a map that is almost 20 year old to plan a hiking expedition as the landscape and footpaths may have changed in that period. Yet, this is effectively what a lot of DEM users are doing, and often users do not fully address or even recognise this issue.

Despite DEMs being frequently used, users are not always aware of DEM errors or how to treat them. Whatever the source, DEM products provide a definite and plausible representation of the terrain which often lulls the user into a false sense of security regarding the accuracy of the product (Wechsler, 2007). Wechsler (2003) provides an intriguing insight into the matter when she surveyed 216 DEM users from 26 countries to gauge perceptions of DEM uncertainty. Half of the respondents recognised that they are 'sometimes' or 'always'

affected by uncertainty, whilst 25% reported a lack of awareness as to whether DEM errors affected their results at all (Wechsler, 2003). Less than half of respondents accounted for uncertainty, with RMSE the most commonly reported metric, and most DEM users, despite recognising the importance of uncertainty, were only willing to dedicate the minimal amount of time to it. As far as we are aware there has been no follow up to this 15-year-old study which highlights the lack of understanding of the impact of DEM uncertainty and the unwillingness to address it. Certainly, in the case of flood modelling, the impact of DEM uncertainty on flood estimates has not been as stridently investigated compared to other sources of uncertainty. As a result, Wechsler (2007) proposed the development of a DEM uncertainty toolbox to be implemented into GIS. This would form a one-stop-shop where DEM error could be quantified, simulated and communicated so users could get a stronger grip on how DEM error impacts on their work.

4.4.3 Global DEM Products

Freely available high accuracy airborne hyper-scale DEMs (<10m horizontal resolution) are only available for a very small proportion of Earth's land surface (~0.005%), so spaceborne global DEMs offer the best source of topographic information for most of the Earth. Several freely and commercially available global DEM products exist as outlined in Table 4-3.

Table 4-3 Overview of Global DEM Products

	Dataset	Coverage	Acquisition Years	Sensor	Wavelength	Resolution (m)	Vertical Accuracy	Reference
Free Global DEMs	ALOS AW3D30	82°S - 82°N	2006-2011	Optical	0.52-0.77um	30	4.4m (RMSE)[1]	Tadono et al. (2014)
	ASTER GDEM	83°S - 83°N	2000-2011	Optical	0.78-0.86	30	17m (95% conf.)[2]	Tachikawa et al. (2011a)
	GMTED2010	Entire Earth	Completed 2010	Derived from 11 sources of elevation information		250,500,1000	26m (RMSE)[3]	Danielson and Gesch (2011)
	SRTM	56°S - 60°N	2000	SAR C Band	5.66cm	30,90	6m (MAE)[4]	Farr et al. (2007)
	TanDEM-X 90	Entire Earth	2010-2015	SAR X Band	3.1cm	30,90	Unknown	Rizzoli et al. (2017)
Error Reduced Versions of SRTM	EarthEnv	60°S - 83°N	ASTER & SRTM			90	4.15m (RMSE)[5]	Robinson et al. (2014)
	NASADEM	Expected release late 2018						Crippen et al. (2016)

	MERIT	Entire Earth	AW3D30, SRTM & Viewfinder Panorama			90	5m (LE90)[6]	Yamazaki et al. (2017)
	Bare-Earth SRTM		Same as SRTM			90	5.9m (RMSE)[7]	O'Loughlin et al. (2016b)
	No Name		Same as SRTM			90	1m reduction in RMSE[8]	Zhao et al. (2018)
	Viewfinder Panorama	Entire Earth	ASTER, SRTM & Other Sources			90	Not Reported	de Ferranti (2014)
Commercial Global DEMs	ALOS AW3D	82°S - 82°N	2006-2011	Optical	0.52-0.77um	5	2.7m (RMSE)[9]	Takaku and Tadono (2017)
	PlanetDEM 30 Plus	Entire Earth	Same as SRTM			30	Not reported	Planet (2017)
	NEXTMap World 10	Entire Earth	Not Reported			10	10m (LE95)[10]	InterMap (2018)
	WorldDEM	Entire Earth	2010-2015	SAR X Band	3.1cm	12	<1.4m (RMSE)[11]	Rizzoli et al. (2017)

N.B. Older Global DEMs ACE GDEM (Berry et al., 2000) and GTOPO30 (Gesch et al., 1999) were not included in the table as these products have been superseded by more recent GDEMs. 1) Tadono et al. (2016) 2) Tachikawa et al. (2011b) 3) Danielson and Gesch (2011) 4) Rodriguez et al. (2006) 5) Robinson et al. (2014) 6) Yamazaki et al. (2017) 7) O'Loughlin et al. (2016b) 8) Zhao et al. (2018) 9) Takaku et al. (2016) 10) InterMap (2018) 11) Wessel et al. (2018)

Of all the global DEM products, the Shuttle Radar Topography Mission (SRTM) remains the most widely used. SRTM is a freely available DEM covering 99.97% of the earth's land surface between 56°S and 60°N (Rabus et al., 2003, Farr et al., 2007) and is the most widely used global DEM product owing to its coverage and accessibility. Data was collected by a single-pass interferometric Synthetic Aperture Radar system over an 11 day period in February 2000. This NASA led mission resulted in a 3 arc second (≈90 m) near global DEM being initially released, before a 1 arc second (≈30 m) was released in late 2015. Various versions of SRTM exist including the original non-void filled SRTM V1, void filled products SRTM V2, SRTM V3 and the CGIAR-CSI developed version (Jarvis et al., 2008). In the near future the NASADEM (Crippen et al., 2016), which will be a reprocessed version of the original SRTM dataset, is due to be released. Other freely available global DEMs include the Advanced Spaceborne Thermal Emission Radiometer (ASTER) (Abrams, 2000) with the global product at 90m and spanning to 83°S and 83°N, the Advanced Land Observing Satellite (ALOS AW3D30) (Tadono et al., 2016) at 30 m, and the Global Multi-resolution Terrain Elevation Data 2010 from 250 m resolution (Danielson and Gesch, 2011). Error reduced versions of SRTM have also been produced, usually by fusing with other DEM products, with examples including EarthEnv (Robinson et al., 2014) and Viewfinder

Panorama (de Ferranti, 2014). These have all superseded older DEMs such as the ACE GDEM (Berry et al., 2000) and GTOPO30 which have a resolution of 1km. Recently, the DLR (German Aerospace Center) led TanDEM-X global DEM (Krieger et al., 2007, Moreira, 2017, Rizzoli et al., 2017) has become increasingly available for educational/research purposes, but the public private partnership consortium nature of the mission has restricted the product's ease of access, resulting in a lack of applications. However, as of the 29/09/2018, a 90 m version of TanDEM-X called TanDEM-X 90 has been released and is freely available. TanDEM-X was collected using a high resolution interferometric SAR configuration, providing a ground resolution of 12 m. Importantly, Tan DEM-X covers all land surfaces, with data collection from December 2010 to early 2015 (Rizzoli et al., 2017), thus providing an important update on SRTM. Performance assessment of the product has found it to out-perform mission criteria, with Rizzoli et al. (2017) finding a vertical error of 3.49m at 90% confidence, or 0.88 m if forested areas and ice are excluded. To date, most applications of TanDEM-X have focussed on quantifying vegetation heights (e.g Schreyer et al. (2016)), with Martone et al. (2018) recently calculating a global forest/non-forest map at 50 m. Flooding related studies have so far been limited to a method proposed by Mason et al. (2016) to improve TanDEM-X in floodplains based on flood extents. Until very recently, there had been no flood inundation studies utilising Tan-DEM-X data, with Archer et al. (2018) demonstrating that the flood model skill scores improves when using TanDEM-X with vegetation removal compared to SRTM, MERIT and the DSM version of TanDEM-X. However, Archer et al. (2018) notes that the complex data acquisition process has limited the use of the product, despite the potential to improve flood inundation estimates. On a similar note, commercially available DEMs are also available (such as Nextmap World10™, World30™ and Airbus WorldDEM™), but their restricted rights, prohibitive costs and lack of independent validation studies comparing them to other DEMs and ground observations make their use limited. With all this considered, the SRTM dataset is generally still favoured, particularly the CGIAR-CSI Version 4 (Jarvis et al., 2008), due to ease of access, greater feature resolution, reduced number of artefacts, lower noise and better vertical accuracy than other global DEM products and older versions of SRTM (Jing et al., 2014, Rexer and Hirt, 2014, Jarihani et al., 2015, Sampson et al., 2016, Hu et al., 2017). Therefore, the SRTM and its derivatives still form a crucial resource in providing topographic information to

many hazard and risk assessment models, particularly in data-poor locations where high resolution topographic data such as LIDAR (light detection and ranging) either does not exist or is not accessible. Despite calls for a concerted effort to produce a free accurate global DEM (Schumann et al., 2014), there is little sign that such a dataset will be produced soon, thus SRTM remains the best option for elevation data for much of the earth now, and for the foreseeable future.

Errors in the SRTM dataset was most comprehensively characterised by a large global study carried out by Rodriguez et al. (2006). Using nearly 9.4 million Kinematic Global Positioning System (KGPS) samples collected along roadways in six continents, Rodriguez et al. (2006) found that 90% of the errors were less than 5m, well within the missions' accuracy requirements of an absolute height error of 16m (Rabus et al., 2003). Other more localised studies have also assessed SRTM absolute errors, with most of these focussed on vertical error (Table 4-4). Reporting vertical accuracy as a single measurement such as root mean square error (RMSE) has its advantages as it is quick to calculate and easy to report, but it does not portray the heterogeneity of the error and can imply on first glance that the error across the DEM is uniform. In section 4.4 we explain why this pitfall is incorrect

Table 4-4 Overview of SRTM Error Studies. Vertical errors from each study are reported, either as Root Mean Squared Error (RMSE) or MAE (Mean Absolute Error). Landcover refers to the landcover class of the location in each study. Inclusion of error assessment from vegetation or terrain, or an analysis of spatial dependence are assessed on a yes/no basis. The stated figures only give a headline and interested readers are referred to the referenced studies for more details on the methods used.

Location	RMSE (m)	MAE (m)	Landcover	Vegetation Error	Terrain Error	Spatial Dependence	Reference
Global		6	Mixed	No	No	Yes	Rodriguez et al. (2006)
Argentina	8.3	-0.6	Mixed	No	Yes	No	Gómez et al. (2012)
Australia	4.5		Mixed	Yes	No	No	Rexer and Hirt (2014)
Bhutan	11.3		Mountainous	No	Yes	No	Fujita et al. (2008)
China		1.5-2.6	Mixed	Yes	Yes	No	Hu et al. (2017)
China	2.26-3.61		Low Relief	No	No	No	Du et al. (2016a)
China		-3.49	Mixed	Yes	Yes	No	Huang et al. (2011)
China	12.44		Mixed	Yes	Yes	No	Jing et al. (2014)
Costa Rica		4.5	Forest	Yes	No	No	Hofton et al. (2006)
Croatia	3.8	0.2	Mixed	Yes	Yes	No	Varga and Bašić (2015)
French Guiana		10.2	Forest	Yes	Yes	No	Bourgine and Baghdadi (2005)

Location	RMSE (m)	MAE (m)	Landcover	Vegetation Error	Terrain Error	Spatial Dependence	Reference
Ghana	4.4-14.5		Mixed	No	No	No	Forkuor and Maathuis (2012)
Greece	25	19	Mixed	No	Yes	No	Miliaresis and Paraschou (2005)
Greece		6.4	Mixed	No	Yes	No	Mouratidis et al. (2010)
India	17.76		Mountainous	No	No	No	Mukherjee et al. (2013)
Indonesia	3.25		Mixed	No	No	No	Suwandana et al. (2012)
Mozambique		1.95	Mixed	No	No	No	Karlsson and Arnberg (2011)
Norway	6.5		Mixed	Yes	No	No	Weydahl et al. (2007)
Poland	14.74	4.31	Mountainous	Yes	Yes	No	Kolecka and Kozak (2014)
Thailand		7.58	Mixed	No	Yes	No	Gorokhovich and Voustianiouk (2006)
Tunisia	3.6	2.9	Dryland	No	No	No	Athmania and Achour (2014)
Turkey	9.8		Mixed	No	No	No	Bildirici et al. (2009)
USA		5	Low Relief	Yes	No	Yes	LaLonde et al. (2010)
USA		4.07	Mixed	No	Yes	No	Gorokhovich and Voustianiouk (2006)
USA	8.6		Mixed	Yes	Yes	Yes	Shortridge and Messina (2011)
USA	7.18		Mixed	No	Yes	No	Falorni et al. (2005)
USA	6.32	3.23	Mixed	Yes	Yes	Yes	Shortridge (2006)

Sources of errors in the SRTM are numerous and complex. Errors can originate from instrument setup, causing characteristics such as speckle noise (Rodriguez et al., 2006, Farr et al., 2007) and striping (Walker et al., 2007, Tarakegn and Sayama, 2013, Sampson et al., 2016). Novel research by Becek (2008) compared elevation data from 302 airport runways worldwide to SRTM heights, thereby concentrating on instrument error and excluding vegetation, with their findings suggesting an RMSE error of ±1.55m with proximity to large metallic objects being a suspected source of the larger SRTM errors in their study. The Becek (2008) study is also important as it focuses on runways which have a low slope. Substantial errors are also found in areas of high and steep relief, with the slope causing frequent data voids (Falorni et al., 2005) and the steeper the slope, the greater the error (Shortridge and Messina, 2011). In their study in the USA, Shortridge and Messina (2011) also analysed aspect and vertical error, concluding that a strong association existed with the greatest positive error magnitudes in northwest orientated aspects and the greatest negative error magnitudes in the southeast orientated aspects. Indeed, the authors surmise that directional error component is almost certainly caused by the sensor's orientation during the mission, with direction of travel on ascending orbits 57° east of north, and 327° on descending orbits,

thereby the largest positive errors being exactly perpendicular to the ascending orbits as illumination over the study region was always towards the north. Yet, the authors could not explain the reason behind the negative bias on the southeast facing slopes. Moreover, SRTM has an inability to resolve features in urban areas owing to resolution and radar reflectance issues (Gamba et al., 2002, Farr et al., 2007, Avtar et al., 2015). Yet, the biggest body of research in this area has focussed on vegetation. The SRTM radar signal tends to be reflected from the canopy or scattered within it. This is primarily due to the C band radar having a similar wavelength (5.6cm) to scattering elements such as leaves, branches and twigs (Walker et al., 2007). Numerous studies have shown the largest errors in SRTM to be found in heavily forested areas, with larger vegetation height correlated to a larger positive bias (Carabajal and Harding, 2006, Hofton et al., 2006, Shortridge, 2006, Weydahl et al., 2007, LaLonde et al., 2010, Shortridge and Messina, 2011). It should also be noted that seasonality can potentially impact the vegetation height error as SRTM was collected in February, thus winter in the northern hemisphere and summer in the southern hemisphere, thereby trees can be either bare leaved or in full foliage respectively. This recognition of vegetation derived error has led to various vegetation removal attempts from SRTM. In a study in the Amazon, Baugh et al. (2013) created a vegetation removed SRTM and assessed its performance in a flood inundation study. Su et al. (2015) applied a regression model to remove vegetation bias in the Sierra Nevada Mountains, California, and Wendi et al. (2016) applied an Artificial Neural Network to the problem for a small forested area in Singapore. In a coastal environment, vegetation and urban features have created a positive bias in elevation resulting in an underestimation of sea level rise and flooding exposure (Kulp and Strauss, 2016), leading to a Coastal bare earth DEM being developed called CoastalDEM (Kulp and Strauss, 2018).Most recently, Ettritch et al. (2018) used Landsat imagery to remove vegetation from SRTM 30m to be used in a LISFLOOD-FP model in The Gambia. Vegetation removal has also been applied to the whole SRTM dataset to create various bare-earth versions of the SRTM DEM (O'Loughlin et al., 2016b, Yamazaki et al., 2017, Zhao et al., 2018) with these products demonstrating an accuracy improvement over the original SRTM dataset.

The recent release of the MERIT (Multi-Error-Removed-Improved-Terrain) DEM sees the most comprehensive error removal from SRTM by not only removing vegetation error, but also separating absolute bias, stripe noise and speckle noise, with the most pronounced improvements reported in flat regions (Yamazaki et al., 2017). Aside from the improvements over SRTM reported by Yamazaki et al. (2017), the only other comparative study between MERIT and SRTM was carried out by Hirt (2018). The Hirt (2018) found that MERIT contained 12x fewer artefacts than CGIAR CSI version 4 (Jarvis et al., 2008) based on 0.1 x 0.1 degrees sub-divisions and a 5m/m slope threshold (or 450m for two adjoining 90 x 90m pixels), with these artefacts largely as a result of the void-filling process with the vast majority found in high topographic areas. At the time of writing, MERIT is the most comprehensive readily available bare-earth version of SRTM and thus the one we will adopt for our analysis.

4.4.4 Geostatistics & DEM Simulation

With the notion that error is spatially autocorrelated, we can explore the error in the DEM with geostatistics. The field of geostatistics fundamentally differs from that of classical statistics in that it assumes the existence of spatial autocorrelation (Olea, 2006). Geostatistics can provide the tools to simulate plausible versions of the DEM, with the methods and examples to do this reviewed in this section.

The *simulation school* (Chrisman, 1989) regards a DEM as a single rendering of a possible realization of the true map, and to characterise the true value requires a number of realizations. Generating equiprobable distributions of maps is referred to as stochastic modelling, or more commonly Monte Carlo Simulation. The basic assumption of Monte Carlo simulation is that the DEM is only a single realization of a host of potential realizations. By simulating DEMs, a single true DEM is not created, but instead the realizations provide a bound where the true values lie.. The Monte Carlo technique is the most popular (Heuvelink et al., 2007) with this being attributed to the simplicity of the concept and the advances in computing power that allow a brute force approach (Heuvelink et al., 2007, Wechsler, 2007), especially as Heuvelink (1998) recommends that 50-2000 simulations are needed to avoid simulations converging. In the following paragraphs, the

methods to translate this idea into practice are given, followed by a comprehensive overview of examples.

An important component of geostatistics is the concept of a random field (RF), or a random function, which can be considered as a set of spatially dependent random variables defined over an area of interest or study site. Taking a step further back, a random variable is a variable that can take a variety of outcomes based on some probability distribution and forms the basis of predictive statistics (Deutsch and Journel, 1998). Random variables can be either discrete or continuous, with Goovaerts (1997) providing an excellent overview of the concept.

In essence the random field represents the potential spatial uncertainty. This error map is subsequently added to the DEM in question to form a realization. This can then be conditioned based on observations, where the implicit DEM error is effectively eliminated at the observation points. By producing multiple random fields, one can produce multiple realizations. Stationarity is a property of the random field model and is needed for inference. The choice of stationarity is a decision made by the user and is not necessarily a characteristic of the phenomenon being investigated (Goovaerts, 1997). To calculate the error Z (or the difference between the simulation and the DEM) at location x, we can use the following equation;

$$Z(x) = u(x) + e(x) \tag{18}$$

Where $u(x)$ is the mean of Z(x) which assuming a normal distribution can be assumed to be zero. The random field is $e(x)$, which assuming second-order stationarity and isotropy has a mean of zero, a variance (random error) and spatial correlation given by the semi-variogram.

In geostatistics the most common tool for investigating the spatial structure of data is the semi-variogram ($\gamma(\mathbf{h})$), which measures the average dissimilarity between data separated by a vector ($\mathbf{h}$), or in geostatistical jargon the lag (Goovaerts, 1997). In other words, a semi-variogram relates semi-variance to spatial separation (Curran, 1988). So in practice, when

two sites are a lag of **h** apart, the semi-variogram is half the average squared difference between the paired data. In the case of DEM error assessment, this is the difference between a DEM and the reference elevation measurement. These error residuals could be any number of things with studies ranging from gravity anomalies (Olea, 2006) to mineral prediction (Goovaerts, 1997).

An empirical semi-variogram and is calculated with the following equation;

$$\gamma(\mathbf{h}) = \frac{1}{2N(\mathbf{h})} \sum_{i=1}^{N(\mathbf{h})} [\{X(s) - X(s')\}]^2 \qquad (19)$$

where γ is the semi-variogram, N(**h**) is the number of pairs, **h** is the lag and s and s′ are the vectors of spatial coordinates X.

To geostatistically simulate, a fitted or modelled semi-variogram becomes mandatory to create a continuous surface. One must decide whether this should be isotropic or anisotropic. Detecting anisotropy is usually carried out by computing semi-variograms in several directions or generating semi-variogram maps, and supplemented by ancillary information about the study site (see 4.6.5)) (Goovaerts, 1997). Fitted semi-variograms are represented by a semi-variogram model which guarantees that the autocovariance function used in further geostatistical analysis is positive definite, or in other words where all possible values for the covariance matrix are nonnegative. Common models include, Spherical, Exponential, Gaussian and Power, although a wide range exist and are presented in Figure 4-3. These semi-variogram models are commonly characterised by three parameters: nugget, sill and range. The nugget represents the magnitude of discontinuity in semi-variance near the origin and occurs because of measurement errors and spatial variability at distances smaller than the shortest sampling distance. The sill refers to the semi-variance value at which the semi-variogram levels off and is the marginal standard deviation. The range refers to the lag distance where the semi-variogram effectively reaches the sill value. For the Exponential and Gaussian models, the semi-variogram reaches the sill asymptotically, so a practical range is defined as the distance at which the model value is at 95% of the sill.

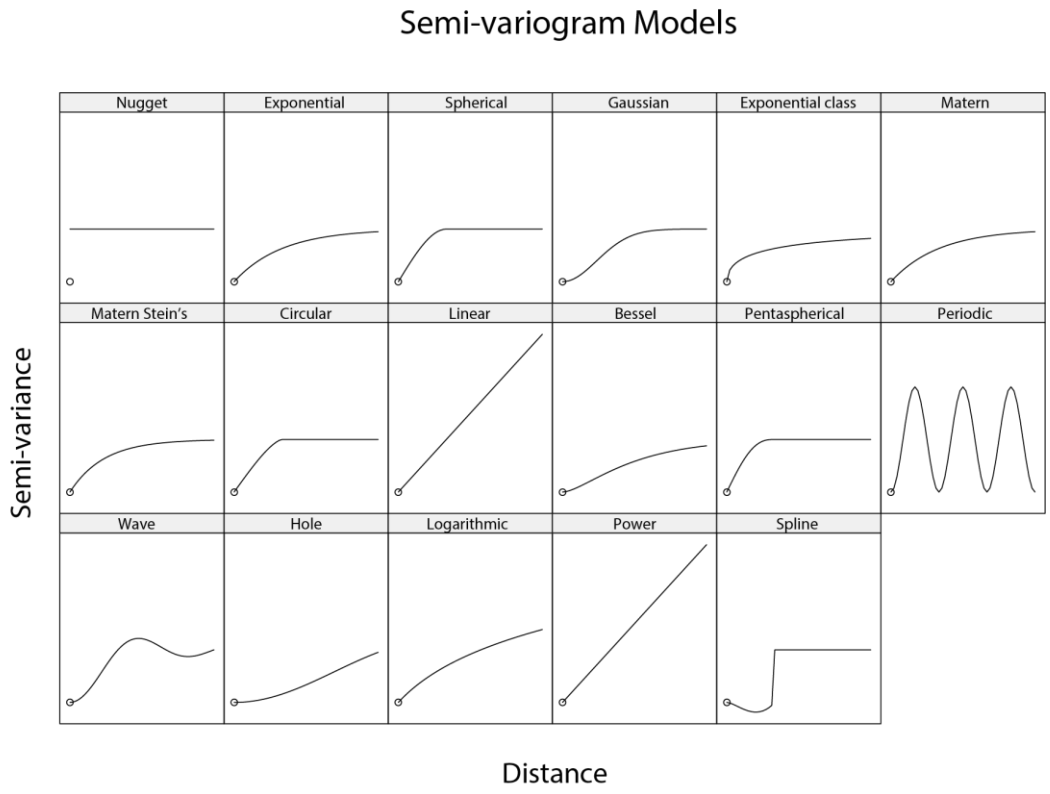

Figure 4-3 - Semi-variogram models available in the gstat package in R (Pebesma, 2004)

Kriging is a well-known set of methods to generate a surface based on a set of generalised least regression methods for minimising the estimation variance defined from a prior covariance model (Deutsch and Journel, 1998). Methods of kriging include simple kriging, ordinary kriging, universal kriging, indicator kriging and co-kriging. Even though kriging gives the best estimate in terms of least squares, the surface is unrealistically smooth as in effect the variogram produced is very different to the original with an evident underestimation in the short-range structure of the random field (Goovaerts, 1997). Thus, to overcome these limitations, stochastic simulation is required.

To simulate a DEM, the random field is required. A simple uncorrelated random field is normally distributed with a mean of 0 and a standard deviation approximately equivalent to the RMSE of the DEM error (Hunter and Goodchild, 1997, Wechsler, 2007, Deutsch and Journel, 1998, Fisher and Tate, 2006). Yet, from section 4.4.1, we know that error is spatially dependent. Indeed, the uncorrelated representation of error fields is seen as the worst case

scenario (Oksanen and Sarjakoski, 2005), with the possible scenario that if spatial autocorrelation of error is ignored a situation can arise whereby adjacent pixels have an error assigned that is at the opposite end of the error envelope (Davis and Keller, 1997b). To address this challenge the following methods have been developed to account for spatial autocorrelation in random fields.

Simulated annealing (Deutsch and Journel, 1998) is the practice of perturbing an original image until it matches the characteristics of a target written as an objective function. This objective function may be a prespecified semi-variogram. To perturb an image, pairs of pixel values are swapped and, thus, the technique is sometimes known as Pixel swapping (Goodchild, 1980, Fisher, 1991). Each perturbation is either accepted or rejected depending on whether the perturbation carries the image towards an objective. The technique can be extremely computationally intensive if used in a brute force manner, so judgements need to be made quickly on the quality of the perturbations and whether the perturbation is moving towards the objective function. The technique can also be vulnerable to converging to local optima. Examples of studies utilising this method include Fisher (1991), Lee et al. (1992), Davis and Keller (1997b), Veregin (1997), Endreny and Wood (2001) and Lindsay (2006).

Spatial moving averages applies a filter to the random field to increase its spatial autocorrelation (Wechsler, 2007). The kernel size of the filter can vary from a simple 3x3 low-pass filter to one that takes into account spatial dependence calculated by a semi-variogram (e.g 9x9 in the Wechsler and Knoll (2006) study). Filter methods can include neighbourhood autocorrelation, mean spatial dependence and weighted spatial dependence (Wechsler and Knoll, 2006). Examples of studies using this technique are Gatziolis and Fried (2004), Widayati et al. (2004), Raaflaub and Collins (2006), Wechsler and Knoll (2006) and Zandbergen (2010).

A spatial autoregressive model was introduced by Hunter and Goodchild (1997). Spatial autocorrelation is introduced based on a spatially autoregressive process where;

$$e = pWe + N(0,1) \tag{20}$$

Where *e* is a vector of values in the random field, *p* a parameter of spatial autocorrelation, W a matrix of weights where 1=rook's case and 0 is other and *N* a vector of independently and normally distributed values. With the rook's case definition, the range of *p* lies between 0 and 0.25, with spatial autocorrelation distinct as values approach 0.25. Examples of studies using this technique are Hunter and Goodchild (1997) and Murillo and Hunter (1997). Like the previous two techniques, this is useful in the absence of explicit information on the spatial autocorrelation of the DEM.

Sequential Gaussian simulation (SGS) generates random fields as follows: (1) A random path is defined so each pixel of the grid is visited once; (2) At each pixel, simple kriging is used to determine the parameters (mean and variance) of the Gaussian local ccdf based on the normal score semi-variogram. Original data values and previously simulated values within the local neighbourhood are considered; (3) Draw a simulated value from the ccdf and insert into the dataset; (4) Repeat steps 2 & 3 until all pixels along random path are visited; (5) Repeat N times for the number of simulations; (6) Back-transform the simulated normal values into a simulated joint realisation of the original variables (Goovaerts, 1997, Holmes et al., 2000, Zhang and Goodchild, 2002). The computational load can be considerably reduced by keeping the same random path since the kriging weights only need to be calculated once (Pebesma, 2004, Oksanen, 2006, Deutsch and Journel, 1998). Yet this can lead to the simulations becoming too similar (Deutsch and Journel, 1998). This method has been used in studies by Kydriakidis et al. (1999), Holmes et al. (2000), Aerts et al. (2003), Oksanen and Sarjakoski (2005), Wilson and Atkinson (2005) and Hengl et al. (2010). This is the most favoured geostatistical simulation method and can utilise prior information on spatial autocorrelation. Consequently, the DEM simulation method proposed in this chapter is based upon this technique.

Sequential indicator simulation is similar to SGS and is perhaps the most-widely used non-Gaussian simulation technique (Goovaerts, 1997). It is a flexible approach where it is possible to define different semi-variogram models for different cut-off values (Zhang and Goodchild, 2002). This approach simulates more conservatively by preserving larger extreme values which can be critical in some Earth science applications where connectivity

of large values is important (Goovaerts, 1997). For a more comprehensive overview of the technique see Goovaerts (1997).

The simulation can be either unconditional or conditional. An unconditional simulation will only honour the semi-variogram model, whereas a conditional model will also honour existing observations (Oksanen, 2006). Thus, for a conditional simulation a reference data are needed (e.g. GPS measurements). Kydriakidis et al. (1999) classifies this sparsely available reference data as 'hard' data and the DEM elevations as 'soft' data. Conditional simulations are favoured over unconditional simulation as the simulations are conditioned by reference data and so conditional simulation makes full use of the statistical and spatial distribution of local error (Fisher, 1998). As a result, numerous studies have applied conditional simulation including Kydriakidis et al. (1999), Holmes et al. (2000), Aerts et al. (2003), Wilson and Atkinson (2005), Darnell et al. (2008), Hengl et al. (2010), Chen and Li (2012) and Leon et al. (2014). But, the usefulness of conditional simulation is restricted by only being able to simulate locations that have reference datasets available. Therefore, unconditional simulations can be fruitful in that a semi-variogram model can be characterised in locations where high accuracy data exists and then applied to similar locations.

4.4.5 A Review of DEM Simulation Studies

The following case studies demonstrate the DEM simulation approach in error propagation and uncertainty in DEMs and the impact it has on surface derivatives and hazard prediction, with an overview provided in Table 4-5.

Since the work of Goodchild (1980), DEM simulation has been practiced by researchers across numerous applications. Pioneering work by Fisher (1991) utilised the pixel swapping technique with spatial autocorrelation added with Moran's I to simulate 19 realizations of a 200x200 pixel subset of the USGS DEM of Prentiss, North Carolina. The work concluded that the viewshed calculated in the original DEM was notably greater than that in the simulations. A year later, this principle was extended to extracting drainage networks in a 100x100 pixel USGS DEM in Tennessee, with the authors concluding that the number of floodplain cells decreases when spatial autocorrelation decreases (Lee et al., 1992).

After a 5 year lull in published studies, numerous articles were published on the subject. Hunter and Goodchild (1997) assessed the influence of DEM error on slope and aspect by using a spatial autoregressive model and simulating 10 realizations of a DEM error for 40 values of p (spatial autocorrelation) where p varied between 0 and 0.25. The results showed that without empirical knowledge of the spatial autocorrelation, p=0.2 could be used as a worst-case scenario and that errors in slope and aspect were dependent on spatial autocorrelation. Similarly, Veregin (1997) assessed the impact of DEM error on flow direction by simulating DEMs using eight combinations of RMSE, autocorrelation and cross-correlation values, demonstrating that flow paths changed. Veregin (1997) concluded that 500 simulations were adequate to avoid convergence, putting into question previous studies that used only 20-30 simulations. This conclusion was since echoed by Heuvelink (1998). Lastly, Veregin (1997) advised that extreme caution should be taken when deriving flow direction from DEMs with a high vertical error as results were only marginally better than when flow paths were assigned randomly.

DEM simulation was applied to landslide risk across several studies in 1997. Murillo and Hunter (1997) initially simulated 180 DEMs in the Pacific Northwest using 10 values of p before simulating a further 50 realizations for the best p value. Using the 50 simulated DEMs overestimated the landslide hazard, with the authors noting this could be suitable for a risk averse approach. For Louise Island in British Columbia, Davis and Keller (1997a), Davis and Keller (1997b) went one stage further and simulated 1500 DEMs using sequential simulation. They found slopes were safer and floodplains were at greater risk than when a single DEM were used.

Table 4-5 DEM Simulation Studies

Reference	Simulation Technique	Location	DEM(s) used	Surface Derivatives
Fisher (1991)	Pixel Swapping	North Carolina, USA	USGS DEM	Viewshed

Reference	Simulation Technique	Location	DEM(s) used	Surface Derivatives
Lee et al (1992)	Pixel Swapping	Tennessee, USA	USGS DEM	Drainage Networks
Hunter & Goodchild (1997)	Spatial Autoregressive Model	Pennsylvania, USA	USGS DEM	Slope and Aspect
Veregin (1997)	Pixel Swapping	Ohio, USA	USGS DEM	Flow Direction
Murillo & Hunter (1997)	Spatial Autoregressive Model	Oregon, USA	USGS DEM	Landslide Hazard
Davis & Keller (1997)	Pixel Swapping	British Columbia, Canada	British Columbia TRIM	Landslide Hazard
Fisher (1998)	Pixel Swapping	Cairngorms, UK	Ordnance Survey Panorama	Viewshed
Kydriakidis et al (1999)	SGS	California, USA	USGS DEM	Spot Heights
Holmes et al (2000)	SGS	California, USA	USGS DEM	Slope, Aspect, Flow Accumulation, Slope Failure
Endreny & Wood (2001)	Pixel Swapping	Oklahoma, USA	USGS DEM	Flow Direction
Canters et al (2002)	Pixel Swapping	Flanders, Belgium	Belgian DEM	Landcover Classification
Aerts et al (2003)	SGS	Alps, Austria	Austrian DEM	Slope (Ski slope planning)

Reference	Simulation Technique	Location	DEM(s) used	Surface Derivatives
Cowell & Zeng (2003)	Uncorrelated Random Fields	Fingal Bay Beach, SE Australia	Australian DEM	Coastal Inundation
Gatziolis & Fried (2004)	Spatial Moving Averages	Michigan, USA	USGS DEM	Drainage Networks
van Niel et al (2004)	Spatial Autoregressive Model	NSW, Australia	Australian DEM	Net Radiation
Widayati et al (2004)	Spatial Moving Averages	Indonesia	Photogrammetry derived	Slope
Yilmaz et al (2004)	Uncorrelated Random Fields	Turkey	Contour-derived DEM	Flood Extent
Wilson & Atkinson (2005)	SGS	Northamptonshire, UK	Ordnance Survey Profile Contour	Flood Extent
Oksanen & Sarjakoski (2005)	SGS	Ruissalo, Finland	Contour derived DEM	Slope, Aspect, Drainage Basin
Oksanen & Sarjakoski (2006)	SGS	Ruissalo, Finland	National Land Survey of Finland DEM & LIDAR	Comparison to LIDAR
Lindsay (2006)	Pixel Swapping	South Pennines, UK	LIDAR	Channel Networks
Raaflaub & Collins (2006)	Spatial Moving Averages	Alberta, Canada	Photogrammetry derived	Slope & Aspect
Wechsler & Knoll (2006)	Spatial Moving Averages	North Carolina, USA	USGS DEM	Slope, Upslope Contributing Area, Topographic Index

Reference	Simulation Technique	Location	DEM(s) used	Surface Derivatives
Darnell et al (2008)	SGS	Slovenia	Slovenian DEM	Landslide Hazard
Hengl et al (2008)	Regression Kriging	Serbia	SRTM & topo-DEM	Comparison to control dataset
Hengl et al. (2010)	SGS	Serbia	topo-DEM	Channel Networks
Zandbergen (2010)	Spatial Moving Averages	North Carolina, USA	LIDAR	Depressions
Chen & Li (2012)	Adaptive Method (non-stationarity)	Sichuan, China	LIDAR	Comparison to control dataset
Leon et al (2014)	SGS	Brisbane, Australia	LIDAR	Coastal Inundation
Fereshtehpour & Karamouz (2018)	SGS	Lower Manhattan, New York, USA	NED & LIDAR	Coastal Inundation
West et al (2018)	Uncorrelated Random Fields	Devon, UK	LIDAR	Coastal Inundation

Fisher (1998) further explored the impact on viewshed when introducing a refined pixel swapping technique for DEM simulation. Heuvelink (1998) simulated 5000 DEMs and concluded that slope accuracy compared to a truth DEM increased with spatial correlation. Another highly influential study came a year later when Kydriakidis et al. (1999) presented a method that conflated sparse high accuracy ('hard') data with a lower accuracy DEM ('soft' data) to produce equiprobable realisations of the unknown higher accuracy elevation surface which could then be subtracted from the original DEM to obtain a realisation of the DEM error. Simulations using SGS was carried out for Death Valley to generate 50 DEMs

with more terrain complexity being represented using this method compared to not using the 'hard data'. Despite the detailed methodology, the complexity of the technique of Kydriakidis et al. (1999) has meant that simpler approaches have been favoured, although some do build upon their work.

The most cited DEM simulation paper is that of Holmes et al. (2000) (305 Google Scholar citations as of May 2019). The coherent methodology of Holmes et al. (2000) presents a simplified version of the work of Kydriakidis et al. (1999) where 50 DEMs of Sedgewick Natural Reserve, California, were simulated based on fitting a semi-variogram model and simulating using SGS. This semi-variogram was estimated by calculating residuals from 2652 GPS points that acted as a reference 'truth' dataset compared to the USGS 30m DEM. The fitted semi-variogram used an exponential model. The authors focussed on surface derivatives such as slope, aspect and flow accumulation and found error propagation was most glaring in valley bottoms and along streamlines. When applying the simulated DEMs to a slope failure model, Holmes et al. (2000) also concluded that the original DEM predicted a 25% smaller area that would suffer slope failure compared to the simulated DEMs, with the probability map from the simulated DEMs closer to what occurred in the 1998 landslide of the area.

Endreny and Wood (2001) generated 2000 DEM simulations by varying RMSE and spatial autocorrelation values to test terrain error sensitivities of 6 runoff flowpath algorithms for the dispersal of NPS pollutants, resulting in a runoff probability map that could be used for delineating optimal areas to intercept pollutant runoff. Canters et al. (2002) simulated 20 DEMs for landscape classification concluding that transition zones were most sensitive to reclassification. Zhang and Goodchild (2002) compared analytical and simulation techniques in simulating 30 DEMs for a suburb of Edinburgh, UK and the impact on slope. In a novel study, Aerts et al. (2003) used 70 GCP points to fit a semi-variogram and SGS to simulate 500 DEMs for ski route planning in Austria. Cowell and Zeng (2003) applied random error with no spatial autocorrelation in simulating DEMs to estimate coastal hazard in Fingal Bay Beach, SE Australia. By increasing spatial autocorrelation values, Gatziolis and Fried (2004) concluded that drainage network delineation improved. By using a Mersenne twister pseudo random number generator, Van Niel et al. (2004) added spatial autocorrelation to

simulated DEMs and concluded that net solar radiation was less sensitive to DEM error than slope and aspect. In Indonesia, Widayati et al. (2004) found slope error to be sensitive to spatial autocorrelation. For a case study in Turkey, Yilmaz et al. (2004) simulated DEMs using uncorrelated random fields based on RMSE to give a basic demonstration of the impact topographic uncertainty can have on flood inundation. In a more complex study, Wilson and Atkinson (2005) simulated DEMs for the River Nene in Northamptonshire, UK using SGS conditioned by GPS data. They found different flood depths, with higher variability in flood depths and timings downstream when using the simulated DEMs. This was the last study to use DEM simulation in fluvial flood inundation studies.

In a comprehensive study in Finland, Oksanen and Sarjakoski (2005) simulated 1000 x 32 sets of error scenarios based on the exponential and Gaussian spatial error models and varying values of sill and range. They refuted the widely held view that uncorrelated random field models were the worst-case scenario as none of the DEM derivatives had maximum variation with these DEMs. In constrained terrain derivatives, such as slope and aspect, the maximum errors occurred when the range value was roughly the size of the derivatives calculation window. For unconstrained terrain derivatives, such as drainage basin delineation, variance increased as the spatial autocorrelation range increased. The shape of the error model was less important than the sill and range values, but did have more influence for constrained terrain derivatives. The same authors fitted semi-variograms using LIDAR as reference data and found different semi-variograms for different areas, with flat areas having a low sill value and large range (Oksanen and Sarjakoski, 2006). For the estimation of channel networks, Lindsay (2006) found larger errors when RMSE values was high and spatial correlation was low. In the Rocky Mountains, Raaflaub and Collins (2006) simulated 500 spatially uncorrelated and correlated DEMs, concluding that slope and aspect error was considerably lower in spatially correlated simulations. Wechsler and Knoll (2006) compared simulating DEMs using spatially uncorrelated RMSE values and spatially autocorrelated versions conditioned using 3 different filter methods. Slope error had a positive bias, and upslope contributing area and topographic index was unbiased, with a greater influence found on slope.

In 2008, Darnell et al presented a workflow using the R Statistical computing language for conditional simulation. For a case study in the Slovenian mountains they concluded that the main slope error is adjacent to the peak of mean elevation error, before using the simulated DEMs in estimating landslide susceptibility. The fact that the workflow depends on the availability of higher accuracy data for the conditioned simulation has possibly resulted in the approach not being especially popular. Hengl et al. (2008) introduced the use of auxiliary maps (distance to streams, terrain complexity, analytical hill shading and Normalized Difference Vegetation Index (NDVI)) using a regression kriging model to improve DEM simulations in Serbia. Later, Hengl et al. (2010) used conditional sequential Gaussian simulation to produce a stream error map, with the least precision in areas of low local relief. Using LIDAR data, Zandbergen (2010) applied the spatial moving averages technique to introduce spatial autocorrelation in order to simulate DEMs to aid in the identifications of false depressions. In a study to combat the problem of non-stationarity, Chen and Li (2012) proposed an adaptive method to identify areas of non-stationarity. Areas of non-stationarity were identified by calculating the standard deviation of mean error using Voronoi maps. If the error exceeding an indicator threshold set at 0.7m, the area was flagged as non-stationary and divided into 4. When stationarity was achieved, conditional simulation was implemented. This was implemented for an area in Sichuan Province, China, simulating 100 DEMs with a total of 16 mostly spherical semi-variograms. For a drainage basin delineation exercise, Eränen et al. (2014) implemented a DEM simulation scheme on a graphics processing unit (GPU) which was much faster than conventional approaches. For a coastal flood inundation exercise in Australia, Leon et al. (2014) simulated 1000 LIDAR DEMs using ordinary and regression kriging, concluding that the simulated DEMs gave a 11% increase in the 1% probability exceedance in inundation extent compared to using the deterministic bathtub approach. The most recent studies have also focussed on coastal inundation. West et al. (2018) simulated DEMs based on the confidence interval estimation estimated by the RMSE equation by Gesch (2009) and assumed no spatial autocorrelation. This was applied to a bathtub model of coastal inundation across various coastal locations in southwest England with varying inundation extents because of DEM simulation. Lastly, Fereshtehpour and Karamouz (2018) simulated 1000 realizations of LIDAR DEMs based on 500 GPS control points in Lower Manhattan using the SGS technique. Using the so-called bathtub approach,

coastal inundation for a 100-year storm surge event is assessed, with a probabilistic approach (i.e using simulated DEMs) outperforming higher resolution DEMs. Accuracy-efficiency analysis suggested a 15m resolution was a suitable resolution. Like the study of Leon et al. (2014) this study relied on the collection of ground control points which is not always possible and is expensive and time-consuming.

Despite over 20 years of research, it is clear that the method of DEM simulation is underutilised with a limited number of studies. Of those studies, very few take advantage of the array of DEM products now available. The reason behind this could be that the variation of methods suggests that an agreement on the best approach has not been reached and that DEM users either do not consider or deem it too complicated/time-consuming (Wechsler, 2007). Nevertheless, it seems a shame with the DEM products and computing resources now available that researchers do not build upon the work of the early-pioneers and make the DEM simulation approach more mainstream in any work that uses DEMs.

4.4.6 DEMs and flood inundation models

Topography is arguably the key factor in the estimation of inundation extent (Bates and De Roo, 2000, Horritt and Bates, 2002). Small errors in topography have the potential to alter inundation extent estimates significantly in low relief floodplain zones. With advancements in remote sensing and computing performance, high resolution DEMs can now be used to build more accurate inundation models (Bates, 2012). Using finer resolution DEMs has the advantage of representing topography more precisely and including micro-topography that can be crucial in the flooding process. This makes results more comparable to the real world and visualisation less abstract to the end user (i.e. landscape features are more recognisable). Moreover, using high resolution topography more correctly represents the wetting and drying of the domain as features that control these processes can be better represented (Neal et al., 2011, Bates, 2012). Despite this, using high-resolution DEMs is not always possible. LIDAR data is becoming increasingly available, but is still largely restricted to developed countries or local municipalities. A great deal of high-resolution terrain data is expensive to obtain or not available for public use. There are also limitations with data storage as LIDAR data sets can be prohibitively large. However, the Environment Agency in the UK have

made their LIDAR data free and publicly available. A selection of Canadian Provinces, Denamrk, Estonia, New Zealand and some states in the USA have followed suit (see the OpenTopography platform, http://www.opentopography.org/)). Unfortunately, whilst the OpenTopography initiative has been commendable in collating free LIDAR data, a great deal of data is missing, and one often needs to painstakingly research geospatial/mapping institutes of national and local governments to find relevant data. An optimistic estimate of current open-access LiDAR data coverage is just 0.005 of the earth's land area based on data from OpenTopography and an extensive search of national mapping agencies. Even if data do exist, computational costs may be too high with a halving of model resolution causing an order of magnitude increase in model runtime (Savage et al., 2016b).

This aforementioned problem of the most suitable model resolution (and thus DEM resolution) has led researchers to coarsen model resolution and subsequently investigate the impact of resolution on model results. Horritt and Bates (2001a) varied flood inundation model resolutions from 1000 to 10 m in a rural catchment and found no improvement in flood predictions below resolutions of 100 m. In an urban catchment, Yu and Lane (2006) found that small changes in model resolution had appreciable effects on predicted inundation and timings, but this could be partially compensated by varying wetting and drying parameters. Also in an urban catchment, Fewtrell et al. (2008) found that resolutions of less than 10 m were needed to resolve buildings and that the resampling strategy used in coarsening DEMs can impact model performance. In a follow up study, Fewtrell et al. (2011) created a 10 cm DEM of Alcester in the UK and investigated model performance by varying resolution up to 5 m. They found that a step change in model performance occurred at 2 m as a result of the degradation in the representation of the road network, demonstrating the importance of kerbs and camber for pluvial flooding. In Carlisle, UK, Neal et al. (2009b) concluded that a resolution of 2 m was required to represent smallest building separations (and thus flow between buildings) and using too coarse a resolution (25 m) resulted in topographic blockages. Similar conclusions were found in Tewkesbury, UK (Neal et al., 2011). In a rural Australian catchment, Jarihani et al. (2015) found that results did not improve with resolutions below 120 m. In an investigation in the Imera basin in Sicily, Savage et al. (2016b) resampled LIDAR data creating 12 DEMs between 10-500 m and found

that model performance deteriorated at resolutions more than 50 m and there was little gain for modelling at resolutions finer than 50 m. This was due to a poor representation of channels at coarser resolutions. Additionally, Savage et al. (2016b) warn that showing deterministic, high-resolution flood maps can lead to a spurious precision in delineated flood extent, and one that is misleading in that it does not represent the overall uncertainties involved in making flood inundation predictions. For the Oti river basin, Komi et al. (2017) varied model resolution between 30 m and 960 m using SRTM terrain data and found no discernible difference in water surface elevation. Flood extent estimations were more sensitive to model resolution, with better model performance at coarser resolutions, which was likely to have been a result of local scale noise in the SRTM DEM used which is smoothed when aggregating to coarser resolutions.

Other researchers have concentrated on investigating the impact that different DEM products have on model performance. For a constrained valley setting, Casas et al. (2006) assessed three different types of DEM products across resolutions and found model results from contour based DEMs to be most sensitive to resolution changes and LIDAR DEMs the least. With the widespread availability of remotely sensed derived DEMs the creation of DEMs by GPS and contour maps are less important. Few studies have compared different global DEMs and their influence on model performance. For two case studies in the USA, Sanders (2007), concluded that LIDAR gave the most accurate flood extent followed by SRTM and DEMs based on the National Elevation Dataset (NED). In Kansas, Li and Wong (2010) found the LIDAR and the NED outperformed SRTM. Jarihani et al. (2015) concluded SRTM outperformed ASTER for a rural catchment in Australia. In unpublished work, Courty et al. (2017) assessed the performance of ASTER, SRTM, AW3D30 and LIDAR at 30 m for flood models of two catchments in Mexico concluding that the AW3D30 global DEM outperformed the SRTM DEM in hilly areas and was similar in flatter areas. However, all the global DEMs were worse than the aggregated LIDAR and the AW3D30 DEM needed considerable processing as it is a DSM. In California, Bhuyian and Kalyanapu (2018) compared ASTER, SRTM, NED and LIDAR across a range of resolutions, concluding that the global DEMs (ASTER & SRTM) considerably over predicted inundation extent and the optimum resolution taking into account performance was 30 m. Yet with its greater

accuracy, wide spatial coverage and ease of access, the SRTM still remains the global DEM of choice in data-sparse regions (Yan et al., 2015a).

Most of the studies presented here are comparing global DEMs to high resolution LIDAR DEMs or aggregated versions of the LIDAR DEM. But what happens if no high-resolution data exists within a study area? As there is a lack of global DEMs and even fewer studies to guide a modeller into choosing a DEM, one is tempted to default to using the SRTM DEM. The danger in this is that this results in a single DEM being used. It is clear that this DEM is wrong, but whilst studies are prepared to acknowledge that an error exists few do anything about it and instead focus on the uncertainty from other flood model parameters. This can lead to spurious precision in using a single deterministic model. This is the very reason why in weather prediction multiple scenarios are run in response to the phenomenon of chaos theory as described by Lorenz (1963). In this work Lorenz (1963) found a notably different weather prediction when he ran his model for the second time. This was a result of a significant figure error, thus giving birth to the idea that a small change in initial conditions can have a large impact on the result.

What is needed is multiple plausible versions of a global DEM so a modeller can have the capacity to explore the impact that topographic uncertainty has on flood model performance. One could do this by resampling global DEMs to coarser resolutions, but this can result in important topographic details being lost. This work proposes that we simulate plausible versions of the DEM at the native resolution. Not only will this allow for more realisations of the DEM through resampling (if one wanted/needed to model at a coarser resolution), but also for a catalogue of DEMs to be created at the native resolution.

4.4.7 Experimental Design

In this chapter, the spatial error structure in the SRTM and MERIT DEMs for 20 lowland locations was quantified. Using the fitted error covariance function, plausible versions of the MERIT and SRTM DEMs were simulated, creating a catalogue of possible DEMs. The impact of using an ensemble of simulated DEMs on estimated flood extent was investiagted by applying the simulated DEMs to a flood model of the An Giang Province in the Vietnamese Mekong Delta and the Ba catchment in Fiji.

4.5 Study Sites

As outlined in the previous section, we aim to calculate the spatial error structure for lowland locations, and for that task we need LIDAR data to act as our ground-truth information. Unfortunately, LIDAR data is often not freely available or readily accessible. Yet with recent initiatives such as the OpenTopography project (http://www.opentopography.org/) this is slowly changing.

An extensive data trawl resulted in LIDAR data for 20 lowland locations being downloaded as shown in Figure 4-4. Details on how these data were processed are outlined in 4.6.1.

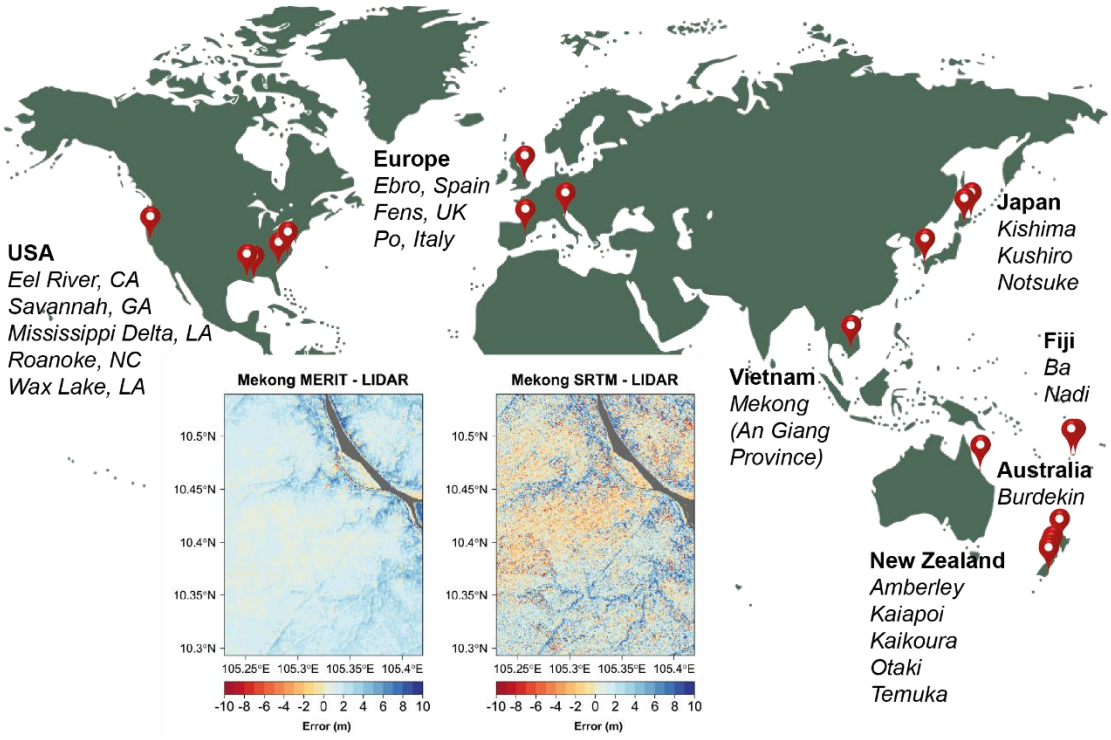

Figure 4-4 Study site locations and visualisation of surface error maps for An Giang Province in the Vietnamese Mekong Delta

4.6 Methodology

According to Olea (2006), 'modelling a semi-variogram remains to the uninitiated the most difficult and intriguing aspect in the application of geostatistics'. Indeed as noted by Goovaerts (1997) and echoed by Olea (2006), there is no best way to carry out this task. This section will expand upon the six stage approach to semi-variogram modelling proposed by

Olea (2006), preceded by a description of the data used and proceeded by a description of the flood inundation model build and parameter choice. The aim of this section is provide a concise narrative to the workflow of this chapter so the reader can replicate the process.

4.6.1 Data Collection

LIDAR data for 20 lowland locations around the world was downloaded to act as our ground truth reference data, with details in Table 4-6. According to Maune (2007), the reference dataset accuracy should be at least three times more accurate than the DEM being assessed. With reported vertical error less than 0.2 m across all sites, the use of LIDAR data as reference data is acceptable as this accuracy comfortably fulfils the accuracy requirement outlined by Maune (2007). Similarly, other geostatistical studies have used LIDAR data as the reference data (Oksanen and Sarjakoski, 2006, Zandbergen, 2008, Januchowski et al., 2010). In total over 5100km^2 of floodplains were used, or an area approximately the size of the US state of Delaware (Table 4-7).

Table 4-6 Summary of LiDAR Metadata. Includes location, resolution, date collected, reported vertical error (if available) and the source of data.

Location	Resolution (m)	Date Collected	Vertical Error (+/-m)	Data Source
Amberley	1	2012	0.2	LINZ
Ba	1	2012	Not Reported	SOPAC
Burdekin	5	2010	0.2	Geoscience Australia
Ebro	5	2009-2010	Not Reported	CNIG
Eel	5	2009-2011	0.1	NOAA
Fens	1	2014	0.05	Environment Agency
Kaiapoi	1	2014	0.2	LINZ
Kaikoura	1	2012	0.2	LINZ
Kishima	5	2011	Not Reported	GSI Japan
Kushiro	5	2011	Not Reported	GSI Japan
Mekong	5	2008	Not Reported	MONRE
Mississippi	2	2011	0.07	USGS
Nadi	1	2012	Not Reported	SOPAC
Notsuke	5	2011	Not Reported	GSI Japan
Otaki	1	2013	0.2	LINZ
Po Delta	5	2006	Not Reported	Regione Del Veneto
Roanoke	5	2014	0.1	NOAA
Savannah	5	2009	0.07	NOAA
Temuka	1	2014	0.2	LINZ
Wax Lake	1	2012-2013	0.086	USGS

Table 4-7 Summary of Study Sites including extent, number of pixels and area. Longitude is referred to as x, and latitude by y.

Study Site	x minimum	x maximum	y minimum	y maximum	Number of Pixels	Area Km²
Amberley	172.6954	172.7979	-43.2471	-43.1446	9888	80
Ba	177.6388	177.7046	-17.5571	-17.4421	7102	58
Burdekin	147.4388	147.6313	-19.7421	-19.4937	46430	376
Ebro	0.684583	0.975417	40.66625	40.78458	23629	191
Eel	-124.353	-124.177	40.57125	40.70042	20172	163
Fens	0.082083	0.147917	52.31458	52.33792	2191	18
Kaiapoi	172.5854	172.7288	-43.4429	-43.2863	24222	196
Kaikoura	173.6029	173.7279	-42.4371	-42.3579	6908	56
Kishima	130.1271	130.2488	33.08542	33.21458	12262	99
Kushiro	144.3288	144.4313	42.97208	43.16375	24092	195
Mekong	105.2296	105.4196	10.29292	10.53958	65890	534
Mississippi	-89.3037	-89.1346	29.06292	29.27542	24082	195
Nadi	177.3513	177.5054	-17.8546	-17.7271	15564	126
Notsuke	145.0804	145.8171	43.21958	43.66375	71904	582
Otaki	175.0746	175.1796	-40.8088	-40.7063	11255	91
Po Delta	12.25625	12.49208	44.85292	44.99875	41806	339
Roanoke	-77.0738	-76.6663	35.80375	35.96875	89630	726
Savannah	-81.3079	-80.8504	31.73042	32.00208	104084	843
Temuka	171.2454	171.4988	-44.2896	-44.1729	26956	218
Wax Lake	-91.4871	-91.3887	29.47542	29.54542	4827	39
					Total	**5126**

Ideally, LIDAR data collected would be collected at the same time as the SRTM product for temporal consistency, but the available LIDAR was typically collected 6-14 years after SRTM acquisition. Using annual satellite imagery in Google Earth, land use change was checked between the SRTM and LIDAR collection period to determine if there had been any major land use changes that could influence the accuracy of the DEM. This check found no obvious significant differences over the land pixels for any of the study sites. A further complication with ensuring comparison of like-for-like terrain data is subsidence, which is a major challenge for many of the world's deltas (Ericson et al., 2006, Syvitski et al., 2009, Schmidt, 2015, Higgins, 2016). Subsidence rates pose a challenge as it changes the land elevation between SRTM and LIDAR collection dates. Relevant subsidence rates, be it measured or estimated, were not found for all locations and are subsequently outlined in Table 4-8.

Whilst these rates are non-zero they do fall well within the vertical error of SRTM and hence were not considered further In the analysis.

Table 4-8 Subsidence rates

Site	Subsidence rate (mm/yr-1)	Citation
Burdekin	1.5	Ericson et al. (2006)
Ebro	6	Ibáñez et al. (2010)
Kishima	22.2	Don et al. (2006)
Mekong (An Giang)	5	Minderhoud et al. (2017)
Mississippi	6	Karegar et al. (2015)
Mississippi	11.2	Jankowski et al. (2017)
Po	6	Fabris et al. (2014)
Savannah	3.5	Davis et al. (1976)
Wax lake	10	Nienhuis et al. (2017)

In addition to the LIDAR data, the relevant MERIT and SRTM data were downloaded from the developer's website (http://hydro.iis.u-tokyo.ac.jp/~yamadai/MERIT_DEM/) and USGS Earthexplorer platform (https://earthexplorer.usgs.gov/) respectively. The least manipulated SRTM product (3 arc second SRTM v1 non-void) for the analysis.

4.6.2 Data Editing

The first step in semi-variogram modelling outlined by Olea (2006) is data editing. This involves eliminating any possible reading, recording or process errors. In practise this meant ensuring all data were in the correct coordinate system and had the same vertical datum. This is no small task. The MERIT and SRTM data are in the WGS84 coordinate system and use the EGM96 vertical datum. Inconveniently, this was rarely the case with the LIDAR data, as often the projections and vertical datums were typically in the systems of that particular country or state. This highlighted the importance of metadata as some potential data did not have enough information and could thus not be used. Transformations were mostly undertaken using Vdatum version 3.8 (https://vdatum.noaa.gov/welcome.html) and the bespoke Concord software (https://www.linz.govt.nz/data/geodetic-services/download-geodetic-software/snap-concord-downloads) for the New Zealand data. These

transformations were then loaded into GIS software and compared to background satellite imagery to check the transformations were sensible.

All the DEM data acquired had undergone extensive processing. Details of these processes are often not well documented, so it is difficult to judge what decisions were made in the processing stage and what errors may have been introduced as a result. The quality checks strived to minimise these effects.

4.6.3 Exploratory Data Analysis – Visualisation

The next stage in the approach is exploratory data analysis. Here, a diversion from the work of Olea (2006) is taken as in the example given in that work the exploratory data analysis sought to determine whether the measurements are concentrated in clusters which is a danger of using data on a non-uniform grid. By using regularly gridded DEMs this is not a problem, but it is nevertheless useful to visualise the errors as a sanity check.

To compare the MERIT and SRTM datasets to LIDAR the arithmetic mean of the LIDAR values that fall within each MERIT/SRTM pixel must be calculated. This allowed for an estimation of the vertical error of each pixel in the coarser DEM. Each MERIT/SRTM pixel is the integration of its interior topography so the arithmetic mean of LIDAR elevation values was used. This overcame the problem associated with using the elevation of grid cell centers to represent elevation as this often does not accurately represent the hydrography of floodplains (Moretti and Orlandini, 2018). Analysis was performed using the raster package of Hijmans et al. (2017) in the statistical computing environment R (R Core R Core Team, 2018).

As a result, surface error maps of MERIT – LIDAR and SRTM – LIDAR were produced, with an example from the Mekong Delta in Figure 4-4. Visualisation was carried out using the rasterVis package (Perpinan Lamigueiro and Hijmans, 2018). Further surface error maps can be found in Figure 4-5 - Figure 4-9. In these maps, red refers to underestimation of elevation by MERIT/SRTM and blue refers to the overestimation of elevation by MERIT/SRTM. Grey pixels indicate pixels where either the MERIT/SRTM or LIDAR pixels are missing or are water bodies. The water body mask is delineated using the Global Water Surface water

occurrence map of Pekel et al. (2016). A water occurrence threshold of 90% was selected based on trial and error, with such pixels not contributing to the estimation of the MERIT/SRTM - LIDAR spatial error structure. These maps are useful to visualise the spatial locations of the error and qualitatively compare them to satellite imagery and landcover maps to assess possible causes of errors.

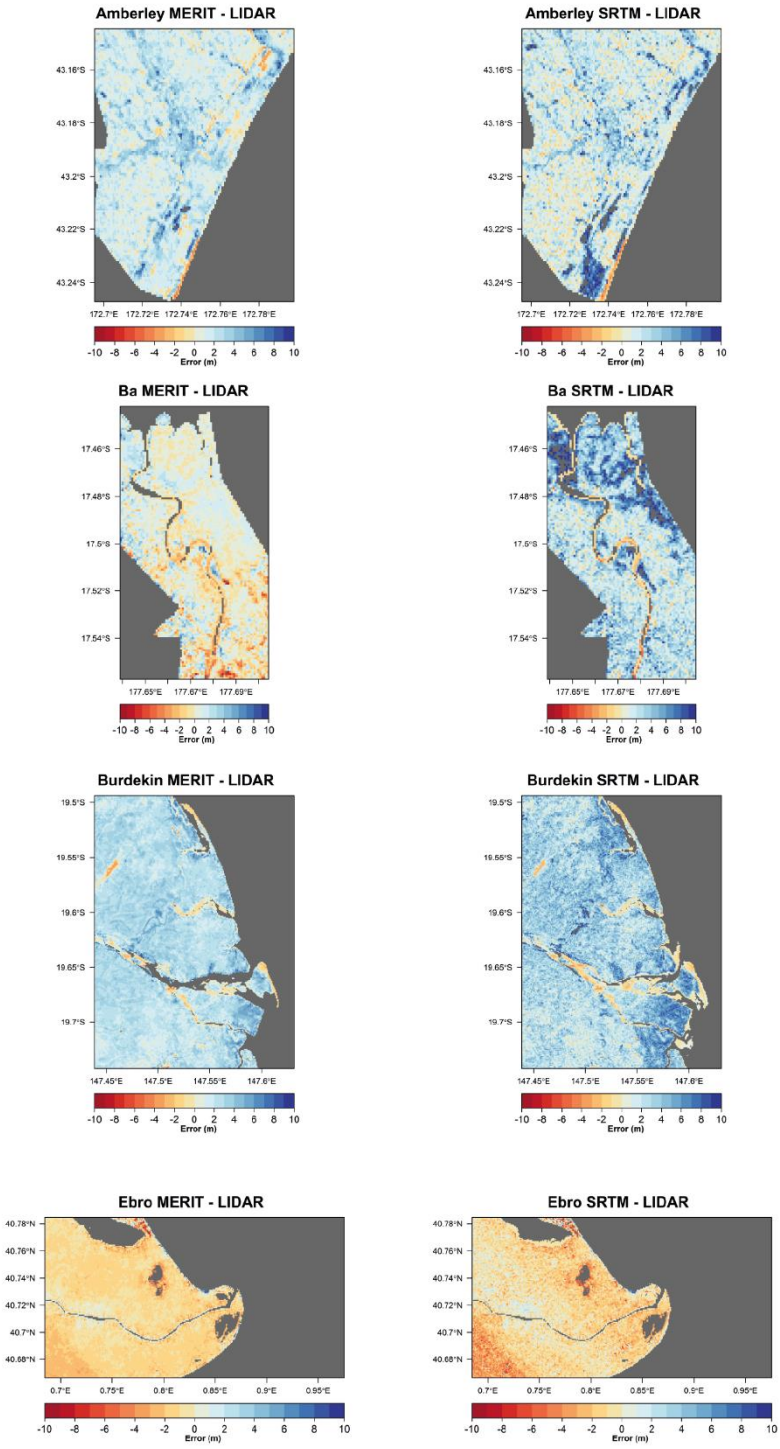

Figure 4-5 Surface Error Maps for the Amberley, Ba, Burdekin and Ebro sites. Red = underestimation of elevation by MERIT/SRTM; Blue = Overestimation of elevation by MERIT/SRTM; Grey = Missing pixels or pixels over water bodies.

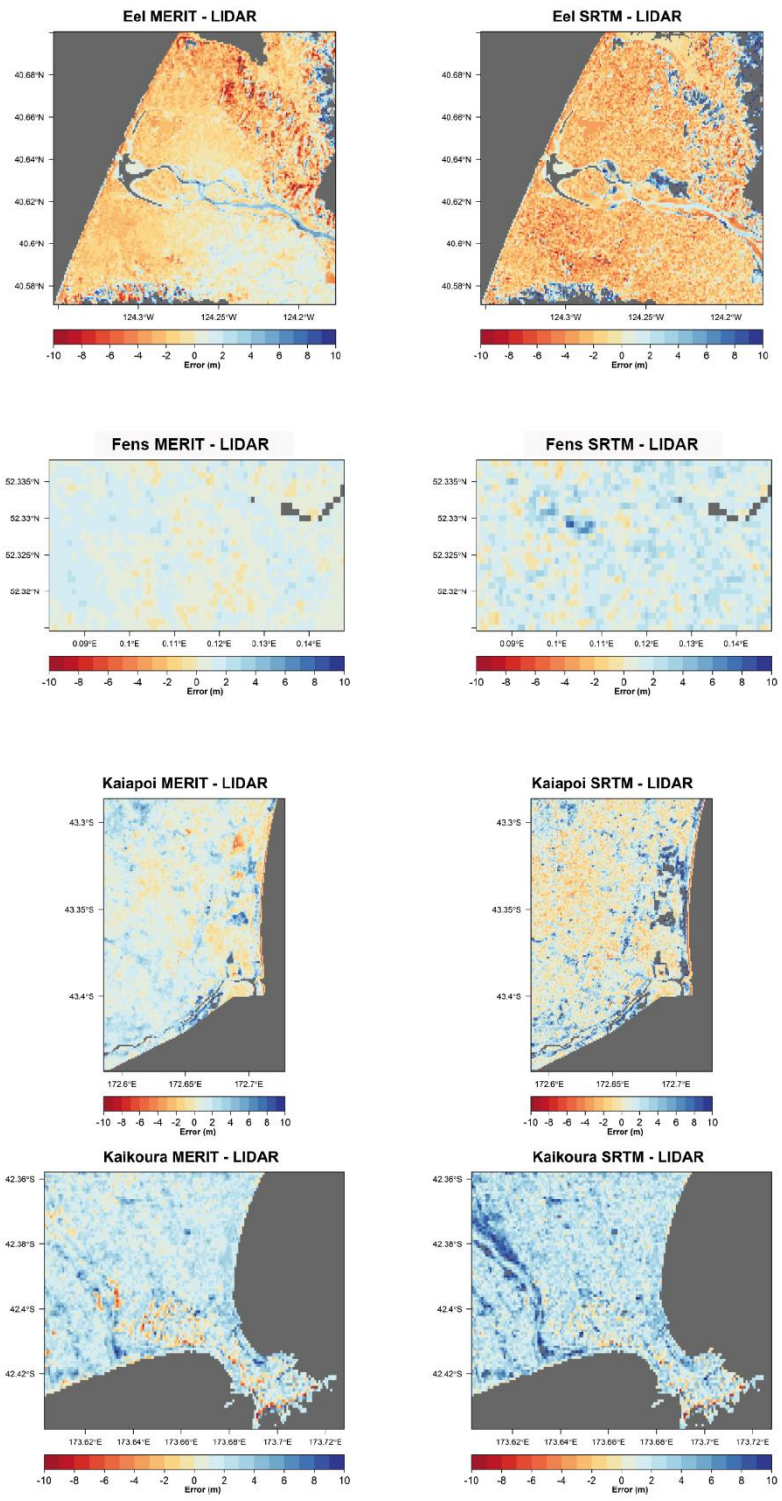

Figure 4-6 Surface Error Maps for the Eel, Fens, Kaiapoi and Kaikoura sites. Red = underestimation of elevation by MERIT/SRTM; Blue = Overestimation of elevation by MERIT/SRTM; Grey = Missing pixels or pixels over water bodies.

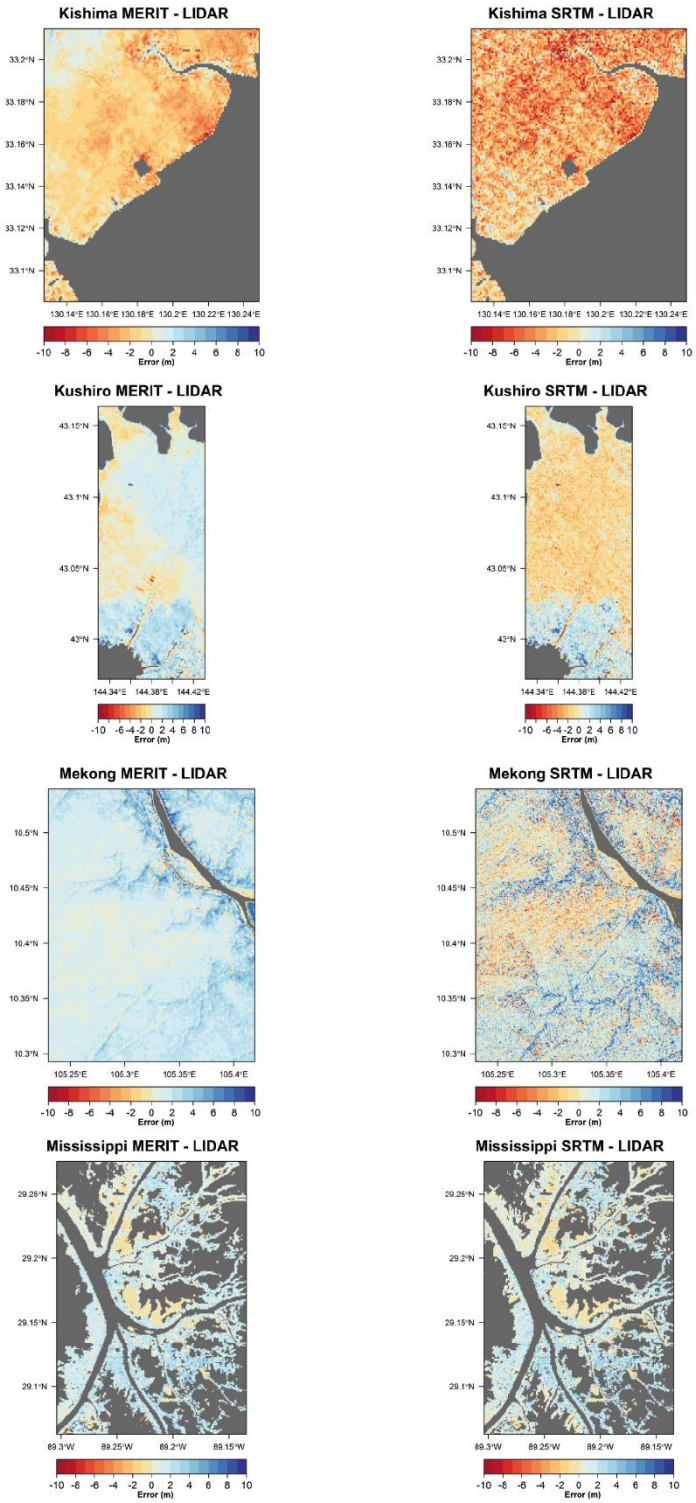

Figure 4-7 Surface Error Maps for the Kishima, Kushiro, Mekong and Mississippi sites. Red = underestimation of elevation by MERIT/SRTM; Blue = Overestimation of elevation by MERIT/SRTM; Grey = Missing pixels or pixels over water bodies.

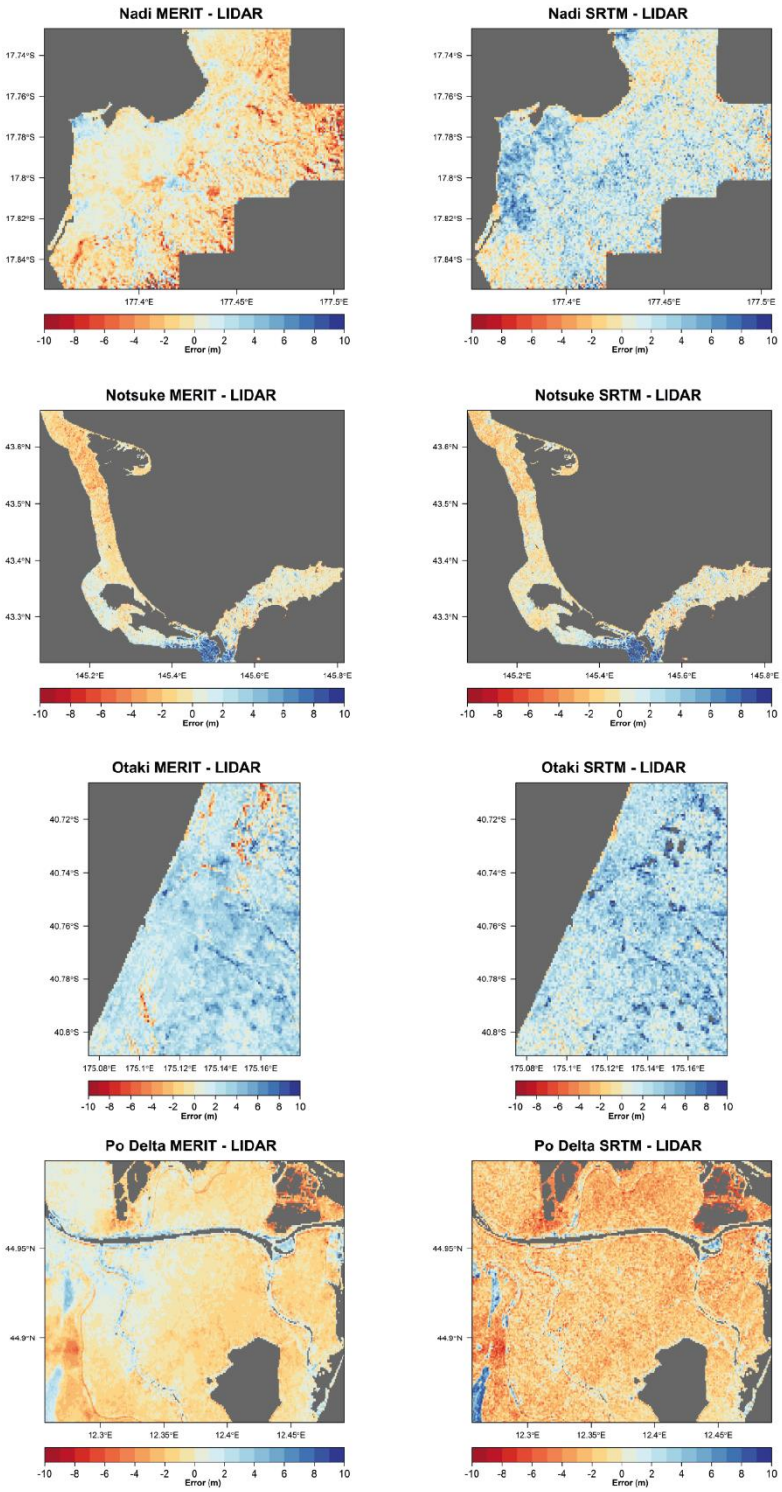

Figure 4-8 Surface Error Maps for the Nadi, Notsuke, Otaki and Po sites. Red = underestimation of elevation by MERIT/SRTM; Blue = Overestimation of elevation by MERIT/SRTM; Grey = Missing pixels or pixels over water bodies.

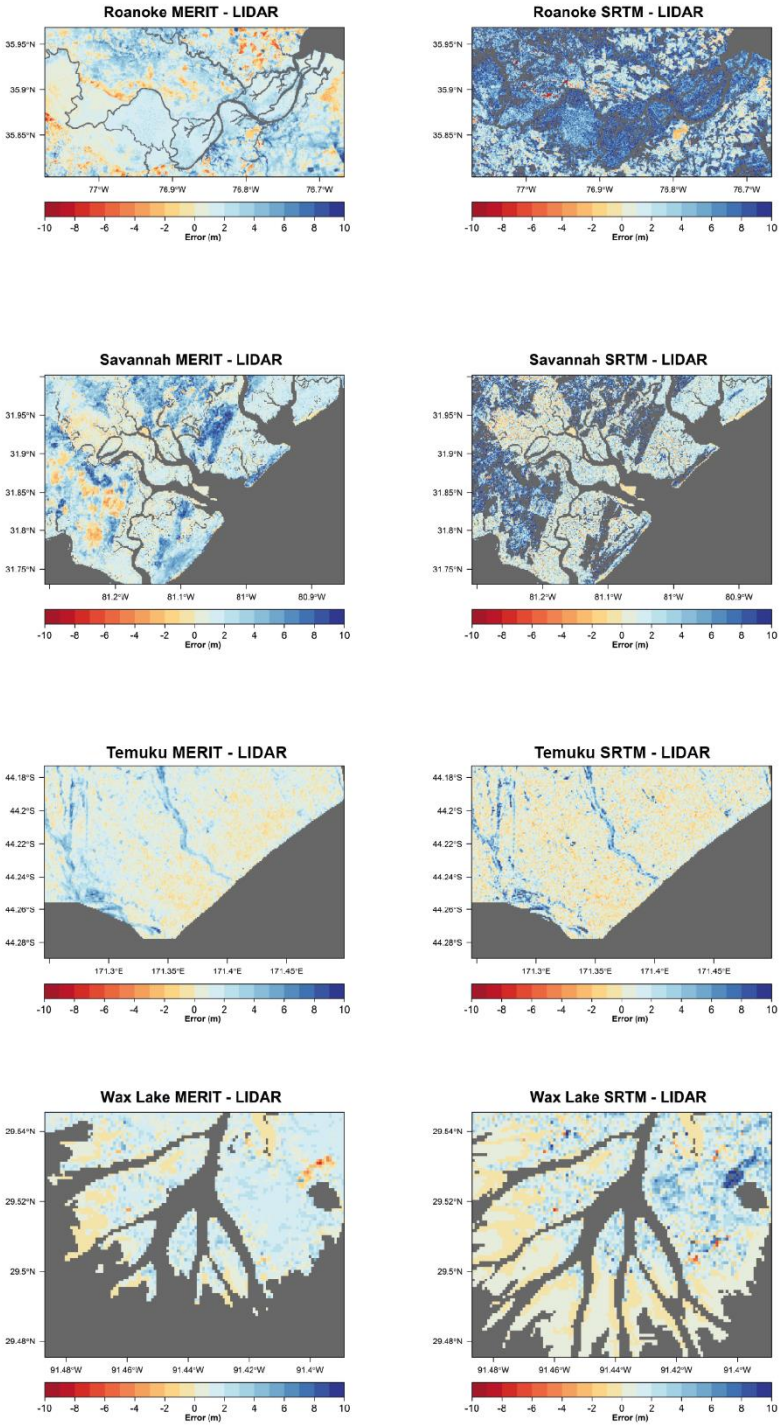

Figure 4-9 Surface Error Maps for the Roanoke, Savannah, Temuku and Wax Lake sites Red = underestimation of elevation by MERIT/SRTM; Blue = Overestimation of elevation by MERIT/SRTM; Grey = Missing pixels or pixels over water bodies..

4.6.4 Semi-variogram estimation

For each study, semi-variograms are fitted to to the difference maps calculated in section 4.6.3, excluding those pixels masked out in grey. A decision is taken to assume stationarity in the model. Stationarity allows pooling of data over an area that are deemed homogeneous and is a property of the Random Field model and not the data. As the terrain analysed in this chapter is flat or very nearly flat, the terrain parameters (e.g. slope) is near homogeneous and, thus, the condition of non-stationarity of DEM error found in more rugged terrain (i.e. mountainous areas with varying slope and aspect) can be relaxed (Gatziolis and Fried, 2004). Moreover, stationarity is needed for inference (Goovaerts, 1997). The model also assumes isotropy, with justification of this decision outlined in Section 4.6.5. Geostatistical analysis was carried out using the gstat package in R (Pebesma, 2004).

If s and s' are the vectors of spatial coordinates and X is the value of the difference between MERIT/SRTM and LIDAR (i.e. the vertical error), then the semi-variogram ($\gamma(\mathbf{h})$) is defined as;

$$\gamma(\mathbf{h}) = \frac{1}{2N(\mathbf{h})} \sum_{i=1}^{N(\mathbf{h})} [\{X(s) - X(s')\}]^2 \qquad (21)$$

where N($\mathbf{h}$) is the number of pairs, and $\mathbf{h}$ is the lag. For the purpose of simulating other places, these empirical semi-variograms must be fitted to form a continuous surface. There is no best semi-variogram model to fit semi-variograms, so one must be careful to choose a model that captures the main features but avoids overfitting (Goovaerts, 1997). As outlined in Figure 4-3 there are numerous models available to fit the empirical semi-variogram. A further strategy is to combine two or more semi-variogram models. For instance, a short-range exponential model may be used with a long-range spherical model. Inspection of the empirical semi-variogram suggested a double-exponential shape would capture the main features. This is consistent with the work of Oksanen and Sarjakoski (2006) who used an

exponential model for their analysis. Therefore the chosen model to fit the semi-variograms has the parametric form;

$$\gamma(h) = \sigma_1^2 \left\{1 - \exp\left(\frac{-h}{a_1}\right)\right\} + \sigma_2^2 \left\{1 - \exp\left(\frac{-h}{a_2}\right)\right\} \quad (22)$$

where (α1, α2) represent the range, σ^2_1 the 'near' component and σ^2_2 the 'far' component. Both these parameters were thus fitted with a double exponential model. Note there is no nugget component in the chosen model. A nugget component was excluded as although it shows measurement error and sources of variation over distances shorter than the shortest sampling interval, it would add further error to the surface being added to the DEM to create the simulated DEM. As an unconditional simulation approach is being taken, this would result in an even noisier resultant DEM simulation. To fit this model, first an exponential semi-variogram using pixels within 0.005 decimal degrees (≈500 m) of each other was calculated, forming the 'near' component. This gives an estimate of the near range parameter α1. Then the sum of two exponential semi-variograms with specified ranges α1 and α2 = 10 α1 to pixels within 0.01 decimal degrees (≈1000 m) of each other, forming the 'far' component. As a result, the sill and range parameters could be estimated. The sill refers to the semi-variance at which the semi-variogram levels off and is the marginal standard deviation. The range is the distance at which the semi-variogram effectively reaches the sill value. For an exponential model, the semi-variogram reaches the sill asymptotically so the range is defined as the distance at which the model value is at 95% of the sill. Range values of the resultant semi-variograms are roughly similar values previously estimated by Rodriguez et al. (2006), Shortridge (2006), LaLonde et al. (2010) and Shortridge and Messina (2011) for SRTM.

4.6.5 Directional Investigation

In the modelling implemented in section 4.6.4, isotropy was assumed. In this section, this assumption is tested as occasionally the spatial dependence can be anisotropic (e.g. Liu and Jezek (1999)) . In other words, it is best practise to check whether the spatial error structures are similar in all directions, or whether the data is anisotropic. Anisotropy can be either 'zonal' or 'geomtric'. Zonal isotropy ivolves sill values varying with direction. Geometric

anisotropy involves semi-variograms having the same shape and sill but different range values.

There are two methods to test anisotropy – directional semi-variograms and semi-variogram maps. Directional semi-variograms are calculated by plotting empirical semi-variograms at differing angles from North (0 in our analysis) with an angular tolerance of 15°. The number of directions to investigate depends on the application, with Goovaerts (1997) recommending that the four cardinal directions should be investigated as a bare minimum. A compromise must be reached as investigating too many directions can result in too few points to form a relationship. For Olea (2006), the more directions investigated the better. If these semi-variograms are similar, isotropy can assumed, so the resultant semi-variogram is omnidirectional. The second method is a semi-variogram map which is particularly suited to large gridded datasets (Goovaerts, 1997) such as many DEMs. If the contour lines in these maps are concentric, the semi-variance is similar in every direction so we can assume isotropy. On the other hand, if the contours are elliptical, the data would exhibit geometric anisotropy. Here, both techniques are used (Figure 4-10 & Figure 4-11) for the Burdekin study site. Goovaerts (1997) recommends that if anisotropy is not clearly evident from the directional semi-variograms, semi-variogram maps or ancillary information, one should assume isotropy. With this mantra isotropy is assumed as no obvious anisotropy was evident. The directional semi-variograms of Figure 4-10 have very similar shapes, albeit with slightly different sill values. For the semi-variogram map (Figure 4-11), the shape is concentric except in the southeast and northwest directions where there is a slight stretch to a more ellipsoidal shape in the mid to far range. Strictly speaking anisotropy is present, but was ignored as it was deemed not strong enough following the recommendation of Goovaerts (1997). This analysis was carried out for all study sites, with no notable differences found, thus it can be concluded that the assumption of isotropy is a valid one.

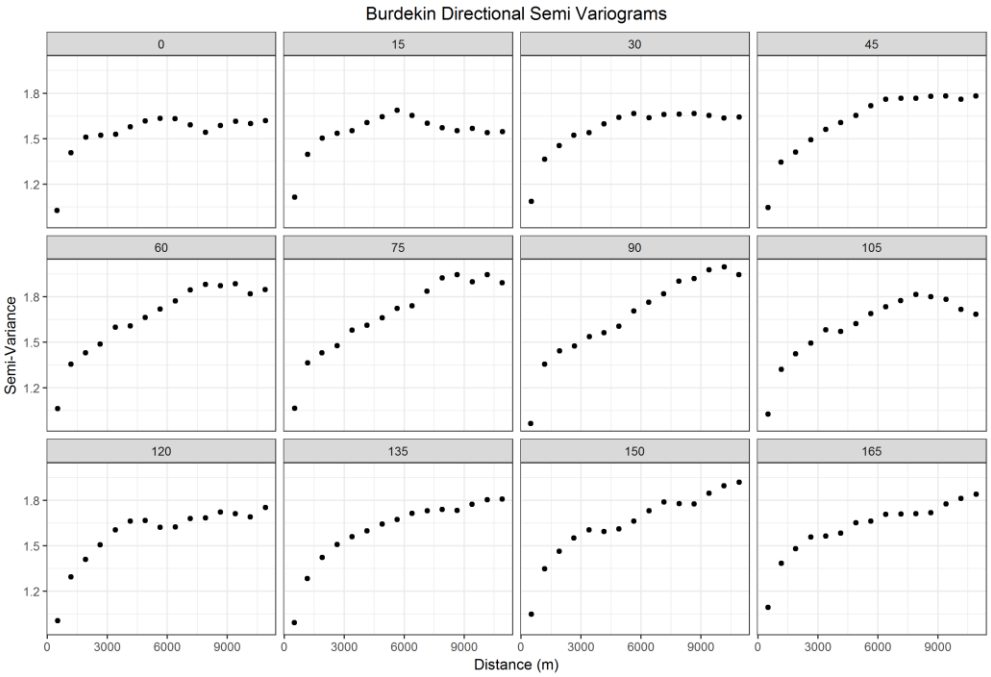

Figure 4-10 Directional semi-variograms for Burdekin. The number in each panel refers to the degrees from north, when north=0 and east=90. There is better long-range spatial continuity (smaller semi-variance values) in the North (0) and North-East directions

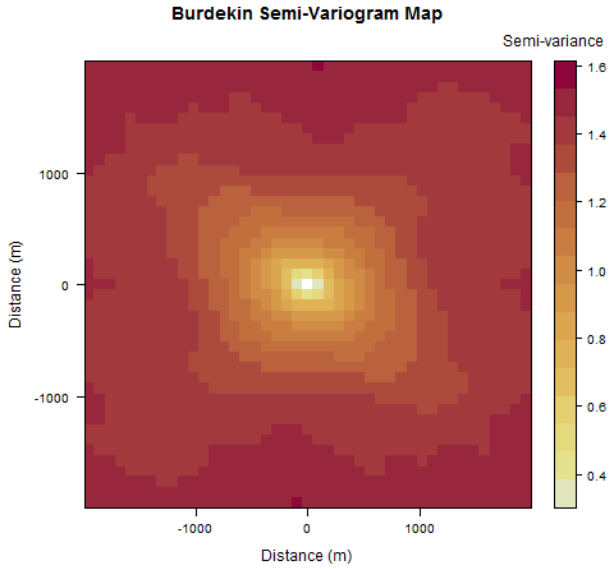

Figure 4-11 Semi-variogram map for Burdekin. A semi-variogram map is a plot of semi-variograms plotted as a series of coordinates with the center (0,0) corresponding to the origin of the semi-variogram. Any cross-section is a traditional 1D semi-variogram. Concentric contours = isotropy. Elliptical contours = anisotropy

4.6.6 DEM Simulation

As outlined in section 4.4.4, a random field of error must be generated which when added to the DEM creates plausible versions of the terrain. For the purpose of this work, conditional simulation is inappropriate as the intended end users are unlikely to have access to high accuracy topographic data. In other words, the aim here is to simulate plausible versions of the MERIT and SRTM DEMs for floodplain locations assuming the user has no reference datasets. However, it should be made clear, that unconditional simulation (unlike conditional simulation) does not eliminate the implicit DEM error (by conditioning to reference data), while at the same time adds the Gaussian error field to the DEM being simulated. This means that the simulated DEM will have inflated values. Whilst this is not desirable, unconditional simulation does not need reference data and is therefore a flexible approach to DEM simulation. However, if reference data is available, a user should attempt condition simulation to obtain a more accurate and realistic simulation of the DEM.

In this chapter, Spatial dependence of error has been characterised using semi-variograms for 20 floodplain locations. This is the sample statistic to characterise spatial dependence of error in floodplains. The assumption made in this thesis is that this estimated spatial dependence is representative of floodplains around the world. This assumption is based on the semi-variograms being broadly similar (Figure 4-13) for each floodplain and the fact the 20 floodplain locations used are across a wide range of locations.

Ideally, a statistical model covering both the DEM and reference observations on the DEM would be constructed. Typically, this model might be a multivariate Gaussian distribution, in which the reference observations might be a subset of the DEM plus noise, where the noise is probabilistically independent of the DEM. The simulated DEM would then be conditioned on the reference observations using samples from the conditional (or `posterior') distribution of the DEM as candidates in a simulation-based approach to computing the inundation probabilities for each pixel of the hazard map. In other words, this is a conditional simulation approach.

Specifying the full covariance structure over both the DEM and the observational data is demanding. Under some conditions, it also turns out to be unnecessary. These conditions are described in Rougier and Zammit-Mangion (2016) (Theorem 3). In essence, the prior variance matrix of the true elevations has to be far larger than the error variance matrix of the observational data. In this case, if there is an observation for every pixel, then the posterior expectation of the true elevations is approximately equal to the observations, and the posterior variance matrix of the true elevations is approximately equal to the measurement error variance (i.e. it inherits the spatial structure of the error). This `plug-in' approach is very intuitive, and quite widely used, so it is reassuring to know that it is approximately correct under an acceptable assumption about a large prior uncertainty.

The plug-in approach is implemented by using either the LIDAR as the observations, and simulating candidate DEMs by adding the random fields generated from the representative semi-variograms to either the MERIT or SRTM DEMs. Random field realizations are generated by sequential Gaussian simulation using the gstat package (Pebesma, 2004) in R (R Core Team (2018). These are unconditional Gaussian simulations. A workflow related to this process and details of the code are given later in this chapter (Figure 4-21).

4.6.7 Flood Model

To test the impact of using an ensemble of simulated DEMs on flood inundation extent, two flood models were built using the sub-grid version of LISFLOOD-FP (Neal et al., 2012a). One model covered a section of An Giang Province in the Vietnamese Mekong Delta and the other a 15 km reach of the Ba catchment in Fiji. These locations were selected as both had LIDAR data, so a representative benchmark model could be built to compare to the simulated DEM results. Moreover, both reaches were small enough that model simulation times were practical for the study.

The An Giang model uses hydrographs from Chau Doc and Vam Nao gauging stations as the upstream boundary condition, whilst the downstream boundary is set as the water level height from the Long Xuyen gauge, with all these records available from the Mekong River Commission (MRC). The year 2001 was selected for hydraulic simulation. This particular year was selected for several reasons. Firstly, the flood was severe with estimated damages

at over US$ 200 million and approximately 300,000 homes damaged in the Vietnamese Mekong Delta (Chinh et al., 2016). Whilst the return period of the 2001 flood is unknown, Le et al. (2007) estimated that the moderately larger flood in 2000 had a return period of 20 years. Secondly, after the floods of 2000 and 2001, and with the shift from low dykes (0-2 m) to high dykes (>3.5 m) to facilitate triple rice cropping (Kontgis et al., 2015), extensive flood prevention structures have been built in An Giang. The expansion of paddies protected from high dykes in An Giang has risen from < 10,000 ha in 2000 to > 140,000 in 2011 (Duc Tran et al., 2018), with these structures being recognized as being important in protecting against damaging floods (Chapman et al., 2016). Considering SRTM was acquired in 2000, the flood prevention structures have changed the topography represented in SRTM, with flood studies analysing later periods needing to update dyke information (Dung et al., 2011, Triet et al., 2017, Duc Tran et al., 2018). Even though the 2011 flood was hydrologically similar to that of the 2000 flood, 71% of An Giang was flooded in 2000 compared to 30% in 2011 (Dang et al., 2016, MRC, 2011b), with flood prevention structures found to be the main cause of hydrological alterations (Dang et al., 2016). Thirdly, the availability of gauge data restricted the years which could be hydraulically simulated. Geometry data for the channels were gathered from the GWD-LR river width database (Yamazaki et al., 2014a) and bathymetry from a 2008 survey conducted by the MRC with cross sections approximately every 250 m. The channel was assumed to have a rectangular shape, with bathymetry values assigned by interpolating the cross-sections. Manning's friction parameters (Chow, 1959) were set as 0.03 for the channel and 0.05 for the floodplain, which are both realistic and performed well in a larger Mekong flood model built with LISFLOOD-FP.

For the Ba model, the model setup as outlined in Archer et al. (2018) was used. They estimated a 50 year hydrograph using the regional flood frequency analysis (RFFA) approach of Smith et al. (2015), utilizing meteorological data from the Fiji Meteorological Office. The downstream water level boundary condition at the coast was set at 0 m ,even though this value is highly uncertain as heavy rainfall is likely to occur at the same time as a storm surge to compound flooding (Zscheischler et al., 2018, Wahl et al., 2015). As the domain size of the Ba reach model is comparatively small, the river width was estimated from Google Earth. The river depth was estimated such that the river conveyed the 1 in 2

year return period before going out of bank. Whilst this bankfull discharge value varies considerably around the world, a return period of 2 year is a generally accepted average value (Pickup and Warner, 1976, Williams, 1978) with a return period of 2 years being found in similar rivers in Fiji (Terry et al., 2002, Terry, 2007). Finally, Manning's friction parameters were set as 0.035 for the channel and 0.04 for the floodplain based on based on typical values for agricultural floodplains used by Archer et al. (2018).

For each location, four models were built to act as our deterministic models – one at 90m resolution using the SRTM DEM, another at 90 m resolution using the MERIT DEM, a further 90 m version using resampled LIDAR and a final 30 m resolution model built using LIDAR data to act as a benchmark model. The 90m resolution was chosen as this is the native resolution of SRTM and MERIT. The 30 m LIDAR based model was selected as a benchmark model as it is based on the most accurate topographic data. In the absence of validation data, the benchmark model is used as observations. A 30 m resolution was chosen for the LIDAR model based on computational resources and was created by aggregating the LIDAR to the desired 30m resolution. Next, the 90m SRTM and MERIT models were replaced with the simulated DEMs, consequently forming the DEM ensembles as multiple simulated DEMs were used to construct each ensemble. Three sets of DEM ensemble models were built – one by simulating the MERIT DEM with the 'average' floodplain semi-variogram of MERIT; another by simulating the MERIT DEM by MERIT landcover semi-variograms; and a final one by simulating the SRTM DEM by SRTM landcover semi-variograms (Introduced in more detail in Section 4.7.2). In this case, the 'average' semi-variogram refers to the average of the semi-variogram parameters across all 20 locations, so this is taken to be representative of a floodplain semi-variogram. Simulation by landcover semi-variograms are detailed further in Figure 4-15 and Section 4.7.2. Thus, in total seven classes of model were created.

For the An Giang model, each DEM ensemble contained 200 DEMs. For the Ba model, each ensemble contained 500 DEMs. The larger number for Ba was a result of the faster computation time of the model (≈1 minute) compared to the 19 minutes it took for the An Giang model. As the aim of the study was to test the impact of topographic uncertainty on the flood extent we kept all other model parameters consistent. To assess the results,

maximum inundation maps were extracted and converted to a binary wet/dry map. Subsequently, these maps are merged together to form an inundation probability map, whereby a percentage score is given based on the number of DEMs that a particular pixel floods within a given DEM ensemble. For the deterministic models, these inundation probabilities would either be 0% (dry) or 100% (wet), whilst for the DEM ensembles the probability can take any value between this ranges. Simulations were carried out on an Intel 3.1GHz quad-core i7-3770S CPU.

4.6.8 Workflow

To summarise the methodology, a workflow is presented here. This has been further consolidated into a package in R called `DEMsimulation` which is detailed in section 4.8.

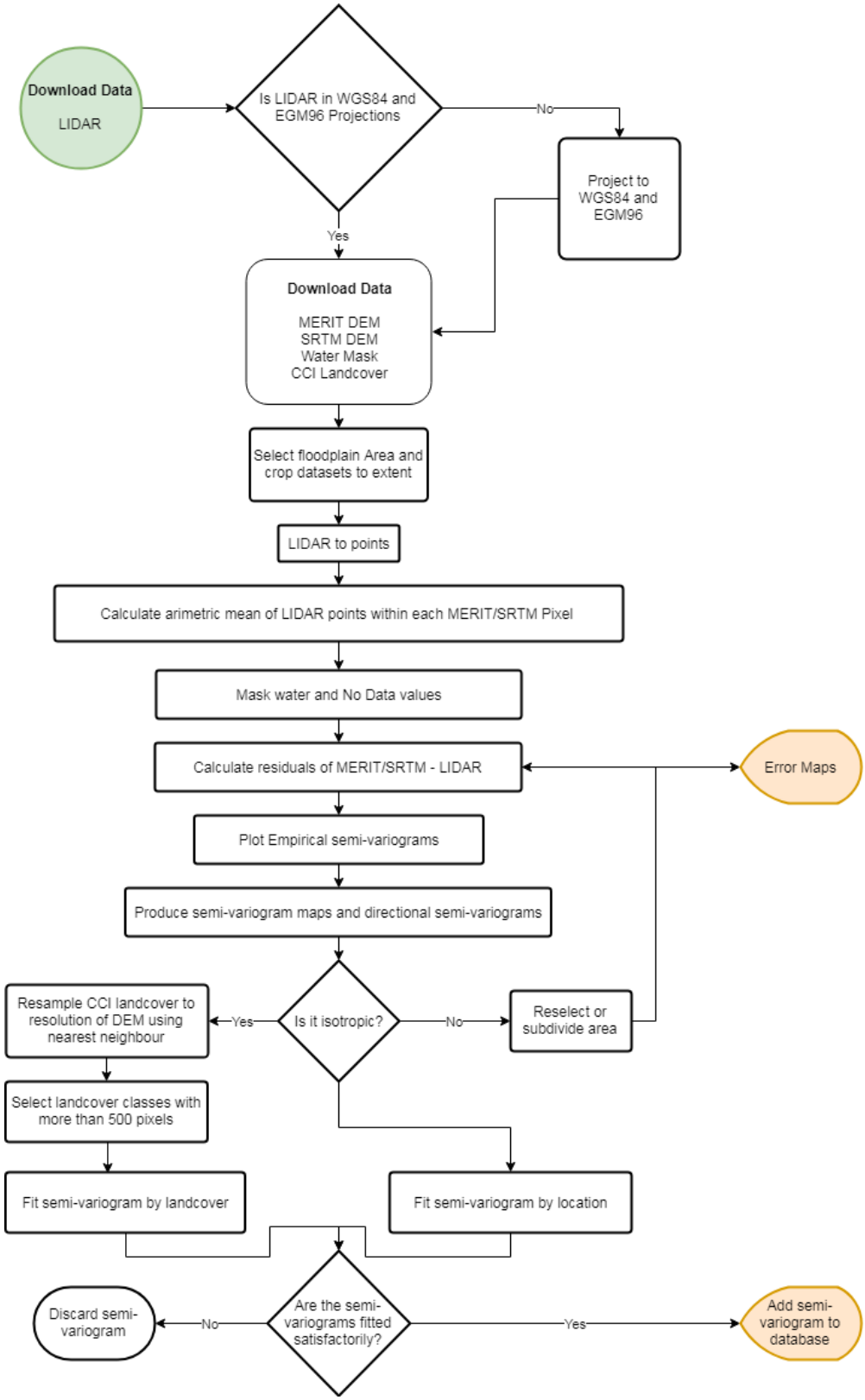

Figure 4-12 Workflow to fit semi-variograms. Orange signifies outputs.

4.7 Results & Discussion

In this section, the results of the three components of our analysis: Semi-variograms, DEM Simulation and Flood Inundation presented and discussed. As each component builds on the previous, a discussion is incorporated in the results section.

4.7.1 Semi-variograms

First, the empirical and fitted semi-variograms for each study site are plotted (Figure 4-13). The fitting procedure is appropriate as the fitted semi-variograms align well with the empirical results.

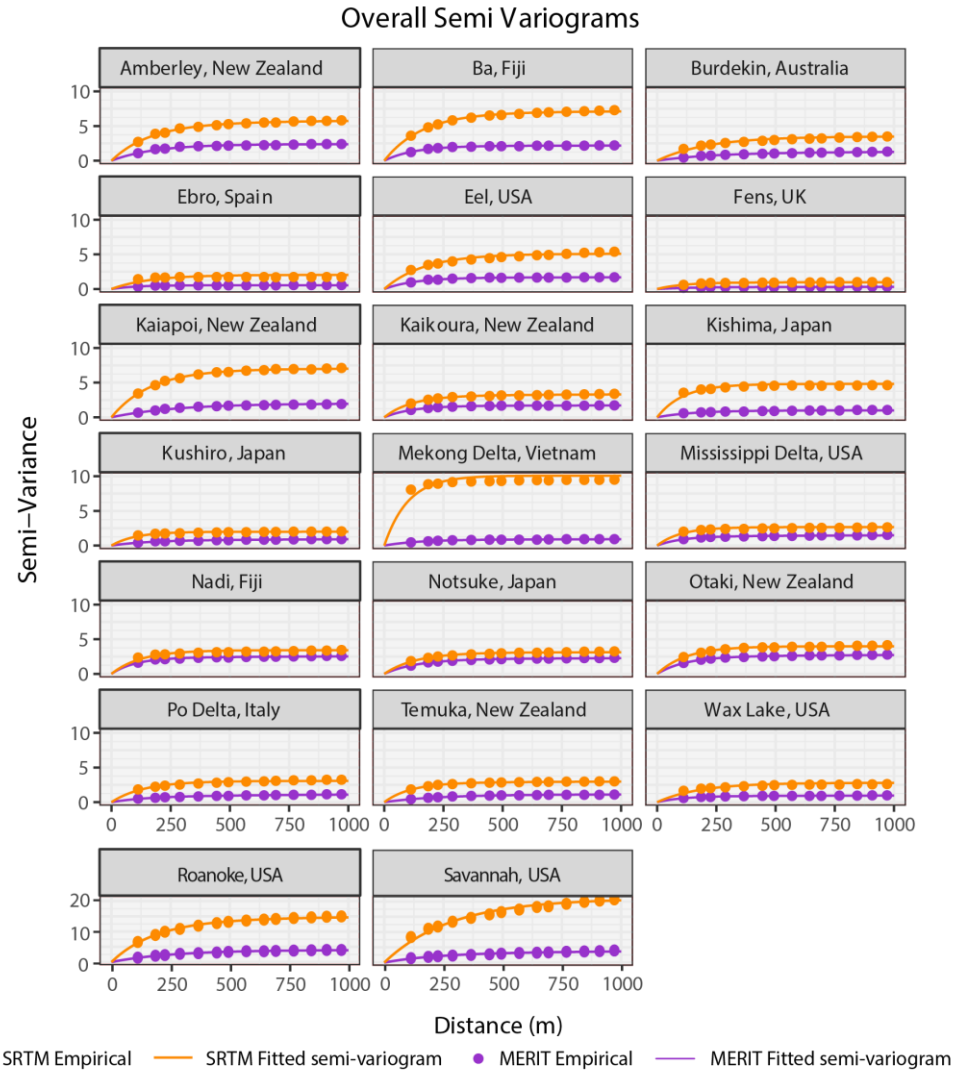

Figure 4-13 Semi-variograms for each study site for the difference between MERIT - LIDAR and SRTM - LIDAR. The resolution of the DEMs is 90m. The 'sill' is the marginal standard deviation, in metres, and the 'range' is the distance, in metres, at which the correlation between two points drops to 0.05. Note that Roanoke and Savannah (bottom) have a different y axis as for these locations the SRTM semi-variograms have a markedly larger sill value.

Broadly speaking, all locations have similar semi-variograms for the MERIT DEM, with these often having considerably different semi-variogram parameter values than the SRTM equivalents (Figure 4-3). For example, the sill values for the MERIT DEM are markedly lower at the Mekong, Roanoke and Savannah sites. Across all study sites, the MERIT DEM has smaller sill values (0.7-2.2m) compared to SRTM (1.0-4.8m), and larger range values as well (308-4364m compared to 298-1931m). A detailed table of fitted semi-variogram parameter values can be found in Table 4-9. Smaller sill values mean that the DEM is more

accurate, and a larger range means that the error is more spatially dependent over a greater distance.

Table 4-9 Estimated semi-variogram parameters for each location for both MERIT and SRTM. The 'sill' is the marginal standard deviation, in metres, and the 'range' is the distance, in metres, at which the correlation between two points drops to 0.05. σ^2_1 the 'near' component and σ^2_2 the 'far' component of the double exponential model.

MERIT						**SRTM**				
Location	σ_1^2	σ_2^2	a_1	Sill, m	Range, m	σ_1^2	σ_2^2	a_1	Sill, m	Range, m
Amberley	0	2.388	0.016	1.5	544	0.874	5.35	0.015	2.5	1698
Ba	0.034	2.154	0.011	1.5	413	0.373	6.946	0.014	2.7	655
Burdekin	0.552	1.078	0.02	1.3	4289	0	3.504	0.019	1.9	639
Ebro	0	0.542	0.009	0.7	308	0	2.037	0.015	1.4	484
Eel	0.09	1.635	0.012	1.3	527	0	5.091	0.015	2.3	506
Fens DSM	0.022	0.287	0.013	0.6	716	0.049	0.926	0.01	1	439
Fens DTM	0.026	0.282	0.013	0.6	846	0.059	0.936	0.01	1	478
Kaiapoi	0	1.993	0.025	1.4	818	0.245	6.911	0.015	2.7	600
Kaikoura	0.066	1.666	0.011	1.3	436	0.36	3.089	0.01	1.9	862
Kishima	0.071	0.965	0.013	1	716	0	4.814	0.01	2.2	329
Kushiro	0.391	0.727	0.014	1.1	2947	0	1.997	0.009	1.4	298
Mekong	0.137	0.843	0.013	1	1460	0	10.096	0.009	3.2	298
Mississippi	0.265	1.311	0.009	1.3	1234	0	2.67	0.009	1.6	298
Nadi	0.348	2.3	0.009	1.6	965	0	3.417	0.011	1.8	376
Notsuke	0.282	2.112	0.012	1.5	1179	0.031	3.099	0.012	1.8	422
Otaki	0.403	2.487	0.011	1.7	1224	0.017	3.976	0.011	2	380
Po Delta	0.572	0.816	0.014	1.2	3229	0.023	3.053	0.012	1.8	429
Roanoke	0	3.975	0.023	2	783	2.252	13.786	0.017	4	1931
Savannah	1.562	3.108	0.021	2.2	4364	0	21.026	0.025	4.6	846
Temuka	0	1.114	0.021	1.1	704	0.289	2.797	0.01	1.8	731
Wax Lake	0.13	0.87	0.01	1	1075	0	2.797	0.016	1.7	539

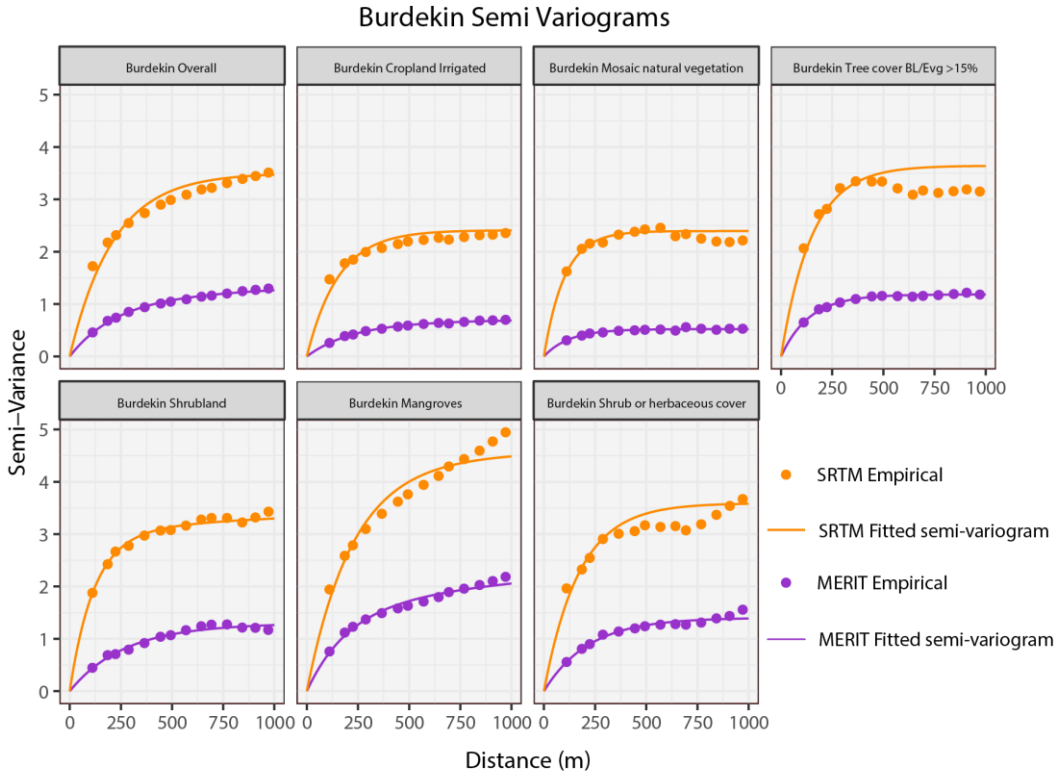

Figure 4-14 Burdekin semi-variograms of vertical error masked by landcover type. The MERIT semi-variograms are broadly similar, whilst there is more variation in the SRTM semi-variograms.

As all sites are floodplains with a similar topography, differences in semi-variogram parameters are likely to come from another source. As noted earlier, vegetation has a large influence on DEM error. Therefore, a further investigation was carried out to mask the vertical error pixels by landcover class and then produce semi-variograms. The purpose of this is to investigate whether landcover affects the DEM error and whether the semi-variograms alter. The landcover dataset used in this study was the CCI Landcover dataset (http://maps.elie.ucl.ac.be/CCI/viewer/). The CCI Landcover dataset has annual records from 1992-2015, with this study analysis using records from 2000 as this was the year of SRTM acquisition. In total there are 38 landcover class and sub-classes. To calculate the semi-variograms, the CCI Landcover dataset was resampled from its 300 m resolution to the resolution of the MERIT DEM (90m). Therefore, each MERIT pixel had an associated landcover class. For each site, landcover classes with over 600 pixels were selected to produce semi-variograms. This pixel threshold was chosen by trial and error to ensure well fitted semi-variograms were produced. Results for the Burdekin site are plotted (Figure

4-14). This analysis was also implemented for all study sites. This resulted in 94 semi-variograms for different landcover classes (Table 4-10). When the semi-variograms have been averaged by landcover class, 20 landcover classes have representative semi-variograms. Whilst this is just over half of the total landcover classes in the CCI dataset, this can be considered a good representation of landcover classes relevant for most floodplain locations as the range of study sites has meant that a wide range of landcover classes are included. Furthermore, those that are not covered (e.g. Permanent snow and ice cover) are not relevant for the vast majority of floodplain areas and thus end users.

Table 4-10 MERIT semi-variogram by study site and landcover. The 'sill' is the marginal standard deviation, in metres, and the 'range' is the distance, in metres, at which the correlation between two points drops to 0.05. σ^2_1 the 'near' component and σ^2_2 the 'far' component of the double exponential model.

Location	Land Cover	Number of Pixels	σ_1^2	σ_2^2	a_1	Sill, m	Range, m
Amberley	Overall	9888	0	2.388	0.016	1.5	544
Amberley	Mosaic cropland (>50%) / natural veg	811	0	1.676	0.014	1.3	482
Amberley	Grassland	7008	0	1.966	0.013	1.4	444
Ba	Overall	7102	0.034	2.154	0.011	1.5	413
Ba	Mosaic cropland (>50%) / natural veg	2605	0	2.299	0.01	1.5	348
Ba	Mangroves	2608	0.064	1.024	0.009	1	440
Burdekin	Overall	46430	0.552	1.078	0.02	1.3	4289
Burdekin	Cropland Irrigated	20621	0.142	0.641	0.02	0.9	2912
Burdekin	Mosaic natural vegetation	888	0	0.521	0.011	0.7	377
Burdekin	Tree cover BL/Evg >15%	2274	0	1.183	0.012	1.1	413
Burdekin	Shrubland	2308	0.142	1.245	0.023	1.2	1900
Burdekin	Shrubland Deciduous	6307	0.575	0.658	0.013	1.1	3151
Burdekin	Mangroves	8742	1.256	1.574	0.018	1.7	4373
Burdekin	Shrub or herbaceous cover	2443	0	1.403	0.02	1.2	654
Ebro	Overall	23629	0	0.542	0.009	0.7	308
Ebro	Cropland Irrigated	19296	0.078	0.211	0.01	0.5	1953
Ebro	Bare areas	1378	0	4.584	0.014	2.1	472
Eel	Overall	20172	0.09	1.635	0.012	1.3	527
Eel	Mosaic natural vegetation	3124	0.113	0.48	0.014	0.8	2021
Eel	Tree cover BL/Dec >15%	1669	0.444	0.941	0.011	1.2	2183
Eel	Grassland	11487	0.178	1.341	0.01	1.2	935
Eel	Bare areas	797	0	3.745	0.015	1.9	495
Fens DSM	Overall	2191	0.022	0.287	0.013	0.6	716
Fens DSM	Cropland Herbaceous cover	2137	0.02	0.29	0.013	0.6	659
Fens DTM	Overall	2191	0.026	0.282	0.013	0.6	846
Fens DTM	Cropland Herbaceous cover	2137	0.023	0.286	0.013	0.6	744

Location	Land Cover	Number of Pixels	σ_1^2	σ_2^2	a_1	Sill, m	Range, m
Kaiapoi	Overall	24222	0	1.993	0.025	1.4	818
Kaiapoi	Cropland	678	0	1.126	0.019	1.1	632
Kaiapoi	Mosaic tree and shrub (>50%) / herbaceous cover (<50%)	811	1.674	5.535	0.032	2.7	5524
Kaiapoi	Mosaic herbaceous cover (>50%) / tree and shrub (<50%)	1062	0	7.348	0.024	2.7	789
Kaiapoi	Grassland	18127	0	1.152	0.022	1.1	724
Kaiapoi	Urban areas	1590	0.068	0.63	0.014	0.8	1024
Kaikoura	Overall	6908	0.066	1.666	0.011	1.3	436
Kaikoura	Grassland	5749	0.179	1.377	0.009	1.2	860
Kishima	Overall	12262	0.071	0.965	0.013	1	716
Kishima	Cropland Herbaceous cover	5011	0.197	0.629	0.009	0.9	1558
Kishima	Cropland Irrigated	6088	0.011	0.8	0.013	0.9	459
Kushiro	Overall	24092	0.391	0.727	0.014	1.1	2947
Kushiro	Cropland	9951	0.115	0.33	0.012	0.7	2164
Kushiro	Cropland Irrigated	2949	0.136	1.398	0.013	1.2	890
Kushiro	Shrub or herbaceous cover	5230	0	0.364	0.027	0.6	887
Kushiro	Urban areas	3545	0.21	0.975	0.012	1.1	1642
Mekong	Overall	65890	0.137	0.843	0.013	1	1460
Mekong	Cropland Irrigated	64120	0.154	0.711	0.013	0.9	1793
Mississippi	Overall	24082	0.265	1.311	0.009	1.3	1234
Mississippi	Tree cover NL/Dec >15%	661	0.218	1.188	0.009	1.2	1132
Mississippi	Shrub or herbaceous cover	11795	0	0.99	0.009	1	298
Nadi	Overall	15564	0.348	2.3	0.009	1.6	965
Nadi	Cropland	1341	2.33	3.202	0.011	2.4	2556
Nadi	Cropland Herbaceous cover	5056	0.137	2.559	0.009	1.6	406
Nadi	Mosaic cropland (>50%) / natural veg	5814	0	2.707	0.009	1.6	298
Nadi	Mangroves	1897	0.029	0.855	0.011	0.9	438
Notsuke	Overall	71904	0.282	2.112	0.012	1.5	1179
Notsuke	Cropland	18886	0.107	1.49	0.01	1.3	538
Notsuke	Cropland Herbaceous cover	1563	0	5.128	0.036	2.3	1213
Notsuke	Cropland Irrigated	2173	0	0.607	0.009	0.8	298
Notsuke	Mosaic cropland (>50%) / natural veg	6750	0	1.635	0.012	1.3	413
Notsuke	Mosaic natural vegetation	6354	0	1.89	0.013	1.4	429
Notsuke	Tree cover BL/Dec >15%	9087	0.22	1.934	0.01	1.5	772
Notsuke	Tree cover BL/Dec >40% (closed)	2171	0	1.459	0.01	1.2	319
Notsuke	Tree cover NL/Evg >15%	4122	0	6.715	0.022	2.6	742
Notsuke	Mosaic tree and shrub (>50%) / herbaceous cover (<50%)	784	0	11.282	0.048	3.4	1591
Notsuke	Grassland	13174	0	1.92	0.009	1.4	298
Notsuke	Urban areas	1302	0	1.938	0.009	1.4	298
Otaki	Overall	11255	0.403	2.487	0.011	1.7	1224
Otaki	Grassland	9033	0.264	2.294	0.01	1.6	841
Otaki	Urban areas	1412	0.467	1.102	0.009	1.3	1784
Po Delta	Overall	41806	0.572	0.816	0.014	1.2	3229
Po Delta	Cropland	6227	0.435	0.865	0.021	1.1	4340
Po Delta	Cropland Herbaceous cover	23946	0.155	0.304	0.013	0.7	2846
Po Delta	Cropland Irrigated	1474	0.519	0.553	0.014	1	3445
Po Delta	Mosaic cropland (>50%) / natural veg	894	0.427	1.63	0.013	1.4	2058

Location	Land Cover	Number of Pixels	σ_1^2	σ_2^2	a_1	Sill, m	Range, m
Po Delta	Shrub or herbaceous cover	2848	0.191	3.121	0.013	1.8	643
Po Delta	Bare areas	1006	0	1.292	0.01	1.1	320
Roanoke	Overall	89630	0	3.975	0.023	2	783
Roanoke	Cropland Herbaceous cover	15921	0.66	1.879	0.021	1.6	3805
Roanoke	Mosaic natural vegetation	11698	0.04	2.599	0.019	1.6	675
Roanoke	Tree cover NL/Evg >15%	15968	0	9.469	0.08	3.1	2652
Roanoke	Tree cover (flooded, fresh, brackish)	42541	0	3.808	0.019	2	630
Roanoke	Urban areas	1114	0	5.022	0.029	2.2	960
Savannah	Overall	104084	1.562	3.108	0.021	2.2	4364
Savannah	Tree cover NL/Evg >15%	30179	1.641	4.238	0.032	2.4	6211
Savannah	Mosaic tree and shrub (>50%) / herbaceous cover (<50%)	753	0.276	2.598	0.009	1.7	678
Savannah	Grassland	1193	0.96	6.887	0.036	2.8	3625
Savannah	Tree cover (flooded, fresh, brackish)	4502	1.03	1.403	0.022	1.6	5149
Savannah	Shrub or herbaceous cover	30338	0	1.944	0.009	1.4	298
Savannah	Urban areas	3999	0.807	2.028	0.013	1.7	2430
Temuka	Overall	26956	0	1.114	0.021	1.1	704
Temuka	Cropland Herbaceous cover	2015	0	0.77	0.018	0.9	614
Temuka	Grassland	23123	0	1.122	0.021	1.1	707
Temuka	Urban areas	829	0	1.182	0.026	1.1	878
Wax Lake	Overall	4827	0.13	0.87	0.01	1	1075
Wax Lake	Tree cover NL/Dec >15%	720	0	1.932	0.016	1.4	532
Wax Lake	Shrub or herbaceous cover	1826	0	0.555	0.009	0.7	298
Wax Lake	Bare areas	828	0.155	0.793	0.01	1	1343

Table 4-11 MERIT semi-variogram parameters by CCI landcover class

Land Cover	Number of Semi-variograms	CCI Number	σ_1^2	σ_2^2	a_1	Sill, m	Range, m
Overall	20	NA	0.236	1.555	0.014	1.3	1543
Mosaic cropland (>50%) / natural veg	5	30	0.085	1.989	0.012	1.4	502
Grassland	8	130	0.089	1.596	0.014	1.3	624
Mangroves	3	170	0.45	1.151	0.013	1.3	2438
Cropland Irrigated	7	20	0.149	0.703	0.013	0.9	1826
Mosaic natural vegetation	4	40	0.038	1.373	0.014	1.2	545
Tree cover BL/Evg >15%	1	50	0	1.183	0.012	1.1	413
Shrubland	1	120	0.142	1.245	0.023	1.2	1900
Shrubland Deciduous	1	122	0.575	0.658	0.013	1.1	3151
Shrub or herbaceous cover	6	180	0.032	1.396	0.014	1.2	542
Bare areas	3	200	0.052	1.943	0.012	1.4	440
Tree cover BL/Dec >15%	2	60	0.332	1.437	0.01	1.3	1477
Cropland Herbaceous cover	7	11	0.149	1.481	0.017	1.3	1173
Cropland	5	10	0.164	0.953	0.015	1.1	1843
Mosaic tree and shrub (>50%) / herbaceous cover (<50%)	1	100	0.276	2.598	0.009	1.7	678

Urban areas	6	190	0.259	1.309	0.014	1.3	1814
Tree cover NL/Dec >15%	2	80	0.109	1.56	0.012	1.3	643
Tree cover BL/Dec >40% (closed)	1	61	0	1.459	0.01	1.2	319
Tree cover NL/Evg >15%	2	70	0.821	6.853	0.056	2.8	4795
Tree cover (flooded, fresh, brackish)	1	160	1.03	1.403	0.022	1.6	5149

When assessing the semi-variograms by landcover, landcovers with higher vegetation heights (e.g. trees) generally have larger sill value. From the example of Burdekin (Figure 4-14), mangrove areas have the largest sill value, so this is the most erroneous landcover type. When averaging semi-variograms by landcover types, landcovers with trees in them have the largest sill values (1.1 m -2.8 m). Mosaicked landcovers also have a large sill value (1.2 m– 1.7 m). Yet some landcover types (e.g. Bare Areas and Grassland) that we would perhaps expect to have a low sill value based on the above hypotheses do in fact have a relatively large sill value of 1.6m, which interestingly is lower than mangroves. Therefore, a confident assertion that sill values are larger for higher landcover classes cannot be made. Despite the number of locations analysed, the number of semi-variograms to create an average of the semi-variogram parameters by landcover is comparatively low (four for bare areas and eight for Grassland), so they are vulnerable to extreme low or high values. For example, for the bare area landcover class, high sill values for the Ebro bias the results. The same is true for Grassland in Savannah. Additionally, there are five landcover classes that only have a single semi-variogram, and thus there is lower confidence about how representative these semi-variograms may be. As more LIDAR data becomes publicly available, more sites can be analysed, thus more representative semi-variograms can be estimated.

4.7.2 DEM Simulation

Based on the calculated semi-variograms, plausible ensembles of the MERIT and SRTM DEMs can be simulated. This allows modellers to move beyond using a single DEM to use a catalogue of DEMs (termed a DEM ensemble in this thesis). In this work, semi-variograms have been calculated for 20 locations to estimate an 'average' floodplain semi-variogram for both the MERIT and SRTM DEMs. With the number of locations, semi-variograms by landcover type were also calculated, resulting in 20 out of the 38 CCI landcover classes

having estimated semi-variograms (Table 4-11). These landcover semi-variogram estimates allows for DEM simulation by landcover class with the workflow outlined in Figure 4-15. For one to simulate by landcover class they first need to extract DEM pixels by landcover class, then apply the associated landcover semi-variograms to those pixels and repeat for the number of landcover classes. When a landcover class does not have a semi-variogram, the 'average' semi-variogram is used. This approach makes this method more relatable to other locations, with these semi-variograms available for both MERIT and SRTM. By generalising these semi-variogram relationships, unconditional simulation is used, so a user does not have to have high-accuracy reference dataset for their given study site, making the approach presented here widely applicable.

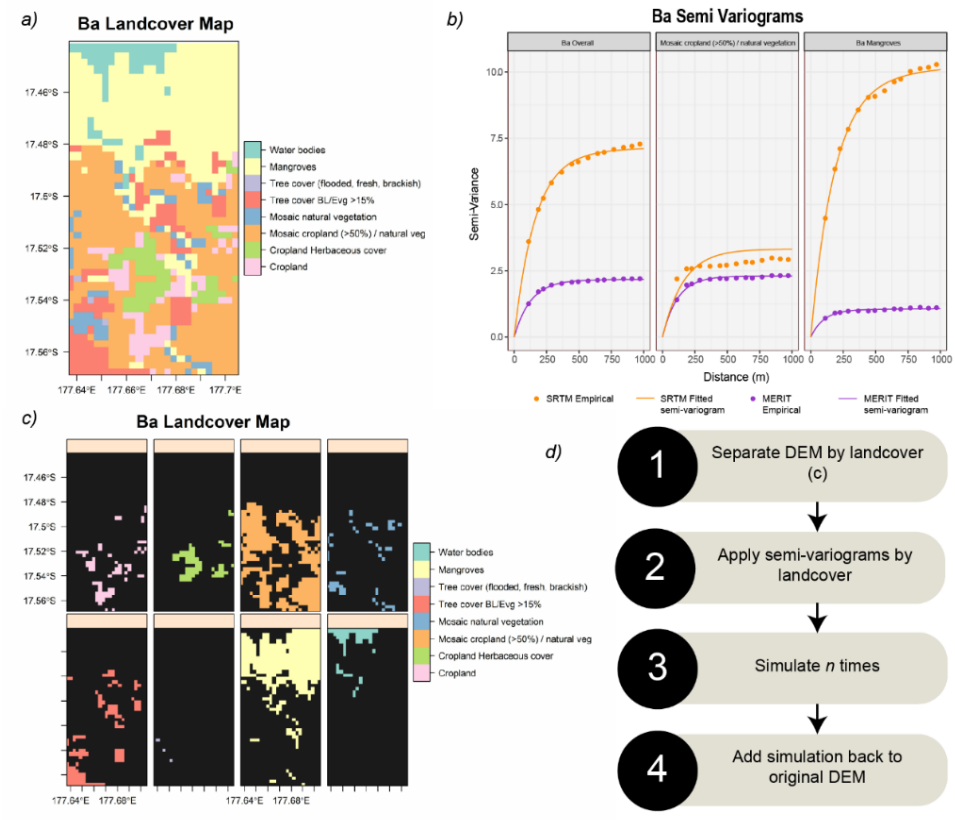

Figure 4-15 Simulation by landcover. a) Landcover map of Ba, Fiji using the CCI data. b) Semivariograms by landcover for Ba, Fiji. C) DEM of Ba separated by landcover class. D) Workflow for DEM simulation by landcover.

To quantitatively test the quality of the DEM ensemble, 2500 DEMs of Ba were simulated and assessed using rank histograms. Rank histograms (or 'Talagrand' diagrams) (Hamill

and Colucci, 1997, Anderson, 1996, Talagrand et al., 1997) are a common tool used to evaluate ensemble forecasts in meteorology, and work by ranking the verification (in this case LiDAR data) relative to the corresponding value in the ensemble in ascending order. An ideal ranked histogram is flat, since the observation is indistinguishable from any ensemble member. Typically, a U-shaped rank histogram suggests under-variability in the ensemble, a dome shape over-variability, and excessive population of the extreme ranks as bias. Yet, ranked histograms are notoriously difficult to evaluate and can lead to misinterpretations if done uncritically (Hamill, 2001). Nevertheless, rank histograms are produced by taking the mean of LiDAR values which fall within each ensemble pixel for all pixels in the Ba catchment in Fiji, as well as pixels by landcover class (Figure 4-16). The rank histogram of all pixels suggests a positive bias in ensemble members as the ranks are clustered to the left. Despite the vegetation correction in MERIT, the rank histogram of mangrove covered pixels shows a large positive bias, whilst cropland has a more uniform shape.

To compensate for errors in observations (LiDAR), random observational noise was added as suggested by Hamill (2001). This made little difference to the shape and are subsequently not presented here. Additionally, three goodness-of-fit measurements are computed (Table 4-12): Pearson X^2; Jolliffe-Primo (JP) slope and JP convexity, with the null hypothesis that the rank histogram is flat (Jolliffe and Primo, 2008). These statistics confirm the stronger bias in mangroves (JP Slope) and suggest possible under-sampling with the relatively high JP convexity values. All these results are statistically significant with p values of virtually zero. Moreover, less than 3% of pixels within the single MERIT DEM were within the error of the LiDAR (~50mm), whilst this was 97% for the ensembles. Therefore, the reliability of the DEM simulation can be deemed satisfactory but can suffer from the error of the global DEM product being used. A higher-accuracy global DEM would therefore make this technique even more effective.

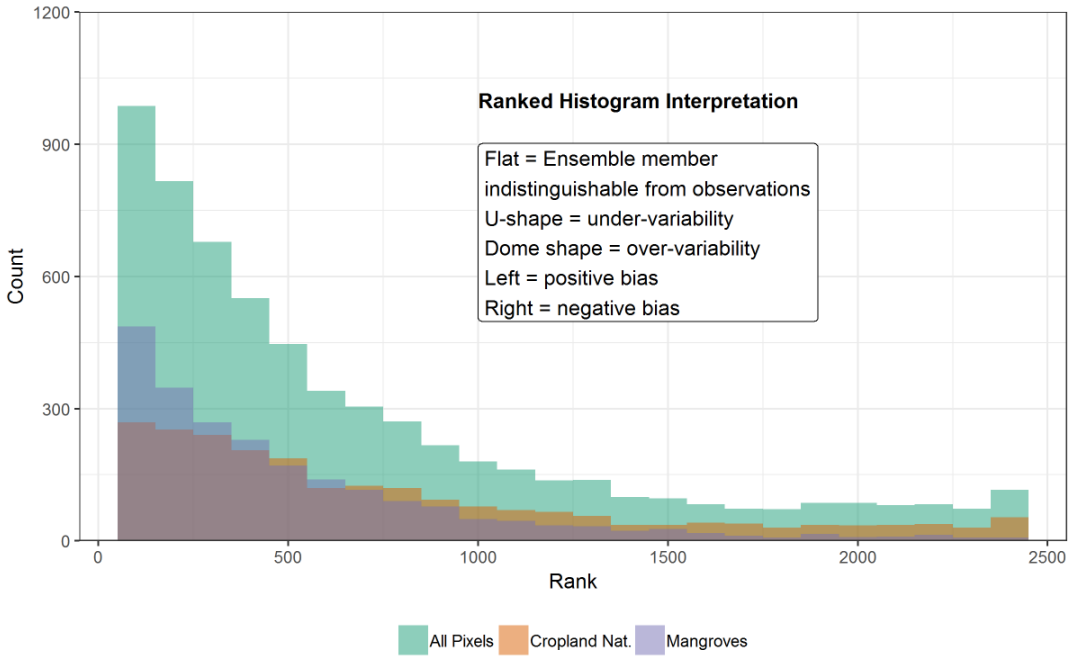

Figure 4-16 Rank Histograms for an ensemble of 2500 DEMs of the Ba catchment in Fiji, simulated from the MERIT DEM using semi-variograms of spatial error structure by landcover class. All Pixels and the 2 landcover classes with the most pixels (Mosaic Cropland/Natural Vegetation and Mangroves) are shown.

Table 4-12 Goodness-of-fit measures to assess DEM simulation

	Pearson chi	JP Slope	JP Convex
All Pixels	24493	5440	3174
Cropland	4000	122	220
Cropland Herbaceous Cover	7728	620	474
Mosaic Cropland/Natural Vegetation	7820	1380	752
Mosaic Natural Vegetation	2626	62	48
Tree cover, BL/Evg, closed to open (>15%)	5953	193	240
Mangroves	11160	3291	1562

4.7.3 Flood Inundation

The simulated DEMs (both MERIT & SRTM, and simulated using the average semi-variogram and landcover semi-variograms) were used subsequently in flood models for two locations - An Giang (Figure 4-17) & Ba (Figure 4-18). These two sites were used to demonstrate the impact of topographic uncertainty on flood predictions for two reasons. First, they represent end members of floodplains, as the Ba floodplain is small and constrained within a valley, whereas the An Giang floodplain is large and is not constrained

by valley sides. Furthermore, data availability at the time meant that flood models could only be constructed for these two locations relatively quickly. DEM ensembles are simulated for the MERIT and SRTM using the average floodplain semi-variograms and semi-variograms disaggregated by landcover as discussed in 4.7.2. By using an ensemble of simulated DEMs flood inundation probability maps were produced, whereby the inundation probability refers to the number of ensemble members in which the pixel in question is flooded. For example, if a pixel was flooded in 300 DEMs in an ensemble of 500 DEMs then the inundation probability would be 60%.

First the flood models are evaluated by calculating four commonly used skill scores: Critical Success Index; Hit Rate, Miss Rate and False Alarm Rate (Horritt and Bates, 2001a, Stephens et al., 2014, Sampson et al., 2015) (Table 4-13). The Critical Success Index (CSI) measures the fraction of correctly predicted events, penalizing for both misses and false alarms. This is an adjustment of the Proportion Correct Score for the quantity being forecast (Wilks, 2011). CSI scores range from 0 indicating no skill to 1 which is a perfect score. The Hit Rate is the rate of correctly predicted inundated pixels. Conversely, the Miss Rate measures pixels that are not predicted in the model but are flooded in the observations (i.e. model under-prediction). The False Alarm Rate refers to incidences where the model predicts flooding, but the observed floodplain state is dry (i.e. model over-prediction). In this analysis, the LIDAR model at 30m was assumed to be the observation. To allow for direct comparison to the 90 m resolution that the other models were run at, the 30 m data was resampled using bilinear interpolation. The LIDAR model at 90 m had the best performance for both sites. However, the LIDAR model at 90 m for An Giang had only a marginally better CSI score than the MERIT and SRTM models, with this due primarily to a relatively high False Alarm Rate. Of the global DEMs, MERIT has better skill scores than SRTM. It is noticeable that there is a marked difference in performance of the two flood models, with An Giang model performing poorly (maximum CSI 0.36) and the Ba model performing very well (maximum CSI 0.9). This goes to highlight the difficulty in modelling small magnitude events in areas where the floodplain is not constrained (An Giang).

Table 4-13 Flood model skill scores for both An Giang and Ba for 3 sets of deterministic DEMs (LIDAR 90m; MERIT, SRTM) and 3 sets of simulated DEMs (MERIT Landcover; MERIT Average). Skill scores assessed include Critical Success Index, Hit Rate, Miss rate and False Alarm ratio

An Giang				
DEM	*CSI*	*Hit Rate*	*Miss Rate*	*False Alarm*
LIDAR 90m	0.36	0.97	0.03	0.22
MERIT	0.26	0.55	0.45	0.15
SRTM	0.24	0.27	0.73	0.02
MERIT Landcover	0.11-0.44	0.20-0.75	0.26-0.80	0.00-0.54
MERIT Average	0.19-0.39	0.20-0.58	0.42-0.79	0.00-0.27
SRTM Landcover	0.12-0.36	0.21-0.54	0.46-0.79	0.00-0.26

Ba				
DEM	CSI	Hit Rate	Miss Rate	False Alarm
LIDAR 90m	0.90	0.92	0.08	0.07
MERIT	0.77	0.78	0.22	0.04
SRTM	0.58	0.6	0.41	0.06
MERIT Landcover	0.60-0.87	0.61-0.91	0.09-0.39	0.03-0.12
MERIT Average	0.59-0.87	0.60-0.95	0.05-0.40	0.03-0.40
SRTM Landcover	0.46-0.55	0.47-0.57	0.43-0.53	0.04-0.09

In Table 4-13 the range of skill scores for each member of the DEM ensembles is given. Using an ensemble of simulated DEMs can give higher skill score values compared to using a single deterministic DEM. Skill scores can vary considerably. For example, the Critical Success Index (CSI) in Ba is 0.77 for the MERIT model, 0.58 for SRTM and ranges from 0.60-0.87 for the DEM ensemble of MERIT simulated using landcover semi-variograms. The Hit Rate and Miss Rate have particularly large ranges for DEM ensembles using MERIT compared to the ensemble using SRTM simulated by landcover semi-variograms. This is likely to be a remnant of the DEM simulation process as the addition of the error field is adding bias. From the semi-variograms presented earlier Figure 4-13, SRTM is noisier than MERIT as indicated by the shorter range values. A noisier DEM indicates that the neighbouring pixels are more random, thus making flow, or connectivity, more unlikely. SRTM also has more bias as indicated by the larger sill values compared to MERIT. The noisiness in SRTM results in a lack of connectivity, and so flooding is underpredicted at both test sites (Figure 4-17 & Figure 4-18). By simulating the MERIT DEM, bias and noise is

added to the DEM, thus reducing connectivity and flooding. Conversely, the DEM simulation process can *correct* some of the key pixels that control connectivity, and thus the inundation extent. To further understand the flood inundation results, flood inundation maps are displayed in Figure 4-17 & Figure 4-18. The simulations using an ensemble of DEMs bracket the predicted extent of the benchmark LIDAR model and deterministic MERIT and SRTM models, with the MERIT simulation being closer to the benchmark for both case studies. Areas of higher inundation probability are generally closer to that of the benchmark LIDAR model.

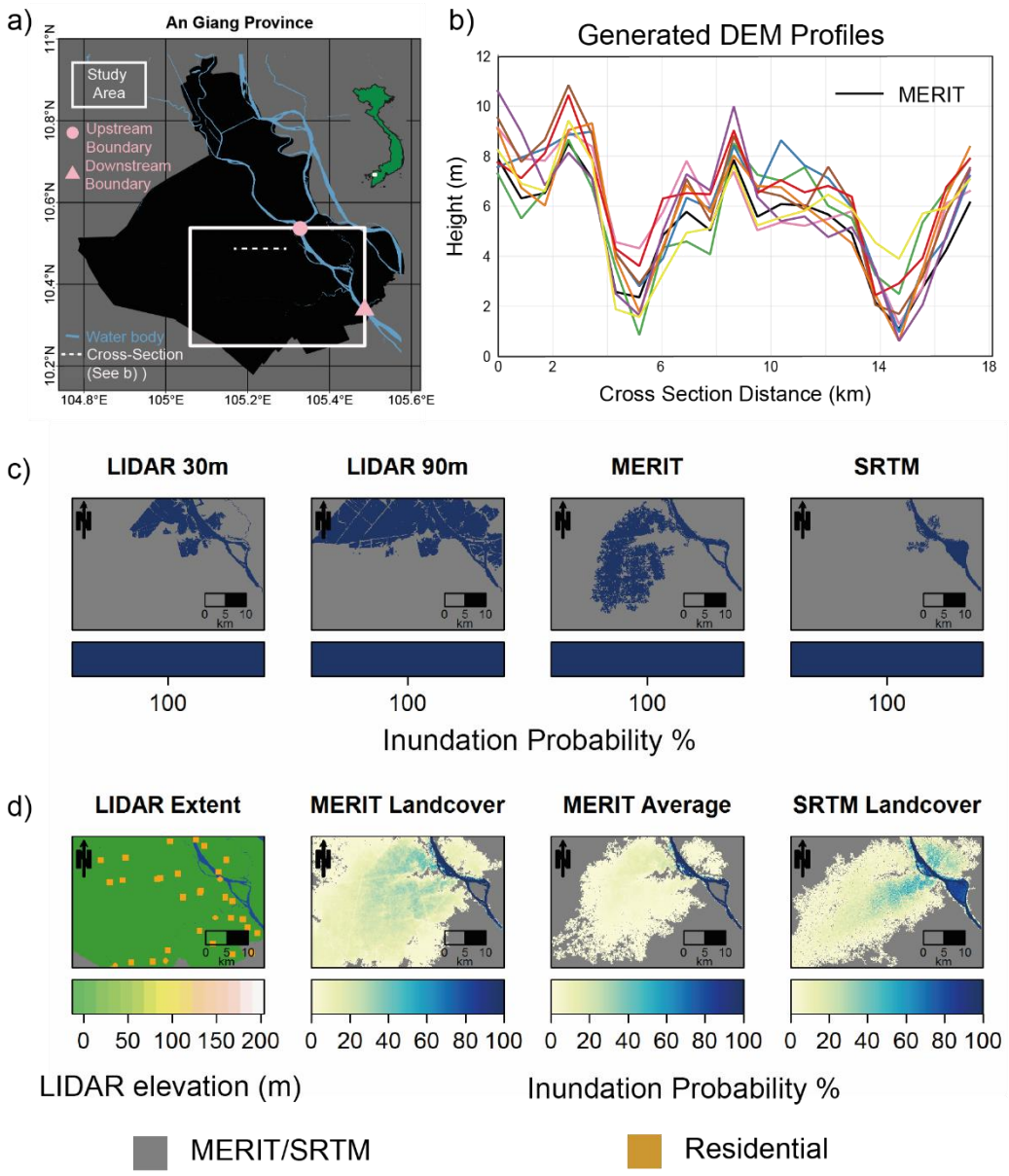

Figure 4-17 Flood Inundation study for an area of An Giang Province, Vietnam. a) Study Site Location. b) A cross sectional profile through the study site showing elevation of the MERIT DEM (black line) and elevations of 10 randomly selected simulated DEMs (coloured lines). c) Maximum inundation extent when a single DEM Used (MERIT, SRTM and LIDAR at 30m and 90m). d) Maximum Inundation extent for DEM ensembles simulated by landcover (MERIT \& SRTM) and by an 'average' semi-variogram (MERIT). The orange squares in d) show residential areas.

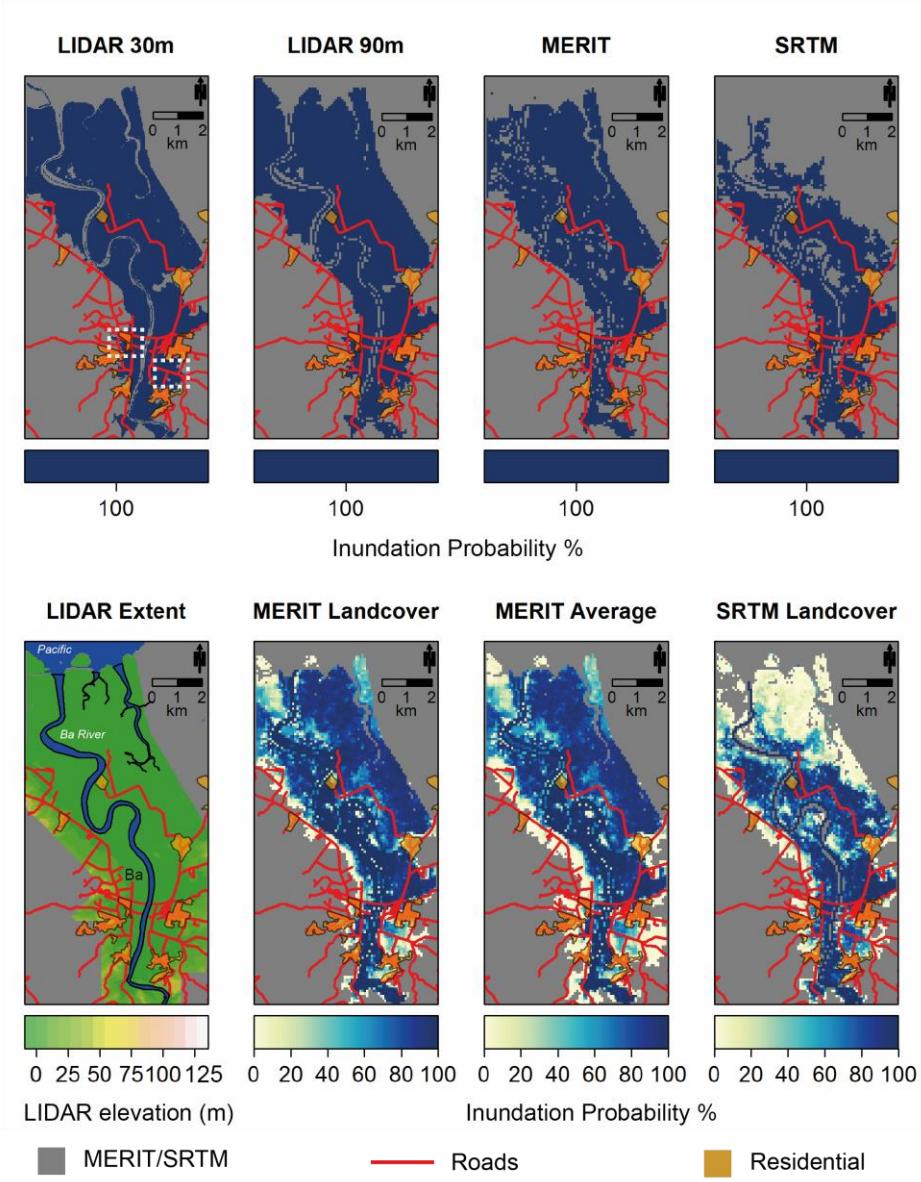

Figure 4-18 Maximum flood extents for a 50 year return period event for Ba, Fiji. Red Lines show roads and the orange polygons residential areas, both extracted from the Open-StreetMap™ database. Areas of interest highlighted by white dashed boxes in the LIDAR model. Extent of LIDAR is marked in the LIDAR Extent Map. Grey background is where MERIT/SRTM is present.

For the An Giang case study, the ensemble of simulated DEMs activates floodplain flow pathways that are present in the higher resolution LIDAR data but are not in MERIT/SRTM. These flow pathways could be activated or deactivated by using an ensemble of DEMs, with inundation extent varying demonstrably. The large variation in inundation extent is also a result of the unconfined floodplain environment of the delta meaning it is difficult to limit the flood. In the MERIT Landcover DEM ensemble, the higher inundation probabilities

(light blue) more closely align with the LIDAR benchmark model, even though there is still some over-prediction in the middle of the domain similar to the deterministic MERIT model (Figure 4-17). Nevertheless, the DEM ensemble models do capture the flooding in the top right of the domain which was not present in the deterministic MERIT model. For the Ba case study, the variation in inundation extent was more constrained with a larger area with higher inundation probability. This is due to the confined river valley setting meaning the large flood fills the valley floor.

In Figure 4-18, inundation probability maps are presented for Ba, with exposed assets of roads and residential areas from the OpenStreetMap™ (https://planet.openstreetmap.org) database overlaid. Asset data was included to determine what the *actual* impacts might be. This adds a qualitative component to the more traditional skill score metrics. Research into the presentation of flood hazard maps is extensive and outside the scope of this thesis, so interested readers should consult the literature (Hagemeier-Klose and Wagner, 2009, Di Baldassarre et al., 2010, Meyer et al., 2012, Alfonso et al., 2016). Some assets are inundated (highlighted by white dashed boxes in Figure 4-18) in the LIDAR models but are not in the MERIT and SRTM models. In this study, a high-resolution benchmark model exists, but in most data-sparse areas a decision maker would be presented with either the deterministic MERIT or SRTM simulations, thereby missing some at-risk assets in this case. By using a DEM ensemble, these assets that have been 'missed' have a relatively high inundation probability (50-70%). Thus, if these probabilistic maps were presented to a decision maker they would be at least aware that these assets may in fact be at risk and could allocate resources as they see fit. In other words, by using an ensemble of simulated DEMs, a range of flood predictions can be made, of which some are more similar than the true situation (with the assumption that the benchmark model is the true flood). In addition, using an ensemble of simulated DEMs avoids the spurious precision in flood estimates by using a single DEM and, thus, allowing risk assessors to identify pivotal locations where (often) limited resources can be used most effectively.

As well as flood extent, it is important to predict flood depth correctly. Water Depth estimation can be used to estimate flood damage through flood depth damage curves (Merz et al., 2010). Therefore, the distribution of water depths from each DEM ensemble is plotted

for four randomly selected locations in Ba (Figure 4-19). In Figure 4-19 B) a flood inundation probability map is plotted for the DEM ensemble of MERIT simulated using Landcover semi-variograms. Further analysis of predicted flood depth (Figure 4-19, C-F) indicate the benefit of using ensembles of simulated DEMs in predicting correct water depths. For example, in Location 2, the MERIT DEM does not flood, whilst the flood depth in SRTM is large (>4.8m), but for the ensembles of DEMs the distribution of predicted flood depths are more closely aligned with the flood depths predicted in the LIDAR models. Additionally, in Location 3, all but the LIDAR 30m deterministic simulations do not flood. In the probabilistic simulations, flooding does occur in some of the simulated DEMs in location 3, thus avoiding the dangerous situation of a flood being missed that occurs in most of the deterministic simulations.

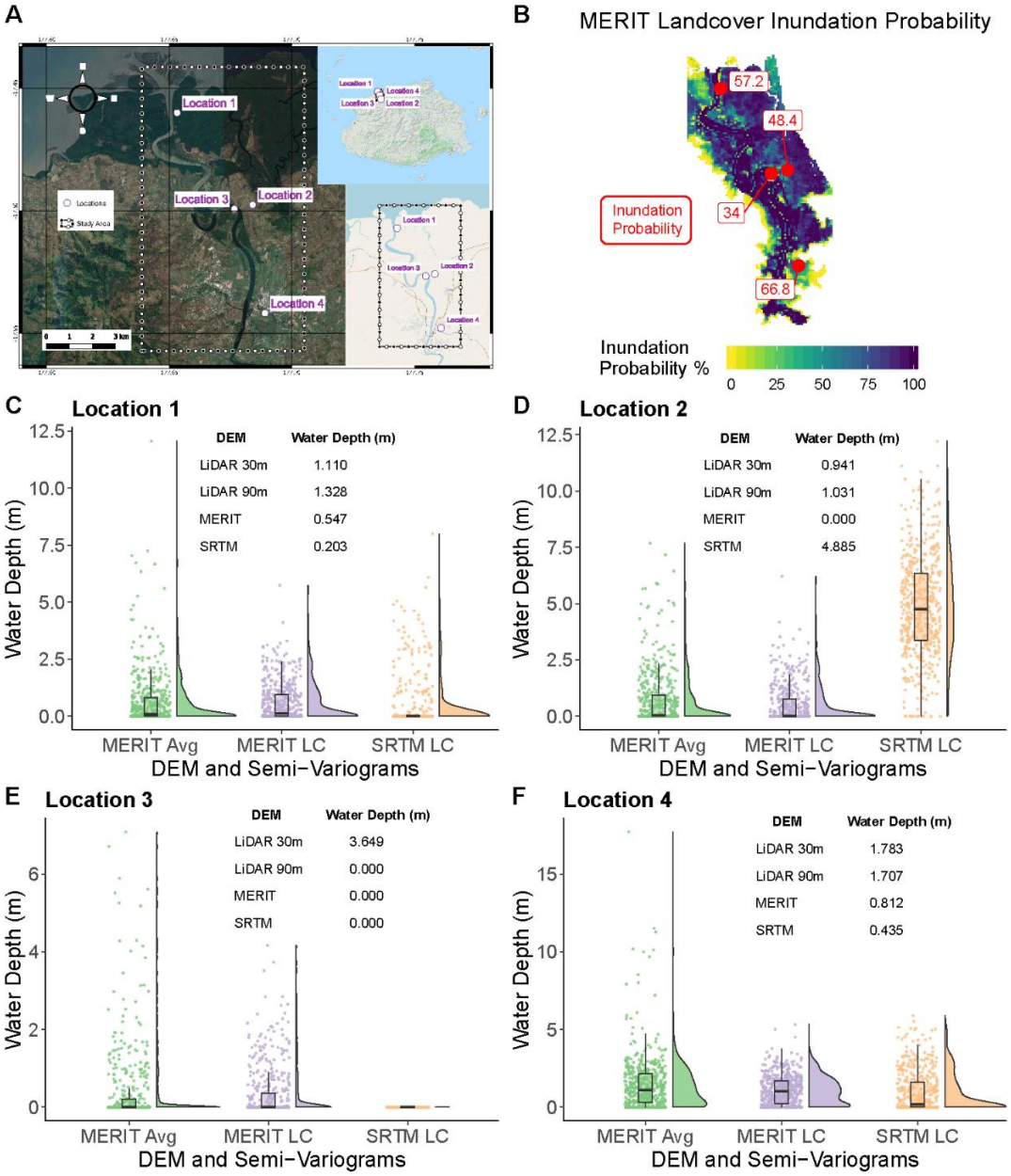

Figure 4-19 Maximum flood water depth at 4 locations in Ba, Fiji for a 50-year return period event. A) Overview of study area, with locations of 4 random locations to investigate differences in water depth. B) Inundation probability (% of DEMs in DEM ensemble that are flooded) for models run with simulated versions of the MERIT DEM simulated using semi-variograms per landcover class. C-F) Maximum water depth distribution of each DEM ensemble simulated by different sets of semi-variograms for location 1-4. MERIT Avg refers to MERIT DEM simulated using an 'average' floodplain semi-variogram, MERIT LC refers to MERIT DEM simulated using semi-variograms by landcover class, SRTM LC refers to SRTM DEM simulated using semi-variograms by landcover class.

To determine which DEM simulation method is most effective at estimating inundation extent density plots for both An Giang and Ba are produced (Figure 4-20). This plot type was chosen over a more conventional histogram as it normalizes the difference in inundated area which is particularly apparent in the An Giang example. In this analysis the LIDAR 30m benchmark model is chosen as the true flood situation in the absence of any flood observation data. Pixels in the LIDAR model are compared to their counterparts in the DEM ensemble for each DEM simulation approach. Pixels are binned into 2 categories: 1) Correctly predicted (blue) when both pixels are inundated, 2) Incorrectly predicted (red) when either pixel in the LIDAR or DEM ensemble model is not inundated. The corresponding inundation probability for the pixel in question is then plotted against the density of observations. This meant that the distribution of inundation probability for correctly and incorrectly predicted pixels could be visualised. The dashed lines show the mean of this distribution. The DEM ensemble simulated using the MERIT DEM and using the fitted Landcover semi-variograms gave the inundation extent closest to that of the LIDAR (indicated by blue dashed line). This was less apparent for Ba as the mean inundation probability value was just 0.3% more than the DEM ensemble of MERIT using the 'average' floodplain semi-variogram. The difference in the distributions in Figure 4-20 not only highlights the challenge of flood inundation estimation in unconstrained floodplains such as for the An Giang case, but also indicates a probability threshold value cannot be specified to delineate pixels that we can be confident will flood. In other words, this distribution is location dependent. For a floodplain environment like the Ba case study, our DEM simulation approach is more effective as the variation in topography simulated in the DEM ensemble has less impact than in an environment like An Giang. Lastly, the MERIT DEM simulation consistently predicts inundation closer to the LIDAR model, with the MERIT DEM simulated using landcover semi-variograms giving predictions closest to the LIDAR model.

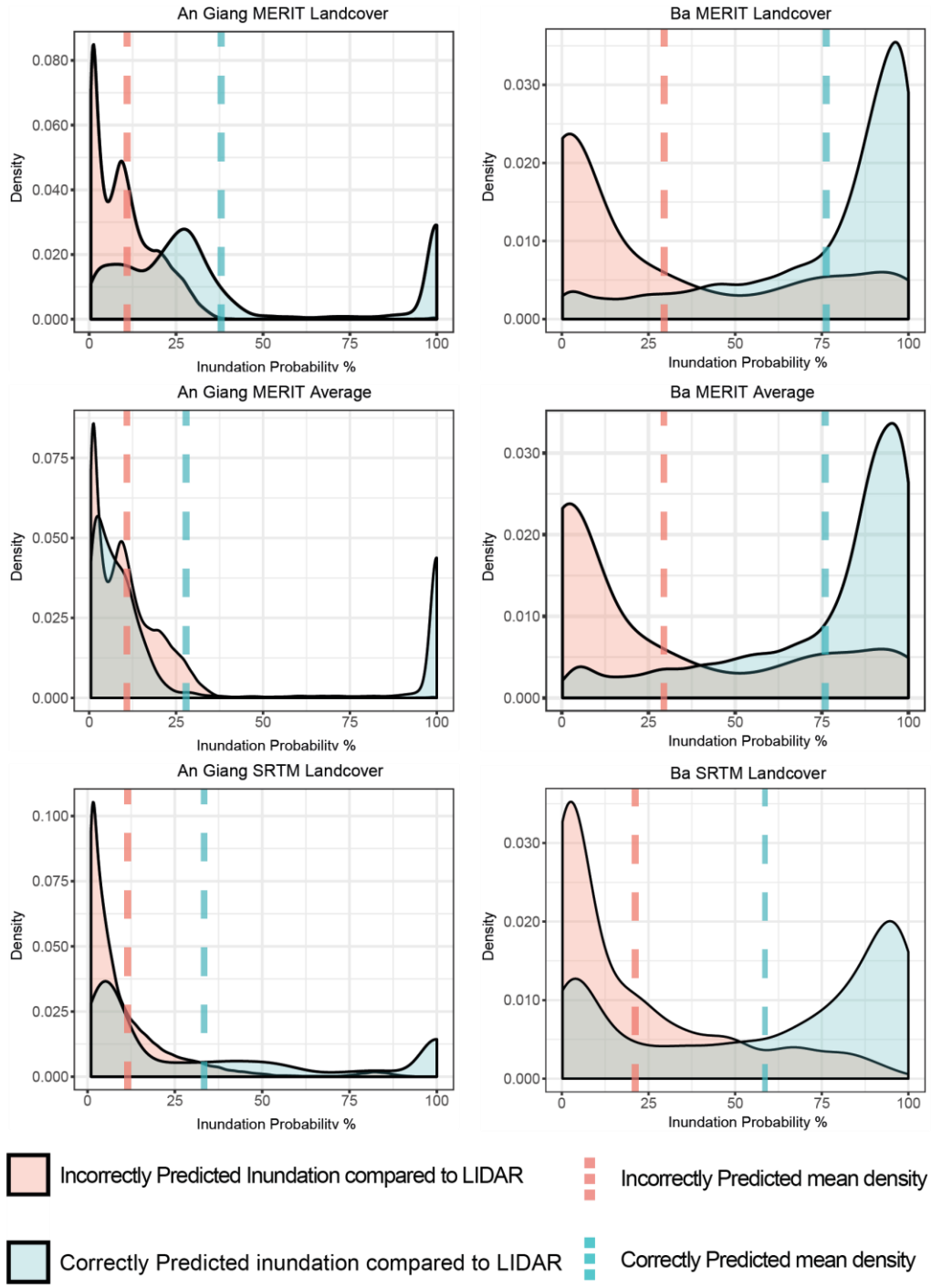

Figure 4-20 Density Plots for the distribution of flooded pixels by inundation probability for each DEM Ensemble. Comparison is made between pixels that correctly predict (compared to LIDAR model) and those that are incorrectly flooded. The dashed line refers to the mean density.

4.7.4 Discussion

In this analysis, only topography has been altered so the impact of topographic error on flood estimates can be assessed. Whilst it is beneficial to incorporate sophisticated approaches such as compound flooding (Zscheischler et al., 2018, Wahl et al., 2015, Moftakhari et al., 2017b) or event generation (Keef et al., 2013, Neal et al., 2013) it would create an unworkable parameter space, thus making it challenging to draw robust conclusions. Yet, beyond this thesis it would be beneficial to utilise such approaches and for others to investigate the contribution of topography against other parameters in flood models.

As effective computing power continues to grow, it is increasingly possible to run multiple flood models to test sensitivity to parameters. These have almost exclusively focused on hydraulic parameters, with topography largely ignored due to the lack of alternative datasets. This chapter has demonstrated that topography has a large impact on inundation extent and should therefore be included in any flood hazard estimation. These results suggest that simulating DEMs by landcover semi-variograms is most appropriate.

In theory, one could take the semi-variograms produced in this study to simulate floodplain MERIT or SRTM DEMs for any location where the MERIT and SRTM datasets exist. Whilst possible and made available through the R Package accompanying this work (4.8), extreme caution should be taken when applying this work globally. By using an unconditional simulation approach, error is being added to the DEM, with this error characterised by the 20 locations that have been analysed in this chapter. Yet in the absence of being able to quantify the spatial error structure for every floodplain location (which remember would need an accurate high-resolution DEM (LIDAR)) and the similarity of the semi-variograms produced here, the work in this chapter can be cautiously implemented if multiple DEMs are required, allowing a modeller to explore the impact of uncertain topography on flood predictions.

4.8 Code

4.8.1 DEMsimulation

The code to simulate DEMs has been made into an R package named `DEMsimulation` and is available on github (https://github.com/laurencehawker/DEMsimulation). Choosing to implement this work in R was based on the fact R is a GPL software so is thus freely accessible to anyone, and that tools already existed in the language to carry out the geostatistical work (gstat). A user does not require a deep understanding of geostatistics and DEM error to use the package, but some background in spatial statistics it recommended. Currently, there are four principle functions as detailed below:

Table 4-14 Functions in `DEMSimulation`

Function	Detail
download.CCI	Download CCI landcover data for the extent of the DEM to simulate and resample to the resolution of that DEM. Required if a user wishes to simulate by landcover
demsimulation	Simulate N versions of either the MERIT or SRTM DEM using a selected semi-variogram. Default is the average semi-variogram for floodplains. The output is a geotiff which can be analysed through the raster package in R (Hijmans et al., 2017).
demsimulation_LC	Simulate N versions of either the MERIT or SRTM DEM using semi-variograms by landcover. Requires a landcover map which can be automatically downloaded and cropped using download.CCI. The output is a geotiff which can be analysed through the raster package in R (Hijmans et al., 2017)
writeRasterDEM	Writes the simulated DEMs into individual raster files.

A user would need to have R installed, with the latest version recommended. To download the `DEMSimulation` package, the *devtools* package first needs to be installed and loaded into the R library, before using *install_github* to install `DEMsimulation` from github. Other

techniques to do this are available, but this is recommended procedure due to the comprehensive documentation available.

A workflow to use `DEMsimulation` is provided in Figure 4-21. The user first needs to select a floodplain DEM of interest from either the MERIT or SRTM DEM. It must be stressed that the semi-variograms in this work have been produced for floodplain locations so it is unknown how results will be affected by simulating a non-floodplain location. Next, the user should mask any water pixels in their DEM, with the water occurrence mask of Pekel et al. (2016) recommended. If a user already has a channel mask from another source that can be used instead. Once this has been completed, the user has a choice of 3 DEM simulation technique: 1) Simulate by 'Average' floodplain semi-variogram; 2) Simulate by Landcover semi-variograms; 3) Simulate by other semi-variograms. It is recommended to simulate by landcover option unless the user has a compelling reason to use another technique. Depending on the simulation technique used, intermediary processes may be required using functions of `DEMsimulation`. The core function, `DEMsimulation`, will then be used to simulate N DEM simulations, with the outputs written to a raster of the desired format. Simulating DEMs can be computationally intensive, with the function providing a display of progress.

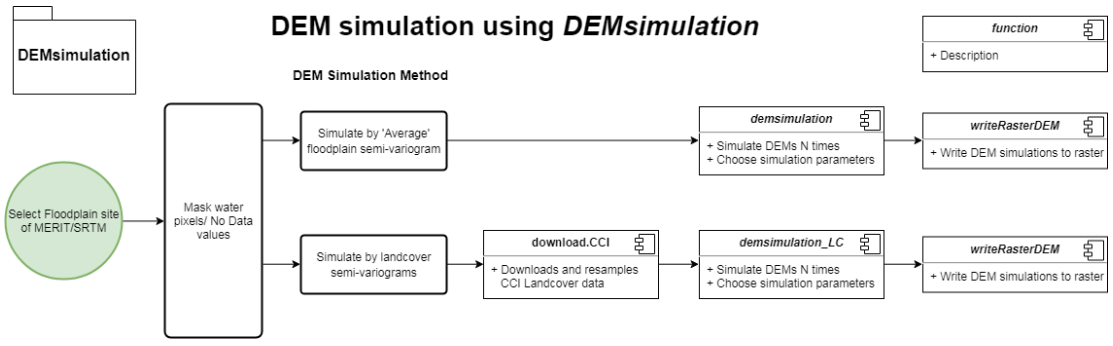

Figure 4-21 Workflow of `DEMsimulation`

4.9 Limitations

The method presented here is intended to give flood modellers primarily working in data-sparse areas a quick and efficient method to simulate plausible DEMs from the MERIT and SRTM global DEMs without needing to go into the field. Ultimately, these simulated DEMs

are not a better version of MERIT/SRTM but are simulations of these DEMs with an error field added to them. Therefore, the simulated DEMs have additional error compared to the DEMs they are originally simulated from. One should remember that the SRTM, and by default MERIT, still contain numerous errors and are becoming outdated as the raw data were collected almost two decades ago. When choosing to use MERIT or SRTM, a modeller should ask themselves whether these DEMs are good enough for the needs of their study. If the answer is a 'yes', this approach can allow modellers to explore the impact of topographic uncertainty on their model results. Even if the answer is a 'no', but higher quality data are unavailable or if the model resolution is prohibitive for available computing, the approach outlined in this chapter can be used to explore the effect of topographic uncertainty on flood predictions and avoid the spurious precision of just using a single DEM. If the aim of the study is to design a highly technical engineering project, MERIT and SRTM are extremely unlikely to be good enough for this purpose, so the modeller and/or their clients should make the effort to finance high-resolution topographic data. One should also consider that modelling at a higher resolution costs substantially more computing power, with Savage et al. (2016b) finding that halving the hydraulic model resolution leads to a 10x increase in compute costs. Thus, even if a higher resolution DEM is available it may be more worthwhile to model at a coarser resolution to explore the sensitivity of not only the DEM but other model parameters, similar to the approach advocated by Savage et al. (2016a).

If a field visit is possible, one could take high-accuracy GPS measurements to either create a semi-variogram or condition the simulation in an approach similar to that of Kydriakidis et al. (1999). There is no golden rule of the number of points that would be needed, but one should aim for as many as possible throughout the domain and in different vegetation types. A disadvantage of this approach is that even if the GPS measurements were made today, they would be almost 20 years after the acquisition of SRTM. Even though the LIDAR data that is used as reference data by this study is newer than SRTM it is not as current as collecting GPS data today. However, with the recent release of TanDEM-X 90 (multi-scene DEM acquired 2011-2015), the impact of temporal inconsistency is lessened. One should also check other parameters in the field site if possible – for instance to check the gauging station

where the hydrograph is produced. This would also for a more detailed examination of uncertainty.

Several of the landcover semi-variograms only have a single semi-variogram (Table 4-11) making the estimated spatial error structures highly uncertain. Once more LIDAR data becomes available, this work will be updated, allowing for more semi-variograms to be put into the database, contributing to a more certain estimation of the semi-variograms.

Lastly, whilst the `DEMsimulation` package has been designed to be as accessible and easy to use as possible, it can suffer from performance issues. For the An Giang domain (>1500km^2), it took just over 20 minutes to simulate 200 DEMs using a standard Intel Core i7 machine. Conversely, it took just over a minute for 500 simulations of the Ba catchment. As domains get larger, performance slows. To overcome this, the domain could be sub-divided, but this could lead to inconsistency when simulating at the boundary edges. Parallelisation of the code is currently being explored and will be added once implemented.

4.10 Conclusion

In this chapter, a method to simulate plausible versions of the MERIT and SRTM DEMs in floodplains has been presented. The impacts of using an ensemble of simulated DEMs on predicted flood inundation for two contrasting case studies was further assessed.

This work first involved calculating the spatial error structure for both the MERIT and SRTM global DEMs by assessing against a reference dataset (LIDAR) for 20 lowland locations distributed across the globe. This is the first time the spatial error structure of the MERIT DEM has been calculated, and the first time this has been compared to the spatial error structure of SRTM. Results from the fitted semi-variograms revealed that the MERIT DEM is consistently more accurate than SRTM (semi-variogram sill values of 0.7-2.2 m compared to 1.0-4.8 m), with the errors in MERIT being more spatially dependent as indicated by larger range values (308-4364 m) compared to SRTM (298-1931 m). Further semi-variograms were produced by landcover class. It was demonstrated that the spatial error structure differs by landcover class, with landcover classes with higher canopy heights generally having a larger sill value. However, this relationship is not clear and should be

investigated further with a larger sample. It was also difficult to separate whether the spatial error structure differences were driven by topography or landcover, although by using similar topography (i.e. floodplains) the effects of topography on the error in the DEM was reduced. In total, 94 semi-variograms covering 20 different landcover classes were produced.

These fitted semi-variograms were then taken to simulate plausible versions of either the MERIT or SRTM using unconditional Gaussian simulation. This procedure has the advantage that it does not require high accuracy reference topographic data to be available (e.g. LIDAR or GPS observations) as conditional simulation requires. However, the unconditional simulation approach has the major disadvantage of not eliminating the error at reference data points, while at the same time add the error filed to create an inflated DEM with larger errors than the original DEM that it was simulated from. Nevertheless, the approach presented in this chapter allows simulation of multiple plausible DEMs for any floodplain location using the spatial error structure relationships that have been estimated for 20 floodplain sites, thus, allowing modellers to explore the impact of topographic uncertainty on their flood predictions by using an ensemble of simulated DEMs. By estimating semi-variograms by landcover, one can simulate DEMs either by using a landcover map, by an 'average' floodplain semi variogram or by one of the 94 semi-variograms we have calculated. A tool to implement this has been created in the GPL software R in a package named `DEMsimulation`, which is freely available (https://github.com/laurencehawker/DEMsimulation).

To test the impact on flood predictions by using an ensemble of simulated DEMs, two hydrodynamic models of contrasting locations (An Giang, Vietnam & Ba, Fiji) were run. These hydrodynamic models were made of four deterministic simulations using LIDAR, MERIT and SRTM DEMs and three sets of ensembles of simulated DEMs. Using an ensemble of simulated DEMs avoids the spurious precision in flood prediction given by deterministic models and allows for an assessment on how topographic uncertainty impacts flood predictions, resulting in probabilistic flood maps based on ensembles of simulated DEMs. Sometimes, by using ensembles of simulated DEMs, skill scores of flood predictions were higher than the deterministic model equivalent, with an upper range in Critical Success

Index of 0.44 (compared to 0.26 for the deterministic MERIT) for An Giang and 0.87 (compared to 0.77 for the deterministic MERIT) for Ba. Conversely, the lower bounds of the skill score range for the ensembles of simulated DEMs also decreased for both sites which is unsurprising as additional error has been introduced to the DEM by the unconditional simulation process. Whilst the simulation approach in this chapter does not produce an ensemble of more accurate DEMs, it does provide a method to explore how topographic uncertainty impacts flood predictions and, thus, highlighting the importance of topography for the quality of flood predictions. The distribution of flood depth estimates by the ensemble of simulated DEMs were compared to the deterministic simulation demonstrating that using an ensemble of DEMs meant that the inundation depth could be more accurately estimated. Simulating the MERIT DEM by landcover class gave the highest skill score for the flood predictions, and is thus the favoured simulation method. The distribution of inundation probability can vary considerably between floodplain locations, so a probability threshold of what to consider to be a flooded pixel is inappropriate. Instead, an inundation probability map should be presented so a decision maker can decide for themselves what to consider at-risk from flooding. This will vary based how risk adverse the decision maker is.

The method presented in this chapter makes it possible to use multiple DEMs even for data-sparse areas. This represents a clear shift in modelling efforts where a lack of topographic data has restricted our attempt to understand the impact of DEM error on predicted inundation extent. Therefore, flood modellers can now explore the sensitivities of their models to uncertainties in topography in addition to the more traditional uncertainty associated with hydraulic parameters. Future work will include adding more semi-variograms and assessing the sensitivity of topography compared to other parameters in flood models. The flexibility of this approach means this method can be used once new DEMs are released, as this technique needs only a DEM and a reference dataset.

4.11 Postscript

This chapter has clearly demonstrated the impact of topographic uncertainty on predicted inundation extent. By varying pixel height, flood pathways can be activated or deactivated. This river channel – floodplain connectivity is critical in controlling inundation extent, with

these connections typically more accurately represented in higher resolution DEMs such as LIDAR. The next chapter will review and expand upon metrics to quantify river channel-floodplain connectivity. Quantification of this connectivity will be applied across varying scales and locations to determine the varying degrees of river channel-floodplain connectivity.

Chapter 5 Measuring Floodplain Connectivity of DEMs

Paper in Preparation

5.1 Preface

This results chapter consists of a paper currently under preparation for Hydrological Processes. Simulations, analysis, writing and figures were completed by the lead author with advice and commenting from Paul Bates & Jeffrey Neal. The TanDEM-X DEM data and flood model of Ba, Fiji was kindly supplied by Leanne Archer. The MERIT DEM is the work of Dai Yamazaki and colleagues.

5.2 Context

In Chapter 4, the spatial error structure of the MERIT and SRTM DEMs for 20 floodplain locations around the world were calculated by comparing to high-resolution LIDAR data. The MERIT data were consistently more accurate than SRTM based on smaller semi-variogram sill values and larger range values indicating that error is more spatially dependent. From the semi-variograms of spatial error structure, plausible versions of the MERIT and SRTM DEMs were simulated based on an average semi-variogram of all 20 floodplain locations and semi-variograms based on landcover class. Simulated versions of the SRTM and MERIT DEMs were used in flood models of An Giang in the Vietnamese Mekong Delta and the Ba Catchment in Fiji. By using an ensemble of simulated DEMs, the skill of the flood predictions improved, with MERIT DEM simulated using semi-variograms disaggregated by landcover class giving the best predictions. This work in theory allows for plausible versions of MERIT/SRTM floodplains to be simulated so modellers can use an ensemble of DEMs and thus produce probabilistic flood maps based on the uncertainty in topography.

In the simulation process, pixels were altered which either opened or closed flood pathways onto the floodplain. The noisier SRTM DEM underpredicted flooding, with this noise preventing the connection of flood pathways. In turn, the smoother MERIT product performed more similar to the higher resolution LIDAR data, but it was difficult to decipher whether the correct flow pathways were being followed or whether the strong results (particularly for the Ba catchment) were a product of the smoother DEM. This leads to the question of how we can tell whether a DEM is suitable for a flood model and whether it is capturing the correct set of hydraulic processes. Therefore, this chapter sets out to measure floodplain connectivity across a range of DEM products and scales in a bid to determine the suitability of a DEM for capturing flow interactions between rivers and floodplains.

5.3 Introduction

Connectivity is an immensely popular concept in science. At the time of writing, a search on Web of Science of peer-reviewed work with the term connectivity in the title reveals there are almost 27,000 articles. The concept of connectivity traverses disciplines such as neuroscience (Wilkins et al., 2014), ecology (Belisle, 2005), geomorphology (Fryirs et al., 2007) and hydrology (Bracken et al., 2013). Yet it's popularity can also be its downfall, with Michaelides and Chappell (2009) noting that the term suffers from a degree of ambiguity as it is both an everyday word and a technical term. However there is a common theme in work on connectivity – the widespread acknowledgement that connectivity is important and not well understood (Michaelides and Chappell, 2009, Bracken et al., 2013).

The focus of this chapter is river-floodplain connectivity for surface water, and particularly during floods. In this section, an overview of hydrological connectivity is provided before considering previous work on measuring surface river-floodplain connectivity. The section is concluded by providing a definition of surface river-floodplain connectivity and setting out the key questions this chapter aims to address.

5.3.1 Hydrological Connectivity

Hydrologic connectivity is the 'water-mediated transfer of matter, energy, or organisms within or between elements of the hydrologic cycle' (Pringle, 2001) (p981). Yet, despite a

number of review articles, (Bracken and Croke, 2007, Bracken et al., 2013, Covino, 2017, Wohl, 2017, Ali and Roy, 2009, Michaelides and Chappell, 2009, Lexartza-Artza and Wainwright, 2009) there is a lack of consensus on how to define and measure hydrologic connectivity. Difficulties arise as 'connectivity comes in multiple flavours' (Ali and Roy, 2010, Calabrese and Fagan, 2004), and thus can mean different things to different members of the hydrological community. At the most basic level, 'water connects hillslopes to channel networks, streams to lakes, subsurface to surface, land to atmosphere, terrestrial to aquatic, and upstream to downstream' (Covino, 2017) (p.133). So, depending on the aspect of hydrology that is being discussed, connectivity can have very different meanings. Whilst, there has been no one size fits all definition (which is hardly appropriate given the complexity of the subject), Ali and Roy (2009) identified that hydrologic connectivity can be defined within : 1) components of the water cycle; 2) landscape features; 3) spatial patterns of hydrological properties, and 4) flow processes. These definitions are also dependent on scale, with Ali and Roy (2009) further distinguishing between watershed and hillslope scale (Table 5-1). The synthesis of definitions of hydrological connectivity presented by Ali and Roy (2009) has seemed to have gained most traction amongst the community. However, recent reviews by Wohl (2017) and in particular Covino (2017) have changed the way in which definitions are categorized with Covino (2017) identifying five types of hydrologic connection (Hillslope; Hyporheic; Stream-groundwater; Riparian/floodplain and Longitudinal). It remains to be seen whether a general consensus of connectivity can be reached even within the different areas of hydrology with our opinion aligning with that of Bracken et al. (2013) that it is not possible to develop a single overarching definition of hydrologic connectivity.

Hydrologic connectivity can be conceptualized by two main elements identified as static/structural and dynamic/functional connectivity (Bracken and Croke, 2007, Bracken et al., 2013, Turnbull et al., 2008). Structural connectivity refers to the physical adjacency of landscape elements which control material transfer by the medium of water (Bracken et al., 2013, Passalacqua, 2017, Rinderer et al., 2018, Turnbull et al., 2008, Wainwright et al., 2011). So structural connectivity can refer to the spatial contact of channels and hillslopes (Bracken et al., 2013), with this being quantified through indices such as flow length. Functional

connectivity refers how the spatial adjacency interacts with temporally varying factors to control fluxes of water, sediments and solutes (Bracken et al., 2013, Turnbull et al., 2008, Rinderer et al., 2018, Larsen et al., 2012, Lexartza-Artza and Wainwright, 2009, Wainwright et al., 2011). Thus, the concepts of structural and functional connectivity are not isolated from one another as structural connectivity is a constraint on functional connectivity (Rinderer et al., 2018). Bracken et al. (2013) note that functional connectivity should go beyond inferring what is happening between snap-shots and try to determine *why* they are happening. The added complexity of the functional aspects of hydrological connectivity has made it more difficult to measure and quantify (Larsen et al., 2012, Bracken et al., 2013). Fine temporal scales are needed to understand the functional connections, but this is often a nearly impossible task with snap-shots often too sparse to understand the actual processes that are at hand (Bracken et al., 2013, Rinderer et al., 2018). An additional issue with functional connectivity in hydrology is the wide use of the term functional having many connotations and interpretations across the discipline. This led to Bracken et al. (2013) proposing that functional connectivity in relation to hydrology should instead be referred to as process-based connectivity. This change of terminology has so far proved to be difficult to take up as the language of functional connectivity is still deeply ingrained when referring to connectivity in ecology and neuroscience. Understanding these two main elements is a key step in informing management practices and hydrologic predictions (Bracken et al., 2013, Passalacqua, 2017).

Table 5-1 Definitions of hydrological connectivity updated from Ali and Roy (2009)

	Definition	Scale	Reference
Water Cycle	An ecological context to refer to water-mediated transfer of matter, energy and/or organisms within or between elements of the hydrologic cycle.	Watershed	(Pringle, 2003)
Landscape Features	Two fluxes 'connected' if they are in close spatial proximity along the river network ... and refer to 'connectivity' as the state of two or more fluxes being connected. 'Dynamic connectivity' is how the connectivity of fluxes changes in time.	Watershed	(Czuba and Foufoula-Georgiou, 2015)

	Definition	Scale	Reference
	Connectivity defined as the transfer of matter between two different landscape compartments	Watershed	(Wester et al., 2014)
	All the former and subsequent positions and times, associated with the movement of water or sediment passing through a point in the landscape.	Watershed	(Bracken and Croke, 2007)
	Flows of matter and energy (water, nutrients, sediments, heat, etc.) between different landscape components	Watershed	(Tetzlaff et al., 2007)
	The extent to which water and matter that move across the catchment can be stored within or exported out of the catchment	Watershed	(Lane et al., 2004)
	The physical linkage of sediment through the channel system, which is the transfer of sediment from one zone or location to another and the potential for a specific particle to move through the system.	Hillslope	(Hooke, 2003)
	The physical coupling between discrete units of the landscape, notably, upland and riparian zones, and its implication for runoff generation and chemical transport	Hillslope	(Stieglitz et al., 2003)
	The internal linkages between runoff and sediment generation in upper parts of catchments and the receiving waters [...] two types of connectivity: direct connectivity via new channels or gullies, and diffuse connectivity as surface runoff reaches the stream network via overland flow pathways.	Hillslope	(Croke et al., 2005)
Spatial Patterns	Hydrologically relevant spatial patterns of properties (e.g. high permeability) or state variables (e.g. soil moisture) that facilitate flow and transport in a hydrologic system (e.g. an aquifer or watershed)	Watershed Hillslope	(Western et al., 2001)
	Spatially connected features which concentrate flow and reduce travel times.	Watershed Hillslope	(Knudby and Carrera, 2005)
Flow Processes	The condition by which disparate regions on a hillslope are linked via lateral subsurface water flow.	Hillslope	(Hornberger et al., 1994, Creed and Band, 1998)

	Definition	Scale	Reference
	Connection, via the subsurface flow system, between the riparian (near stream) zone and the upland zone (also known as the hillslope) occurs when the water table at the upland-riparian zone interface is above the confining layer.	Hillslope	(Ocampo et al., 2006, Vidon and Hill, 2004)

As noted, hydrologic connectivity is based on physical adjacency (structural connectivity) and time (functional connectivity). Therefore, connections occur via the surface or subsurface in 4 dimensions: the spatial dimensions of lateral, vertical and longitudinal, and the fourth dimension being time (Ward, 1989, Pringle, 2001, Covino, 2017, Amoros and Bornette, 2002). This is schematically represented in Figure 5-1. Scales of spatial connectivity can range from submeter to thousands of kilometers, and temporal scales can range from fractions of seconds to millennia (Ward, 1989, Covino, 2017). Connectivity along the lateral and vertical directions are bidirectional, whereas in the longitudinal direction they are typically unidirectional (with the exception of processes such as the backwater effect). Vertical connectivity occurs between channel-water and subsurface processes, and is very difficult to measure. Lateral connectivity occurs at the surface via overbank and overland flow and at the subsurface.

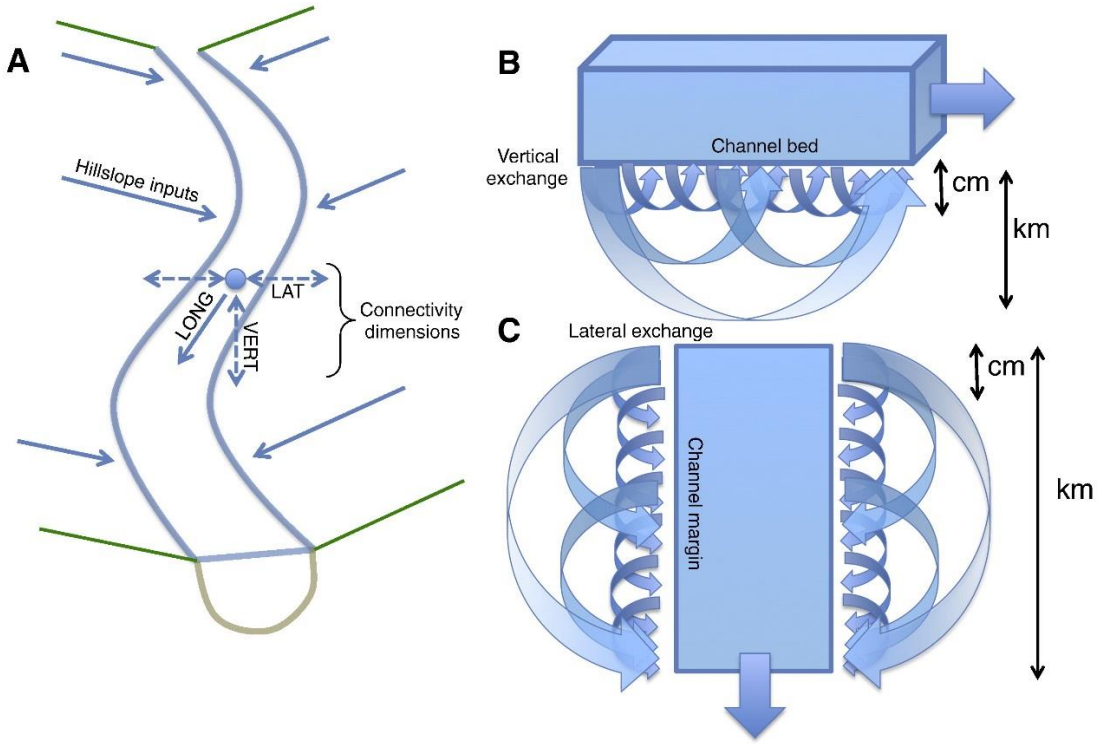

Figure 5-1 Conceptual diagram depicting the dimensionality of hydrologic connectivity. A) 3 spatial dimensions of connectivity with LAT referring to lateral, LONG to longitudinal and VERT to vertical. B) Vertical exchanges. C) Lateral exchanges. Figure from Covino (2017)

The increasing number of articles discussing hydrologic connectivity demonstrates that the field is very much active, with the importance of connectivity being widely recognized (Figure 5-2). Yet some issues remain. This is namely the lack of locations studied (with multi-site/inter-site research being rare), the lack of comparison across spatial and temporal scales and the difficulty in quantification (Michaelides and Chappell, 2009, Bracken et al., 2013, Ali and Roy, 2010, Wohl, 2017).

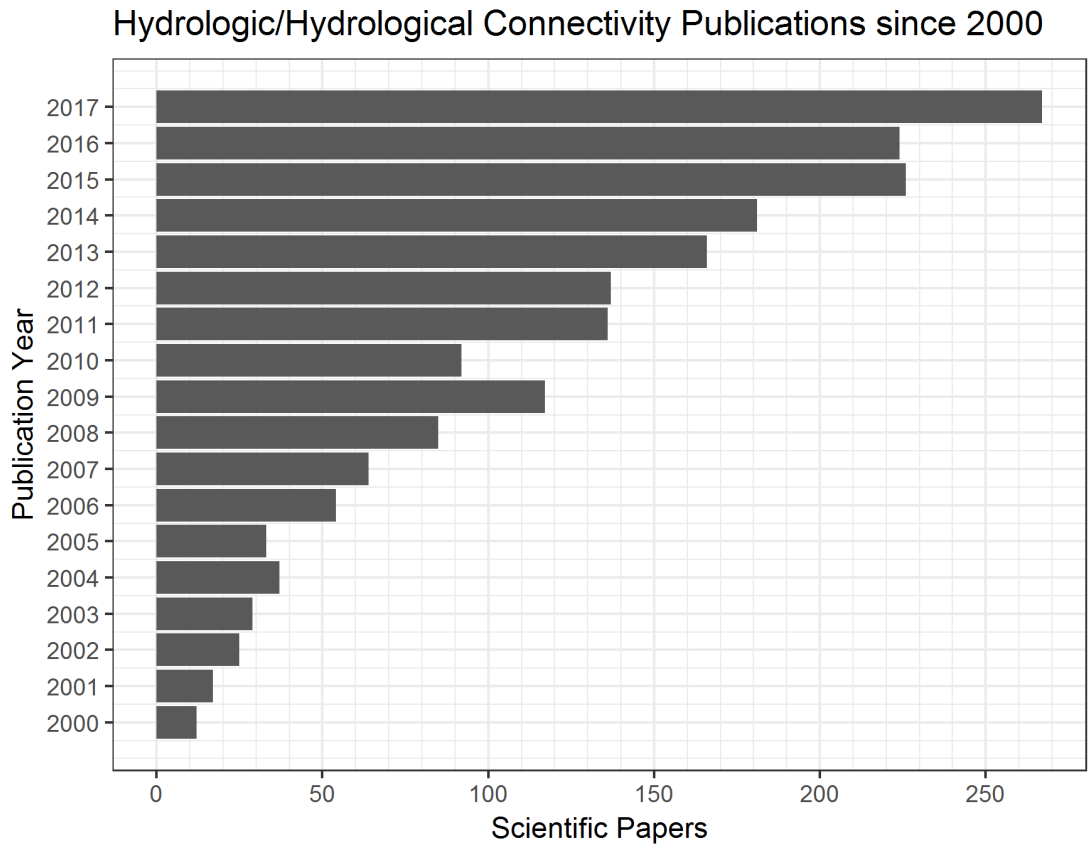

Figure 5-2 Scientific papers where the topic is either 'hydrologic connectivity' or 'hydrological connectivity' during the 2000-2017. Search was carried out on Web of Science. This is an update of a similar analysis in Ali and Roy (2009)

5.3.2 River-Floodplain Connectivity

For the purpose of this chapter, river-floodplain connectivity is defined as the bidirectional interaction of a river and a floodplain along the lateral dimension. Here the lateral dimension refers to overbank and overland flow. This definition also includes interaction between floodplains that may become connected in flood scenarios. Whilst river and floodplains are also connected via the subsurface along the vertical dimension (Malard et al., 2002, Mertes, 1997), this is less significant than lateral connectivity, and not to mention almost impossible to measure at scales larger than the field scale.

Taking a step back, we define a river as a permanent large body of flowing water contained within a channel. Definitions of floodplains are numerous with an early example from Schmudde (1968) defining "The floodplain is defined as the relatively flat alluvial landform

adjacent to the river channel and subject to periodic flooding." Syvitski et al. (2012) later defined a floodplain as "as the relatively flat area surrounding the active river channel that floods during high discharge events." Despite numerous definitions, Strick (2016) notes that floodplains can be essentially described in 3 ways: Hydrologically - next to the river channel, Topographically – a relatively flat area of land that has undergone erosion and deposition by the river channel, and sedimentological - with the presence of alluvial deposits.

The processes of river-floodplain connectivity is more than the simple matter of overtopping river banks (Macklin and Lewin, 2015, Mertes, 1997, Trigg et al., 2012, Tockner et al., 1999, Lewin and Ashworth, 2014b). River-floodplain connectivity is highly complex and is controlled by a number of negative and positive relief forms. Negative relief forms act as mechanisms to connect the river to the floodplain, whilst positive relief forms (e.g. levees) disconnect rivers from their floodplains or can shape the pattern of connectivity. In the field of geomorphology, research on identifying and describing the processes behind these positive and negative relief forms is rich. Whilst the pioneering work of Nanson and Croke (1992) describes floodplain classification based on main channel interaction, the recent work of Lewin and Ashworth (2014b) provides a comprehensive overview of negative relief forms for large river floodplains (and to a lesser extent positive relief forms) based on their extra complexity (termed plurality by (Lewin and Ashworth, 2014b). An overview of the 11 identified negative relief forms is summarized in Table 5-2 . It is out of the scope of this chapter to meander through the raft of geomorphic literature describing the processes and relief forms associated with river-floodplain connectivity, but we feel it is beneficial to (very) briefly acknowledge some of these processes. We would urge interested readers to consult the literature cited here to further their understanding. Note that only lateral river-floodplain connectivity is being considered.

Table 5-2 Negative relief forms at the meso- and macro-scale, which are defined as ranging from metres to kilometers by Lewin and Ashworth (2014b). By the scale definitions in this chapter these features traverse all scales. Figure adapted from Lewin and Ashworth (2014b)

Genetic Zone	Negative Relief Form
Rheic	Main Channels; Accessory through channels; Tributary channels
Transitional	Channel margin slackwater zones; bar-shelter backwaters; contiguous channel remnants; Tie Channels; Internal drainage channel networks
Perirheic	Cutoff paleochannel segments; accretionary swales and irregular unsedimented voids; large-scale flood basins occluded by channel-belt aggradation

Negative relief forms are created and/or maintained by active erosion, insufficient sediment supply for infilling and/or bounding by positive relief sediment bodies (Lewin and Ashworth, 2014a, Lewin and Ashworth, 2014b). Further active deposition across floodplains, termed as spillage sedimentation, are associated with associated negative relief forms (Lewin et al., 2017). For large rivers, Lewin and Ashworth (2014b) split negative relief forms into 3 genetic zones: rheic, transitional, perirheic. As the river stage rises, a river first connects to the floodplain via negative relief forms in the rheic zone. These are in the form of main channels, accessory through channels and tributary channels. In this rheic zone, these channels are geomorphologically active and are dominated by flowing surface water. With further rising of river stage and initial river-connectivity via the negative relief in the rheic zone, negative relief forms in the transitional zone come into play. Negative relief forms in the transitional zone are geomorphically transitional but hydrologically connected and include features such as slackwater zones, bar-shelter backwaters and contiguous paleochannels. In extreme overbank flow, negative relief forms in the perirheic zone are activated. Normally, these negative relief forms in the perirheic zone are geomorphologically and hydrologically disconnected and include forms such as cutoff paleochannels, accretionary swales and cutoff flood basins. Patterns of river-floodplain connectivity also depend on antecedent conditions - or whether the floodplain is dry or wet (Lewin and Ashworth (2014b), their Figure 4). In contrast, positive relief forms are formed by sedimentation, and also act as controls on river-floodplain connectivity. Examples of positive relief forms include side and point bars, levees, splays and channel plugs, overbank sedimentation, scrolls and alluvial terraces (see Lewin and Ashworth (2014b) their Table 2

for a more comprehensive overview). Perhaps the easiest positive relief form to conceptualise as acting as a control of floodplain are levees, especially due their prevalence as a manmade feature (Tockner and Stanford, 2002). Facilitated by the recent wider availability of DEM's, remote sensing imagery and improved dating of sediments, a number of studies have identified the relief forms involved across a number of floodplains including (but by no means limited to) the Amazon (Trigg et al., 2012, Rudorff et al., 2014), Rio Parana (Lewin and Ashworth, 2014a) and the Mississippi (Strick et al., 2018). In another study, Scown et al. (2016) proposes an index to calculate floodplain landscape complexity, with an application to 8 floodplains.

As the river recedes, water on the floodplain reduces due to return flow back to the main channel, evaporation and infiltration. Hence, the exchange of water between a river and floodplain is bidirectional and thus this is included in our definition of river-floodplain connectivity. The effects of floodplain topography is key in controlling the pattern of inundation, with Macklin and Lewin (2015) noting that only a large and long lasting flood can drown out the effects of floodplain topography. Therefore, river-floodplain connectivity varies with flow return period.

The connectivity of river and floodplains is pivotal to the functioning of the floodplain system, with this connectivity having profound ecological importance. The flood pulse concept pioneered by Junk et al. (1989) and extended by Tockner et al. (2000) takes the view that rivers and their floodplains are integrated components of a single dynamic system, with habitat productivity a product of interacting water sources and different pathways. In the flood pulse concept, Junk et al. (1989) uses the analogy of the river as a highway with biota needing to periodically leave (i.e. leave the river for the floodplain) for sustenance. Floodplains also have a striking cultural and economic importance, with early civilizations learning to cultivate the fertile floodplains in order to prosper (Tockner and Stanford, 2002). For example, early civilizations along the Huang He, Indus, Nile, Tigris and Euphrates rivers were almost entirely dependent on river-floodplain interactions (see Macklin and Lewin (2015) for a comprehensive review). Today, floodplains still serve as focal points for agriculture and urban development. Increasingly, and despite the recognized benefits of river-floodplain connectivity, connections between the river and floodplains are becoming

severed (Covino, 2017, Tockner and Stanford, 2002, Kondolf et al., 2006, Ward and Stanford, 1995, Hupp et al., 2009). Flow regulation in the form of dams, reservoirs and diversions have made flows of a magnitude to connect to the floodplain increasingly unlikely. In addition, levees and channelization has constrained rivers in a bid to protect from flooding. Covino (2017) note that decreased flow variability and channelization create a positive feedback, with the likelihood of the river reconnecting to the floodplain becoming increasingly improbable. Reduced river-floodplain connectivity is prevalent across scales, with small rivers also being affected (i.e. channelization to create mills).

Tockner & Stanford (2002) estimated that up to 90% of North American and European floodplains are 'cultivated' and thus functionally extinct. More recently, calls have been made to reconnect rivers to floodplains (Opperman et al., 2009, Friberg et al., 2016), with cited benefits including increased ecological services and resilience to climate change, as well as reduced flood risk. Additionally, research has promoted the idea of considering floodplains as human-water systems by considering the links between hydrological and social processes (Di Baldassarre et al., 2013, Zischg, 2018). These ideas have been translated into management practices such as natural flood management (Lane, 2017, SEPA, 2011), 'room for the river' (Rijke et al., 2012, Zevenbergen et al., 2013) and eco-engineering decision scaling (Poff et al., 2016). However, a crucial prerequisite of the aforementioned management strategies is an understanding of river-floodplain connectivity. Currently there is no accepted way of quantifying this connectivity objectively, with previous attempts focusing on single scales and/or locations (see 5.3.3).

5.3.3 Current state of measuring river-floodplain connectivity

Despite the accepted importance of river-floodplain connectivity, there is a lack of studies that quantify this connectivity. Indeed, most studies rely on qualitative analysis. Wohl (2017) notes that many aspects of connectivity are 'intuitively obvious once they have been identified'. We identify 3 categories of river-floodplain connectivity measurements based on 1) Remote Sensing, 2) Hydrodynamic models and 3) Topography.

Recent advances and the wider availability of remote sensing datasets has provided opportunities to assess river-floodplain connectivity. For the middle Amazon, Trigg et al.

(2012) used a mosaic of Landsat imagery supplemented with field data to delineate and quantify the spatial characteristics of river-floodplain connectivity and relate these to floodplain hydrologic units. They estimated that 96% of floodplain channels identified in their analyses were not well, if at all, represented in the 90m SRTM DEM upon which many geoscience models rely. Using a geostastical connectivity approach, surface water connectivity for the 2011 Bangkok floods was quantified using a time series of MODIS (Moderate Resolution Imaging Spectroradiometer) by Trigg et al. (2013). The authors developed and utilized a gap-filling approach to fill missing data, resulting in quantification of flooded area and connectivity function curves (results were presented along the two orthogonals (North-South and West-East) but the calculation was also possible along the two diagonals (NW-SE and NE-SW) as either D4 or D8 connectivity can be implemented). The accompanying Matlab code is available online. Ward et al. (2013a) used MODIS and Landsat to map floodplain extent and dynamics in an Australian savanna catchment. More recently, MODIS & PALSAR have been used to map river-floodplain connectivity in the lower Amazon (Park and Latrubesse, 2017). Whilst not actively marketed as a river-floodplain connectivity product, the global water mask product (particularly occurrence, change, seasonality and recurrence) of Pekel et al. (2016) could in theory be used to map water on floodplains and potentially utilize techniques such as that of Trigg et al. (2013) to quantify connectivity. The remote sensing approach has the benefit of being able to include the temporal dimension but can suffer from missing and/or unobservable data.

The second category of techniques concerns using hydrodynamic models. Hydrodynamic models have the advantage over more simple topography based techniques in that they also consider other factors such as slope, vegetation and surface roughness in addition to relative elevation, thus making representations more realistic. However, this comes at a cost of setting up the model which can be time-consuming and computationally expensive. Furthermore, results are heavily dependent on the calibration of multiple parameters creating uncertainty in the results. Lastly, hydrodynamic models do not explicitly quantify the connectivity but instead provide a spatial representation (Zhao et al., 2017). Wetland connectivity for fish movement was estimated for the Tully-Murray floodplain in Australia using the 2D MIKE21 hydrodynamic model and a 30 m DEM supplemented with high-

resolution LIDAR data (Karim et al., 2012). Connectivity between the river and wetlands was assessed by applying a water threshold, with connectivity adjudged to be when a wetland received overbank flow and became disconnected when water receded below the bank level. From this, the duration of connectivity could be calculated which has important implications for fish ecology. The same authors later included climate change implementations as well as MODIS data to calibrate the model to assess river-wetland connectivity (Karim et al., 2016). Using TUFLOW, Croke et al. (2013) assessed the hydrologic and sediment connectivity during a large flood event, with their analysis restricted to the identification of nine reaches that demonstrate channel-floodplain connectivity without any further quantification (except sediment budgets). The biggest advancement in using hydrodynamic models for floodplain connectivity is the work of Zhao et al. (2017). They apply and compare three connectivity algorithms (classic nearest neighbor search (NNS), progressive nearest neighbor search (PNNS) and progressive iterative nearest neighbor search (PiNNS)) to flood extents of the Flinders and Norman rivers in Australia simulated using the MIKE21 hydrodynamic model. The PNNS and PiNNS algorithms successfully captured the spatial heterogeneity and continuity of connectivity and were successfully used to trace the connected path from a critical river section to the inundated floodplain cell. This work is useful as it identifies not only where the floodwater originates from but how it flows to selected parts of the floodplain, with the PiNNS algorithm demonstrating the most promising results. The authors note that when applying this data-driven method it is important to first validate the hydrodynamic model and simulation data to give sensible results, and that such a data-driven method cannot explain the processes that generate the data. The algorithms proposed by Zhao et al. (2017) have the potential to be used with remote sensing as they rely on binary wet/dry maps, but to date this has not been carried out.

The third category of river-floodplain connectivity quantification is topography based using DEMs. Current work on using DEMs for river-floodplain interaction has not engaged in the connectivity discourse but has instead focused on detecting flood-prone areas. Nevertheless, the processes go hand in hand, with these topography based methods having potential to analyse river-floodplain connectivity. Notwithstanding, the current methods capture more

the spatial extent of river-floodplain interaction as opposed to any quantification per se. Manfreda et al. (2011) proposed a modified version of the topographic index developed by Beven and Kirkby (1979) derived from a DEM to delineate flood prone areas. They compared various DEM products at different resolutions and found results similar to flood inundation maps obtained by hydraulic simulations. In Manfreda et al. (2014), the modified topographic index method of Manfreda et al. (2011) was compared to the linear binary classifier method of Degiorgis et al. (2012) (also requires flood hazard maps), and the hydrogeomorphic method of Nardi et al. (2006) (requires design peak flood at outlet basin). Samela et al. (2015) applied the linear classifier method to several ungauged catchments in Africa. Most recently, Samela et al. (2017), Samela et al. (2018) proposed the Geomorphic Flood Index which requires a DEM and a detailed flood map that should cover at least 2% of the domain. Therefore, only the method of Manfreda et al. (2011) is based solely on a DEM and does little to quantify river-floodplain connectivity.

Table 5-3 Methods to measure river-floodplain connectivity split into 3 categories

Category	Method Description	Reference
Remote Sensing	Landsat Imagery and field data used for river-floodplain connectivity of the middle Amazon	Trigg et al. (2012)
	Geostatistical connectivity method applied to MODIS imagery of 2011 Bangkok Floods	Trigg et al. (2013)
	Landsat & MODIS in an Australian Savanna catchment	Ward et al. (2013a)
	Surface water detection at 30m for last 32 years. Not directly related to river-floodplain connectivity	Pekel et al. (2016)
	MODIS and PALSAR for lower Amazon	Park and Latrubesse (2017)
Hydrodynamic model	2D MIKE hydrodynamic model of Tully Murray basin to estimate river-wetland connectivity	Karim et al. (2012)

Category	Method Description	Reference
	TUFLOW hydrodynamic model of Lockyer Creek identifying inundation and connected reaches	Croke et al. (2013)
	2D MIKE hydrodynamic model calibrated with MODIS data with climate change scenarios to assess river wetland connectivity	Karim et al. (2016)
	Three connectivity algorithms applied to flood extent maps from a 2D MIKE 21 model in Australia. Shows origin and connectivity of inundated floodplain cell	Zhao et al. (2017)
Topography	Modified Topographic Index	Manfreda et al. (2011)
	Linear classification scheme Also needs a flood hazard map layer	Degiorgis et al. (2012)
	Geomorphic Flood Index. Also needs a flood hazard map layer	Samela et al. (2017)

5.3.3.1 Limitations of current river-floodplain connectivity methods

The aforementioned methods (Table 5-3) have a number of limitations. Most (with the exception of Trigg et al. (2013) and Zhao et al. (2017)) do not quantify the connectivity between the river and the floodplain. Instead, most methods delineate the river-floodplain connectivity and infer the origins and pathways of connections. Remotely sensed based techniques have the benefit of being relatively easy to set up and implement compared to building a hydrodynamic model, but can suffer from missing data (unobservable water) and gaps in the temporal record. Methods based on hydrodynamic models can be potentially temporally rich, but they do rely on the time consuming calibration, potentially long computation times and the need for validation. Topography based methods have not been readily considered to measure river-floodplain connectivity, perhaps partially because they cannot measure the temporal dimension. Yet such topography based methods have the potential to be used to assess the quality of a DEM in relation to being able to represent river-floodplain connectivity. As noted in the previous chapter, the quality of the DEM is of

key importance to the quality of flood model predictions (Horritt and Bates, 2001a, Yamazaki et al., 2012) with the SRTM DEM that is typically favoured for global flood models and flood models in data-sparse areas being unable to represent floodplain channels that are crucial for river-floodplain connectivity (Trigg et al., 2012). Currently there is no method to quantify river-floodplain connectivity using just a DEM. Thus far all topography-based methods have focused solely on delineating flood prone areas. Furthermore, the methods in Table 5-3 only consider a single location at a time, and except for Manfreda et al. (2011) do not consider different scales. Whilst not focused on river-floodplain connectivity, several studies have found that DEM resolution is important for hydraulic connectivity (Habtezion et al., 2016, López-Vicente and Álvarez, 2018), thus the effect of DEM resolution on connectivity should be investigated within the context of river-floodplain connectivity. This deficiency of not investigating multiple locations or scales aligns with the observations of Michaelides and Chappell (2009).

5.3.4 Research Questions

In light of the identified research gaps discussed throughout this section, the following research questions are pursued:

- How does floodplain connectivity differ across scales and DEM products?
- Is the accurate representation of floodplain connectivity more important for smaller floods than larger floods?
- What is more important in selecting a DEM for a flood model - RMSE or floodplain connectivity?
- Can a river-floodplain connectivity metric be created to describe DEM products, and can this be used as a guide in assessing the suitability of a DEM to accurately represent flooding?

To answer the above research questions, a novel method based on connected component labelling and landscape patch statistics to quantify river-floodplain connectivity across a range of scales and DEM products is developed. The method is applied to a case study of the

Ba catchment in Fiji using 15 DEM products as well as DEM's simulated using the procedure documented in Chapter 4.

5.4 Study Site & Data

The study site was selected based on data availability. As the research questions aim to quantify river-floodplain connectivity across a range of scales and DEM products, the Ba catchment in Fiji was chosen, primarily as the new Tan-DEM-X DEM product (Rizzoli et al., 2017) was available for this site. Analysis of the Tan-DEM-X product is in its infancy, thus it is interesting to include it in the analysis. Needless to say, the method proposed here can be used for any location to assess river-floodplain connectivity.

5.4.1 Study Site - Ba Catchment, Fiji

The Ba catchment is located on the island of Viti Levu which is the main island of the upper-middle income small island developing state of Fiji in the South pacific. The catchment experiences a tropical maritime climate driven by trade winds, the South Pacific Convergence Zone and the El Niño Southern Oscillation, with 70% of annual rainfall falling between November and April during the cyclone season (Mataki et al., 2006). A number of recent flooding events (January 2009; 2012; March 2012; April 2018) have caused widespread damage, with cyclone Winston (the strongest cyclone ever recorded in the South Pacific) affecting 62% of the population of Fiji with damages equivalent to 20% of Fiji's GDP. The Ba catchment was chosen for this study because it was one of the worst affected during the aforementioned flood events. In particular, the main floodplain area of the Ba catchment area was chosen which contains a river reach of 22 km. The main urban centre in the Ba floodplain is Ba Town, which in 2007 had a population of 18,526 (Fiji Bureau of Fiji Bureau of Statistics, 2018). The floodplain is dominated by cropland (63.85%:Fiji Bureau of Fiji Bureau of Statistics (2010)). Using records from Rarawai Sugar Mill, Yeo (2015) described 32 floods that occurred in the Ba floodplain between 1892 to 2014. Thus flooding occurred on average every 3.8 years. This frequent flooding suggests a relatively strong river-floodplain connectivity and therefore make the study site of interest.

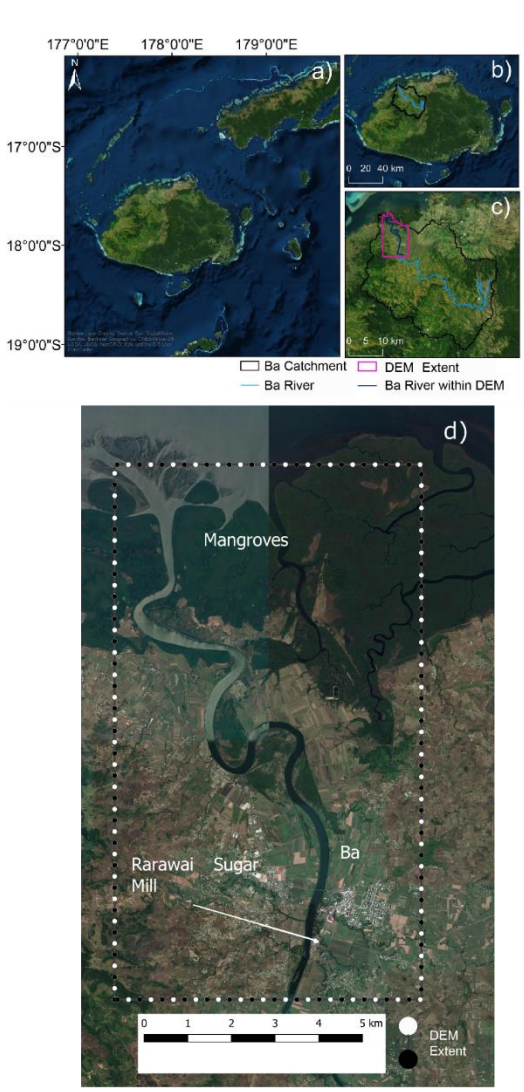

Figure 5-3 Map of the Study Site a) Map of Fiji b)Map of Ba catchment on positioned on the main island of Viti Levu c) DEM extent positioned within the Ba catchment d) DEM extent of Ba catchment floodplain in more detail. Adapted from (Archer et al., 2018)

5.4.2 Data

5.4.2.1 DEM Data

For the Ba catchment a total of 5 DEM products were used - Advanced Land Observing Satellite (ALOS) AW3D30 (Tadono et al., 2014, Takaku and Tadono, 2017); Light Detection & Ranging (LIDAR); Multi Error Removed Improved Terrain (MERIT) (Yamazaki et al., 2017); Shuttle Radar Topography Mission CGIAR-CSI Version 4 (Jarvis et al., 2008); TanDEM-X (Rizzoli et al., 2017, Krieger et al., 2007). Other DEMs are available but were not selected based on 1) having worse reported vertical accuracy and resolution and thus being no

longer favoured (e.g. Advanced Spaceborne Thermal Emission and Reflection Radiometer (ASTER) (Abrams, 2000) and ACE GDEM (Berry et al., 2000)), 2) being expensive to obtain (e.g. Nextmap World10™, World30™ and Airbus WorldDEM™), 3) not being readily accessible despite being free for research purposes (e.g CoastalDEM (Kulp and Strauss, 2018) or a vegetation error removed version of SRTM (Zhao et al., 2018)). Two of the DEM products are Digital Surface Models (DSM) (ALOS AW3D30 & TanDEM-X). A digital terrain version (DTM) of TanDEM-X was processed using a combination of image classification of the Amplitude Map and Progressive Morphological Filtering (AMP/PMF) as described in Archer et al. (2018). This particular image processing method was chosen based on creating the most accurate DEM, with the method and results presented in Archer et al. (2018). Additional coarser DEMs of LIDAR, TanDEM-X, ALOS AD3D30 and MERIT were created by taking an average of the aggregated pixels. Finally, 2500 versions of the MERIT DEM were simulated using semi-variograms by landcover class as per the method set out in the previous chapter.

Table 5-4 Summary of DEMs used in this study

DEM	Resolutions	Acquisition	Reported vertical accuracy
LIDAR	5m; 10m; 30m; 45m; 90m	2012	73.6mm (Thomas, 2012)
TanDEM-X DSM	12m; 90m	2010-2015	<2m for low slope areas (<20%) (Wessel et al., 2018)
TanDEM-X DTM	12m; 90m	2010-2015	Unknown
AW3D30 DSM	30m; 90m	2006-2011	2.6m in 'plains' (Hu et al., 2017)
MERIT	90m; 180m; 270m	2000	58% <2m (Yamazaki et al., 2017)
SRTM CGIAR Version 4.1	90m	2000	6.2m for islands (Farr et al., 2007); 5-10m Solomon Islands (Albert et al., 2013)

DEM	Resolutions	Acquisition	Reported vertical accuracy
MERIT DEM simulated by semi-variograms by landcover class	90m	2000	Semi-variogram dependent

5.5 Methodology

In this section, the justification of the selection of the connected component labelling method is provided as well as some background on the method. After that the workflow of the method developed in this chapter is presented as well as information on landscape statistics.

5.5.1 Generic Properties of Required Method

To quantify river-floodplain connectivity, a method is needed that recognizes connectivity of adjoining pixels and groups adjoining pixels into patches. In turn, these patches then need to be quantified using landscape statistics. The method should be computationally efficient to allow for a range of water height scenarios (i.e. different return flows). Moreover, the method should be simple enough to not have to rely on outputs from other models; such as the hydrodynamic models (Karim et al., 2016; Zhao et al 2018) or flood maps (Samela et al., 2017) or processing remotely sensed data (Trigg et al., 2013). No current method that assesses river-floodplain connectivity adheres to these requirements. As a result, the field of image classification is explored, with the connected component labeling algorithm subsequently chosen as it meets all the aforementioned requirements.

5.5.2 Connected Component Labelling

Connected component labelling is a processing procedure for assigning a unique label to each object (set of connected pixels) in a binary image (He et al., 2017, Wu et al., 2009). Labelling is required when a computer needs to recognize objects and is required in almost all image based applications such as fingerprint identification, character recognition, automated inspection, target recognition, face recognition, medical image analysis and computer aided diagnosis (He et al., 2009). However, to the best of the authors' knowledge

connected component labelling in the geosciences is rare, with the only example being the detection of atmospheric rivers (Byna et al., 2011).

Since the inception of the idea in the 1960s (Rosenfield and Pfaltz, 1966), various algorithms have been proposed, with their use dependent on computer architecture and data structure. A timeline of connected component labelling algorithms split into 5 classes (multi-scan, two-scan, contour-tracing, parallel and light speed) is provided in Figure 5-4. For the most recent comprehensive review of the state-of-the-art in connected component labelling algorithms we refer the reader to He et al. (2017). For this study a connected component labeling algorithm that works on normal computers and for 2D images is all that is required.

To implement connected component labelling a binary image is first needed. A binary image is thus first created by thresholding each pixel based on a threshold value. This results in a binary image, with foreground pixels (called object pixels in the connected component labelling literature and denoted by grey pixel shading in the subsequent diagrams) and background pixels (denoted as white pixels in subsequent diagrams). Object pixels have a value of 1, and background pixels have a value of 0. Object pixels in a 2D image can be connected to 4 neighbours (D4 connectivity) or 8 neighbours (D8 connectivity) (see Figure 5-5 for reference). Once object and background pixels have been identified (Figure 5-6, a) and the connectivity neighbourhood defined, the connected component labeling problem assigns each object pixel a label, with each connected object pixel assigned the same label (Figure 5-6, b&c). Each unique label is termed an object. Then each object is extracted by its label and landscape statistics such as area, perimeter, shape index etc. subsequently calculated.

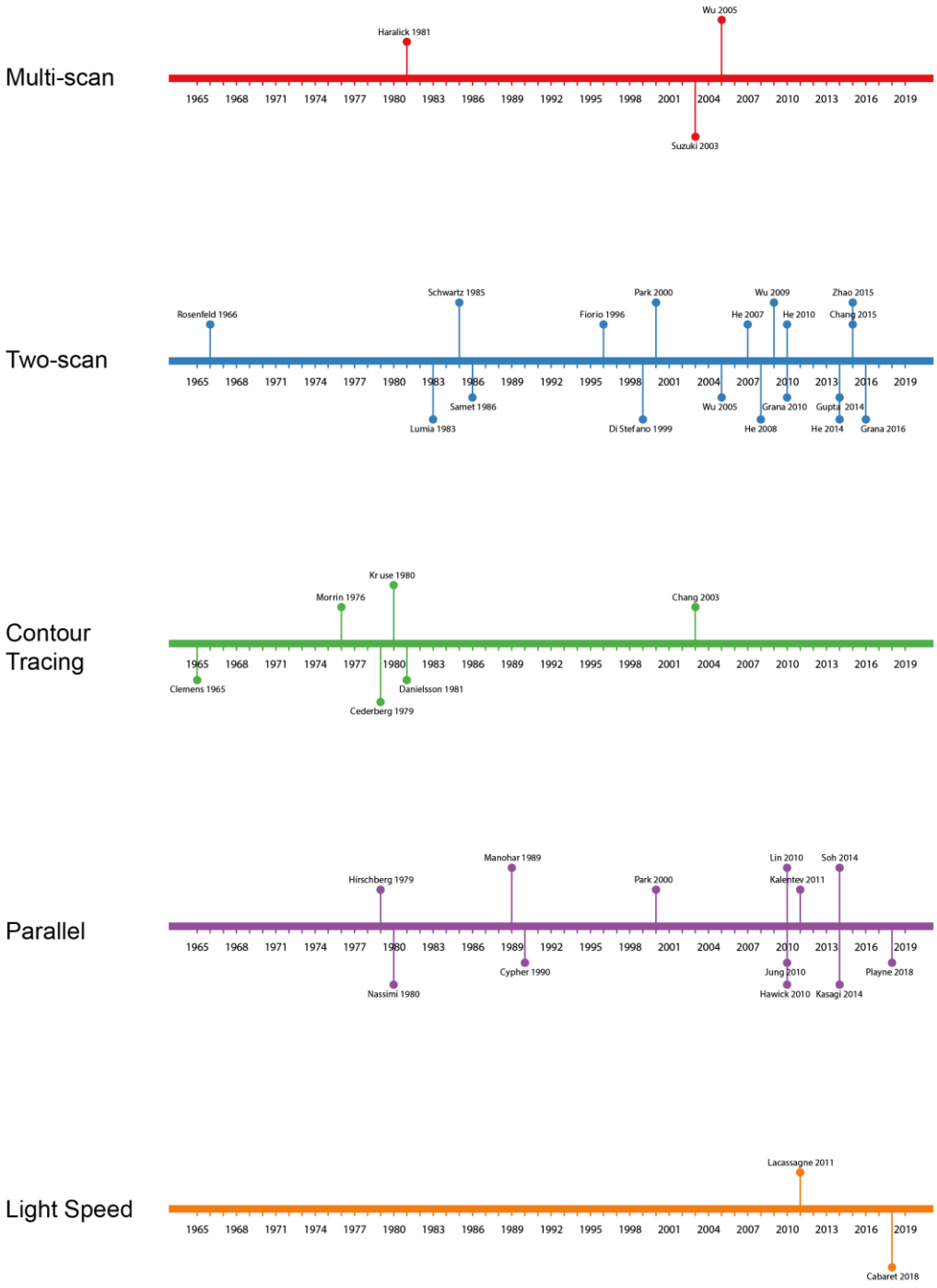

Figure 5-4 Timeline showing the evolution of connected component labelling algorithms divided into multi-scan, two-scan, contour tracing, parallel and light speed. Only first author name shown. Updated and reimagined from Grana et al. (2010)

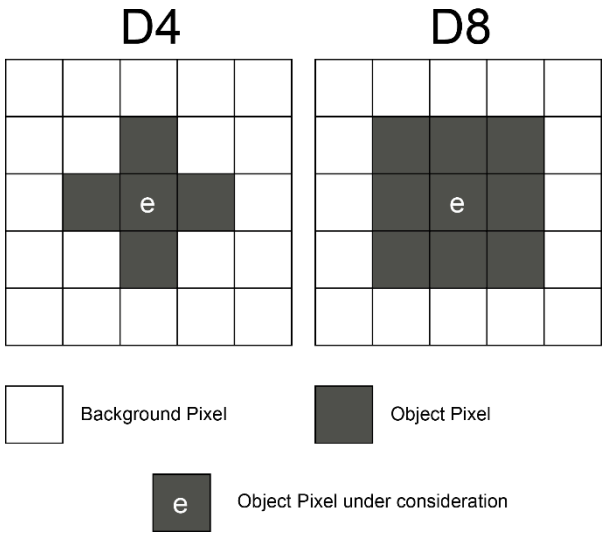

Figure 5-5 Types of connectivity. D4 refers to 4 neighbours. D8 refers to 8 neighbours

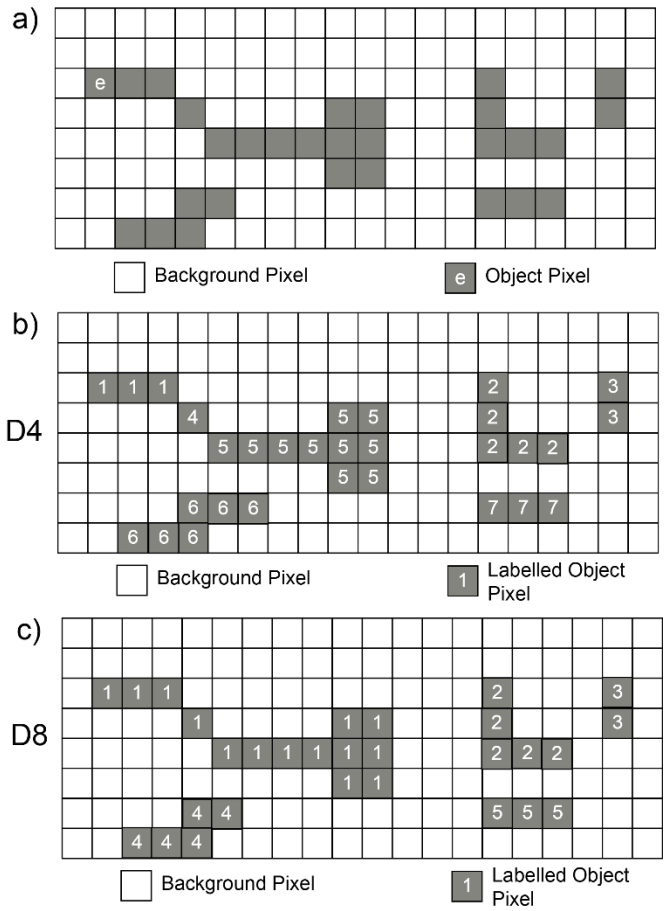

Figure 5-6 8 Connected component labelling for 4 pixel neighbourhood (D4) and 8 pixel neighbourhood (D8). a) Binary image. b) Labelling of Connected component considering a 4 pixel neighbourhood (D4) c) Labelling of Connected component considering a 8 pixel neighbourhood (D8)

For our analysis, the `connectedComponents` function from the Open Source Computer Vision Library (OpenCV) version 3.4.1 was used. Originally written in C++, with interfaces now in Python, Java and MATLAB, the library has over 2500 optimized algorithms. The `connectedComponents` function currently has the functionality of 2 connected component algorithms – Scan plus Array-based Union-Find (SAUF) (Wu et al., 2009) and Block-Based Decision Tree Table (BBDT) (Grana et al., 2010). Both of these algorithms are known as Two-scan algorithms and are parallelized, with the default settings using SAUF for D4 connectivity and BBDT for 8 way connectivity. These algorithms were chosen as the most efficient by the authors of OpenCV. Studies have assessed the performance of various connected component labeling algorithms, such as the Yet Another Connected Components Labelling Benchmark (YACCLAB) (Grana et al 2016), but found little performance difference for 2D images of the complexity of a DEM. Therefore, it was not deemed worthwhile to code additional algorithms for performance testing, especially as the development of OpenCV is so mature.

Two-scan algorithms work as the name suggests by scanning the image twice. Two scan algorithms consist of 4 phases: 1) Provisional label assigning; 2) equivalent label recording; 3) label-equivalence resolving and finally 4) label replacing (He et al., 2017). For the SAUF algorithm a forward scan mask is applied with *e* being the current pixel (Figure 5-7, a), with optimizisation coming through the use of decision trees (Figure 5-7, b,c) to reduce the number of pixels assessed. An efficient union-find-tree strategy, which is 4x quicker than other union-find algorithms, replaces labels on the second scan (Wu et al., 2009). The BBDT algorithm (Grana et al., 2010) is a block based two scan algorithm. A block is a set of 2x2 pixels. A block is considered an object block if it contains 1 or more object pixels. Otherwise, if the block contains only background pixels it is considered a background block. Object pixels in the same object block must belong to the same object and are thus assigned the same label in the first scan. The mask used for the BBDT algorithm considers 20 pixels – or 5 blocks of 4 (Figure 5-8, a). Note that the shape of the mask is the same as the forward scan mask in (Figure 5-7, a). Object block labels are then used for final label assignment in the second scan. An improved block based algorithm was proposed by Chang et al. (2015) but has not yet been coded in OpenCV. Yet the performance gains of some of the more recent

algorithms are negligible for images of the complexity of DEMs, so it was deemed not worthwhile to code these in an adapted version of OpenCV.

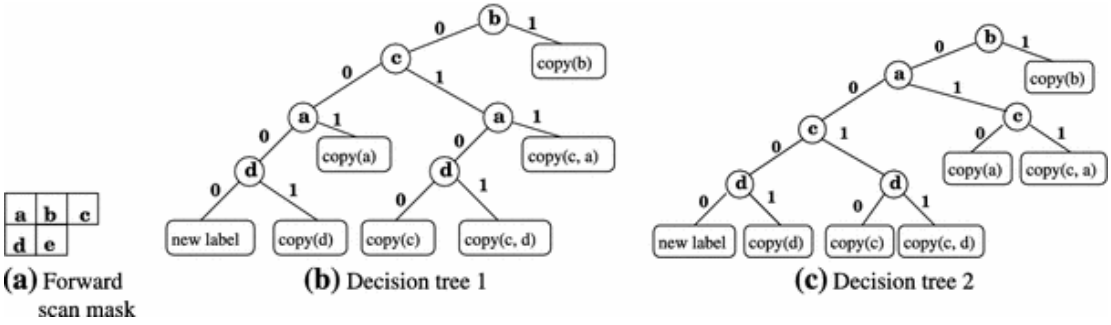

Figure 5-7 SAUF algorithm decision trees used for D8 connectivity. a) Forward Scan mask b) Decision Tree 1 c) Decision Tree 2. Figure from Wu et al. (2009)

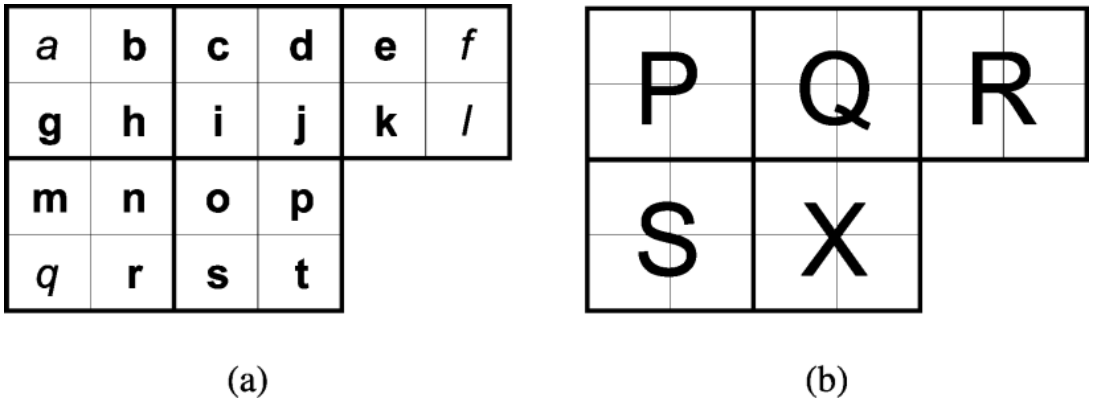

Figure 5-8 Mask for Block Based Decision-Tree Table (BBDT). An area of 2x2 pixels are called a block. a) Identifiers of each pixel considered in the mask (a,f,l and q are not used). B) Block identifiers with X the block under consideration. Figure from Grana et al. (2010)

The `reticulate` package is used to import the Python modules of OpenCV into R. The `connectedComponent` function was tested against various connected component labelling functions including the `clump` function of the raster package in R (Hijmans et al., 2017), `floodfill` from OpenCV, `ConnectedComponents with Stats` from OpenCV, and the `label` function from scipy (Figure 5-9). Performance was assessed for a 79x139 pixel image, with the `connectedComponents` function of OpenCV being the fastest, with performance an order of magnitude quicker than the clump function in raster. Performance advantages increased with image size.

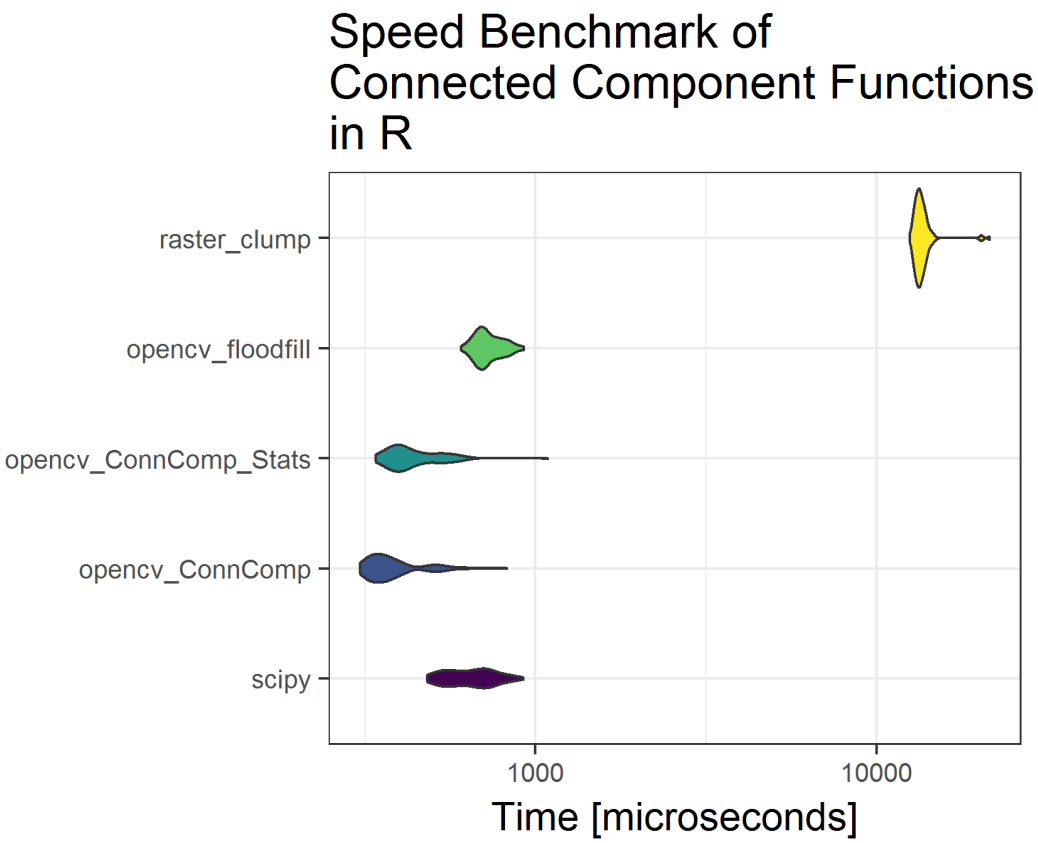

Figure 5-9 Speed Benchmark of Connected Component Functions in R for a 79x138 pixel image. Raster_clump refers to the clump function in the raster package (Hijmans et al., 2017); opencv_floodfill is the `floodfill` function in OpenCV; opencv_ConnComp_Stats is the `connectedComponents` function in OpenCV with very basic statistics; opencv_ConnComp is the `connectedComponents` function in OpenCV; `scipy` is the label function from scipy

Next, how a connected component labelling algorithm can be applied to river-floodplain connectivity is explained. Considering our definition of river-floodplain connectivity outlined in 5.3.2, only lateral connectivity is examined. Therefore, for the river and floodplain to become connected the elevation of the water surface height of the river must be greater than the adjacent river bank pixel. When this is the case, the bank pixel is 'breached' and thus the barrier prohibiting river-floodplain connectivity is overcome. Accordingly, the river and bank pixels must be identified (Figure 5-10, a). In this work, water extent mask of the global surface water dataset of Pekel et al. (2016) is used to identify river pixels. This water extent dataset is based on Landsat imagery and thus has a resolution of 30m. To align with DEM resolution, the water mask is resampled using bilinear interpolation to the

resolution of the DEM. Next, bank pixels are identified using the boundaries function in the raster package in R (Hijmans et al., 2017). Heights of the bank pixels are also extracted.

The next important step is identifying which bank pixels are breached at a selected water level. As a consequence, an estimate of the water surface elevation of each river pixel is needed. First the river was delineated using the water extent layer from the global surface water dataset of Pekel et al. (2016). As no gauges are available for the chosen site, river water surface elevation is estimated by first selecting the most downstream bank pixel and the most upstream bank pixel and delineating a profile along all bank pixels between these two points. Then a gradient was calculated along this profile of bank elevations by fitting a simple linear model. This gradient was then applied as a water surface height with the assumption, following Archer et al. (2018), that the most downstream pixel where the river discharges to the ocean has a water elevation of 0 m. By using a smooth gradient as estimated by the linear model, the water surface height also had a smooth, realistic gradient. Whilst an approximation, this assumption is reasonable as a first order solution as sea-level is approximately equal to 0 m in a DEM. When available, ICESat measured water surface heights from the dataset of O'Loughlin et al. (2016a) could be used to interpolate the river water surface, but one should be careful when using this dataset as measurements are taken across different times of year. The ICESat-derived inland water surface spot height database has over 585,000 unique locations measured from 2003 to 2009 with a reported RMSE value of 0.259 m. However, spot heights are measured for rivers greater than 3 arc seconds (~90 m), thus smaller rivers, such as the channel main stem in the Ba catchment, are not covered. Nevertheless, the database provides a useful resource in estimating water surface heights in rivers, especially when there is a lack of gauge data that can be used as a reference for the estimates. In the end, whatever method is used, each river pixel must have a water surface height elevation. The water surface elevation estimate for Ba is taken as a baseline, or average. Elevations are then added based on a water surface height scenario. In this case, incremented height increases of 0.25m up to a maximum of 4m are used. Therefore, 16 water surface height scenarios are analysed, with the maximum water surface height of the river being 4m above our baseline scenario. If a flood frequency analysis were available these water surface height scenarios could be aligned to flood return periods. Now that the water

surface height has been estimated for the river, breached bank pixels can be identified by comparing the elevation of the bank pixel to the adjacent river water surface height. When the river water surface height is greater than the bank pixel elevation it can be considered to be breached. To minimize the number of breached bank pixels to be analysed, an extra condition is added in that to be considered a breached bank pixel a neighboring pixel must be of the same height or less than the river water pixel height. In this way, breached bank pixels that are not connected to any other floodplain pixel are excluded.

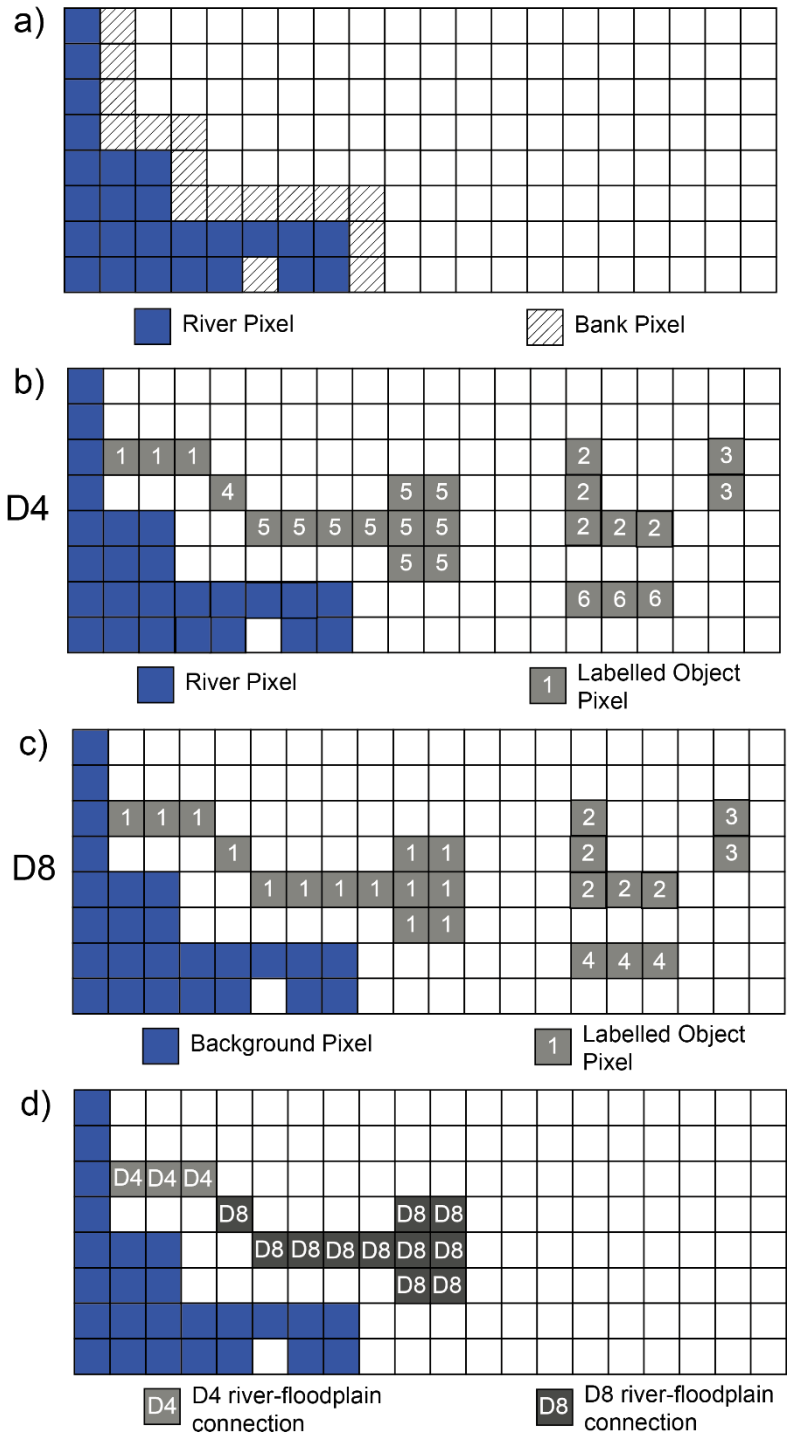

Figure 5-10 Connected pixels to bank pixels for D4 and D8 connectivity. a) River and bank pixels b) D4 connectivity of bank pixel selected c) D8 connectivity of bank pixel selected d) River-floodplain connection for D4 and D8 connectivity

As a result, a list of breached bank pixels is produced. To produce the binary image required for connected component labelling, the DEM is thresholded based on the river water surface height. All Pixels below the river water surface elevation under consideration are given a

value of 1 (and are thus object pixels) and all those pixels over the river surface water height are not considered to be connected so are given a value of 0 (background pixel). Take the following scenario. For a scenario when the river is 1m above normal, there is a list of breached bank pixels. So, a breached bank pixel may have an elevation of 2m, but the water height of the river pixel adjacent to the breached bank pixel in question is 2.5m. In this case, the DEM is converted to a binary image by classifying object pixels as all those at 2.5m or below, and all those above are background pixels. For efficiency, a list of pre-processed binary images are produced and subsequently selected so the thresholding does not need to be carried out each time. Then the connected component labelling algorithm is applied either for D4 (SAUF algorithm) or D8 (BBDT algorithm). From this a labelled image is produced either for D4 connectivity (Figure 5-10, b), or D8 connectivity (Figure 5-10, c). As we are only interested in the river-floodplain connectivity for the breached bank pixel under consideration, the label value at the coordinates of the breached bank pixel under consideration is taken and all other label values are set to 0, or background pixels. This subsequently leaves a single object of connected pixels, which is then assigned a label value of 1 and added to a stack of images for the water level scenario under consideration (in this case 1m above normal river height). For the remainder of this chapter, these object images will be referred to as patches to align to the language of landscape statistics.

For each water height scenario, the stack of patch images are combined to calculate the number of connections each floodplain cell has to a river cell (Figure 5-11). As each patch is given a label of 1, simple raster addition is used. Furthermore, for each patch landscape statistics are calculated using the FRAGSTATS program (McGarigal et al., 2002) found within the SDMTools package in R. Output statistics include number of cells in a patch, perimeter area, area, core area, shape index and fractal dimension index.

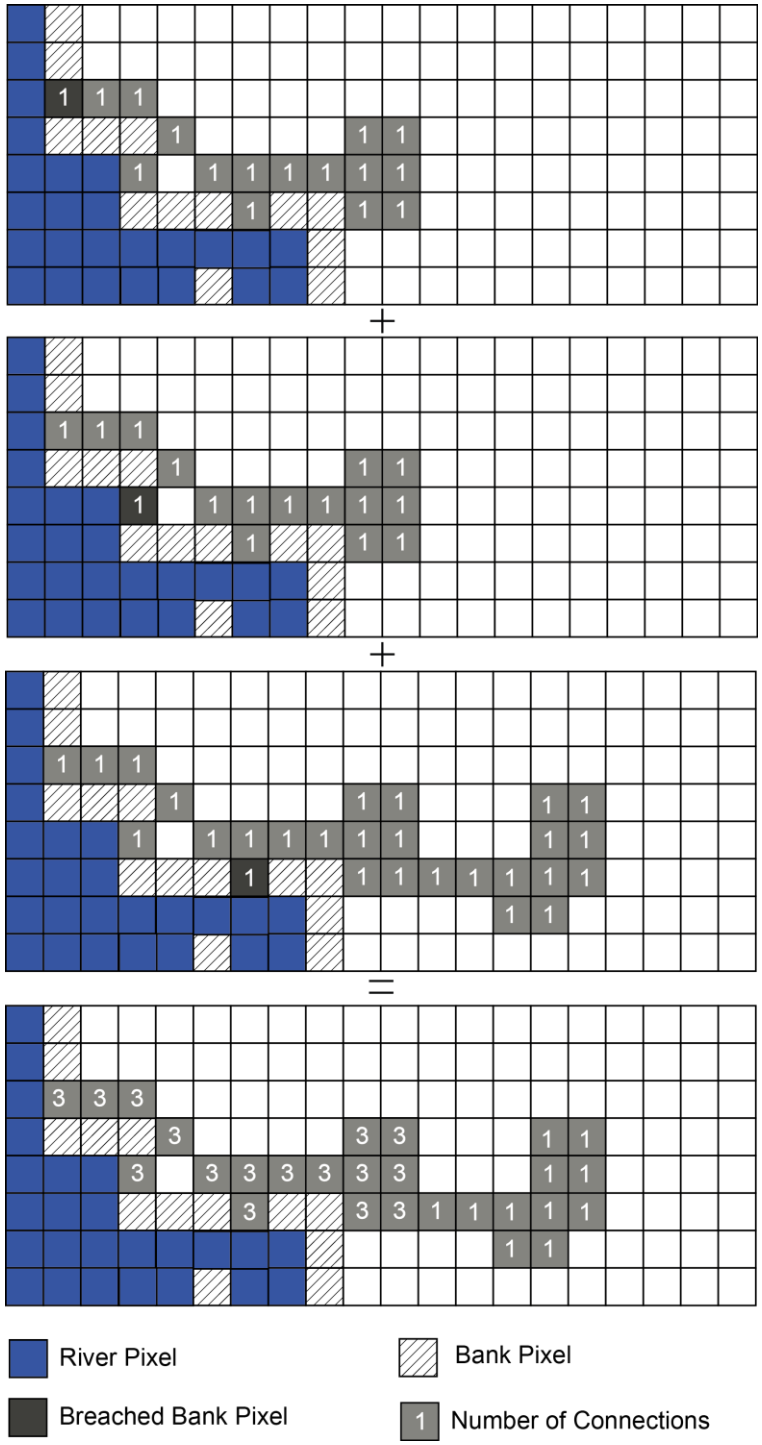

Figure 5-11 Total number of connections for a scenario where 3 bank pixels are breached. The top three panels are the floodplain pixels connected to the breached bank pixel. The bottom image is the number of breached bank pixels that it is connected too which is calculated by summing the top three images

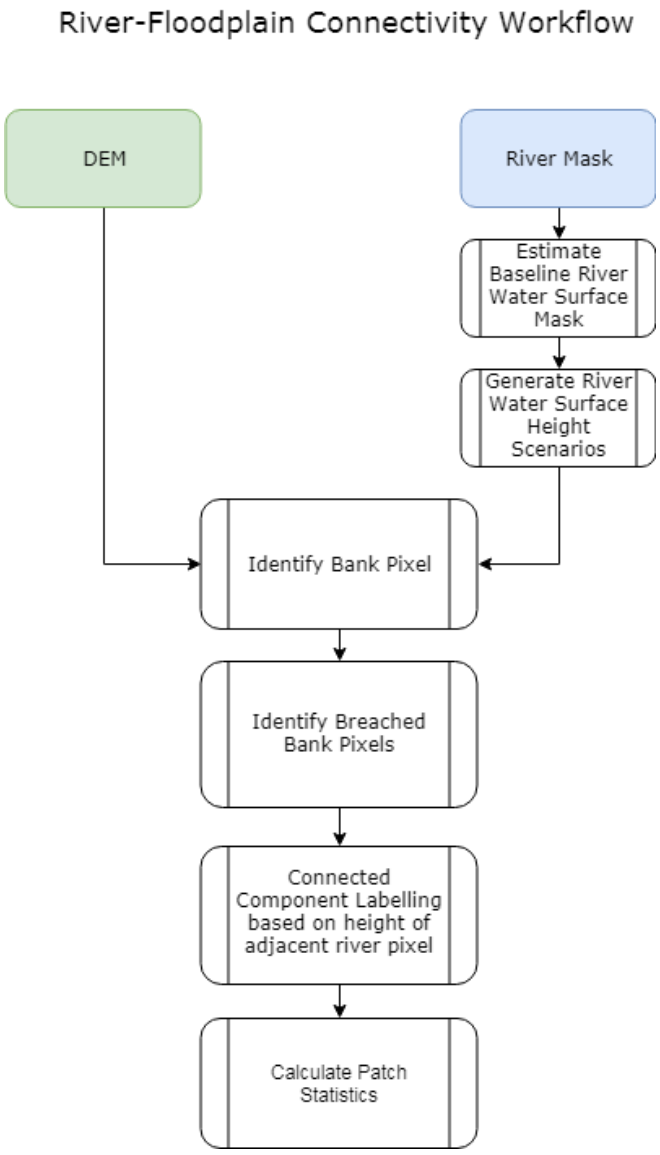

Figure 5-12 River-Floodplain Connectivity Workflow Diagram

5.6 Results

Here results are presented for 16 water height scenarios for 15 DEMs for the Ba floodplain catchment. Connectivity is analysed for both D4 and D8 neighbourhoods. Additionally, boxplots of simulated DEMs are included to determine how the DEM simulation process effects river-floodplain connectivity. Maps of river-floodplain connectivity can be found in section 5.6.5.

5.6.1 Landscape Statistics for all DEMs

First, landscape statistics are presented for all DEMs. For some statistics (e.g. Number of Patches) normalization is needed as a higher resolution DEM has more breached bank pixels and thus more patches. All figures are presented from the highest resolution in the top left and the coarsest resolution in the bottom right, with resolution becoming progressively more coarse as you read from left to right. Where there are noticeable differences in river-floodplain connectivity between D4 and D8 neighbourhoods, figures are presented for both. Otherwise, figures are only presented for D8 connectivity as this represents the more complex connectivity pattern.

For all DEMs, landscape statistics are presented for Total Patch Area and Maximum Connectivity (number of connections) normalized by number of patches. For Total Patch Area, as water height increases, the total patch area increases. Another way to think of total patch area is the area of floodplain pixels that are connected to the river. Alternatively, it could be considered to be a 'flood' but as the hydrodynamics are not explicitly considered in the connected component labelling method it is felt that this language is inappropriate. Instead, total patch area should be thought of as the area of floodplain pixels connected to the river. In both D4 and D8 connectivity, the MERIT DEM has the largest total patch area. However, the total patch area varies between D4 and D8 connectivity, with maximum values for the MERIT DEM of 36km^2 and 41.8km^2 for D4 and D8 connectivity respectively. In addition, the MERIT DEM at 180m has a maximum total patch area of 41.8km^2 for D8 connectivity but just 7.7km^2 for D4 connectivity. Indeed, both the MERIT at 90m and MERIT at 180m have considerably different Total Patch Areas between D4 and D8 connectivity (Figure 5-15) with these differences coming at different water heights. The differences in the other DEMs between Total patch Area at D4 and D8 connectivity are considerably less but are non-negligible. DEMs that are considered noisy (DSM's and SRTM) have very low total patch area values.

Maximum connectivity (number of connections to a patch) normalized by number of patches is also presented. The number of patches refers to the number of independent patches in a DEM at a given water height scenario. Using this metric, LIDAR at 45m and

MERIT at 270m have the highest values, even though their distributions are very different with MERIT at 270m having no connections at lower water heights. The highest resolution DEMs (LIDAR at 5m and 10m) have an almost linear increase in maximum connectivity normalized by number of patches, whilst all other DEMs have a more variable pattern.

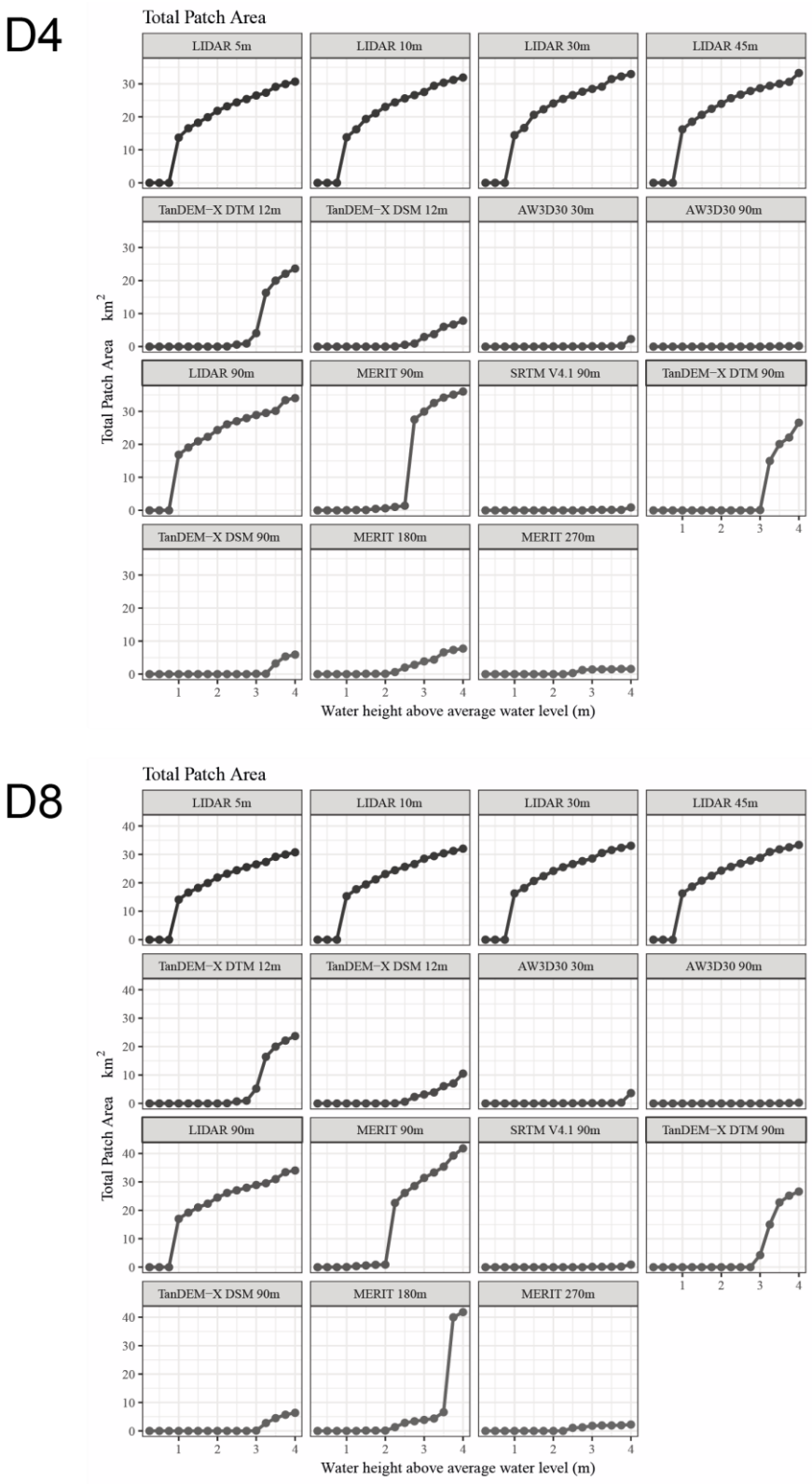

Figure 5-13 Total Patch Area for all DEMs for D4 and D8 connectivity

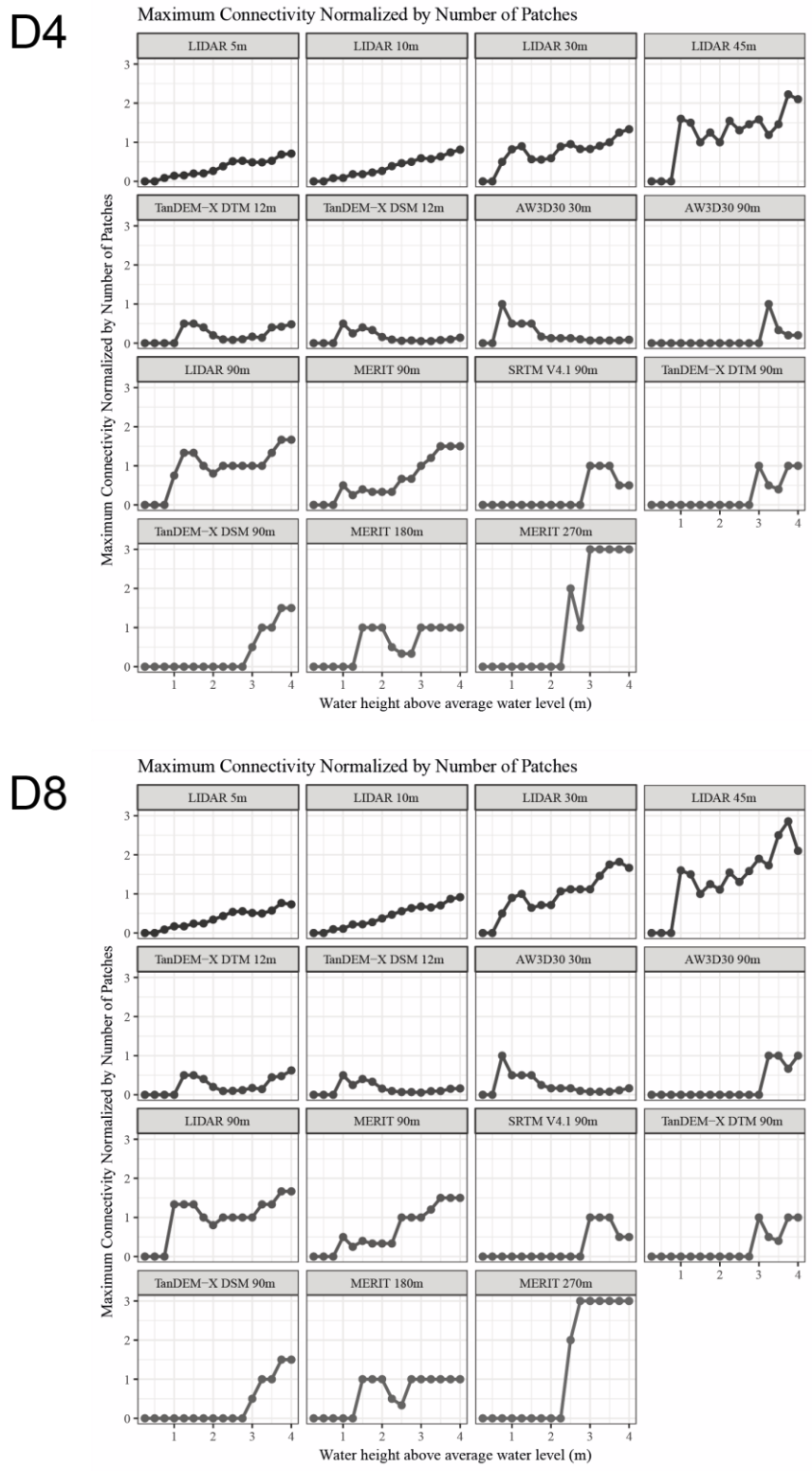

Figure 5-14 Maximum Connectivity (number of connections) normalized by number of patches for all DEMs for D4 and D8 connectivity. Maximum connectivity refers to the maximum number of times a floodplain cell is connected to breached bank pixels. See Figure 5-11 for a schematic of Maximum connectivity.

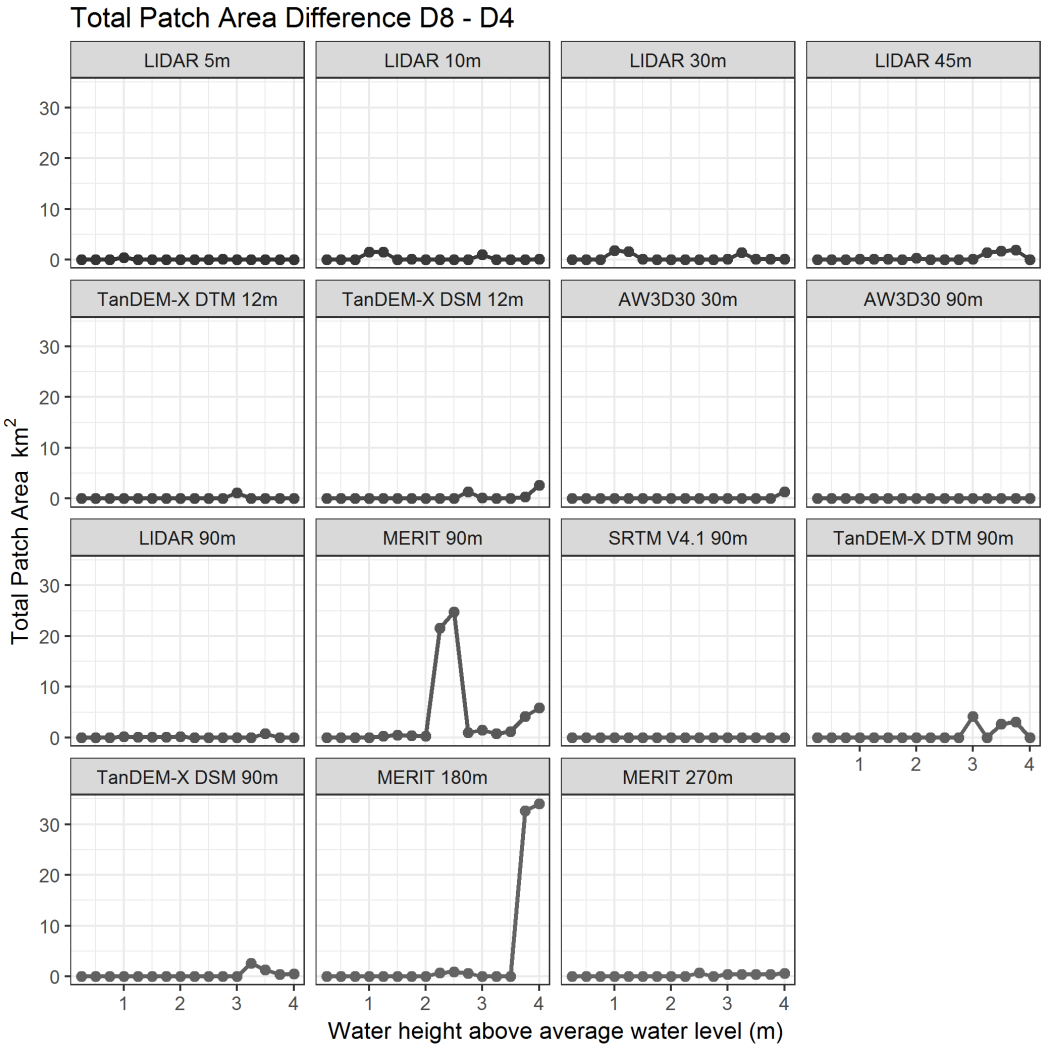

Figure 5-15 Total Patch Area Difference between D8 and D4 connectivity

5.6.2 Landscape Statistics for 90 m DEMs

To negate the effects of resolution, landscape statistics for DEMs at 90m were selected. This results in 6 DEMs being analysed (AW3D30, LIDAR, MERIT, TanDEM-X DSM, Tan-DEM-X DTM and SRTM). Moreover, landscape statistics that are not scale dependent (Number of Patches) could be fairly compared. Additionally, figures were also included depicting shape complexity using the shape index metric. The shape index is calculated by dividing the sum of patch perimeter by the square root of patch area, with a value of 1 referring to a square shape and increasing above 1 for more irregular shapes, with this value scale independent (McGarigal et al., 2002). The rationale to exploring shape complexity indices is that they may be able to indicate the types of mechanism for river-floodplain connectivity (i.e. a channel

may have a long shape, whilst a flooded depression may have a simpler more block-like shape).

Total Patch Area for only 90 m DEMs are shown in Figure 5-16. DSMs and SRTM have very low Total Patch Areas indicating poor river-floodplain connectivity. LIDAR at 90 m is more connected at lower water heights than both TanDEM-X DTM and MERIT, but at larger water heights the difference is less. Number of Patches indicate the number of separate patches that are connected to the river. For three DEMs (LIDAR, MERIT, TanDEM-X DTM) the number of patches increases, before decreasing at the highest water levels suggesting that the patches merge at the highest water height, and thus there is intra-floodplain connectivity at the highest water heights. Patches merge at the highest water heights as sheet flow over the floodplain becomes more dominant than the negative relief forms (see Table 5-2 for a reminder of negative relief forms) that are more prominent at lower water heights. For SRTM and the DSMs, the number of patches increase as the river-floodplain gradually becomes more connected with increased water height. No reduction in the number of patches at the highest water heights for SRTM and DSMs, suggests a lack of intra-floodplain connectivity as patches are not merging. There is minimal difference between D4 and D8 connectivity, with the number of patches greater for D4 as the smaller connectivity neighbourhood means connectivity between patches is more difficult.

Maximum connectivity (maximum number of river pixels connected to a patch) does not need to be normalized for resolution so a direct comparison can be made (Figure 5-18). For all DEMs the maximum connectivity increases with water height. This is not surprising as more bank pixels are breached so there are more river-floodplain connection points. Moreover, patches tend to merge at higher water heights (as indicated by the number of patches), so each larger patch will have more points connected to the river.

Shape Index was also plotted (Figure 5-19). A discernable trend was difficult to identify. Values close to 1 indicate a square shape, whilst larger values indicate a more irregular shape. Thus, in general the average shape of the patches became more irregular as water height increased. The fractal dimension index which also measures shape complexity was also calculated but is not plotted as it was similarly inconclusive.

D4

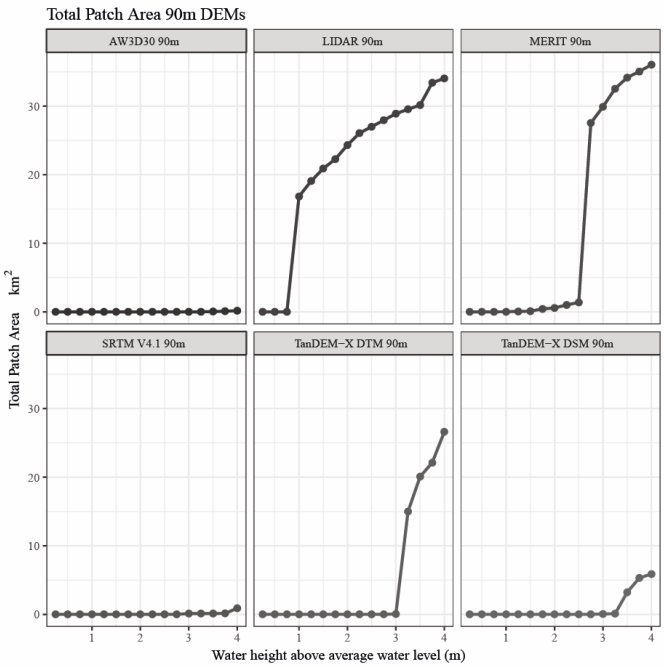

D8

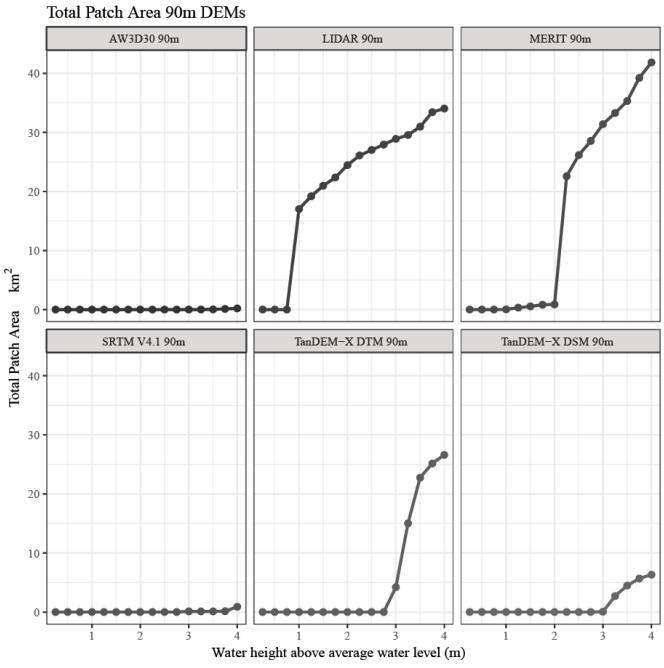

Figure 5-16 Total Patch Area for all 90 m DEMs for D4 and D8 connectivity

D4

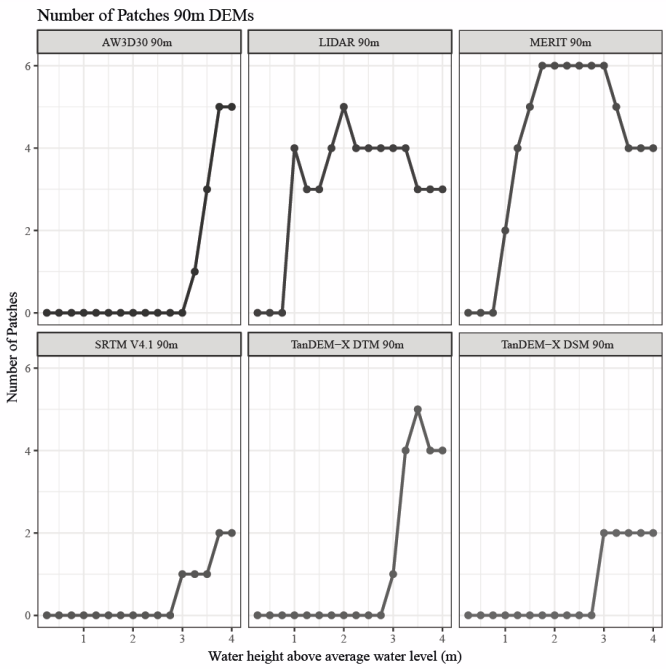

D8

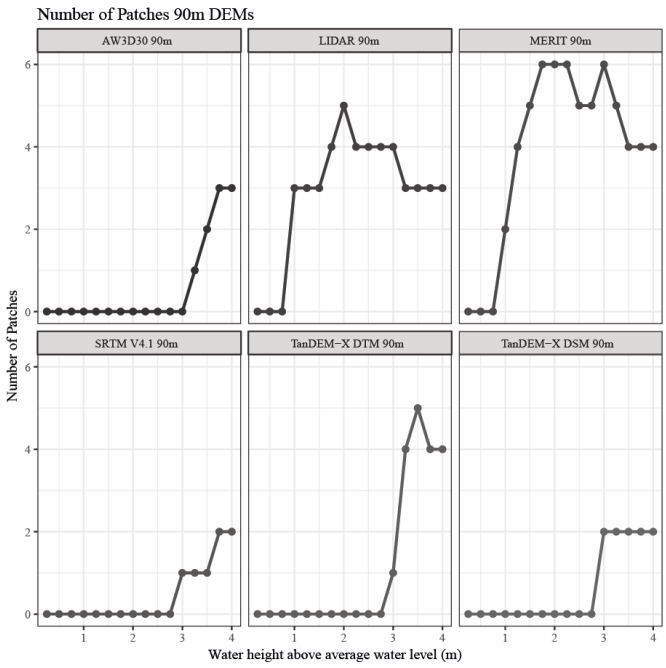

Figure 5-17 Number of Patches for all 90 m DEMs for D4 and D8 connectivity

D4

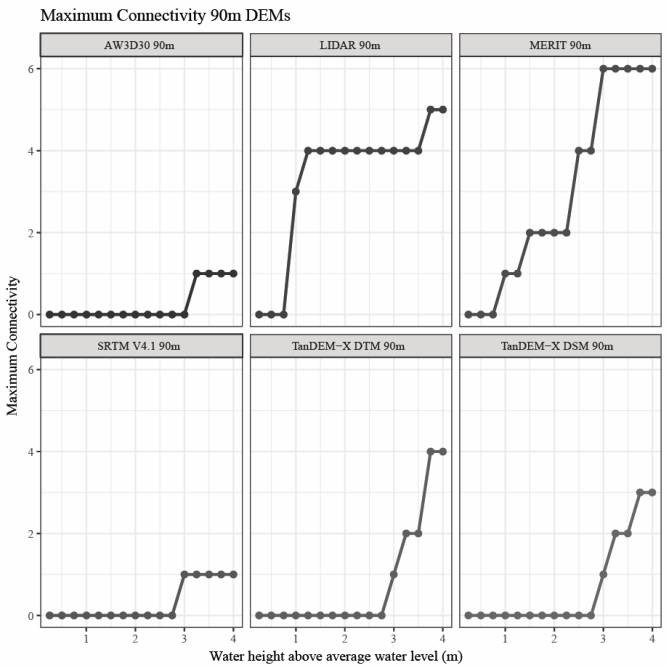

D8

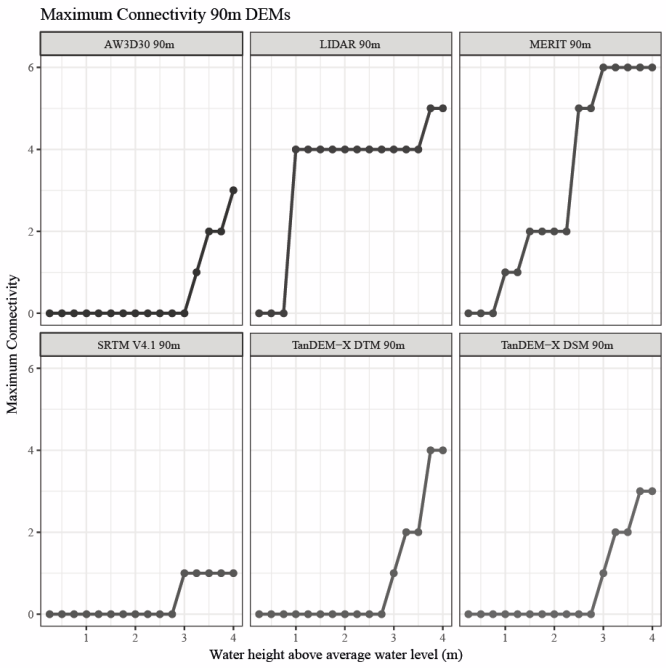

Figure 5-18 Maximum Connectivity (Number of Connections) for all 90 m DEMs for D4 and D8 connectivity

D4

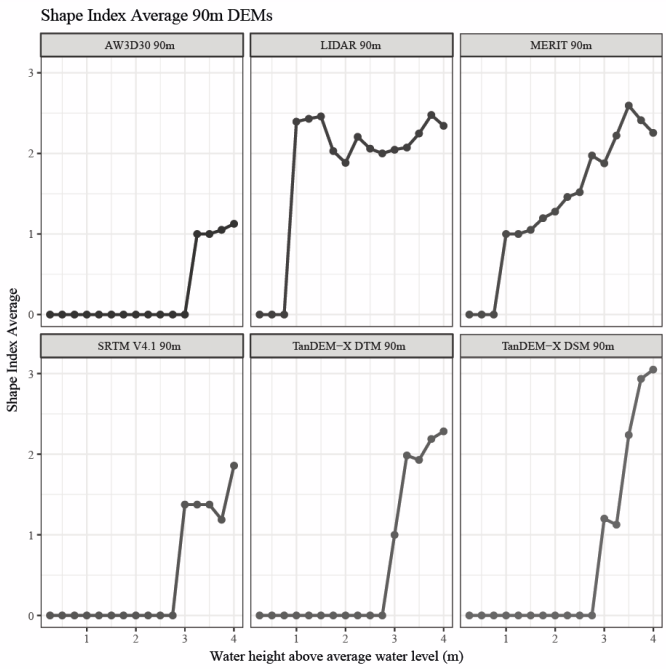

D8

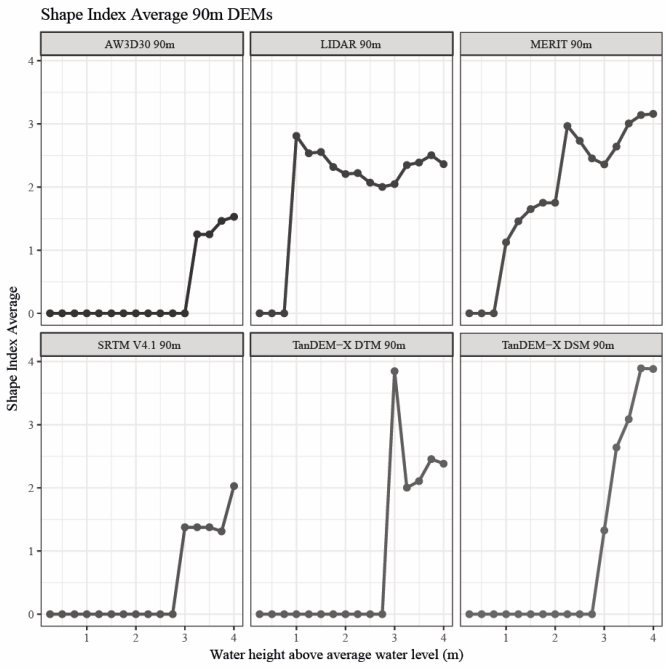

Figure 5-19 Shape Index for all 90 m DEMs for D4 and D8 connectivity

5.6.3 Breach Points by Water Height

To determine where breach points (river-floodplain connection points) are and whether they are distributed differently between DEMs, breach point locations at the water height at which they are first breached for MERIT and LIDAR at 90 m (Figure 5-20) and LIDAR at 5m

and 30m (Figure 5-21) are visualized. Therefore, the smaller the circles, the lower the water height at which a breach point is first breached, or in other words becomes connected. For brevity, only results for D4 connectivity are presented here. Intuitively, the higher the resolution the more breach points, with this creating a somewhat messy picture of connectivity for higher resolution DEMs (Figure 5-21). By comparing DEMs at the same resolution, the effects of resolution could be controlled for. It is interesting to see the differing spatial distribution of breach points, with these connections becoming activated at different water heights as indicated by the size of the dots on the maps (Figure 5-20). For instance, for the LIDAR DEM at 90m, river-floodplain connectivity occurred at lower water heights than MERIT in the north of the domain, with the black triangle on the LIDAR 90m map highlighting the breach point that is causing the extra connectivity for that part of the floodplain.

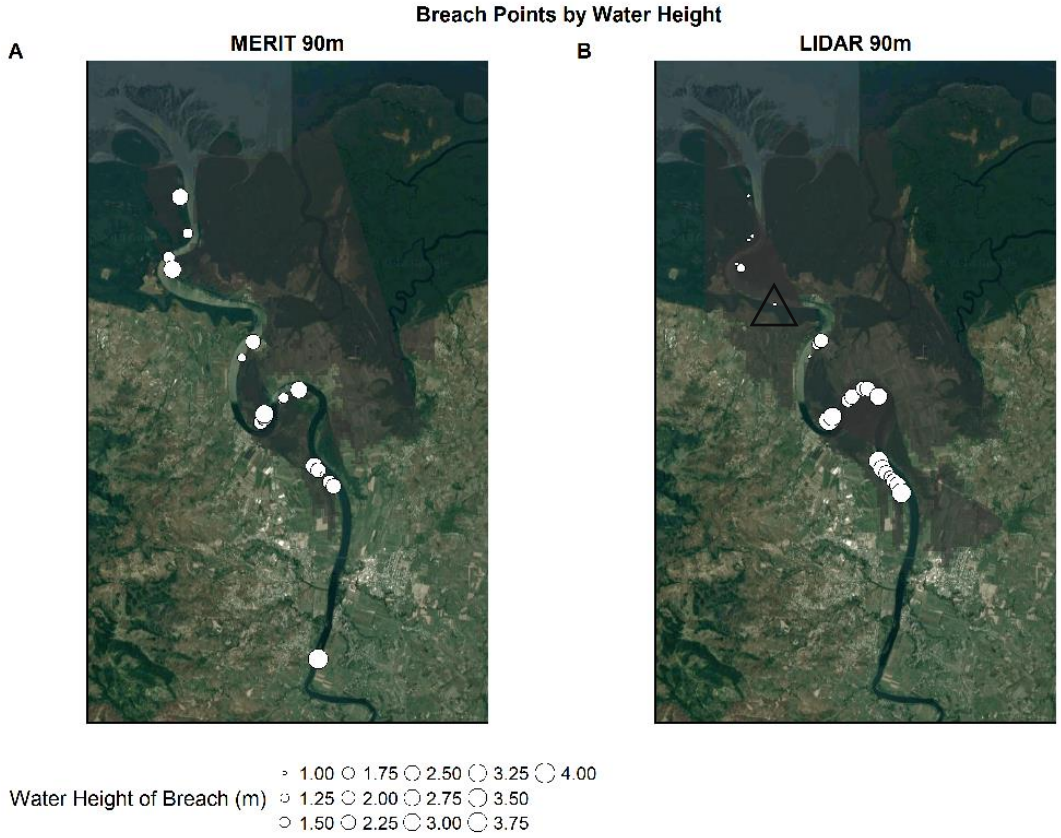

Figure 5-20 Breach Points by Water Height for MERIT at 90m and LIDAR at 90m

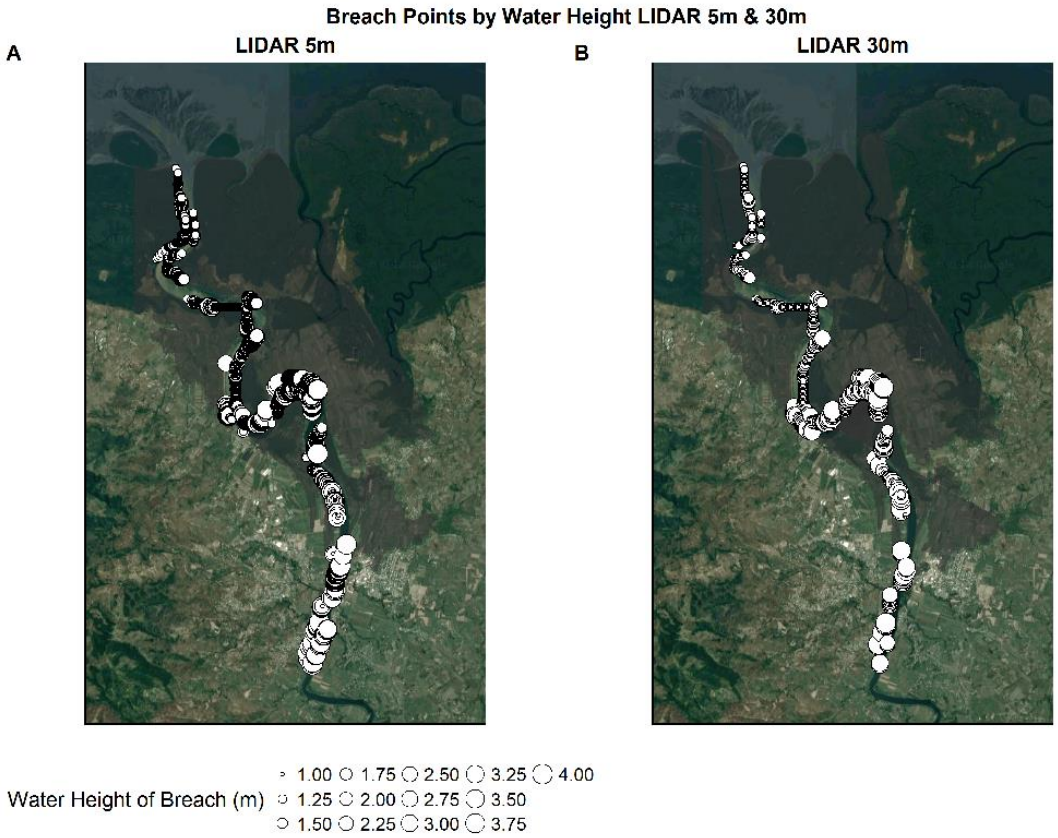

Figure 5-21 Breach Points by Water Height for LIDAR at 5m and 30m

5.6.4 Comparison to Simulated DEMs

To determine how river-floodplain connectivity alters in simulated DEMs, 2500 DEMs were simulated at 90m based on the MERIT DEM. Simulations of the MERIT DEM was chosen based on the better accuracy (lower RMSE) of MERIT over SRTM and the fact the semi-variograms to simulate were available from work outlined in the previous results chapter. The DEMs were simulated using semi-variograms by landcover class as this was found to give the best results as outlined in the previous chapter. Landscape statistics for the simulated DEMs are plotted as boxplots against the other DEMs.

Simulated DEMs had consistently lower Total Patch Area compared to MERIT and the LIDAR DEMs. By adding a random field, the river-floodplain connectivity decreased for both D4 and D8 connectivity as the simulated DEMs are noisier than the original MERIT DEMs. Thus, there are fewer floodplain pixels below the threshold elevation (i.e. the water

surface height) so there are less floodplain pixels that are connected to the breached bank pixles. Total Patch Area also differed between D4 and D8 connectivity, with more variability in D4 connectivity, especially for water heights scenarios of 3.25m and 3.5m. It is important to note that the Total Patch Area does not give information on the spatial distribution of the river-floodplain connectivity. Work in the previous chapter suggests that using a stochastic approach gives less spurious flood predictions compared to using a single DEM and gives results closer to a higher quality DEM (in that case LIDAR). Thus a similar approach could be used here - but instead creating probability maps of river-floodplain connectivity.

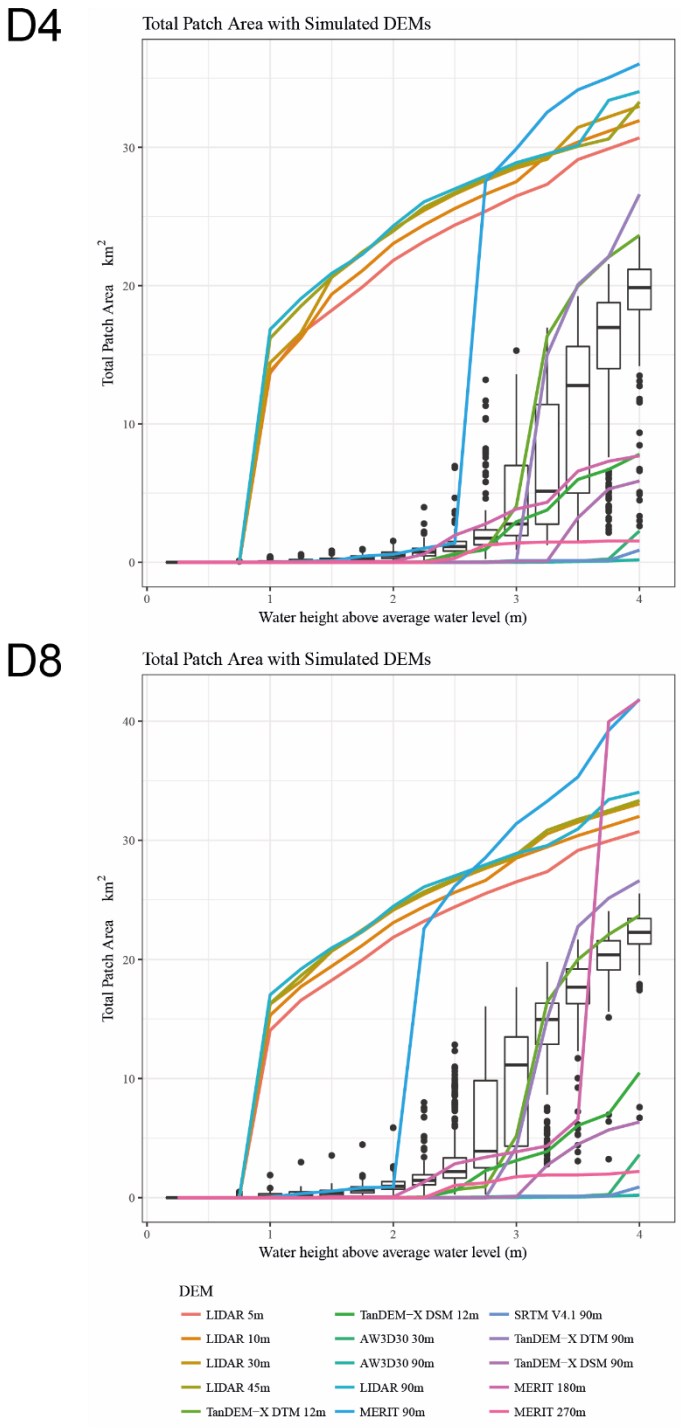

Figure 5-22 Total Patch Area for 2500 simulated DEMs for D4 and D8 connectivity together with boxplots of Total Patch Area for MERIT DEMs simulated by semi-variograms by landcover class.

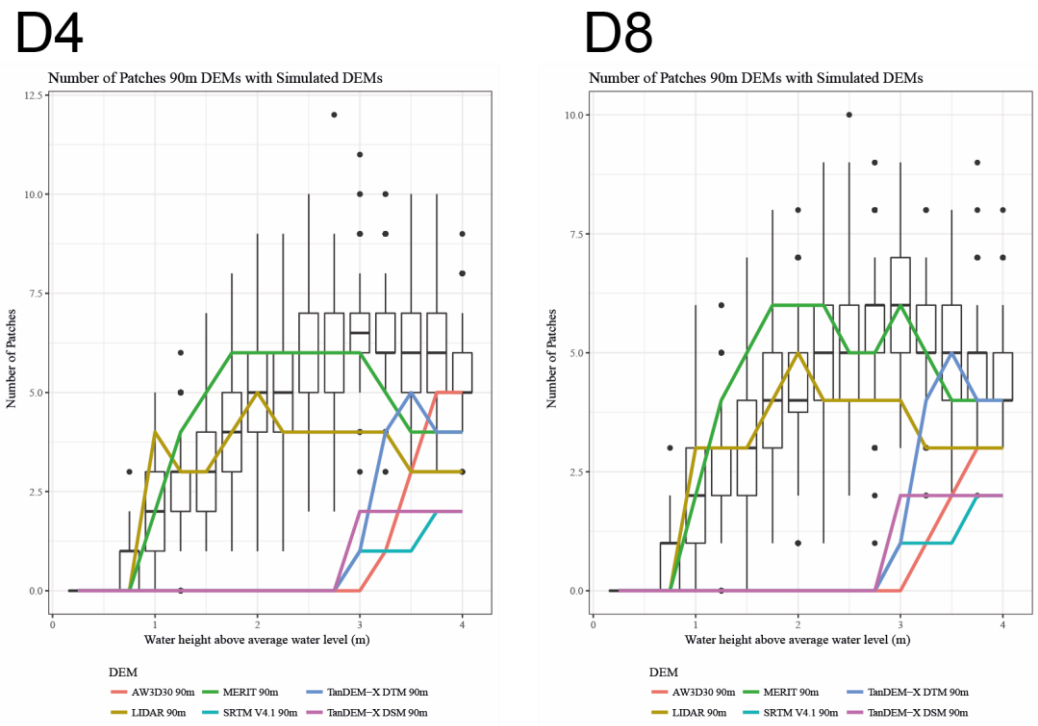

Figure 5-23 Number of Patches for 2500simulated DEMs for D4 and D8 connectivity together with boxplots of Total Patch Area for MERIT DEMs simulated by semi-variograms by landcover class.

Simulated DEMs had a wide variation in the number of patches, with the greatest variability for D4 connectivity at 2.75m with the number of patches ranging from 2 to 11 (Figure 5-23).

5.6.5 Connectivity Maps

Maps showing the Maximum connectivity (maximum number of connections per patch) for each water height scenario are presented for each DEM here (Figure 5-24-Figure 5-30). By displaying the maximum connectivity on a map, the spatial extent of connectivity is also delineated. For the LIDAR based DEMs, significant connectivity starts to occur at water height scenarios of 1m, whilst for MERIT significant connectivity does not occur until water heights reach 2.25m. At the highest water height scenarios, the spatial extent of the connectivity is largely similar between MERIT and LIDAR, but the maximum connectivity values change. A selection of maps of simulated DEMs can also be found in Figure 5-31 to Figure 5-33.

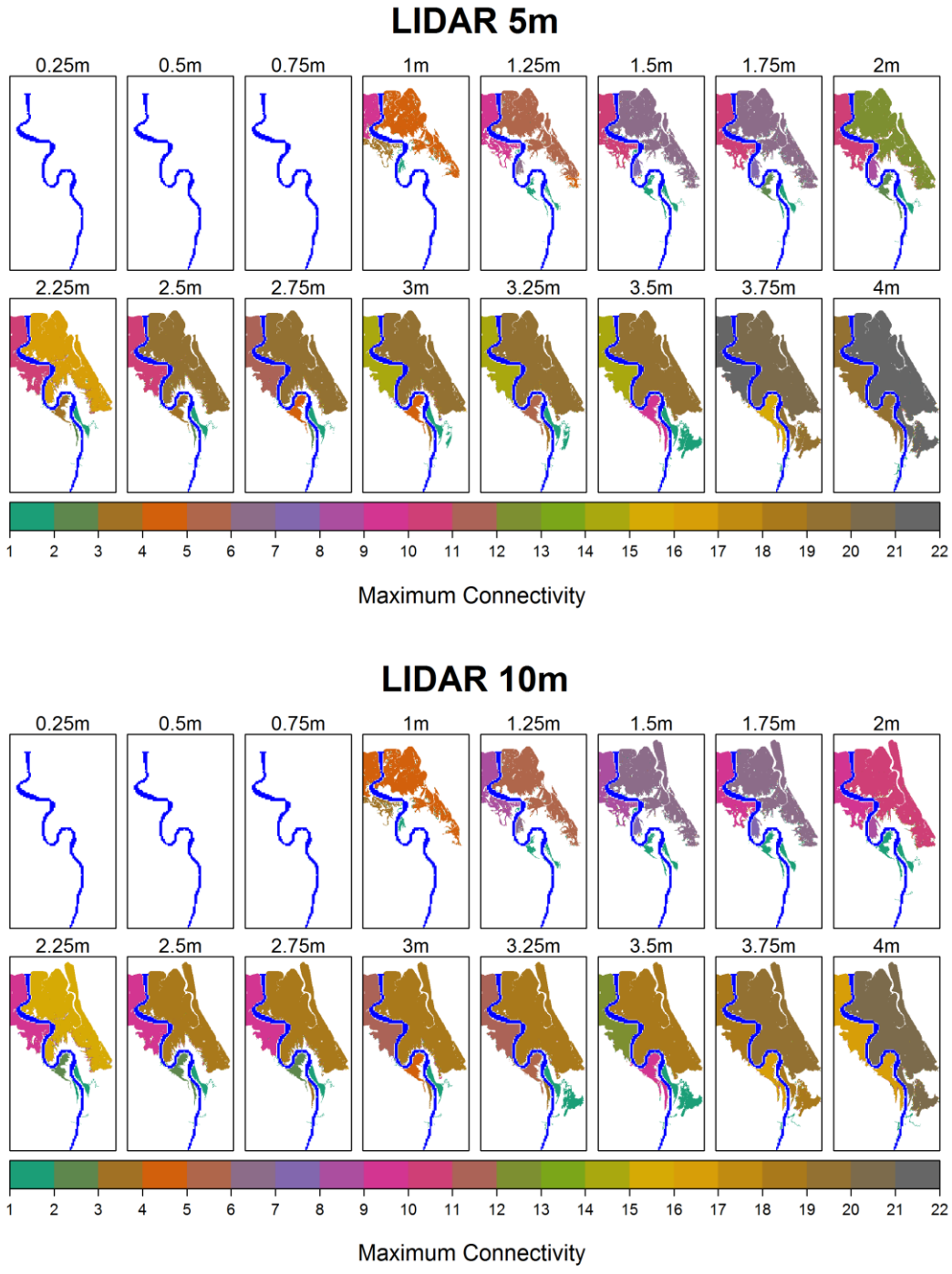

Figure 5-24 Maximum Connectivity (Number of river-floodplain connections per patch) for D8 connectivity for LIDAR at 5m and 10m resolution

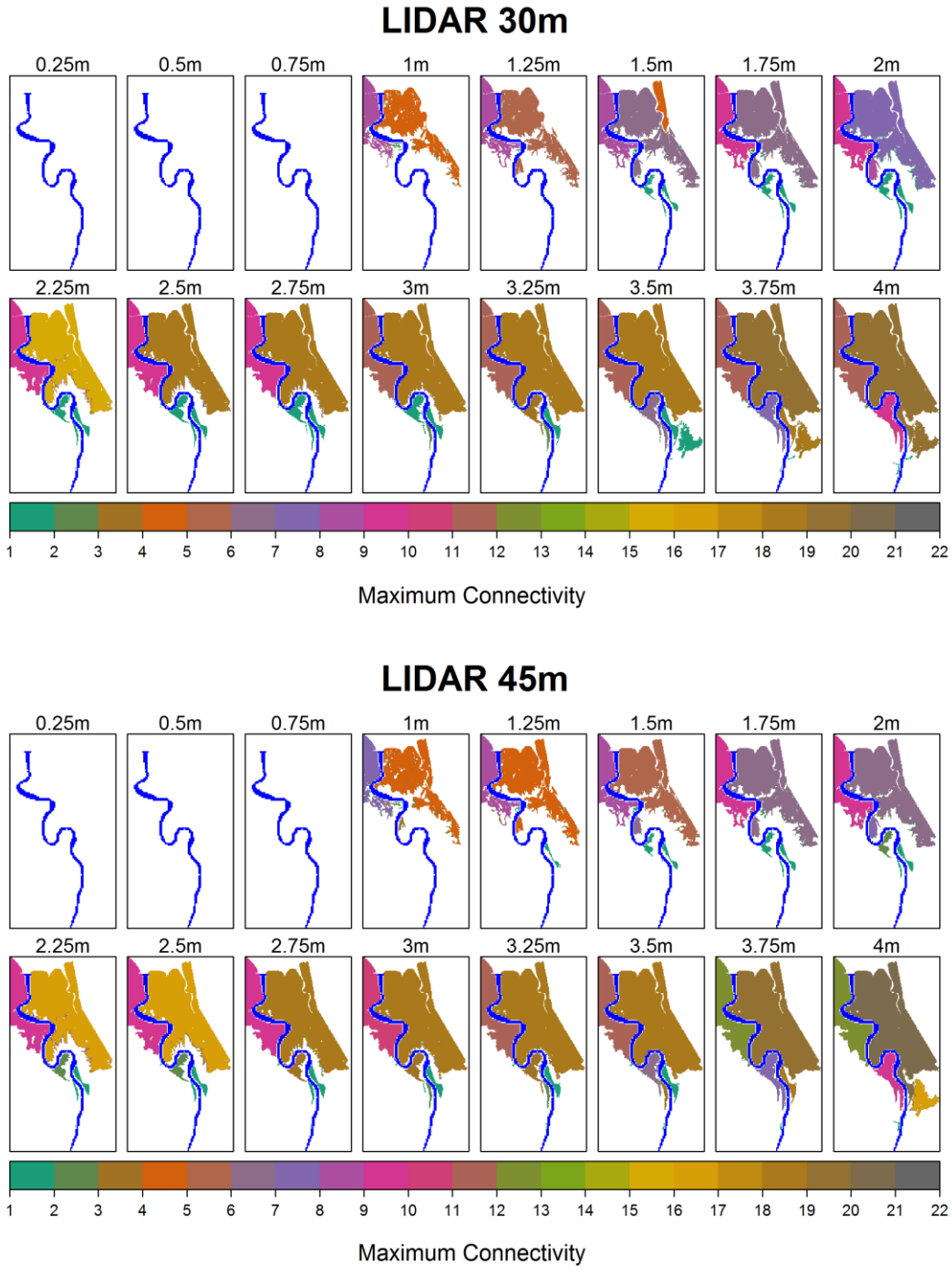

Figure 5-25 Maximum Connectivity (Number of river-floodplain connections per patch) for D8 connectivity for LIDAR at 30m and 45m resolution

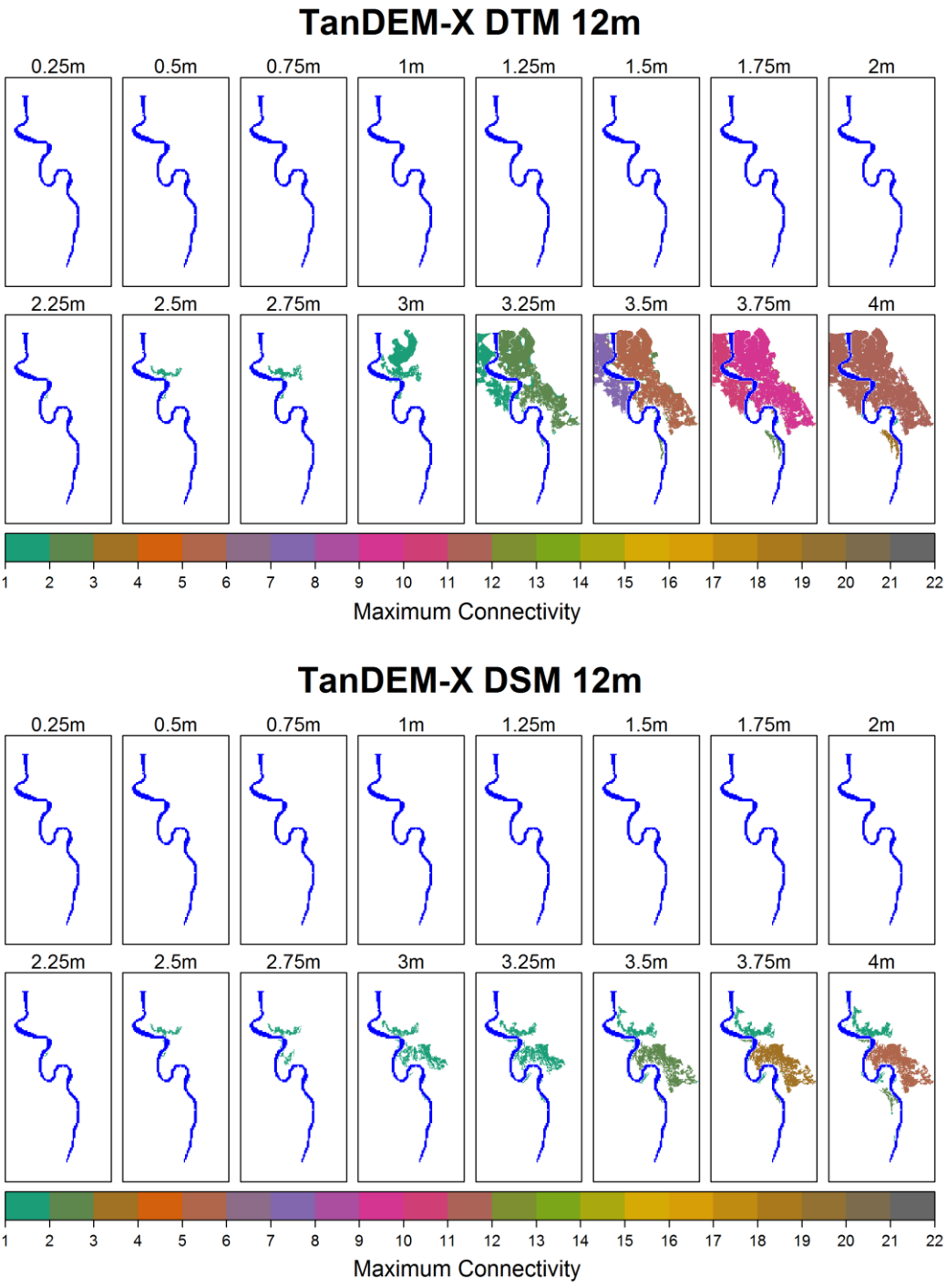

Figure 5-26 Maximum Connectivity (Number of river-floodplain connections per patch) for D8 connectivity for TanDEM-X 12m DTM and DSM

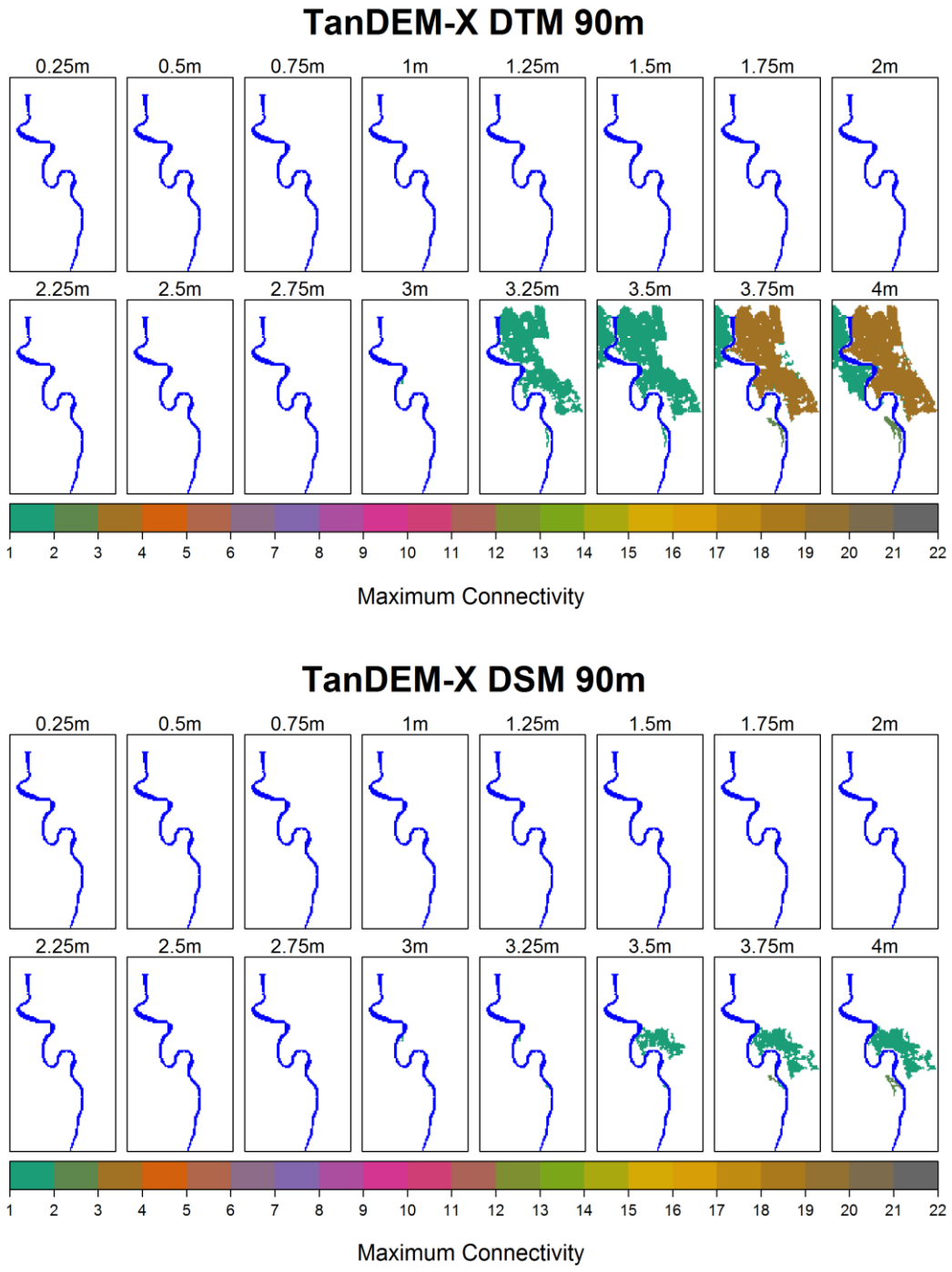

Figure 5-27 Maximum Connectivity (Number of river-floodplain connections per patch) for D8 connectivity for TanDEM-X 90m DTM and DSM

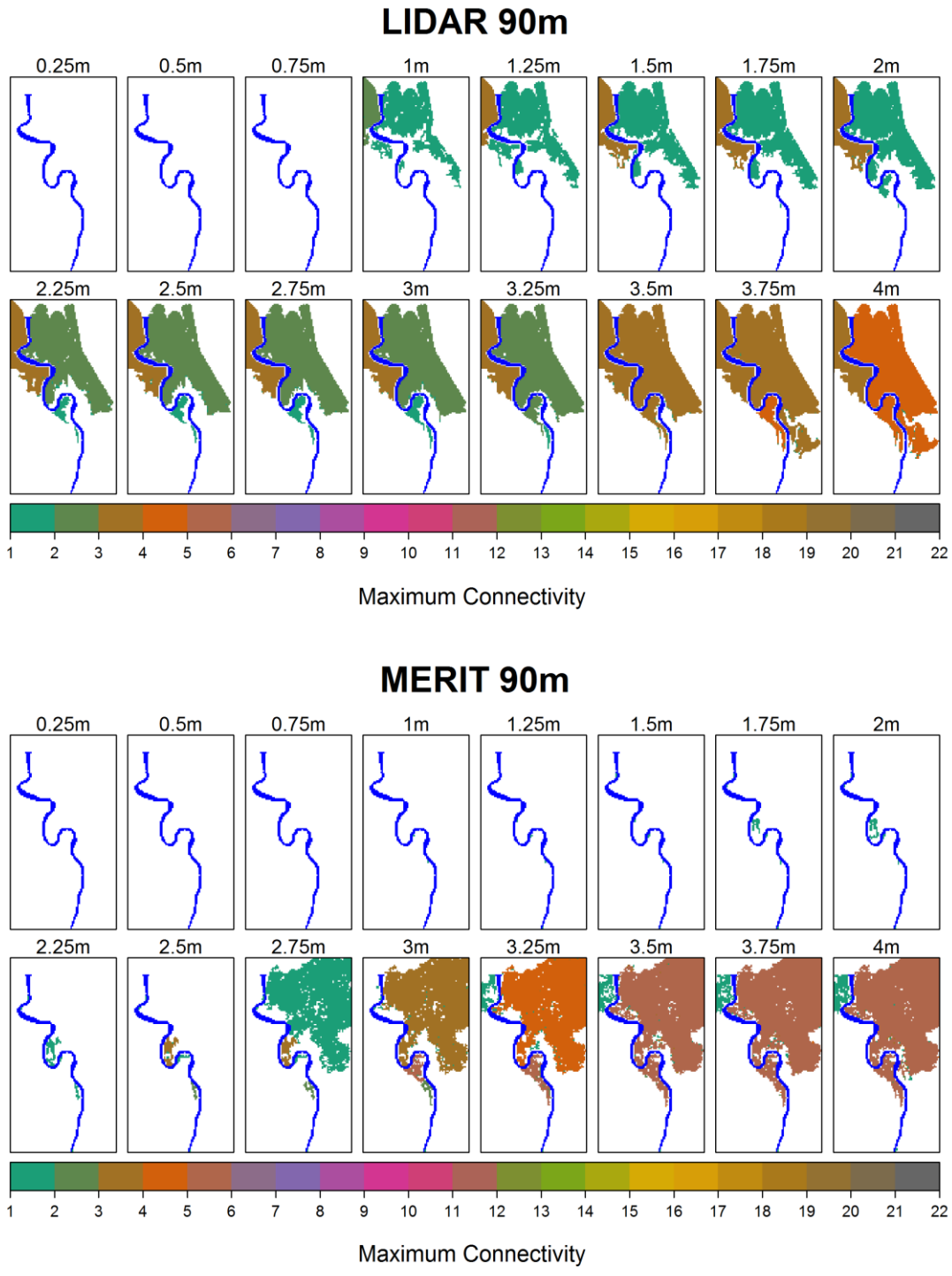

Figure 5-28 Maximum Connectivity (Number of river-floodplain connections per patch) for D8 connectivity for LIDAR at 90m and MERIT at 90m

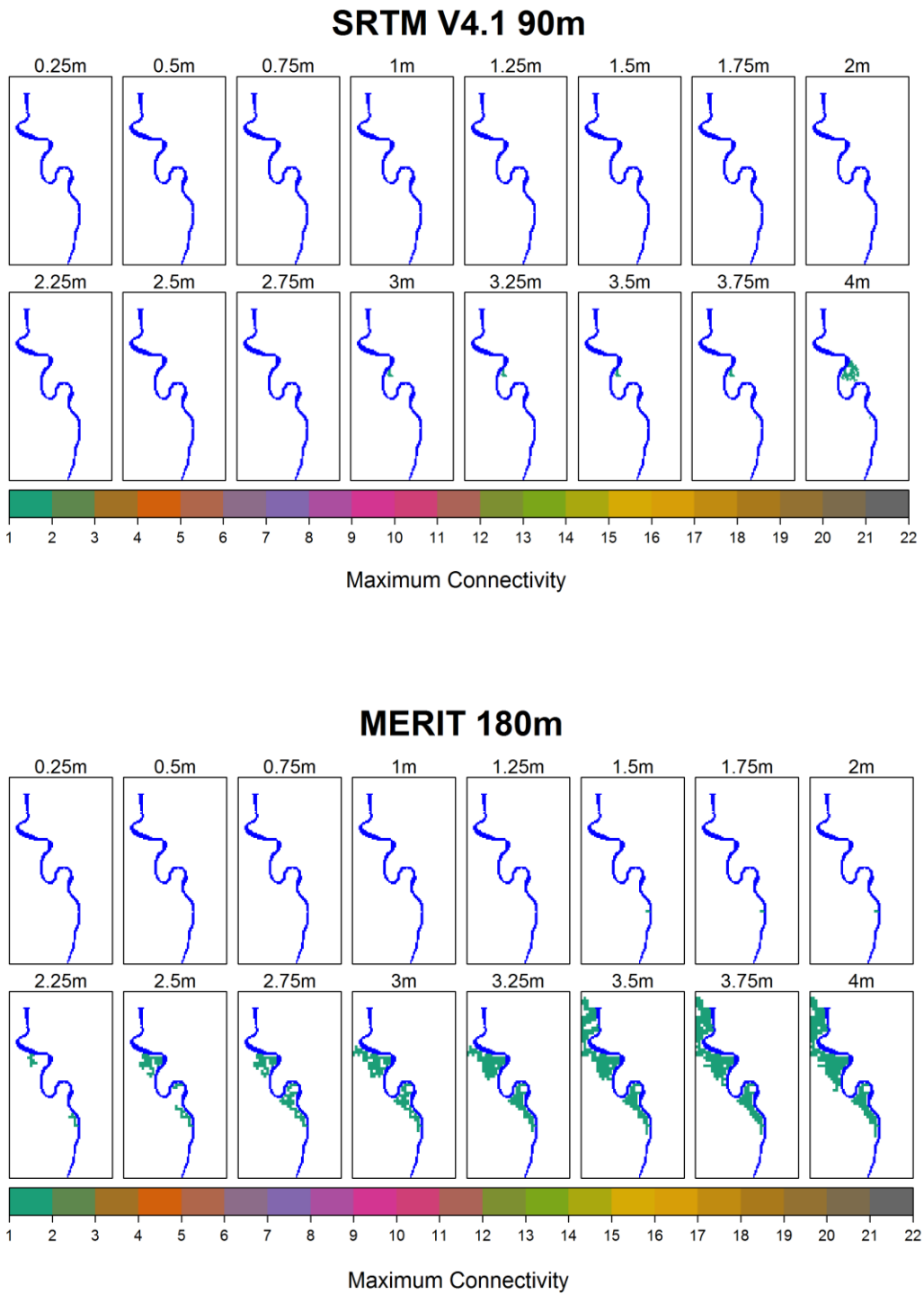

Figure 5-29 Maximum Connectivity (Number of river-floodplain connections per patch) for D8 connectivity for SRTM v4.1 at 90m and MERIT at 180m

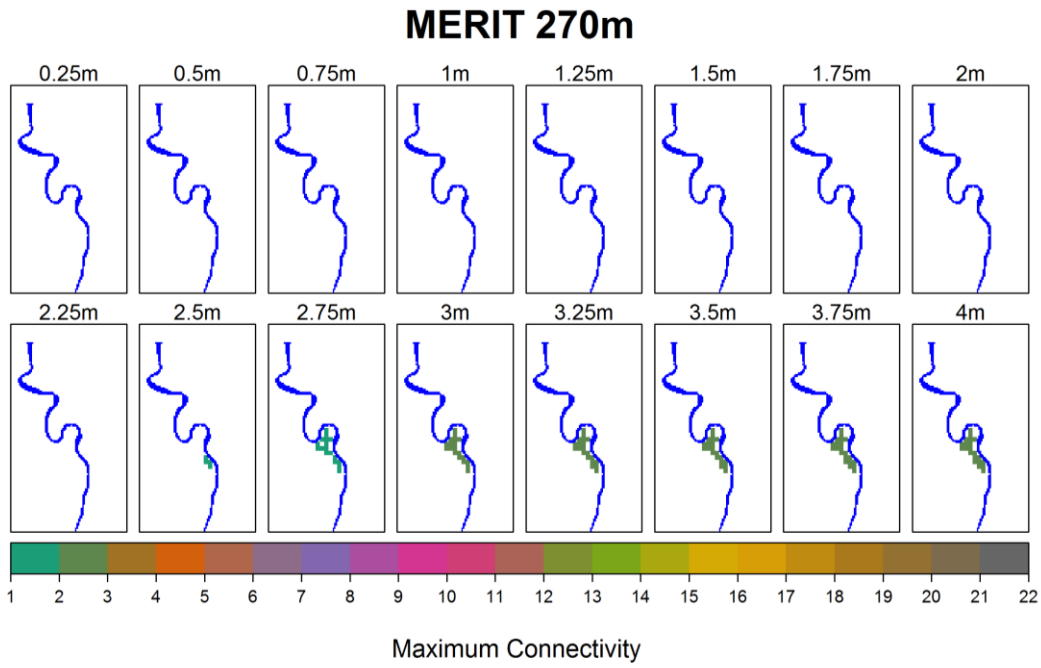

Figure 5-30 Maximum Connectivity (Number of river-floodplain connections per patch) for D8 connectivity for MERIT at 270m

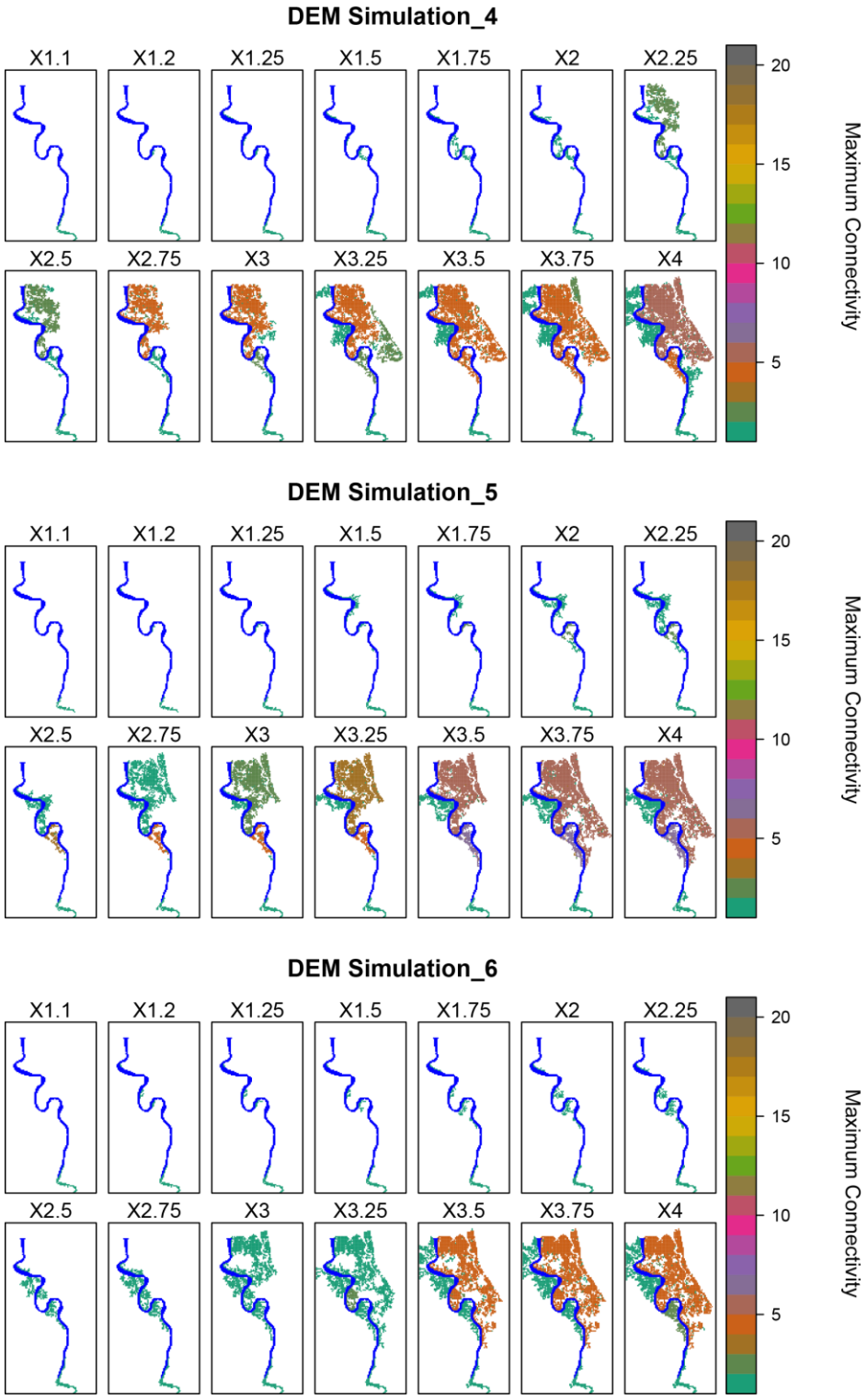

Figure 5-31 Maximum Connectivity (Number of river-floodplain connections per patch) for D8 connectivity for 3 Simulated MERIT DEMs (Sample 1)

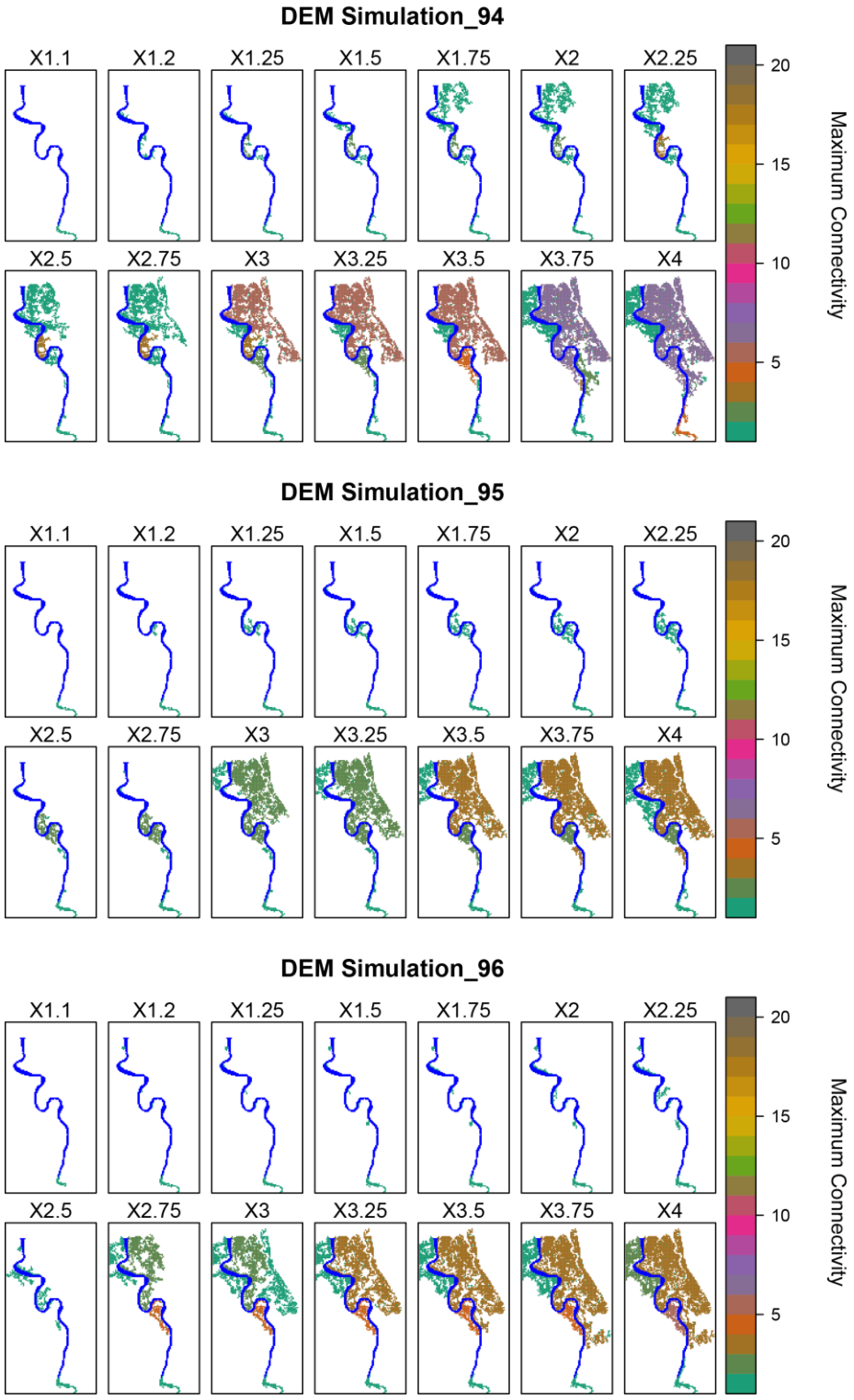

Figure 5-32 Maximum Connectivity (Number of river-floodplain connections per patch) for D8 connectivity for 3 Simulated MERIT DEMs (Sample 2)

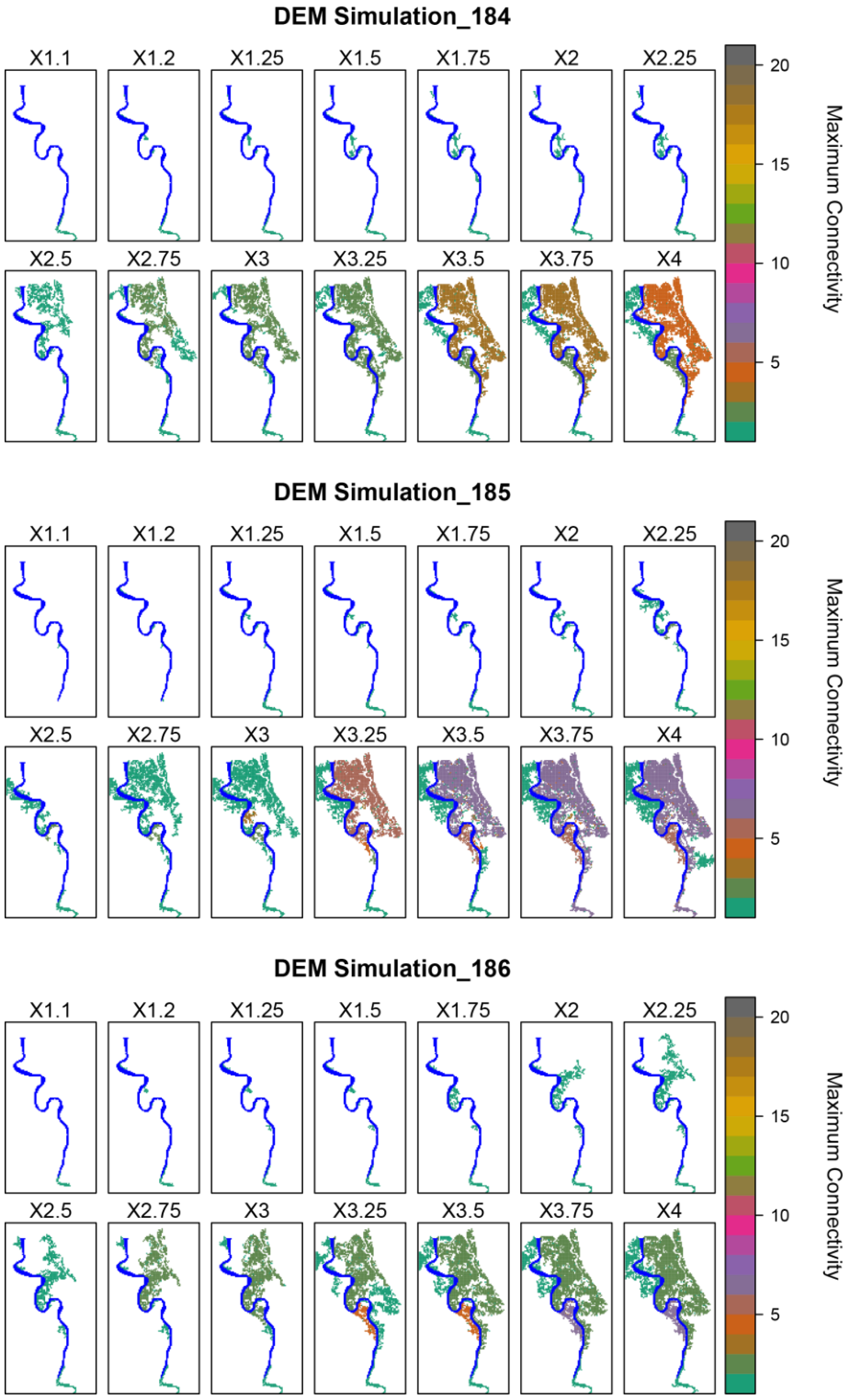

Figure 5-33 Maximum Connectivity (Number of river-floodplain connections per patch) for D8 connectivity for 3 Simulated MERIT DEMs (Sample 3)

5.7 Discussion

The discussion section is formatted based on addressing the research questions outlined in section 5.3.4.

5.7.1 How does floodplain connectivity differ across resolution and DEM products?

It is clear that river-floodplain connectivity varies widely across DEMs and resolution when comparing all DEMs (5.6.1) and when only considering 90m DEMs (5.6.2). Airborne DEMs (LIDAR) show a more consistent progression of river-floodplain connectivity compared to Spaceborne DEMs, with connectivity beginning at lower water heights. In Spaceborne DEMs, there is a 'jump' in connectivity at higher water heights, where the DEMs have little connectivity at lower water heights to a high amount of connectivity at high water heights. This suggests that spaceborne DEMs have too few breaching points, and instead only inundate when banks are overtopped and the floodplains are connected by sheet flow. Various field observations in the UK (Nicholas and Mitchell, 2003, Bates et al., 2006), Canada (Smith et al., 2009), Papua New Guinea (Day et al., 2008) and the Amazon (Trigg et al., 2012) find that river floodplain connectivity is far more complex with minor channels and negative relief forms pivotal for inundation and dewatering. Indeed when describing the Fly River, Day et al. (2008) describes the complex network of minor channels and negative relief forms as creating a 'depositional web'. The airborne DEMs can represent more of these features, so airborne DEMs can more accurately represent the correct river-floodplain connectivity processes compared to spaceborne DEMs. Furthermore, as resolution is coarsened, river-floodplain connectivity as measured by Total Patch Area is found to increase for LIDAR, decrease for MERIT and slightly increase for TanDEM-X and AW3D30. Therefore, by coarsening noisier DEMs (TanDEM-X and AW3D30), the effective resolution of the DEM becomes more similar to that of the LIDAR at 5m, as measured by the Total Patch Area. However, for the already smooth MERIT DEM the coarsening of the DEM acts to reduce the river-floodplain connectivity as the number of breach points decreases markedly. For instance, at the 2m water height scenario, MERIT at 90m has 12 breach points (or river-floodplain connectivity points), MERIT at 180m has only 3 points, and there are just

one for MERIT at 270m. Therefore, by coarsening MERIT, river-floodplain connections are lost. For all other DEMs, coarsening DEMs enhances river-floodplain connectivity (in terms of Total Patch Area), but this increase may not be correct. It is assumed that the most realistic connectivity is for the LIDAR at 5m as LIDAR has the best vertical accuracy and is the highest resolution. The Total Patch Area does not increase demonstrably across resolutions for LIDAR suggesting that the quality of DEM is more important than the resolution. Additionally, noisier DEMs (DSMs and SRTM) have poor river-floodplain connectivity, as indicated by a low Total Patch Area and an increasing number of patches by water height (Figure 5-17). The number of patches increases with water height in SRTM and DSMs but decreases in other DEMs. This increasing number of patches indicates that intra-floodplain connectivity is not represented in noisier DEMs as patches do not join. Instead smaller patches of the floodplain are connected to the river as water height increases but these patches do not join. Therefore, vegetation removal/smoothing of DEM is needed to improve the connectivity. Interestingly, the type of neighbourhood connectivity can give surprisingly different results for some DEMs. For example, the Total Patch Area for MERIT and 90m and 180m is considerably more for D8 connectivity than it is for D4 connectivity (Figure 5-15). This could have implications for models that depict river-floodplain connectivity (i.e hydrodynamic models) as if the model uses D8 connectivity, more river-floodplain connectivity will be represented as across all DEMs there is more river-floodplain connectivity when considering D8 connectivity. Simulated DEMs were also included in the analysis with results suggesting that the simulated DEMs have worse connectivity than the DEM they were simulated from (MERIT) as the Total Patch Area is less (Figure 5-22). Moreover, there is a greater range in the number of patches (Figure 5-23) indicating that the river-floodplain connectivity is more isolated which is similar to the pattern observed for DSM's and SRTM. However, these statistics do not indicate the spatial pattern. By taking a stochastic approach using multiple DEMs improved flood model predictions in the previous results chapter, so it is expected that if the river-floodplain connectivity maps were combined they could have a more accurate picture of river-floodplain connectivity. Taken individually the river-floodplain connectivity of the simulated DEMs are similar to that of SRTM and DSMs.

5.7.2 Is the accurate representation of floodplain connectivity more important for smaller floods than larger floods?

Yes. In the LIDAR DEMs significant river-floodplain connectivity occurs at heights of 1m, but for other DEMs significant connectivity does not occur until at least water heights of 2.75m for MERIT and 3m for TanDEM-X. When significant connectivity does start to occur in spaceborne DEMs, there is a large jump in Total Patch Area, whilst for airborne DEMs this progression is much smoother. With the assumption that the LIDAR DEM are most accurate, and thus most correctly represents river-floodplain connectivity, it is concluded that other DEMs do not contain the features that enable river-floodplain connectivity at lower water heights. Therefore, spaceborne DEMs do not contain as many features such as tributary channels, contiguous channel remnants and internal drainage networks that airborne DEMs do, and thus do not have river-floodplain connectivity at lower water heights. This finding agrees with analysis of missing features in the SRTM for the middle reach of the Amazon by Trigg et al. (2012). As water height increases sheet flow becomes more dominant. Only these sheet flows can flow over noise in the DEM and thus do not always follow flow pathways. For this reason, the predicted flood inundation in global flood models tend to perform well even if the extent is reached by incorrect flow pathways. Conversely, when small features are a key control in flooding (e.g. in urban areas), DEMs that capture river-floodplain connectivity correctly are essential. In spaceborne DEMs, urban areas (Neal et al., 2011) (and indeed areas with tall vegetation) typically have a positive bias and are noisy, so only the highest water heights will cause any river-floodplain connectivity. There is a degree of equifinality about the good performance of MERIT and other spaceborne DEMs at higher water heights. Is connectivity good because flow pathways are being represented, or does the over-smoothed nature of MERIT allow this connectivity? We suspect the former as indicated by the difference in river-floodplain connectivity locations (breach points) as these differ between LIDAR and MERIT and become connected at different water heights. Therefore, to successfully represent smaller flood events which are crucial for ecology and agriculture (e.g. paddies in the Vietnamese Mekong Delta, see first results chapter), DEMs need be able to represent river-floodplain connections by including features (e.g. contiguous channel remnants) that are important for initial connectivity. For higher water heights (i.e. larger floods), accurately depicting river-floodplain connectivity is

less important as the predicted flooded area (Total Patch Area) is similar between DEMs. So for applications where river-floodplain connectivity at lower water heights (i.e. smaller floods) are the main focus, DEMs that accurately depict features that enable river-floodplain connectivity (e.g. contiguous channel remnants) are crucial. Either a high-quality airborne DEM should be used or a spaceborne DEM should be edited to depict such features.

5.7.3 What is more important in selecting a DEM for a flood model - RMSE or floodplain connectivity?

RMSE should not be the only metric used in choosing a DEM for a flood model, or indeed any application where river-floodplain connectivity is important for the processes being represented. It is true that a large RMSE is indicative of a worse quality DEM, but this metric cannot describe river-floodplain connectivity. For instance, the TanDEM-X DTM at 12m has a better RMSE than MERIT but the metrics produced here (Total Patch Area) suggests that it does not have such good river-floodplain connectivity. Whilst there may be some degree of equifinality with this result as MERIT may or may not actually depict the river-flow connections correctly, it is clear that users should look beyond RMSE as a metric in choosing a DEM and consider more subtle, more difficult to measure metrics such as spatial dependence (previous results chapter) and river-floodplain connectivity.

5.7.4 Can a river-floodplain connectivity metric be created to describe DEM products, and can this be used as a guide in assessing the suitability of a DEM to accurately represent flooding?

Yes and Yes. In this chapter, numerous metrics to quantify river-floodplain connectivity have been presented. These metrics include Total Patch Area, Number of Patches, Maximum Connectivity, Maximum Connectivity normalized by Number of Patches, Shape Index, as well as maps showing river-floodplain connections points (bank breach points) and maximum connectivity. Whilst these metrics do not give a single river-floodplain connectivity value, they do quantify and visualise river-floodplain connectivity. A single value to describe river-floodplain connectivity is difficult due to the non-linearity of connectivity for different river water heights and the different resolutions involved. Some of

the metrics presented (Total patch Area and Maximum Connectivity normalized by Number of Patches) can be used across DEM resolutions, whilst others (Number of Patches) are dependent on scale for a valid comparison. Shape Index as a metric was found not to be an effective metric to measure river-floodplain connectivity as it could not distinguish the features that enable river-floodplain connectivity.

The five metrics presented in this chapter (Total Patch Area, Number of Patches, Maximum Connectivity, Maximum Connectivity normalized by Number of Patches, Shape Index) are ranked in Table 5-5 based on their ability to quantify river-floodplain connectivity. Metrics that are scale independent and can be mapped are favoured so multiple DEMs across resolutions can be analyzed and visualized.

Table 5-5 Ranking of River-Floodplain Connectivity Metrics

Ranking	Metric	Scale Independent?	Can the metric be mapped?
1	Total Patch Area	Yes	No
2	Maximum Connectivity normalized by Number of Patches	Yes	Yes
3	Number of Patches	No	No
4	Maximum Connectivity	No	Yes
5	Shape Index	No	No

Total Patch Area is ranked as the most useful river-floodplain connectivity as it allows for an easy to understand comparison of DEMs across multiple resolutions. Effectively, the Total Patch Area is the total flooded area, so this metric allows for comparisons on how the DEM is expected to flood (i.e. river-floodplain connectivity) at various water levels. One could use this metric to determine whether different DEM products and resolutions give substantially different results which could influence the selection of a DEM. The Maximum Connectivity

normalized by number of Patches is also scale independent but can also be mapped. This metric tells us how many breached bank pixels are connected to a floodplain pixel and is useful in determining whether the river-floodplain connectivity is dominated by a small number of breached bank pixels or by a larger number. This metric has not been ranked as high as the Total Patch Area as although it can be mapped, it is more difficult to conceptualise. Third and fourth in the rankings are the Number of Patches and Maximum connectivity as these metrics are scale dependent, making them less useful when investigating river-floodplain connectivity across resolutions. Lastly, the Shape Index metric was ranked fifth (and last) as it did not show any discernible trends. Although this may be the case for this investigation, it would be worth to continue to consider it in future analysis to determine whether the metric is in fact useful.

Although not a metric, the river-floodplain connection points (bank breach points) were found to be useful. By identifying the river-floodplain connection points associated with each patch, the source of the connection between the floodplain and river can be determined, as well as the water height at which the connection occurs (see examples in Figure 5-20 and Figure 5-21). This information is useful in identifying critical bank pixels that enable river-floodplain connectivity and can be used as a guide to check whether the elevation of these critical bank pixels are realistic or erroneous. Whilst the flood pathways were not estimated as in the method outlined by Zhao et al. (2017), the origin of river-floodplain connectivity is determined in the method presented here. Moreover, the method presented in this chapter can also be applied to surface water extents from hydrodynamic models or remote sensing imagery as all the connected component algorithms need is a binary image of water extent. For a hydrodynamic model, the modeled water surface elevation of the river could also be used as opposed to our interpolation technique. Whilst applying the method presented in this chapter to hydrodynamic model and remote sensing outputs could give more realistic floodplain water extents as other controlling processes (slope, friction etc.) are parameterized, it does not tell us anything about the ability of a DEM to represent river-floodplain connectivity. Overall, the method presented in this chapter should be thought of as a simple guide to potential river-floodplain connectivity in DEMs which users can utilize to guide decisions on the suitability of the DEM for their application.

5.8 Limitations

The connected component labelling based method presented in this chapter has a number of assumptions. Firstly, the method does not consider water surface slope or friction which ultimately effects how water spreads across the floodplain. To consider these factors a hydrodynamic model is needed, but that comes with the caveat that it can take considerable time and resources to build and is difficult to calibrate and validate. The method presented here could instead be thought of as a measure of the maximum potential river-floodplain connectivity as in reality water will not reach as far into the floodplains as predicted as it is controlled by other factors (e.g. friction, the volume of water entering the floodplain over the course of the hydrograph). Therefore, the spatial extent of floodplain inundation is likely to be overestimated. Even remote sensing of water extent can suffer from misclassification of water pixels and/or the limitations of the observation technique to measure water under canopies, so no method comes without its flaws.

Secondly, the water surface height of the river is a key control in the method presented here. It has been rather roughly estimated for the Ba floodplain and there is no easy way of knowing whether it is indeed realistic. Where data are available, these estimations will be more accurate. Interpolating ICESat derived water surface heights could be a useful method to estimate river surface water heights especially in data sparse areas. In addition, a constant water surface gradient is assumed, but for larger rivers especially this is not the case (O'Loughlin et al., 2013, Altenau et al., 2017). Accurately interpolating the water surface elevation of the river is a key challenge. Yet with the upcoming SWOT mission, we are set to greatly enhance our knowledge and measurement of freshwater on land (Srinivasen et al., 2014). However, the estimation approach taken in this chapter is still valid as a range of water surface elevations are used so the sensitivity to elevations are estimated.

Thirdly, the metrics presented here only represents lateral river-floodplain connectivity of surface water as per our definition. River-floodplain connectivity by groundwater is not represented owing to the fact that it is extremely difficult to measure over a large area.

Finally, the method presented in this chapter has failed to provide a single metric to describe river-floodplain connectivity. Whilst the metrics presented in this chapter do quantify river-floodplain connectivity for given water surface elevations in the river as well as represent this spatially, a single number for any given water height has not been produced. Simply, river-floodplain connectivity is highly non-linearly and is impossible to quantify across all water heights.

5.9 Conclusions

This chapter has quantified river-floodplain connectivity for a range of different DEM products across multiple scales using a novel method based on connected component labelling. The method was applied to the Ba floodplain in Fiji, with outputs of Total Patch Area, Number of Patches, Maximum Connectivity, Maximum Connectivity normalized by Number of Patches, Shape Index, as well as maps showing river-floodplain connections points (bank breach points) and maximum connectivity are calculated. Four main conclusions were reached. First, river-floodplain connectivity varies substantially across DEM products and to a lesser degree resolution. Second, airborne DEMs (LIDAR) can represent river-floodplain connectivity at lower river water elevation scenarios, whilst spaceborne DEMs can give similar values of river-floodplain connectivity only for large floods. This suggests that although spaceborne DEMs can give good flood predictions in global flood models, they may not be giving the correct result for the right reason as the flood is unlikely to follow the correct flow pathway. Third, river-floodplain connectivity should be also be considered when selecting a DEM for a flood model as other DEM quality statistics (e.g. RMSE and Mean Error) do not indicate whether river-floodplain connectivity is depicted. Lastly, whilst a single one size fits all metric to describe river-floodplain connectivity could not be produced, a set of metrics are presented that can be used to diagnose the suitability of a DEM for applications where river-floodplain connectivity is important. The metrics have been ranked with Total Patch Area and Maximum Connectivity normalized by Number of Patches ranked as the most useful metrics in measuring river-floodplain connectivity as these metrics are independent of scale. Furthermore, identifying the river-floodplain connection points (bank breach points) and their associated water heights is useful to map so the critical bank pixel elevations can be checked for their quality.

This chapter has answered criticisms of previous hydrological connectivity studies that consider only a single scale, with this study being novel in considering a wide range of DEM products including simulated DEMs. Yet, the chapter has not responded to the challenge of comparing metrics across locations, so further work should go on to apply these methods in other locations. Currently work is ongoing to apply the method presented here over a much large region in the Congo Basin. There is also potential for the presented method to be used with hydrodynamic model outputs or remote sensing imagery as well as a further exploration of the landscape statistics on offer.

Chapter 6 Conclusions

6.1 Main Findings

Intermediate scale hydrodynamic models that can effectively utilise limited data and have an appropriate computation time that allows for Monte Carlo simulations are needed to improve our understanding of the flood hazard in data-sparse areas, which are often the most at-risk areas. Large river deltas are understudied in this area but have a high amount of exposure to flooding. However, due to the incredibly flat topography of a delta, topography is very likely to be a key source of uncertainty in making flood predictions. To this end, this thesis aims to assess the skill of a hydrodynamic model built at the intermediate scale for a large river delta, before investigating the impact of uncertain topography on flood predictions and how river-floodplain connectivity relates to this and whether this can be quantified. As a result, this thesis had 3 mains objectives which were 1) Determine whether an intermediate hydrodynamic model at a regional scale can accurately represent flooding in a data-sparse delta 2) Assess the implications of simulating global DEMs for flood inundation studies and 3) Identify and quantify river-floodplain connectivity of DEMs across resolutions. The following section will summarise the conclusions from each results chapter that addresses each objective in turn.

6.1.1 An intermediate Scale Hydrodynamic Model of the Mekong Delta built using freely available data

Objective 1: Determine whether an intermediate hydrodynamic model at a regional scale can accurately represent flooding in a data-sparse delta

To further our understanding of how uncertain topographic information impacts flood predictions in data-sparse environments, a pre-requisite was to build a hydrodynamic model at an intermediate scale. The Mekong Delta is used as an initial case study as

intermediate scale models of large river deltas have not been developed despite the high flood risk in these areas. To this end, a hydrodynamic model at 540m resolution was built using LISFLOOD-FP to test whether an intermediate scale model had any skill in making flood predictions. The model was built using freely available data and included estimation of the downstream tidal boundary condition using harmonic analysis. The most detailed model that included some bathymetric data and smaller channels demonstrated a good level of skill with an average RMSE value of 0.608m across the 5 gauges assessed, an average NSE value of 0.627 and a CSI score of 0.62. The model performed better in wetter periods which is of most importance for predicting flooding. A sensitivity analysis was carried out by varying friction parameters and by varying the detail of bathymetry data and the number of channels. The model was found to be more sensitive to channel friction than floodplain friction, with optimum values of 0.0225 and 0.050 respectively. Moreover, this chapter found that estimating bathymetry using bankfull discharge gave only marginally worse predictions than if bathymetry was known, suggesting that bathymetric data may not necessarily essential to make skilful predictions. Additionally, including smaller channels resulted in less total flooded area suggesting that maximum inundation is dominated by sheet flow and thus including the smaller channels that are important for river-floodplain connectivity is not important for the largest floods. However, the inclusion of smaller channels are important for smaller floods and the dewatering of the floodplain. The model developed in this chapter had a similar skill to other models of the Mekong Delta that relied on some non-freely available data. This chapter also found that the MERIT DEM had a better performance than SRTM. Later, LiDAR data became available for a single province in the Vietnamese part of the Mekong delta and allowed for a more comprehensive comparison between model resolution and DEM products. Coupled with a ground-truthing campaign, we found considerable discrepancies between elevations in the DEMs and predicted flood extents. Therefore, a more comprehensive analysis on the impact of uncertain topography on flood extent predictions was needed as the typical deterministic treatment of topography (i.e. using a single DEM) can lead to spuriously precise (and incorrect) predictions.

6.1.2 Implications of Simulating Global Digital Elevation Models for Flood Inundation Studies.

Objective 2: Assess the implications of simulating global DEMs for flood inundation studies

Modellers tend to use only a single DEM in their hydrodynamic model owing to a perceived lack of available global DEM products. In this chapter, a geostatistical method was implemented to simulate plausible versions of the freely available MERIT and SRTM global DEMs in floodplains and to assess the impact of using an ensemble of DEMs has on flood extent. First, the spatial error structure was calculated for both the MERIT and SRTM DEMs for 20 lowland locations around the world by comparing these DEMs to a reference hyper resolution LiDAR DEM for each site. This was the first time the spatial error structure was calculated for MERIT and also builds on the limited research of the spatial error structure of SRTM. Semi-variograms were produced and revealed that the MERIT DEM is consistently more accurate than SRTM (semi-variogram sill values of 0.7-2.2m compared to 1.0-4.8m), with the errors in MERIT being more spatially dependent as indicated by larger range values (308-4364m) compared to SRTM (298-1931m). In addition, semi-variograms were also produced by landcover class. It was found that the spatial error structure differed by landcover class with higher canopy heights generally having a larger sill value, although the relationship was not clear. The fitted semi-variogram parameters were then taken to simulate plausible versions of MERIT or SRTM based on unconditional Gaussian simulation. This procedure does not require hyper/high resolution data to be available and is thus suitable to simulate DEMs in any lowland location. However, by using unconditional simulation, the DEM error at observation points are not eliminated and a Gaussian error field is being added to the simulated DEM, thereby creating a more errorneous DEM. DEMs were simulated either using an 'average' of the semi-variograms produced or by semi-variograms characterised by landcover class. To test the impact of using ensembles of simulated DEMs on flood extent predictions, two flood models of contrasting locations (An Giang, Vietnam and Ba, Fiji) were built. These hydrodynamic models were made of four

deterministic simulations using LIDAR, MERIT and SRTM DEMs and three sets of DEM ensembles. Results indicated that using an ensemble of simulated DEMs avoids the spurious precision in prediction given by models that use a single deterministic DEM and allows the user to explore the impact of topographic uncertainty on flood predictions. Using an ensemble of simulated DEMs can produce higher flood prediction skill score values (e.g. CSI score), despite the simulated DEM being having a larger error than the original DEM. This is likely to be due to the DEM simulation process perturbing the DEM in such a way that river-floodplain connectivity is more conducive, despite the addition of error to the DEM. Flood depth estimates were also explored, with simulated DEMs demonstrating skill in predicting flood depths, potentially avoiding the over-estimation or missing estimates of flood depth. Simulating the MERIT DEM by landcover class consistently gave inundation estimates closest to that of the most detail model which was assumed to be closest to the true situation owing to a lack of validation data. This chapter demonstrated that uncertain topography has a large impact on flood predictions and presented a method where it is now possible to use multiple DEMs even in data-sparse areas. The work has been disseminated through a freely available R package called `DEMsimulation`.

6.1.3 Measuring Floodplain Connectivity of DEMs

Objective 3: Identify and quantify river-floodplain connectivity of DEMs across resolutions

Connectivity is an immensely popular concept in science, with the situation being no different in hydrology. However, there has been a lack of consensus on what exactly is meant by connectivity, how to quantify it and a lack of studies investigating across scales and locations. In this chapter, river-floodplain connectivity was quantified across multiple scales using different DEM products by a novel technique based on connected component labelling and landscape statistics. River-floodplain connectivity was found to vary substantially between DEM products and to a lesser degree across scales. Airborne DEMs (LiDAR) can represent river-floodplain connectivity at lower water elevation scenarios, whilst spaceborne DEMs can only demonstrate similar connectivity at higher river levels.

This suggests that spaceborne DEMs can give good flood predictions in global flood models for large floods but are unable to represent the river-floodplain connectivity that are crucial for smaller floods. However, even though spaceborne DEMs may give the correct result, this may not be for the correct reason as the flood is unlikely to follow the correct pathway given the lack of river-floodplain connectivity representation. This work also suggests that when selecting a DEM to use in a hydrodynamic model that the river-floodplain connectivity should be considered in addition to more traditional accuracy metrics such as RMSE. Whilst a single metric to quantify river-floodplain connectivity could not be produced, this chapter did present 5 metrics as well as maps of river-floodplain connection points, with Total Patch Area and Maximum Connectivity normalized by Number of Patches identified as the most useful to measure river-floodplain connectivity. The method developed in this chapter does not require calibration of a hydrodynamic model and has the potential to be used on hydrodynamic model outputs or remote sensing imagery.

6.2 Synthesis

Accurate flood prediction using hydrodynamic models are crucial for making decisions to reduce flood risk. Large river deltas are some of the most at risk areas from flooding but have not been modelled extensively. Uncertain information on topography has been shown to be highly influential on flood predictions, with this effect even more pronounced in large river deltas due to the extremely flat topography. This thesis has applied hydrodynamic models, geostatistics and image classification techniques to assess the impact of uncertain topographic information on flood predictions. The major scientific findings from this thesis are: 1) An intermediate scale hydrodynamic model of the Mekong Delta built using freely available data shows a good level of skill in flood predictions with topography a major control on predicted extent; 2) Plausible versions of MERIT and SRTM global DEMs can be simulated using spatial error structure characteristics without the need of a reference DEM; 3) Using an ensemble of simulated DEMs avoids the spurious precision in flood predictions when using a single deterministic DEM; 4) Probabilistic flood maps derived from using an ensemble of simulated DEMs gave a range of flood predictions; 5) Airborne DEMs have a more realistic representation of river-floodplain connectivity; 6) Spaceborne DEMs often cannot represent river-floodplain connectivity but still give accurate flood predictions at

high flood levels as sheet flow becomes the dominant process. However, whilst giving reasonable flood predictions at high flood levels, spaceborne DEMs cannot represent the correct river-connectivity processes and thus are getting the right result for the wrong reason; and 7) 5 metrics to quantify river-floodplain connectivity have been proposed.

This thesis has demonstrated that the reductionist view that higher resolution is better for hydrodynamic models is not always appropriate. Uncertain topography has a striking impact on flood predictions, and using a single deterministic DEM leads to spuriously precise estimates. Indeed, a spuriously precise flood inundation map can lull practitioners and decision makers into a fall sense of over-confidence in their results. Therefore, using multiple DEMs are essential to understand how topographic uncertainty impacts on flood predictions. Using multiple DEM products can do this, which is now increasingly possible with the release of TanDEM-X 90. Even better, is the combination of multiple DEMs and simulating DEMs to create an ensemble of DEMs. Thus, there is no reason why any future flood study that uses a global DEM should be using just a single DEM.

The quality of a DEM is important in making accurate flood predictions but traditional accuracy assessment metrics such as RMSE are not necessarily the best metric to use when choosing a DEM to use in a hydrodynamic model. Indeed, the ability of a DEM to represent realistic river-floodplain pathways is crucial as ultimately these connections enable flooding to occur. It is usually the case that a handful of pixels in the DEM control river-floodplain connectivity and correctly assessing the elevations of these pixels is more important than having a more accurate DEM overall. Airborne DEMs (LiDAR) have been found to represent river-floodplain connectivity more realistically but often LiDAR is not available for most locations (only approximately 0.005% of Earth's land area). Spaceborne DEMs have been found to have a poor river-floodplain connectivity at low water levels, and a reasonable river-floodplain connectivity at higher water levels, thus for larger floods the ability of a DEM to represent river-floodplain connectivity is less important. Yet the DEM simulation approach allows us to alter these crucial river-floodplain connectivity points, helping modellers explore the bounds of uncertainty within a DEM.

Despite offering five metrics of quantification of river-floodplain connectivity, it was difficult to devise a single metric. Nevertheless, the easy to implement method presented in this thesis allows for a quick analysis of the ability of a DEM to represent river-floodplain connectivity and can be used in helping to decide the most appropriate DEM to use in the hydrodynamic model. As discussed, modellers should forget about choosing just a single DEM and instead turn their attention to use multiple DEMs to help understand the impact of uncertain topography on their flood estimates. Of course, this depends on the computational resources available. The reason of not having multiple DEMs available is no longer valid owing to the multiple freely accessible global DEM products now available and the DEM simulation approach discussed in this thesis.

The findings in this thesis can help scientists across a range of disciplines and scales. We now know that a hydrodynamic model at an intermediate scale can make skillful predictions of flood extents in large deltas, even if no locally available data is incorporated. This means a worldwide delta flood hazard analysis is possible. We also know that uncertain topography has a significant impact on flood predictions. Previously, different scales have been focused upon, but we now know that there is large variations between DEM products even at the same scale. Using multiple DEMs is essential in helping to determine the impact of topography on flood predictions. DEM simulation has been proved in this thesis to be an invaluable technique to make this possible. Work from this thesis has made world of geostatistical simulation more accessible through the R package `DEMsimulation`, so even if a hydraulic modeller has little or no knowledge of geostatistics, they can take advantageous of the power of geostatistics. Whilst this thesis has focused on the intermediate scale and has used a single hydrodynamic model, the findings from this work can be utilised across scales and models. Topography is hugely important for any terrestrial model but our imperfect representation of it means that the uncertainty involved in it must be explored in order to avoid making spuriously precise predictions. As Davis and Keller (1997b) noted “Landscapes are not uncertain, but knowledge about them is”.

6.3 Recommendations for Future Research

We are in an exciting time for DEM research. Recently, the TanDEM-X mission has released a 3 arc-second DEM product (although *predominantly* a DSM) that covers the whole world. An initial accuracy assessment by myself suggests that TanDEM-X 90 has a better vertical accuracy than SRTM, and only marginally worse than MERIT. When considering landcover types, TanDEM-X 90 has a better vertical accuracy than MERIT for all landcovers except tree-covered areas. Therefore, if vegetation bias can be removed from TanDEM-X 90 it is very possible that it could become the benchmark in global DEMs. TanDEM-X has the additional advantage of having a number of auxiliary files that can be utilised for error removal. In addition, new technologies could make the hyper-resolution global DEM a reality. For instance, ArcticDEM at 2 m resolution may well become available for the entire world. Alternatively, the proliferation of cubesat constellations (in particular Planet Labs) provides an opportunity to create DEMs from photogrammetry as recently demonstrated by Ghuffar (2018) with resolutions at 5 m. PlanetScope imagery has the additional benefit that images are collected at hyper resolution (3.7 m) and daily, so DEMs can be updated and dynamic processes tracked. So it would appear that the days of SRTM are nearly over. The SRTM has well and truly served its purpose and has provided an invaluable dataset for scores of scientific application. Now we are moving from the era of SRTM to a new era of global DEMs.

This thesis has shown that DEM simulation is an important strategy in exploring the impact of uncertain topography on flood predictions. However, this work is only the beginning in reinvigorating the practice of DEM simulation. Additional research is urgently needed to characterise the spatial error structure of more DEM products (e.g. TanDEM-X 90) and to analyse additional locations to we can have more confidence in the spatial error structure relationships found in this thesis. To do this, more reference topographic data is needed. Luckily, LiDAR is becoming increasingly freely available, especially through initiatives such as OpenTopography. Whilst having more LiDAR data is invaluable, better metadata is often required as for a valid investigation into the spatial error structure, we must be confident

about the quality (and most importantly the datum) of the reference data. As more locations are analysed, we can have more confidence in the relationships found in this thesis.

Sticking to the theme of DEM simulation, additional research is needed into fusing simulated DEMs together. When DEMs are simulated by landcover semi-variograms, how can we ensure that the overall DEM are not too noisy as often the areas which are mosaicked together to make the overall DEM are small. For instance, should a smoothing filter be applied over the resultant simulated DEM? And if so, what would be an appropriate filter? Indeed, an aggressive filter may over-smooth the resultant DEM, negating the noisifying effect of simulating DEMs.

A further recommendation for research is to improve the performance of the `DEMsimulation` package. In this thesis, DEM simulation was only performed on relatively small areas. The `DEMsimulation` package has been used to simulate DEMs over a 300x200km area in the Congo Basin with this taking over a day on the hydrology servers at the University of Bristol. Whilst not an excessive amount of time, most of the intended users will not have access to such facilities. For the Congo basin case, memory issues were an issue when trying to run on a Desktop computer. Therefore, optimisation of the code is needed to overcome the memory limitations and to parallelise, with the later potentially leading to considerable performance gains if the simulation by landcover type approach is followed.

Whilst probabilistic hazard maps are useful in conveying the uncertainty in flood prediction, they can be difficult to understand for the non-expert. Therefore, further research is needed to build on the existing literature (Hagemeier-Klose and Wagner, 2009, Di Baldassarre et al., 2010, Meyer et al., 2012, Alfonso et al., 2016, Macchione et al., 2018, Kuser Olsen et al., 2018) into the presentation of probabilistic flood hazard maps. There also needs to be more flood hazard map co-production so the maps show the most useful information for the end user (Luke et al., 2018, Lane et al., 2011).

A final recommendation is to further develop the river-floodplain connectivity methodology. Whilst work in this thesis has quantified river-floodplain connectivity of DEMs across scales, it has not explored it over multiple locations. An additional challenge will be normalizing the quantification of river-floodplain connectivity so different locations at different scales can be compared. Ideally this would be a single value that would be prescribed to each DEM. The question remains whether this is even possible given the complexity of river-floodplain connectivity, but this thesis has demonstrated the image classification and landscape statistics has potential to quantify river-floodplain connectivity without using hydrodynamic models.

This thesis has proved the significant impact that uncertain topography has on flood predictions. The sensitivity of hydrodynamic models to different DEMs at different resolutions is a highly complex and location dependent problem. We therefore urge modellers to not focus so much on the sensitivity of hydrodynamic models to hydraulic parameters, but to further consider the impact of topographic uncertainty in their predictions by either using multiple DEM products and/or simulated DEMs.

Chapter 7 References

ABBOT, M. B. 1979. *Computational Hydraulics: Elements of the Theory of Free Surface Flows,* London, Pitman.

ABRAMS, M. 2000. The Advanced Spaceborne Thermal Emission and Reflection Radiometer (ASTER): Data products for the high spatial resolution imager on NASA's Terra platform. *International Journal of Remote Sensing,* 21, 847-859.

ADNAN, N. A. & ATKINSON, P. M. 2012. Remote Sensing of River Bathymetry for Use in Hydraulic Model Prediction of Flood Inundation. *IEEE 8th International Colloquium on Signal Processing and its Applications.*

AERTS, J., GOODCHILD, M. F. & HEUVELINK, G. B. M. 2003. Accounting for Spatial Uncertainty in Optimization with Spatial Decision Support Systems. *Transactions in GIS,* 7, 211-230.

AFSHARI, S., TAVAKOLY, A. A., RAJIB, M. A., ZHENG, X., FOLLUM, M. L., OMRANIAN, E. & FEKETE, B. M. 2018. Comparison of new generation low-complexity flood inundation mapping tools with a hydrodynamic model. *Journal of Hydrology,* 556, 539-556.

ALBERT, S., ABERNETHY, K., GIBBES, B., GRINHAM, A., TOOLER, N. & ASWANI, S. 2013. Cost-Effective Methods for Accurate Determination of Sea Level Rise Vulnerability: A Solomon Islands Example. *Weather, Climate, and Society,* 5, 285-292.

ALFIERI, L., BISSELINK, B., DOTTORI, F., NAUMANN, G., DE ROO, A., SALAMON, P., WYSER, K. & FEYEN, L. 2017. Global projections of river flood risk in a warmer world. *Earth's Future,* 5, 171-182.

ALFIERI, L., SALAMON, P., BIANCHI, A., NEAL, J., BATES, P. & FEYEN, L. 2014. Advances in pan-European flood hazard mapping. *Hydrological Processes,* 28, 4067-4077.

ALFONSO, L., MUKOLWE, M. M. & DI BALDASSSARRE, G. 2016. Probabilistic flood maps to support decision-making: Mapping the Value of Information. *Water Resources Research*, n/a-n/a.

ALI, G. A. & ROY, A. G. 2009. Revisiting Hydrologic Sampling Strategies for an Accurate Assessment of Hydrologic Connectivity in Humid Temperate Systems. *Geography Compass,* 3, 350-374.

ALI, G. A. & ROY, A. G. 2010. Shopping for hydrologically representative connectivity metrics in a humid temperate forested catchment. *Water Resources Research,* 46.

ALI, H. T. 2016. *Digital Urban Terrain Characterization for 1D2D Hydrodynamic Flood Modelling in Kigali, Rwanda.* Master of Science, University of Twente.

ALLEN, G. H. & PAVELSKY, T. M. 2018. Global Extent of Rivers and Streams. *Science*.

ALLEN, M. B., SAVILLE, C., BLANC, E. J. P., TALEBIAN, M. & NISSEN, E. 2013. Orogenic plateau growth: Expansion of the Turkish-Iranian Plateau across the Zagros fold-and-thrust belt. *Tectonics,* 32, 171-190.

ALLEN, T. I. & WALD, D. J. 2009. On the Use of High-Resolution Topographic Data as a Proxy for Seismic Site Conditions (VS30). *Bulletin of the Seismological Society of America,* 99, 935-943.

ALTENAU, E. H., PAVELSKY, T. M., BATES, P. D. & NEAL, J. C. 2017. The effects of spatial resolution and dimensionality on modeling regional-scale hydraulics in a multichannel river. *Water Resources Research,* 53, 1683-1701.

AMOROS, C. & BORNETTE, G. 2002. Connectivity and biocomplexity in waterbodies of riverine floodplains. *Freshwater Biology,* 47, 761-776.

ANDERSON, J. L. 1996. A Method for Producing and Evaluating Probabilistic Forecasts from Ensemble Model Integrations. *Journal of Climate,* 9, 1518-1530.

ANDREADIS, K. M., SCHUMANN, G. J. P. & PAVELSKY, T. 2013. A simple global river bankfull width and depth database. *Water Resources Research,* 49, 7164-7168.

ANH, D. T., HOANG, L. P., BUI, M. D. & RUTSCHMANN, P. 2018. Modelling seasonal flows alteration in the Vietnamese Mekong Delta under upstream discharge changes, rainfall changes and sea level rise. *International Journal of River Basin Management*, 1-15.

ANH, L. T., TAKAGI, H., THAO, N. & ESTEBAN, M. 2017. Investigation of Awareness of Typhoon and Storm Surge in the Mekong Delta – Recollection of 1997 Typhoon Linda. *Journal of Japan Society of Civil Engineers, Ser. B3 (ocean Engineering),* 73, 168-173.

ANTHONY, E. J., BRUNIER, G., BESSET, M., GOICHOT, M., DUSSOUILLEZ, P. & NGUYEN, V. L. 2015. Linking rapid erosion of the Mekong River delta to human activities. *Sci Rep,* 5, 14745.

APEL, H., ARONICA, G. T., KREIBICH, H. & THIEKEN, A. H. 2009. Flood risk analyses—how detailed do we need to be? *Natural Hazards,* 49, 79-98.

APEL, H., MARTÍNEZ TREPAT, O., HUNG, N. N., CHINH, D. T., MERZ, B. & DUNG, N. V. 2016. Combined fluvial and pluvial urban flood hazard analysis: concept development and application to Can Tho city, Mekong Delta, Vietnam. *Natural Hazards and Earth System Sciences,* 16, 941-961.
APEL, H., MERZ, B. & THIEKEN, A. H. 2008. Quantification of uncertainties in flood risk assessments. *International Journal of River Basin Management,* 6, 149-162.
ARCEMENT, G. & SCHNEIDER, V. 1989. Guide for Selecting Manning's Roughness Coefficients for Natural Channels and Floodplains. *U.S. Geological Survey Water Supply Paper 2339.* U. S. Government Printing Office.
ARCHER, L., NEAL, J., BATES, P. & HOUSE, J. 2018. Comparing TanDEM-X Data with Frequently Used DEMs for Flood Inundation Modelling. *Water Resources Research,* 54, 10,205–10,222.
ARIAS, M. E., PIMAN, T., LAURI, H., COCHRANE, T. A. & KUMMU, M. 2014. Dams on Mekong tributaries as significant contributors of hydrological alterations to the Tonle Sap Floodplain in Cambodia. *Hydrology and Earth System Sciences,* 18, 5303-5315.
ARNELL, N. W. & GOSLING, S. N. 2016. The impacts of climate change on river flood risk at the global scale. *Climatic Change,* 134, 387-401.
ARNELL, N. W., LOWE, J. A., LLOYD-HUGHES, B. & OSBORN, T. J. 2018. The impacts avoided with a 1.5 °C climate target: a global and regional assessment. *Climatic Change,* 147, 61-76.
ARONICA, G., BATES, P. D. & HORRITT, M. S. 2002. Assessing the uncertainty in distributed model predictions using observed binary pattern information within GLUE. *Hydrological Processes,* 16, 2001-2016.
ATHMANIA, D. & ACHOUR, H. 2014. External Validation of the ASTER GDEM2, GMTED2010 and CGIAR-CSI- SRTM v4.1 Free Access Digital Elevation Models (DEMs) in Tunisia and Algeria. *Remote Sensing,* 6, 4600-4620.
AVTAR, R., YUNUS, A. P., KRAINES, S. & YAMAMURO, M. 2015. Evaluation of DEM generation based on Interferometric SAR using TanDEM-X data in Tokyo. *Physics and Chemistry of the Earth, Parts A/B/C,* 83-84, 166-177.
BAILEY, J. E., SELF, S., WOOLLER, L. K. & MOUGINIS-MARK, P. J. 2007. Discrimination of fluvial and eolian features on large ignimbrite sheets around La Pacana Caldera, Chile, using Landsat and SRTM-derived DEM. *Remote Sensing of Environment,* 108, 24-41.
BARNES, R., LEHMAN, C. & MULLA, D. 2014. Priority-flood: An optimal depression-filling and watershed-labeling algorithm for digital elevation models. *Computers & Geosciences,* 62, 117-127.
BARTHÉLÉMY, S., RICCI, S., MOREL, T., GOUTAL, N., LE PAPE, E. & ZAOUI, F. 2018. On operational flood forecasting system involving 1D/2D coupled hydraulic model and data assimilation. *Journal of Hydrology,* 562, 623-634.
BATER, C. W. & COOPS, N. C. 2009. Evaluating error associated with lidar-derived DEM interpolation. *Computers & Geosciences,* 35, 289-300.
BATES, P. & DE ROO, A. P. J. 2000. A simple raster-based model for flood inundation simulation. *Journal of Hydrology,* 236, 54-77.
BATES, P., HORRITT, M., HUNTER, N. M., MASON, D. & COBBY, D. M. 2005a. Numerical modelling of floodplain flow. *In:* BATES, P., LANE, S. N. & FERGUSON, R. I. (eds.) *Computational fluid dynamics: applications in environmental hydraulics.* Chichester: Wiley.
BATES, P. D. 2012. Integrating remote sensing data with flood inundation models: how far have we got? *Hydrological Processes,* 26, 2515-2521.
BATES, P. D., DAWSON, R. J., HALL, J. W., HORRITT, M. S., NICHOLLS, R. J., WICKS, J. & MOHAMED AHMED ALI MOHAMED, H. 2005b. Simplified two-dimensional numerical modelling of coastal flooding and example applications. *Coastal Engineering,* 52, 793-810.
BATES, P. D., HORRITT, M. S., ARONICA, G. & BEVEN, K. 2004. Bayesian updating of flood inundation likelihoods conditioned on flood extent data. *Hydrological Processes,* 18, 3347-3370.
BATES, P. D., HORRITT, M. S. & FEWTRELL, T. J. 2010. A simple inertial formulation of the shallow water equations for efficient two-dimensional flood inundation modelling. *Journal of Hydrology,* 387, 33-45.
BATES, P. D., WILSON, M. D., HORRITT, M. S., MASON, D. C., HOLDEN, N. & CURRIE, A. 2006. Reach scale floodplain inundation dynamics observed using airborne synthetic aperture radar imagery: Data analysis and modelling. *Journal of Hydrology,* 328, 306-318.
BAUGH, C. A., BATES, P. D., SCHUMANN, G. & TRIGG, M. A. 2013. SRTM vegetation removal and hydrodynamic modeling accuracy. *Water Resources Research,* 49, 5276-5289.

BECEK, K. 2008. Investigating error structure of shuttle radar topography mission elevation data product. *Geophysical Research Letters,* 35.
BELISLE, M. 2005. Measuring Landscape Connectivity: The challenge of Behavioral Landcape Ecology. *Ecology,* 86, 1988-1995.
BERG, H., EKMAN SÖDERHOLM, A., SÖDERSTRÖM, A.-S. & TAM, N. T. 2017. Recognizing wetland ecosystem services for sustainable rice farming in the Mekong Delta, Vietnam. *Sustainability Science,* 12, 137-154.
BERNER, Z. A., BLEECK-SCHMIDT, S., STÜBEN, D., NEUMANN, T., FUCHS, M. & LEHMANN, M. 2012. Floodplain deposits: A geochemical archive of flood history – A case study on the River Rhine, Germany. *Applied Geochemistry,* 27, 543-561.
BERRY, P. A. M., PINNOCK, R. A., HILTON, R. D. & JOHNSON, C. P. D. ACE: a new global digital elevation model incorporating satellite altimeter derived heights. ERS-Envisat Symposium. 2000, 2000.
BESSET, M., ANTHONY, E. J., BRUNIER, G. & DUSSOUILLEZ, P. 2016. Shoreline change of the Mekong River delta along the southern part of the South China Sea coast using satellite image analysis (1973-2014). *Géomorphologie : relief, processus, environnement,* 22, 137-146.
BEVEN, K. & KIRKBY, M. J. 1979. A Physically based, variable contributing area model of basin hydrology. *Hydrological Sciences Bulletin,* 24, 43-69.
BEVEN, K., SMITH, P. J. & WOOD, A. 2011. On the colour and spin of epistemic error (and what we might do about it). *Hydrology and Earth System Sciences,* 15, 3123-3133.
BEVEN, K. & WESTERBERG, I. 2011. On red herrings and real herrings: disinformation and information in hydrological inference. *Hydrological Processes,* 25, 1676-1680.
BEVEN, K. J., ASPINALL, W. P., BATES, P. D., BORGOMEO, E., GODA, K., HALL, J. W., PAGE, T., PHILLIPS, J. C., SIMPSON, M., SMITH, P. J., WAGENER, T. & WATSON, M. 2018. Epistemic uncertainties and natural hazard risk assessment – Part 2: What should constitute good practice? *Natural Hazards and Earth System Sciences,* 18, 2769-2783.
BHUYIAN, M. N. M. & KALYANAPU, A. 2018. Accounting digital elevation uncertainty for flood consequence assessment. *Journal of Flood Risk Management,* 11, S1051-S1062.
BIANCAMARIA, S., BATES, P. D., BOONE, A. & MOGNARD, N. M. 2009. Large-scale coupled hydrologic and hydraulic modelling of the Ob river in Siberia. *Journal of Hydrology,* 379, 136-150.
BIGGS, D. A. 2010. *Quagmire: Nation-Building and nature in the Mekong Delta,* Seattle, University of Washington Press.
BILDIRICI, O. I., USTUN, A., SELVI, Z. H., ABBAK, A. R. & BUGDAYCI, I. 2009. Assessment of Shuttle Radar Topography Mission Elevation Data Based on Topographic Maps in Turkey. *Cartography and Geographic Information Science,* 36, 95-104.
BOURGINE, B. & BAGHDADI, N. 2005. Assessment of C-band SRTM DEM in a dense equatorial forest zone. *Comptes Rendus Geoscience,* 337, 1225-1234.
BOX, G. E. P. & JENKINS, G. M. 1970. *Time Series Analysis: Forecasting and Control,* San Francisco, USA, Holden Day Press.
BRACKEN, L. J. & CROKE, J. 2007. The concept of hydrological connectivity and its contribution to understanding runoff-dominated geomorphic systems. *Hydrological Processes,* 21, 1749-1763.
BRACKEN, L. J., WAINWRIGHT, J., ALI, G. A., TETZLAFF, D., SMITH, M. W., REANEY, S. M. & ROY, A. G. 2013. Concepts of hydrological connectivity: Research approaches, pathways and future agendas. *Earth-Science Reviews,* 119, 17-34.
BRANDIMARTE, L. 2012. Theoretical background: steady flow. *In:* DI BALDASSARRE, G. (ed.) *Floods in a Changing Climate: Inundation Modelling.* Cambridge: Cambridge University Press.
BRÁZDIL, R., CHROMÁ, K., ŘEZNÍČKOVÁ, L., VALÁŠEK, H., DOLÁK, L., STACHOŇ, Z., SOUKALOVÁ, E. & DOBROVOLNÝ, P. 2014. The use of taxation records in assessing historical floods in South Moravia, Czech Republic. *Hydrology and Earth System Sciences,* 18, 3873-3889.
BRÁZDIL, R., KUNDZEWICZ, Z. W. & BENITO, G. 2006. Historical hydrology for studying flood risk in Europe. *Hydrological Sciences Journal,* 51, 739-764.
BRUNIER, G., ANTHONY, E. J., GOICHOT, M., PROVANSAL, M. & DUSSOUILLEZ, P. 2014. Recent morphological changes in the Mekong and Bassac river channels, Mekong delta: The marked impact of river-bed mining and implications for delta destabilisation. *Geomorphology,* 224, 177-191.

BURNHAM, K. P. & ANDERSON, D. R. 2002. *Model Selection and Multimodel Inference,* New York, Springer.
BURROUGH, P. A. & MCDONNELL, R. A. 1998. *Principles of Geographical Information systems,* Oxford, UK, Oxford University Press.
BYNA, S., PRABHAT, WEHNER, M. F. & WU, K. Detecting Atmospheric Rivers in Large Climate Datasets Proc. 2nd Int. Workshop Petascale Data Analytics: Challenges Opportunities, Nov 14, 2011 2011.
CABARET, L., LACASSAGNE, L. & ETIEMBLE, D. 2018. Parallel Light Speed Labeling: an efficient connected component algorithm for labeling and analysis on multi-core processors. *Journal of Real-Time Image Processing,* 15, 173-196.
CALABRESE, J. M. & FAGAN, W. F. 2004. A comparison-shopper's guide to connectivity metrics. *Frontiers in Ecology and the Environment,* 2, 539-536.
CALLOW, J. N., VAN NIEL, K. P. & BOGGS, G. S. 2007. How does modifying a DEM to reflect known hydrology affect subsequent terrain analysis? *Journal of Hydrology,* 332, 30-39.
CAMPBELL, I. C. 2012. Biodiversity of the Mekong Delta. *In:* RENAUD, F. G. & KUENZER, C. (eds.) *The Mekong Delta System: Interdisciplinary Analyses of a River Delta.* Dordrecht: Springer Netherlands.
CANTERS, F., GENST, W. D. & DUFOURMONT, H. 2002. Assessing effects of input uncertainty in structural landscape classification. *International Journal of Geographical Information Science,* 16, 129-149.
CARABAJAL, C. C. & HARDING, D. J. 2006. SRTM C-Band and ICESat Laser Altimetry Elevation Comparisons as a Function of Tree Cover and Relief. *Photogrammetric Engineering & Remote Sensing,* 72.
CARLISLE, B. H. 2005. Modelling the Spatial Distribution of DEM Error. *Transactions in GIS,* 9, 521-540.
CARRERE, L., LYARD, F., CANCET, M. & GUILLOT, A. 2015. FES 2014, a new tidal model on the global ocean with enhanced accuracy in shallow seas and in the Arctic region *EGU General Assembly 2015.* Vienna.
CASAS, A., BENITO, G., THORNDYCRAFT, V. R. & RICO, M. 2006. The topographic data source of digital terrain models as a key element in the accuracy of hydraulic flood modelling. *Earth Surface Processes and Landforms,* 31, 444-456.
CEDERBERG, R. L. T. 1979. Chain-Link Coding and Segmentation for Raster Scan Devices *Computer Graphics and Image Processing,* 10, 224-234.
CHANG, W. Y., CHIU, C. C. & YANG, J. H. 2015. Block-Based Connected-Component Labeling Algorithm Using Binary Decision Trees. *Sensors (Basel),* 15, 23763-87.
CHAPLOT, V. 2005. Impact of DEM mesh size and soil map scale on SWAT runoff, sediment, and NO3–N loads predictions. *Journal of Hydrology,* 312, 207-222.
CHAPLOT, V., DARBOUX, F., BOURENNANE, H., LEGUÉDOIS, S., SILVERA, N. & PHACHOMPHON, K. 2006. Accuracy of interpolation techniques for the derivation of digital elevation models in relation to landform types and data density. *Geomorphology,* 77, 126-141.
CHAPMAN, A. D., DARBY, S. E., HỒNG, H. M., TOMPKINS, E. L. & VAN, T. P. D. 2016. Adaptation and development trade-offs: fluvial sediment deposition and the sustainability of rice-cropping in An Giang Province, Mekong Delta. *Climatic Change,* 137, 593-608.
CHAUBEY, I., COTTER, A. S., COSTELLO, T. A. & SOERENS, T. S. 2005. Effect of DEM data resolution on SWAT output uncertainty. *Hydrological Processes,* 19, 621-628.
CHAUDHRY, M. H. 2007. *Open-Channel Flow*, Springer.
CHEN, A. S., EVANS, B., DJORDJEVIĆ, S. & SAVIĆ, D. A. 2012. A coarse-grid approach to representing building blockage effects in 2D urban flood modelling. *Journal of Hydrology,* 426-427, 1-16.
CHEN, C. & LI, Y. 2012. An Adaptive Method of Non-stationary Variogram Modeling for DEM Error Surface Simulation. *Transactions in GIS,* 16, 885-899.
CHEN, H., LIANG, Q., LIU, Y. & XIE, S. 2018. Hydraulic correction method (HCM) to enhance the efficiency of SRTM DEM in flood modeling. *Journal of Hydrology,* 559, 56-70.
CHINH, D. T., BUBECK, P., DUNG, N. V. & KREIBICH, H. 2016. The 2011 flood event in the Mekong Delta: preparedness, response, damage and recovery of private households and small businesses. *Disasters,* 40, 753-78.
CHOW, T. E. & HODGSON, M. E. 2009. Effects of lidar post-spacing and DEM resolution to mean slope estimation. *International Journal of Geographical Information Science,* 23, 1277-1295.
CHOW, V. 1959. *Open-channel Hydraulics,* New York, McGraw Hill.

CHRISMAN, N. Error in Categorical maps: Testing versus Simulation. Auto-Carto 9: Proceedings of the 9th International Symposium on Computer-Assisted Cartography, 1989 Baltimore, Maryland. ASPRS/ACSM, 521-529.
CLAESSENS, L., HEUVELINK, G. B. M., SCHOORL, J. M. & VELDKAMP, A. 2005. DEM resolution effects on shallow landslide hazard and soil redistribution modelling. *Earth Surface Processes and Landforms,* 30, 461-477.
CLEMENS, J. K. 1965. *Optical character recognition for reading machine applications.* Ph.D, Massachussets Institute of Technology.
COCHRANE, T. A., ARIAS, M. E. & PIMAN, T. 2014. Historical impact of water infrastructure on water levels of the Mekong River and the Tonle Sap system. *Hydrology and Earth System Sciences,* 18, 4529-4541.
COLEMAN, J. M. & HUH, O. K. 2004. Major deltas of the world: A perspective from Space. Baton Rouge, LA: Coastal Studies Institute, Louisiana State University.
COOK, A. & MERWADE, V. 2009. Effect of topographic data, geometric configuration and modeling approach on flood inundation mapping. *Journal of Hydrology,* 377, 131-142.
COULTHARD, T. J., NEAL, J. C., BATES, P. D., RAMIREZ, J., DE ALMEIDA, G. A. M. & HANCOCK, G. R. 2013. Integrating the LISFLOOD-FP 2D hydrodynamic model with the CAESAR model: implications for modelling landscape evolution. *Earth Surface Processes and Landforms,* 38, 1897-1906.
COURTY, L., SORIANO-MONZALVO, J. & PEDROZO-ACUNA 2017. Evaluation of open-access global digital elevation models (AW3D30, SRTM and ASTER) for flood modelling purposes.
COVENEY, S. & ROBERTS, K. 2017. Lightweight UAV digital elevation models and orthoimagery for environmental applications: data accuracy evaluation and potential for river flood risk modelling. *International Journal of Remote Sensing,* 38, 3159-3180.
COVINO, T. 2017. Hydrologic connectivity as a framework for understanding biogeochemical flux through watersheds and along fluvial networks. *Geomorphology,* 277, 133-144.
COWELL, P. J. & ZENG, T. Q. 2003. Integrating Uncertainty Theories with GIS for Modeling Coastal Hazards of Climate Change. *Marine Geodesy,* 26, 5-18.
CREED, I. F. & BAND, L. E. 1998. Exploring functional similarity in the export of Nitrate-N from forested catchments: A mechanistic modeling approach. *Water Resources Research,* 34, 3079-3093.
CRIPPEN, R., BUCKLEY, S., AGRAM, P., BELZ, E., GURROLA, E., HENSLEY, S., KOBRICK, M., LAVALLE, M., MARTIN, J., NEUMANN, M., NGUYEN, Q., ROSEN, P., SHIMADA, J., SIMARD, M. & TUNG, W. 2016. Nasadem Global Elevation Model: Methods and Progress. *ISPRS - International Archives of the Photogrammetry, Remote Sensing and Spatial Information Sciences,* XLI-B4, 125-128.
CROKE, J., FRYIRS, K. & THOMPSON, C. 2013. Channel–floodplain connectivity during an extreme flood event: implications for sediment erosion, deposition, and delivery. *Earth Surface Processes and Landforms,* 38, 1444-1456.
CROKE, J., MOCKLER, S., FOGARTY, P. & TAKKEN, I. 2005. Sediment concentration changes in runoff pathways from a forest road network and the resultant spatial pattern of catchment connectivity. *Geomorphology,* 68, 257-268.
CUNGE, J. A. 2003. Of data and models. *Journal of Hydroinformatics,* 5, 75-99.
CURRAN, P. J. 1988. The Semivariogram in Remote Sensing An Introduction *Remote Sensing of Environment,* 24, 493-507.
CYPHER, R. E., SANZ, J. L. C. & SNYDER, L. 1990. Algorithms for image component labeling on SIMD mesh-connected computers. *IEEE Transactions on Computers,* 39, 276-281.
CZUBA, J. A. & FOUFOULA-GEORGIOU, E. 2015. Dynamic connectivity in a fluvial network for identifying hotspots of geomorphic change. *Water Resources Research,* 51, 1401-1421.
DANG, T. D., COCHRANE, T. A., ARIAS, M. E. & TRI, V. P. D. 2018. Future hydrological alterations in the Mekong Delta under the impact of water resources development, land subsidence and sea level rise. *Journal of Hydrology: Regional Studies,* 15, 119-133.
DANG, T. D., COCHRANE, T. A., ARIAS, M. E., VAN, P. D. T. & DE VRIES, T. T. 2016. Hydrological alterations from water infrastructure development in the Mekong floodplains. *Hydrological Processes,* 30, 3824-3838.
DANIELSON, J. J. & GESCH, D. B. 2011. Global multi-resolution terrain elevation data 2010 (GMTED2010).
DANIELSON, P. E. 1981. An Improvement of Kruse's Segmentation Algorithm *Computer Graphics and Image Processing,* 17, 394-396.

DARNELL, A. R., TATE, N. J. & BRUNSDON, C. 2008. Improving user assessment of error implications in digital elevation models. *Computers, Environment and Urban Systems,* 32, 268-277.
DAVIS, G. H., COUNTS, H. & HOLDAHL, S. Further examination of subsidence at Savannah, Georgia, 1955-1975. Proceedings of the Anaheim Symposium December 1976, 1976. International Association of Hydrological Sciences.
DAVIS, T. J. & KELLER, C. P. 1997a. Modelling and visualizing multiple spatial uncertainties. *Computers & Geosciences,* 23, 397-408.
DAVIS, T. J. & KELLER, C. P. 1997b. Modelling uncertainty in natural resource analysis using fuzzy sets and Monte Carlo simulation: slope stability prediction. *International Journal of Geographical Information Science,* 11, 409-434.
DAY, G., DIETRICH, W. E., ROWLAND, J. C. & MARSHALL, A. 2008. The depositional web on the floodplain of the Fly River, Papua New Guinea. *Journal of Geophysical Research,* 113.
DAY, J. W., AGBOOLA, J., CHEN, Z., D'ELIA, C., FORBES, D. L., GIOSAN, L., KEMP, P., KUENZER, C., LANE, R. R., RAMACHANDRAN, R., SYVITSKI, J. & YAÑEZ-ARANCIBIA, A. 2016. Approaches to defining deltaic sustainability in the 21st century. *Estuarine, Coastal and Shelf Science,* 183, 275-291.
DE ALMEIDA, G. A. M., BATES, P., FREER, J. E. & SOUVIGNET, M. 2012. Improving the stability of a simple formulation of the shallow water equations for 2-D flood modeling. *Water Resources Research,* 48.
DE FERRANTI, J. 2014. Viewfinder Panorama.
DEGIORGIS, M., GNECCO, G., GORNI, S., ROTH, G., SANGUINETI, M. & TARAMASSO, A. C. 2012. Classifiers for the detection of flood-prone areas using remote sensed elevation data. *Journal of Hydrology,* 470-471, 302-315.
DELGADO, J. M., MERZ, B. & APEL, H. 2012. A climate-flood link for the lower Mekong River. *Hydrology and Earth System Sciences,* 16, 1533-1541.
DENG, Y., WILSON, J. P. & BAUER, B. O. 2007. DEM resolution dependencies of terrain attributes across a landscape. *International Journal of Geographical Information Science,* 21, 187-213.
DESMET, P. J. J. 1997. Effects of interpolation errors on the analysis of DEMs. *Earth Surface Processes and Landforms,* 22, 563-580.
DEUTSCH, C. V. & JOURNEL, A. G. 1998. *GSLIB: Geostatistical Software Library and User's Guide,* New York, Oxford University Press.
DI BALDASSARRE, G. 2012a. Model building. *In:* DI BALDASSARRE, G. (ed.) *Floods in a Changing Climate: Inundation Modelling.* Cambridge: Cambridge University Press.
DI BALDASSARRE, G. 2012b. Model evaluation. *In:* DI BALDASSARRE, G. (ed.) *Floods in a Changing Climate: Inundation Modelling.* Cambridge: Cambridge University Press.
DI BALDASSARRE, G., KOOY, M., KEMERINK, J. S. & BRANDIMARTE, L. 2013. Towards understanding the dynamic behaviour of floodplains as human-water systems. *Hydrology and Earth System Sciences,* 17, 3235-3244.
DI BALDASSARRE, G. & MONTANARI, A. 2009. Uncertainty in river discharge observations: a quantitative analysis. *Hydrology and Earth System Sciences,* 13, 913-921.
DI BALDASSARRE, G., SCHUMANN, G., BATES, P. D., FREER, J. E. & BEVEN, K. J. 2010. Flood-plain mapping: a critical discussion of deterministic and probabilistic approaches. *Hydrological Sciences Journal,* 55, 364-376.
DI BALDASSARRE, G., SCHUMANN, G., BRANDIMARTE, L. & BATES, P. 2011. Timely Low Resolution SAR Imagery To Support Floodplain Modelling: a Case Study Review. *Surveys in Geophysics,* 32, 255-269.
DI STEFANO, L. & BULGARELLI, A. A Simple and Efficient Connected Components Labeling Algorithm. International Conference on Image Analysis and Processing IEEE, 1999. 322-327.
DOMENEGHETTI, A., CASTELLARIN, A. & BRATH, A. 2012. Assessing rating-curve uncertainty and its effects on hydraulic model calibration. *Hydrology and Earth System Sciences,* 16, 1191-1202.
DOMENEGHETTI, A., VOROGUSHYN, S., CASTELLARIN, A., MERZ, B. & BRATH, A. 2013. Probabilistic flood hazard mapping: effects of uncertain boundary conditions. *Hydrology and Earth System Sciences,* 17, 3127-3140.
DON, N. C., HANG, N. T. M., ARAKI, H., YAMANISHI, H. & KOGA, K. 2006. Groundwater resources management under environmental constraints in Shiroishi of Saga plain, Japan. *Environmental Geology,* 49, 601-609.

DONNER, W. & RODRIGUEZ, H. 2008. Population Composition, Migration and Inequality: The Influence of Demographic Changes on Disaster Risk and Vulnerability. *Social Factors,* 87, 1089-1114.
DOTTORI, F., DI BALDASSARRE, G. & TODINI, E. 2013. Detailed data is welcome, but with a pinch of salt: Accuracy, precision, and uncertainty in flood inundation modeling. *Water Resources Research,* 49, 6079-6085.
DOTTORI, F., SZEWCZYK, W., CISCAR, J.-C., ZHAO, F., ALFIERI, L., HIRABAYASHI, Y., BIANCHI, A., MONGELLI, I., FRIELER, K., BETTS, R. A. & FEYEN, L. 2018. Increased human and economic losses from river flooding with anthropogenic warming. *Nature Climate Change,* 8, 781-786.
DOUGLAS, I., ALAM, K., MAGHENDA, M., MCDONNELL, Y., MCLEAN, L. & CAMPBELL, J. 2008. Unjust waters: climate change, flooding and the urban poor in Africa. *Environment and Urbanization,* 20, 187-205.
DOYLE, F. J. 1978. Digital Terrain Models: An Overview. *Photogrammetric Engineering & Remote Sensing,* 44, 1481-1485.
DOYLE, T. W., DAY, R. H. & MICHOT, T. C. 2010. Development of Sea Level Rise Scenarios for Climate Change Assessments of the Mekong Delta, Vietnam. U.S Geological Survey.
DU, X., GUO, H., FAN, X., ZHU, J., YAN, Z. & ZHAN, Q. 2016a. Vertical accuracy assessment of freely available digital elevation models over low-lying coastal plains. *International Journal of Digital Earth,* 9, 252-271.
DU, Y., ZHANG, Y., LING, F., WANG, Q., LI, W. & LI, X. 2016b. Water Bodies' Mapping from Sentinel-2 Imagery with Modified Normalized Difference Water Index at 10-m Spatial Resolution Produced by Sharpening the SWIR Band. *Remote Sensing,* 8.
DUC TRAN, D., VAN HALSEMA, G., HELLEGERS, P. J. G. J., PHI HOANG, L., QUANG TRAN, T., KUMMU, M. & LUDWIG, F. 2018. Assessing impacts of dike construction on the flood dynamics of the Mekong Delta. *Hydrology and Earth System Sciences,* 22, 1875-1896.
DUN, O. 2011. Migration and Displacement Triggered by Floods in the Mekong Delta. *International Migration,* 49, e200-e223.
DUNG, N. V., MERZ, B., BÁRDOSSY, A., THANG, T. D. & APEL, H. 2011. Multi-objective automatic calibration of hydrodynamic models utilizing inundation maps and gauge data. *Hydrology and Earth System Sciences,* 15, 1339-1354.
DUONG, V. H. T., TRINH CONG, V., FRANZ, N., PETER, O. & NYUGEN TRUNG, N. Land use based flood hazards analysis for the mekong delta. Proceedings of the 19 Th IAHR–APD Congress, 2014.
DURAND, M., ANDREADIS, K. M., ALSDORF, D. E., LETTENMAIER, D. P., MOLLER, D. & WILSON, M. 2008. Estimation of bathymetric depth and slope from data assimilation of swath altimetry into a hydrodynamic model. *Geophysical Research Letters,* 35.
DUTTA, D., ALAM, J., UMEDA, K., HAYASHI, M. & HIRONAKA, S. 2007. A two-dimensional hydrodynamic model for flood inundation simulation: a case study in the lower Mekong river basin. *Hydrological Processes,* 21, 1223-1237.
ENDRENY, T. A. & WOOD, E. F. 2001. Representing elevation uncertainty in runoff modelling and flowpath mapping. *Hydrological Processes,* 15, 2223-2236.
ERÄNEN, D., OKSANEN, J., WESTERHOLM, J. & SARJAKOSKI, T. 2014. A full graphics processing unit implementation of uncertainty-aware drainage basin delineation. *Computers & Geosciences,* 73, 48-60.
ERBAN, L. E. & GORELICK, S. M. 2016. Closing the irrigation deficit in Cambodia: Implications for transboundary impacts on groundwater and Mekong River flow. *Journal of Hydrology,* 535, 85-92.
ERBAN, L. E., GORELICK, S. M. & ZEBKER, H. A. 2014. Groundwater extraction, land subsidence, and sea-level rise in the Mekong Delta, Vietnam. *Environmental Research Letters,* 9, 084010.
ERDOGAN, S. 2009. A comparision of interpolation methods for producing digital elevation models at the field scale. *Earth Surface Processes and Landforms,* 34, 366-376.
ERICSON, J., VOROSMARTY, C., DINGMAN, S., WARD, L. & MEYBECK, M. 2006. Effective sea-level rise and deltas: Causes of change and human dimension implications. *Global and Planetary Change,* 50, 63-82.
ETTRITCH, G., HARDY, A., BOJANG, L., CROSS, D., BUNTING, P. & BREWER, P. 2018. Enhancing digital elevation models for hydraulic modelling using flood frequency detection. *Remote Sensing of Environment,* 217, 506-522.

FABRIS, M., ACHILLI, V. & MENIN, A. 2014. Estimation of Subsidence in Po Delta Area (Northern Italy) by Integration of GPS Data, High-Precision Leveling and Archival Orthometric Elevations. *International Journal of Geosciences,* 05, 571-585.
FALORNI, G., TELES, V., VIVONI, E. R., BRAS, R. L. & AMARATUNGA, K. S. 2005. Analysis and characterization of the vertical accuracy of digital elevation models from the Shuttle Radar Topography Mission. *Journal of Geophysical Research,* 110.
FARR, T. G., ROSEN, P. A., CARO, E., CRIPPEN, R., DUREN, R., HENSLEY, S., KOBRICK, M., PALLER, M., RODRIGUEZ, E., ROTH, L., SEAL, D., SHAFFER, S., SHIMADA, J., UMLAND, J., WERNER, M., OSKIN, M., BURBANK, D. & ALSDORF, D. 2007. The Shuttle Radar Topography Mission. *Reviews of Geophysics,* 45.
FERESHTEHPOUR, M. & KARAMOUZ, M. 2018. DEM Resolution Effects on Coastal Flood Vulnerability Assessment: Deterministic and Probabilistic Approach. *Water Resources Research,* 54.
FERNÁNDEZ, A., NAJAFI, M. R., DURAND, M., MARK, B. G., MORITZ, M., JUNG, H. C., NEAL, J., SHASTRY, A., LABORDE, S., PHANG, S. C., HAMILTON, I. M. & XIAO, N. 2016. Testing the skill of numerical hydraulic modeling to simulate spatiotemporal flooding patterns in the Logone floodplain, Cameroon. *Journal of Hydrology,* 539, 265-280.
FEWTRELL, T. J., BATES, P. D., HORRITT, M. & HUNTER, N. M. 2008. Evaluating the effect of scale in flood inundation modelling in urban environments. *Hydrological Processes,* 22, 5107-5118.
FEWTRELL, T. J., DUNCAN, A., SAMPSON, C. C., NEAL, J. C. & BATES, P. D. 2011. Benchmarking urban flood models of varying complexity and scale using high resolution terrestrial LiDAR data. *Physics and Chemistry of the Earth, Parts A/B/C,* 36, 281-291.
FIORIO, C. & GUSTEDT, J. 1996. Two linear time Union-Find strategies for image processing *Theoretical Computer Science,* 154, 165-181.
FISHER, P. F. 1991. First Experiments in Viewshed Uncertainty: The Accuracy of the Viewshed Area. *Photogrammetric Engineering & Remote Sensing,* 57, 1321-1327.
FISHER, P. F. 1998. Improved Modeling of Elevation Error with Geostatistics. *GeoInformatica,* 2, 215-233.
FISHER, P. F. & TATE, N. 2006. Causes and consequences of error in digital elevation models. *Progress in Physical Geography,* 30, 467-489.
FORKUOR, G. & MAATHUIS, B. 2012. Comparison of SRTM and ASTER Derived Digital Elevation Models over Two Regions in Ghana - Implications for Hydrological and Environmental Modeling. *Studies on Environmental and Applied Geomorphology*, 219-240.
FRIBERG, N., ANGELOPOULOS, N. V., BUIJSE, A. D., COWX, I. G., KAIL, J., MOE, T. F., MOIR, H., O'HARE, M. T., VERDONSCHOT, P. F. M. & WOLTER, C. 2016. Effective River Restoration in the 21st Century. *Large-Scale Ecology: Model Systems to Global Perspectives.*
FRYIRS, K. A., BRIERLEY, G. J., PRESTON, N. J. & KASAI, M. 2007. Buffers, barriers and blankets: The (dis)connectivity of catchment-scale sediment cascades. *Catena,* 70, 49-67.
FUJIHARA, Y., HOSHIKAWA, K., FUJII, H., KOTERA, A., NAGANO, T. & YOKOYAMA, S. 2016. Analysis and attribution of trends in water levels in the Vietnamese Mekong Delta. *Hydrological Processes,* 30, 835-845.
FUJII, H., GARSDAL, H., WARD, P., ISHII, M., MORISHITA, K. & BOIVIN, T. 2003. Hydrological roles of the Cambodian floodplain of the Mekong River. *International Journal of River Basin Management,* 1, 253-266.
FUJITA, K., SUZUKI, R., NUIMURA, T. & SAKAI, A. 2008. Performance of ASTER and SRTM DEMs, and their potential for assessing glacial lakes in the Lunana region, Bhutan Himalaya. *Journal of Glaciology,* 54, 220-228.
GALLAND, J.-C., GOUTAL, N. & HERVOUET, J.-M. 1991. TELEMAC: A new numerical model for solving shallow water equations. *Advances in Water Resources,* 14, 138-148.
GALLEGOS, H. A., SCHUBERT, J. E. & SANDERS, B. F. 2009. Two-dimensional, high-resolution modeling of urban dam-break flooding: A case study of Baldwin Hills, California. *Advances in Water Resources,* 32, 1323-1335.
GAMBA, P., DELL ACQUA, F. & HOUSHMAND, B. 2002. SRTM data characterization in urban areas. *International Archives of Photogrammetry Remote Sensing and Spatial Information Sciences,* 34, 55-58.
GARSCHAGEN, M. 2013. Risky change? Dynamics in vulnerability and adaptation to natural hazards between transformation and climate change in Can Tho City, Vietnam. . Cologne: University of Cologne.

GATZIOLIS, D. & FRIED, J. S. 2004. Adding Gaussian noise to inaccurate digital elevation models improves spatial fidelity of derived drainage networks. *Water Resources Research,* 40.
GESCH, D. B. 2009. Analysis of Lidar Elevation Data for Improved Identification and Delineation of Lands Vulnerable to Sea-Level Rise. *Journal of Coastal Research,* 10053, 49-58.
GESCH, D. B., VERDIN, K. & GREENLEE, S. K. 1999. New land surface digital elevation model covers the Earth. *EOS Transactions American Geophysical Union,* 80, 69-70.
GHUFFAR, S. 2018. DEM Generation from Multi Satellite PlanetScope Imagery. *Remote Sensing,* 10.
GILES, J. R. A., MARSH, S. H. & NAPIER, B. 2010. Dataset Acquisition to Support Geoscience. *In:* FLEMING, C. (ed.) *Elevation Models for Geoscience.* London: Geological Society.
GIOSAN, L. 2014. Protect the world's deltas. *Nature,* 516, 31.
GLASER, R. & STANGL, H. 2001. Climate and floods in Central Europe since AD 1000: Data, Methods, Results and Consequences. *Surveys in Geophyscis,* 25, 485-510.
GÓMEZ, M. F., LENCINAS, J. D., SIEBERT, A. & DÍAZ, G. M. 2012. Accuracy Assessment of ASTER and SRTM DEMs: A Case Study in Andean Patagonia. *GIScience & Remote Sensing,* 49, 71-91.
GONÇALVES, J. A. & HENRIQUES, R. 2015. UAV photogrammetry for topographic monitoring of coastal areas. *ISPRS Journal of Photogrammetry and Remote Sensing,* 104, 101-111.
GONGA-SAHOLIARILIVA, N., GUNNELL, Y., PETIT, C. & MERING, C. 2011. Techniques for quantifying the accuracy of gridded elevation models and for mapping uncertainty in digital terrain analysis. *Progress in Physical Geography,* 35, 739-764.
GOODCHILD, M. F. 1980. Algorithm 9: Simulation of autocorrelation for aggregate data. *Environment and Planning A,* 12, 1073-1081.
GOOVAERTS, P. 1997. *Geostatistics for Natural Resource Evaluation,* Oxford, Oxford University Press.
GOROKHOVICH, Y. & VOUSTIANIOUK, A. 2006. Accuracy assessment of the processed SRTM-based elevation data by CGIAR using field data from USA and Thailand and its relation to the terrain characteristics. *Remote Sensing of Environment,* 104, 409-415.
GOULDEN, T., HOPKINSON, C., JAMIESON, R. & STERLING, S. 2016. Sensitivity of DEM, slope, aspect and watershed attributes to LiDAR measurement uncertainty. *Remote Sensing of Environment,* 179, 23-35.
GRANA, C., BARALDI, L. & BOLELLI, F. 2016. Optimized Connected Components Labeling with Pixel Prediction. *Advanced Concepts for Intelligent Vision Systems.*
GRANA, C., BORGHESANI, D. & CUCCHIARA, R. 2010. Optimized block-based connected components labeling with decision trees. *IEEE Trans Image Process,* 19, 1596-609.
GRIMALDI, S., LI, Y., WALKER, J. P. & PAUWELS, V. R. N. 2018. Effective Representation of River Geometry in Hydraulic Flood Forecast Models. *Water Resources Research,* 54, 1031-1057.
GRUMBINE, R. E. & XU, J. 2011. Mekong Hydropower Development. *Science,* 332, 178-179.
GUO, Q., LI, W., YU, H. & ALVAREZ, O. 2010. Effects of Topographic Variability and Lidar Sampling Density on Several DEM Interpolation Methods. *Photogrammetric Engineering & Remote Sensing,* 6, 701-712.
GUPTA, S., PALSETIA, D., PATWARY, M. M. A., AGRAWAL, A. & CHOUDHARY, A. 2014. A New Parallel Algorithm for Two-Pass Connected Component Labeling. *2014 IEEE International Parallel & Distributed Processing Symposium Workshops.*
GUZZETTI, F., CARDINALI, M. & REICHENBACH, P. 1994. The AVI Project: A Bibliographical and Archive Inventory of Landslides and Floods in Italy. *Environmental Management,* 18, 623-633.
HABTEZION, N., TAHMASEBI NASAB, M. & CHU, X. 2016. How does DEM resolution affect microtopographic characteristics, hydrologic connectivity, and modelling of hydrologic processes? *Hydrological Processes,* 30, 4870-4892.
HAGEMEIER-KLOSE, M. & WAGNER, K. 2009. Evaluation of flood hazard maps in print and web mapping services as information tools in flood risk communication. *Natural Hazards and Earth System Science,* 9, 563-574.
HAILE, A. T. & RIENTJES, T. H. M. 2005. Effects of LiDAR DEM resolution in flood modelling: a model sensitivity study for the city of Tegucigalpa, Honduras. *ISPRS - International Archives of the Photogrammetry, Remote Sensing and Spatial Information Sciences,* 3, 12-14.
HALL, J. W., TARANTOLA, S., BATES, P. D. & HORRITT, M. S. 2005. Distributed Sensitivity Analysis of Flood Inundation Model Calibration. *Journal of Hydraulic Engineering,* 131, 117-126.
HALLEGATTE, S., GREEN, C., NICHOLLS, R. J. & CORFEE-MORLOT, J. 2013. Future flood losses in major coastal cities. *Nature Climate Change,* 3, 802-806.

HAMILL, T. M. 2001. Interpretation of Rank Histograms for Verifying Ensemble Forecasts. *Monthly Weather Review,* 129, 550-560.
HAMILL, T. M. & COLUCCI, S. J. 1997. Verification of Eta–RSM short-range ensemble forecasts. *Monthly Weather Review,* 125, 1312-1327.
HANCOCK, G. R. 2005. The use of digital elevation models in the identification and characterization of catchments over different grid scales. *Hydrological Processes,* 19, 1727-1749.
HANCOCK, G. R. & WILLGOOSE, G. 2001. The Production of Digital Elevation Models for Experimental Model Landscapes *Earth Surface Processes and Landforms,* 26, 475-490.
HANINGTON, P., TO, Q. T., VAN, P. D. T., DOAN, N. A. V. & KIEM, A. S. 2017. A hydrological model for interprovincial water resource planning and management: A case study in the Long Xuyen Quadrangle, Mekong Delta, Vietnam. *Journal of Hydrology,* 547, 1-9.
HARALICK, R. M. 1981. Some neighborhood operations. *Real Time Parallel Computing: Image Analysis.* New York: Plenum Press.
HAWICK, K. A., LEIST, A. & PLAYNE, D. P. 2010. Parallel graph component labelling with GPUs and CUDA. *Parallel Computing,* 36, 655-678.
HE, L., CHAO, Y. & SUZUKI, K. 2007. A Linear-Time Two-Scan Labeling Algorithm. *2007 IEEE International Conference on Image Processing.* San Antonio, TX, USA.
HE, L., CHAO, Y. & SUZUKI, K. 2008. A run-based two-scan labeling algorithm. *IEEE Trans Image Process,* 17, 749-56.
HE, L., CHAO, Y. & SUZUKI, K. 2010. A Run-Based One-and-a-Half-Scan Connected-Component Labeling Algorithm. *International Journal of Pattern Recognition and Artificial Intelligence,* 24, 557-579.
HE, L., CHAO, Y., SUZUKI, K. & WU, K. 2009. Fast connected-component labeling. *Pattern Recognition,* 42, 1977-1987.
HE, L., REN, X., GAO, Q., ZHAO, X., YAO, B. & CHAO, Y. 2017. The connected-component labeling problem: A review of state-of-the-art algorithms. *Pattern Recognition,* 70, 25-43.
HE, L., ZHAO, X., CHAO, Y. & SUZUKI, K. 2014. Configuration-Transition-Based Connected-Component Labeling. *IEEE Trans Image Process,* 23, 943-51.
HELLWEGER, F. 1997. AGREE - DEM surface reconditioning system.
HENGL, T., BAJAT, B., BLAGOJEVIĆ, D. & REUTER, H. I. 2008. Geostatistical modeling of topography using auxiliary maps. *Computers & Geosciences,* 34, 1886-1899.
HENGL, T., HEUVELINK, G. B. M. & VAN LOON, E. E. 2010. On the uncertainty of stream networks derived from elevation data: the error propagation approach. *Hydrology and Earth System Sciences,* 14, 1153-1165.
HERGET, J. & MEURS, H. 2010. Reconstructing peak discharges for historic flood levels in the city of Cologne, Germany. *Global and Planetary Change,* 70, 108-116.
HERITAGE, G. L., MILAN, D. J., LARGE, A. R. G. & FULLER, I. C. 2009. Influence of survey strategy and interpolation model on DEM quality. *Geomorphology,* 112, 334-344.
HERNÁNDEZ ENCINAS, A., HERNÁNDEZ ENCINAS, L., HOYA WHITE, S., MARTÍN DEL REY, A. & RODRÍGUEZ SÁNCHEZ, G. 2007. Simulation of forest fire fronts using cellular automata. *Advances in Engineering Software,* 38, 372-378.
HERVOUET, J.-M. 2007. Resolution of the Saint-Venant Equations. *Hydrodynamics of Free Surface Flows: Modelling with the Finite Element Method.* John Wiley & Sons.
HEUVELINK, G. B. M. 1998. *Error Propagation in Environmental Modelling in GIS,* London, UK, Taylor & Francis.
HEUVELINK, G. B. M., BURROUGH, P. A. & STEIN, A. 2007. Developments in Analysis of Spatial Data Uncertainty Since 1989. *In:* FISHER, P. F. (ed.) *Classics from IJGIS: twenty years of the Internation Journal of Geographical Information Science and Systems.* Boca Raton, FL: Taylor & Francis.
HIEN, H. M., TRUNG, T. N., LOOIJEN, W. & HULSBERGEN, K. 2005. *Flood vulnerability analysis and mapping in Vietnam,* Dordrecht, Springer.
HIGGINS, S. A. 2016. Review: Advances in delta-subsidence research using satellite methods. *Hydrogeology Journal,* 24, 587-600.
HIJMANS, R. J., VAN ETTEN, J., CHENG, J., MATTIUZZI, M., SUMNER, M., GREENBERG, J. A., PERPINAN LAMIGUEIRO, O., BEVAN, A., RACINE, E. B., SHORTRIDGE, A. & GHOSH, A. 2017. raster: Geographic Data Analysis and Modeling. 2.6-7 ed.
HILLDALE, R. C. & RAFF, D. 2008. Assessing the ability of airborne LiDAR to map river bathymetry. *Earth Surface Processes and Landforms,* 33, 773-783.

HIRABAYASHI, Y., MAHENDRAN, R., KOIRALA, S., KONOSHIMA, L., YAMAZAKI, D., WATANABE, S., KIM, H. & KANAE, S. 2013. Global flood risk under climate change. *Nature Climate Change,* 3, 816-821.
HIRSCHBERG, D. S., CHANDRA, A. K. & SARWATE, D. V. 1979. Computing connected components on parallel computers. *Communications of the ACM,* 22, 461-464.
HIRT, C. 2018. Artefact detection in global digital elevation models (DEMs): The Maximum Slope Approach and its application for complete screening of the SRTM v4.1 and MERIT DEMs. *Remote Sensing of Environment,* 207, 27-41.
HOA, L. T. V., SHIGEKO, H., NHAN, N. H. & CONG, T. T. 2008. Infrastructure effects on floods in the Mekong River Delta in Vietnam. *Hydrological Processes,* 22, 1359-1372.
HOCH, J. M., NEAL, J. C., BAART, F., VAN BEEK, R., WINSEMIUS, H. C., BATES, P. D. & BIERKENS, M. F. P. 2017. GLOFRIM v1.0 – A globally applicable computational framework for integrated hydrological–hydrodynamic modelling. *Geoscientific Model Development,* 10, 3913-3929.
HOFTON, M., DUBAYAH, R., BLAIR, J. B. & RABINE, D. 2006. Validation of SRTM Elevations Over Vegetated and Non-vegetated Terrain Using Medium Footprint Lidar. *Photogrammetric Engineering & Remote Sensing,* 72, 279-285.
HÖHLE, J. & HÖHLE, M. 2009. Accuracy assessment of digital elevation models by means of robust statistical methods. *ISPRS Journal of Photogrammetry and Remote Sensing,* 64, 398-406.
HOLMES, K. W., CHADWICK, O. A. & KYDRIAKIDIS, P. C. 2000. Error in a USGS 30-meter digital elevation model and its impact on terrain modelling. *Journal of Hydrology,* 233, 154-173.
HOOKE, J. 2003. Coarse sediment connectivity in river channel systems: a conceptual framework and methodology. *Geomorphology,* 56, 79-94.
HORNBERGER, G. M., BENCALA, K. E. & MCKNIGHT, D. M. 1994. Hydrological controls on dissolved organic carbon during snowmelt in the Snake River near Montezuma, Colorado. *Biogeochemistry,* 25, 147-165.
HORRITT, M. & BATES, P. 2002. Evaluation of 1D and 2D numerical models for predicting river flood inundation. *Journal of Hydrology,* 268, 87-99.
HORRITT, M., DI BALDASSARRE, G., BATES, P. & BRATH, A. 2007. Comparing the performance of a 2-D finite element and a 2-D finite volume model of floodplain inundation using airborne SAR imagery. *Hydrological Processes,* 21, 2745-2759.
HORRITT, M. S. & BATES, P. 2001a. Effects of spatial resolution on a raster based model of flood flow. *Journal of Hydrology,* 253, 239-249.
HORRITT, M. S. & BATES, P. D. 2001b. Predicting floodplain inundation: raster-based modelling versus the finite-element approach. *Hydrological Processes,* 15, 825-842.
HORSTMAN, E. M., DOHMEN-JANSSEN, C. M., NARRA, P. M. F., VAN DEN BERG, N. J. F., SIEMERINK, M. & HULSCHER, S. J. M. H. 2014. Wave attenuation in mangroves: A quantitative approach to field observations. *Coastal Engineering,* 94, 47-62.
HOWIE, C. 2011. *Co-operation and contestation: farmer-state relations in agricultural transformation, An Giang Province, Vietnam* PhD, Royal Holloway, University of London.
HRODADKA, T. V. & YEN, C. C. 1986. A diffusion hydrodynamic model (DHM). *Advances in Water Resources,* 9, 118-170.
HU, Z., PENG, J., HOU, Y. & SHAN, J. 2017. Evaluation of Recently Released Open Global Digital Elevation Models of Hubei, China. *Remote Sensing,* 9.
HUANG, X., XIE, H., LIANG, T. & YI, D. 2011. Estimating vertical error of SRTM and map-based DEMs using ICESat altimetry data in the eastern Tibetan Plateau. *International Journal of Remote Sensing,* 32, 5177-5196.
HUGGEL, C., SCHNEIDER, D., MIRANDA, P. J., DELGADO GRANADOS, H. & KÄÄB, A. 2008. Evaluation of ASTER and SRTM DEM data for lahar modeling: A case study on lahars from Popocatépetl Volcano, Mexico. *Journal of Volcanology and Geothermal Research,* 170, 99-110.
HUNG, N. N., DELGADO, J. M., TRI, V. K., HUNG, L. M., MERZ, B., BÁRDOSSY, A. & APEL, H. 2012. Floodplain hydrology of the Mekong Delta, Vietnam. *Hydrological Processes,* 26, 674-686.
HUNTER, G. J. & GOODCHILD, M. F. 1997. Modelling the uncertainty of slope and aspect derived from spatial databases. *Geophysical Analysis,* 29, 35-50.
HUNTER, N. M., BATES, P., HORRITT, M. & WILSON, M. D. 2006. Improved simulation of flood flows using storage cell models. *Proceedings of the Institution of Civil Engineers Water Management 159*, 9-18.

HUNTER, N. M., BATES, P. D., HORRITT, M. S. & WILSON, M. D. 2007. Simple spatially-distributed models for predicting flood inundation: A review. *Geomorphology,* 90, 208-225.
HUNTER, N. M., BATES, P. D., NEELZ, S., PENDER, G., VILLANUEVA, I., WRIGHT, N. G., LIANG, D., FALCONER, R. A., LIN, B., WALLER, S., CROSSLEY, A. J. & MASON, D. C. 2008. Benchmarking 2D hydraulic models for urban flooding. *Proceedings of the Institution of Civil Engineers - Water Management,* 161, 13-30.
HUNTER, N. M., HORRITT, M. S., BATES, P. D., WILSON, M. D. & WERNER, M. G. F. 2005. An adaptive time step solution for raster-based storage cell modelling of floodplain inundation. *Advances in Water Resources,* 28, 975-991.
HUPP, C. R., PIERCE, A. R. & NOE, G. B. 2009. Floodplain geomorphic processes and environmental impacts of human alteration along Coastal Plain rivers, USA. *Wetlands,* 29, 413-429.
HUTCHINSON, M. F. 1989. A new procedure for gridding elevation and stream line data with automatic removal of spurious pits. *Journal of Hydrology,* 106, 211-232.
HUTCHINSON, M. F. & GALLANT, J. C. 2000. Digital elevation models and representation of terrain shape. *In:* WILSON, J. P. & GALLANT, J. C. (eds.) *Terrain Analysis: Principles and Applications.* New York: John Wiley and Sons.
IBÁÑEZ, C., SHARPE, P. J., DAY, J. W., DAY, J. N. & PRAT, N. 2010. Vertical Accretion and Relative Sea Level Rise in the Ebro Delta Wetlands (Catalonia, Spain). *Wetlands,* 30, 979-988.
IKEUCHI, H., HIRABAYASHI, Y., YAMAZAKI, D., KIGUCHI, M., KOIRALA, S., NAGANO, T., KOTERA, A. & KANAE, S. 2015. Modeling complex flow dynamics of fluvial floods exacerbated by sea level rise in the Ganges–Brahmaputra–Meghna Delta. *Environmental Research Letters,* 10.
IKEUCHI, H., HIRABAYASHI, Y., YAMAZAKI, D., MUIS, S., WARD, P. J., WINSEMIUS, H. C., VERLAAN, M. & KANAE, S. 2017. Compound simulation of fluvial floods and storm surges in a global coupled river-coast flood model: Model development and its application to 2007 Cyclone Sidr in Bangladesh. *Journal of Advances in Modeling Earth Systems,* 9, 1847-1862.
INTERMAP 2018. NextMap World 10.
ISIKDOGAN, F., BOVIK, A. & PASSALACQUA, P. 2017. RivaMap: An automated river analysis and mapping engine. *Remote Sensing of Environment*.
JANKOWSKI, K. L., TORNQVIST, T. E. & FERNANDES, A. M. 2017. Vulnerability of Louisiana's coastal wetlands to present-day rates of relative sea-level rise. *Nat Commun,* 8, 14792.
JANSSEN, J. 2015. *Living with the Mekong,* Wageningen, Blauwdruk.
JANUCHOWSKI, S. R., PRESSEY, R. L., VANDERWAL, J. & EDWARDS, A. 2010. Characterizing errors in digital elevation models and estimating the financial costs of accuracy. *International Journal of Geographical Information Science,* 24, 1327-1347.
JARIHANI, A. A., CALLOW, J. N., MCVICAR, T. R., VAN NIEL, T. G. & LARSEN, J. R. 2015. Satellite-derived Digital Elevation Model (DEM) selection, preparation and correction for hydrodynamic modelling in large, low-gradient and data-sparse catchments. *Journal of Hydrology,* 524, 489-506.
JARVIS, A., REUTER, H. I., NELSON, A. & GUEVARA, E. 2008. Hole-filled SRTM for the globe Version 4. *In:* DATABASE, C.-C. S. M. (ed.).
JAVERNICK, L., BRASINGTON, J. & CARUSO, B. 2014. Modeling the topography of shallow braided rivers using Structure-from-Motion photogrammetry. *Geomorphology,* 213, 166-182.
JING, C., SHORTRIDGE, A., LIN, S. & WU, J. 2014. Comparison and validation of SRTM and ASTER GDEM for a subtropical landscape in Southeastern China. *International Journal of Digital Earth,* 7, 969-992.
JOLLIFFE, I. T. & PRIMO, C. 2008. Evaluating Rank Histograms Using Decompositions of the Chi-Square Test Statistic. *Monthly Weather Review,* 136, 2133-2139.
JONGMAN, B., WARD, P. J. & AERTS, J. C. J. H. 2012. Global exposure to river and coastal flooding: Long term trends and changes. *Global Environmental Change,* 22, 823-835.
JUNG, I.-Y. & JEONG, C.-S. Parallel Connected-Component Labeling Algorithm for GPGPU Applications. Communications and Information Technologies (ISCIT) IEEE, 2010, 2010. 1149-1153.
JUNK, W. J., BAYLEY, P. B. & SPARKS, R. E. 1989. The Flood Pulse Concept in River-Floodplain Systems. *Can. Spec. Publ. Fish. Aquat. Sci,* 106, 110-127.
KÄKÖNEN, M. 2008. Mekong Delta at the Crossroads: More Control or Adaptation? *AMBIO: A Journal of the Human Environment,* 37, 205-212.

KALENTEV, O., RAI, A., KEMNITZ, S. & SCHNEIDER, R. 2011. Connected component labeling on a 2D grid using CUDA. *Journal of Parallel and Distributed Computing,* 71, 615-620.
KANTOUSH, S., BINH, D. V., SUMI, T. & TRUNG, L. V. 2017. Impact of Upstream Hydropower Dams and Climate Change on Hydrodynamics of Vietnamese Mekong Delta. *Annual journal of Hydraulic Engineering, JSCE,* 73, I_109-114.
KAPLAN, S. & GARRICK, B. J. 1981. On The Quantiative Definition of Risk. *Risk Analysis,* 1, 11-26.
KAREGAR, M. A., DIXON, T. H. & MALSERVISI, R. 2015. A three-dimensional surface velocity field for the Mississippi Delta: Implications for coastal restoration and flood potential. *Geology,* 43, 519-522.
KARIM, F., KINSEY-HENDERSON, A., WALLACE, J., ARTHINGTON, A. H. & PEARSON, R. G. 2012. Modelling wetland connectivity during overbank flooding in a tropical floodplain in north Queensland, Australia. *Hydrological Processes,* 26, 2710-2723.
KARIM, F., PETHERAM, C., MARVANEK, S., TICEHURST, C., WALLACE, J. & HASAN, M. 2016. Impact of climate change on floodplain inundation and hydrological connectivity between wetlands and rivers in a tropical river catchment. *Hydrological Processes,* 30, 1574-1593.
KARIM, M. & MIMURA, N. 2008. Impacts of climate change and sea-level rise on cyclonic storm surge floods in Bangladesh. *Global Environmental Change,* 18, 490-500.
KARLSSON, J. M. & ARNBERG, W. 2011. Quality analysis of SRTM and HYDRO1K: a case study of flood inundation in Mozambique. *International Journal of Remote Sensing,* 32, 267-285.
KASAGI, A., NAKANO, K. & ITO, Y. 2014. Fast image component labelling on the GPU. *Bulletin of Networking, Computing, Systems, and Software,* 3, 76-80.
KEEF, C., TAWN, J. A. & LAMB, R. 2013. Estimating the probability of widespread flood events. *Environmetrics,* 24, 13-21.
KENNY, F., MATTHEWS, B. & TODD, K. 2008. Routing overland flow through sinks and flats in interpolated raster terrain surfaces. *Computers & Geosciences,* 34, 1417-1430.
KHUE, N. N. 1986. Modelling of Tidal Propagation and Salinity Intrusion in the Mekong Main Estuarine System. *Technical paper of Mekong Delta Sallinity Intruction Studies, Phase II.* Bangkok: Mekong Secretariat.
KIDNER, D. B. 2003. Higher-order interpolation of regular grid digital elevation models. *International Journal of Remote Sensing,* 24, 2981-2987.
KIENZLE, S. 2004. The Effect of DEM Raster Resolution on First Order, Second Order and Compound Terrain Derivatives. *Transactions in GIS,* 8, 83-111.
KISS, A. 2009. Floods and weather in 1342 and 1343 in the Carpathian Basin. *Journal of Environmental Geography,* 2, 37-47.
KLERK, W. J., WINSEMIUS, H. C., VAN VERSEVELD, W. J., BAKKER, A. M. R. & DIERMANSE, F. L. M. 2015. The co-incidence of storm surges and extreme discharges within the Rhine–Meuse Delta. *Environmental Research Letters,* 10.
KNUDBY, C. & CARRERA, J. 2005. On the relationship between indicators of geostatistical, flow and transport connectivity. *Advances in Water Resources,* 28, 405-421.
KOLECKA, N. & KOZAK, J. 2014. Assessment of the Accuracy of SRTM C- and X-Band High Mountain Elevation Data: a Case Study of the Polish Tatra Mountains. *Pure and Applied Geophysics,* 171, 897-912.
KOMI, K., NEAL, J., TRIGG, M. A. & DIEKKRÜGER, B. 2017. Modelling of flood hazard extent in data sparse areas: a case study of the Oti River basin, West Africa. *Journal of Hydrology: Regional Studies,* 10, 122-132.
KONDOLF, G. M., BOULTON, A. J., O'DANIEL, S., POOLE, G. C., RAHEL, F. J., STANLEY, E. H., WOHL, E., BANG, A., CARLSTROM, J., CRISTONI, C., HUBER, H., KOLJONEN, S., LOUHI, P. & NAKAMURA, K. 2006. Process-Based Ecological River Restoration: Visualizing Three-Dimensional Connectivity and Dynamic Vectors to Recover Lost Linkages. *Ecology and Society,* 22.
KONDOLF, G. M., GAO, Y., ANNANDALE, G. W., MORRIS, G. L., JIANG, E., ZHANG, J., CAO, Y., CARLING, P., FU, K., GUO, Q., HOTCHKISS, R., PETEUIL, C., SUMI, T., WANG, H.-W., WANG, Z., WEI, Z., WU, B., WU, C. & YANG, C. T. 2014. Sustainable sediment management in reservoirs and regulated rivers: Experiences from five continents. *Earth's Future,* 2, 256-280.
KONTGIS, C., SCHNEIDER, A. & OZDOGAN, M. 2015. Mapping rice paddy extent and intensification in the Vietnamese Mekong River Delta with dense time stacks of Landsat data. *Remote Sensing of Environment,* 169, 255-269.

KOTERA, A., NAGANO, T., HANITTINAN, P. & KOONTANAKULVONG, S. 2016. Assessing the degree of flood damage to rice crops in the Chao Phraya delta, Thailand, using MODIS satellite imaging. *Paddy and Water Environment,* 14, 271-280.
KOTSUKI, S. & TANAKA, K. 2015. SACRA – a method for the estimation of global high-resolution crop calendars from a satellite-sensed NDVI. *Hydrology and Earth System Sciences,* 19, 4441-4461.
KRAMER, K., DEGEN, B., BUSCHBOM, J., HICKLER, T., THUILLER, W., SYKES, M. T. & DE WINTER, W. 2010. Modelling exploration of the future of European beech (Fagus sylvatica L.) under climate change—Range, abundance, genetic diversity and adaptive response. *Forest Ecology and Management,* 259, 2213-2222.
KRIEGER, G., MOREIRA, A., FIEDLER, H., HAJNSEK, I., WERNER, M. & ZINK, M. 2007. TanDEM-X: A Satellite Formation for High-Resolution SAR Interferometry. *IEEE Transactions on Geoscience and Remote Sensing,* 45, 3317-3340.
KRUSE, B. A fast algorithm for segmentation of connected components in binary images. Scandinavian Conf. Image Analysis, 1980 Lund, Sweden.
KUENZER, C., GUO, H., HUTH, J., LEINENKUGEL, P., LI, X. & DECH, S. 2013. Flood Mapping and Flood Dynamics of the Mekong Delta: ENVISAT-ASAR-WSM Based Time Series Analyses. *Remote Sensing,* 5, 687-715.
KUENZER, C., KLEIN, I., ULLMANN, T., GEORGIOU, E., BAUMHAUER, R. & DECH, S. 2015. Remote Sensing of River Delta Inundation: Exploiting the Potential of Coarse Spatial Resolution, Temporally-Dense MODIS Time Series. *Remote Sensing,* 7, 8516-8542.
KULP, S. & STRAUSS, B. H. 2016. Global DEM Errors Underpredict Coastal Vulnerability to Sea Level Rise and Flooding. *Frontiers in Earth Science,* 4.
KULP, S. A. & STRAUSS, B. H. 2018. CoastalDEM: A global coastal digital elevation model improved from SRTM using a neural network. *Remote Sensing of Environment,* 206, 231-239.
KUMMU, M. & SARKKULA, J. 2008. Impact of the Mekong River Flow Alteration on the Tonle Sap Flood Pulse. *AMBIO: A Journal of the Human Environment,* 37, 185-192.
KUMMU, M., TES, S., YIN, S., ADAMSON, P., JÓZSA, J., KOPONEN, J., RICHEY, J. & SARKKULA, J. 2014. Water balance analysis for the Tonle Sap Lake-floodplain system. *Hydrological Processes,* 28, 1722-1733.
KUNDZEWICZ, Z. W., KANAE, S., SENEVIRATNE, S. I., HANDMER, J., NICHOLLS, N., PEDUZZI, P., MECHLER, R., BOUWER, L. M., ARNELL, N., MACH, K., MUIR-WOOD, R., BRAKENRIDGE, G. R., KRON, W., BENITO, G., HONDA, Y., TAKAHASHI, K. & SHERSTYUKOV, B. 2014. Flood risk and climate change: global and regional perspectives. *Hydrological Sciences Journal,* 59, 1-28.
KUSER OLSEN, V. B., MOMEN, B., LANGSDALE, S. M., GALLOWAY, G. E., LINK, E., BRUBAKER, K. L., RUTH, M. & HILL, R. L. 2018. An approach for improving flood risk communication using realistic interactive visualisation. *Journal of Flood Risk Management,* 11, S783-S793.
KYDRIAKIDIS, P. C., SHORTRIDGE, A. & GOODCHILD, M. F. 1999. Geostatistics for conflation and accuracy assessment of digital elevation models. *International Journal of Geographical Information Science,* 13, 677-707.
LACASSAGNE, L. & ZAVIDOVIQUE, B. 2011. Light speed labeling: efficient connected component labeling on risc architectures. *Journal of Real-Time Image Processing,* 6, 117-135.
LALONDE, T., SHORTRIDGE, A. & MESSINA, J. 2010. The Influence of Land Cover on Shuttle Radar Topography Mission (SRTM) Elevations in Low-relief Areas. *Transactions in GIS,* 14, 461-479.
LANE, S. N. 2017. Natural flood management. *Wiley Interdisciplinary Reviews: Water,* 4.
LANE, S. N., BROOKES, C. J., KIRKBY, M. J. & HOLDEN, J. 2004. A network-index-based version of TOPMODEL for use with high-resolution digital topographic data. *Hydrological Processes,* 18, 191-201.
LANE, S. N., ODONI, N. A., LANDSTROM, C., WHATMORE, S. J., WARD, N. & BRADLEY, S. 2011. Doing flood risk science differently: an experiment in radical scientific method. *Transactions of the Insitute of British Geographers,* 36, 15-36.
LARSEN, L. G., CHOI, J., NUNGESSER, M. K. & HARVEY, J. W. 2012. Directional connectivity in hydrology and ecology. *Ecological Applications,* 22, 2204-2222.
LAURI, H., DE MOEL, H., WARD, P. J., RÄSÄNEN, T. A., KESKINEN, M. & KUMMU, M. 2012. Future changes in Mekong River hydrology: impact of climate change and reservoir operation on discharge. *Hydrology and Earth System Sciences,* 16, 4603-4619.

LE, T. N., BREGT, A. K., VAN HALSEMA, G. E., HELLEGERS, P. J. G. J. & NGUYEN, L.-D. 2018. Interplay between land-use dynamics and changes in hydrological regime in the Vietnamese Mekong Delta. *Land Use Policy,* 73, 269-280.
LE, T. V. H., NGUYEN, H. N., WOLANSKI, E., TRAN, T. C. & HARUYAMA, S. 2007. The combined impact on the flooding in Vietnam's Mekong River delta of local man-made structures, sea level rise, and dams upstream in the river catchment. *Estuarine, Coastal and Shelf Science,* 71, 110-116.
LEANDRO, J., CHEN, A. S., DJORDJEVIC, S. & SAVIC, D. A. 2009. Comparison of 1D/1D and 1D/2D Coupled (Sewer/Surface) Hydraulic Models for Urban Flood Simulation. *Journal of Hydraulic Engineering,* 135, 495-506.
LEE, J., GHORBANIDEHNO, H., FARTHING, M. W., HESSER, T. J., DARVE, E. F. & KITANIDIS, P. K. 2018. Riverine Bathymetry Imaging With Indirect Observations. *Water Resources Research,* 54, 3704-3727.
LEE, J., SNYDER, P. & FISHER, P. F. 1992. Modeling the Effect of Data Errors on Feature Extraction from Digital Elevation Models. *Photogrammetric Engineering & Remote Sensing,* 58, 1461-1467.
LEGLEITER, C. J. & OVERSTREET, B. T. 2012. Mapping gravel bed river bathymetry from space. *Journal of Geophysical Research: Earth Surface,* 117, n/a-n/a.
LEHNER, B., VERDIN, K. & JARVIS, A. 2008. New global hydrography derived from spaceborne elevation data. *EOS Transactions American Geophysical Union,* 89, 93-94.
LEON, J. X., HEUVELINK, G. B. M. & PHINN, S. R. 2014. Incorporating DEM Uncertainty in Coastal Inundation Mapping. *PLoS ONE,* 9, e108727.
LEONARD, M., WESTRA, S., PHATAK, A., LAMBERT, M., VAN DEN HURK, B., MCINNES, K., RISBEY, J., SCHUSTER, S., JAKOB, D. & STAFFORD-SMITH, M. 2014. A compound event framework for understanding extreme impacts. *Wiley Interdisciplinary Reviews: Climate Change,* 5, 113-128.
LEOPOLD, L. B. & MADDOCK, T. 1953. *Hydraulic geometry of stream channels and some physiographic implications,* Washington D.C, US Government Printing Office.
LEWIN, J. & ASHWORTH, P. J. 2014a. Defining large river channel patterns: Alluvial exchange and plurality. *Geomorphology,* 215, 83-98.
LEWIN, J. & ASHWORTH, P. J. 2014b. The negative relief of large river floodplains. *Earth-Science Reviews,* 129, 1-23.
LEWIN, J., ASHWORTH, P. J. & STRICK, R. J. P. 2017. Spillage sedimentation on large river floodplains. *Earth Surface Processes and Landforms,* 42, 290-305.
LEWIS, M., BATES, P., HORSBURGH, K., NEAL, J. & SCHUMANN, G. 2013. A storm surge inundation model of the northern Bay of Bengal using publicly available data. *Quarterly Journal of the Royal Meteorological Society,* 139, 358-369.
LEXARTZA-ARTZA, I. & WAINWRIGHT, J. 2009. Hydrological connectivity: Linking concepts with practical implications. *Catena,* 79, 146-152.
LI, J. & WONG, D. W. S. 2010. Effects of DEM sources on hydrologic applications. *Computers, Environment and Urban Systems,* 34, 251-261.
LIN, C.-Y., LI, S.-Y. & TSAI, T.-H. A scalable parallel hardware architecture for connected compoent labeling. IEEE 17th International Conference on Image Processing, September 26-29 2010 Hong Kong.
LINARD, C., TATEM, A. J. & GILBERT, M. 2013. Modelling spatial patterns of urban growth in Africa. *Appl Geogr,* 44, 23-32.
LINDSAY, J. B. 2006. Sensitivity of channel mapping techniques to uncertainty in digital elevation data. *International Journal of Geographical Information Science,* 20, 669-692.
LINDSAY, J. B. 2016. The practice of DEM stream burning revisited. *Earth Surface Processes and Landforms,* 41, 658-668.
LINDSAY, J. B. & CREED, I. F. 2005. Sensitivity of Digital Landscapes to Artifact Depressions in Remotely-sensed DEMs. *Photogrammetric Engineering & Remote Sensing,* 9, 1029-1036.
LING, F. H., TAMURA, M., YASUHARA, K., AJIMA, K. & TRINH, C. V. 2015. Reducing flood risks in rural households: survey of perception and adaptation in the Mekong delta. *Climatic Change,* 132, 209-222.
LIU, H. & JEZEK, K. C. 1999. Investigating DEM Error Patterns by Directional Variograms and Fourier Analysis. *Geographical Analysis,* 31, 249-265.
LÓPEZ-VICENTE, M. & ÁLVAREZ, S. 2018. Influence of DEM resolution on modelling hydrological connectivity in a complex agricultural catchment with woody crops. *Earth Surface Processes and Landforms,* 43, 1403-1415.

LOPEZ, C. 1997. Locating some types of random errors in Digital Terrain Models. *International Journal of Geographical Information Science,* 11, 677-698.
LORENZ, E. N. 1963. Deterministic Nonperiodic Flow. *Journal of the Atmospheric Sciences,* 20, 130-141.
LU, X. X., LI, S., KUMMU, M., PADAWANGI, R. & WANG, J. J. 2014. Observed changes in the water flow at Chiang Saen in the lower Mekong: Impacts of Chinese dams? *Quaternary International,* 336, 145-157.
LUKE, A., SANDERS, B. F., GOODRICH, K. A., FELDMAN, D. L., BOUDREAU, D., EGUIARTE, A., SERRANO, K., REYES, A., SCHUBERT, J. E., AGHAKOUCHAK, A., BASOLO, V. & MATTHEW, R. A. 2018. Going beyond the flood insurance rate map: insights from flood hazard map co-production. *Natural Hazards and Earth System Sciences,* 18, 1097-1120.
LUMIA, R., SHAPIRO, L. & ZUNIGA, O. 1983. A New Connected Components Algorithm for Virtual Memory Computers. *Computer Vision, Graphics and Image Processing,* 22, 287-300.
MACCHIONE, F., COSTABILE, P., COSTANZO, C. & DE SANTIS, R. 2018. Moving to 3-D flood hazard maps for enhancing risk communication. *Environmental Modelling & Software*.
MACKLIN, M. G. & LEWIN, J. 2015. The rivers of civilization. *Quaternary Science Reviews,* 114, 228-244.
MALARD, F., TOCKNER, K., DOLE-OLIVIER, M.-J. & WARD, J. 2002. A landscape perspective of surface–subsurface hydrological exchanges in river corridors. *Freshwater Biology,* 47.
MANFREDA, S., DI LEO, M. & SOLE, A. 2011. Detection of Flood-Prone Areas Using Digital Elevation Models. *Journal of Hydrologic Engineering,* 16, 781-790.
MANFREDA, S., NARDI, F., SAMELA, C., GRIMALDI, S., TARAMASSO, A. C., ROTH, G. & SOLE, A. 2014. Investigation on the use of geomorphic approaches for the delineation of flood prone areas. *Journal of Hydrology,* 517, 863-876.
MANH, N. V., DUNG, N. V., HUNG, N. N., KUMMU, M., MERZ, B. & APEL, H. 2015. Future sediment dynamics in the Mekong Delta floodplains: Impacts of hydropower development, climate change and sea level rise. *Global and Planetary Change,* 127, 22-33.
MANH, N. V., DUNG, N. V., HUNG, N. N., MERZ, B. & APEL, H. 2014. Large-scale suspended sediment transport and sediment deposition in the Mekong Delta. *Hydrology and Earth System Sciences,* 18, 3033-3053.
MANOHAR, M. & RAMAPRIYAN, R. 1989. Connected Component Labeling of Binary Images on a Mesh Connected Massively Parallel Processor *Computer Vision, Graphics and Image Processing,* 45, 133-149.
MARCHAND, M., PHAM, D. Q. & LE, T. 2014. Mekong Delta: Living with Water, But for How Long? *Built Environment,* 40, 230-243.
MARTONE, M., RIZZOLI, P., WECKLICH, C., GONZÁLEZ, C., BUESO-BELLO, J.-L., VALDO, P., SCHULZE, D., ZINK, M., KRIEGER, G. & MOREIRA, A. 2018. The global forest/non-forest map from TanDEM-X interferometric SAR data. *Remote Sensing of Environment,* 205, 352-373.
MARTZ, L. W. & GARBRECHT, J. 1999. An outlet breaching algorithm for the treatment of closed depressions in a raster DEM. *Computers & Geosciences,* 25, 835-844.
MASHIMBYE, Z. E., DE CLERCQ, W. P. & VAN NIEKERK, A. 2014. An evaluation of digital elevation models (DEMs) for delineating land components. *Geoderma,* 213, 312-319.
MASON, D. C., TRIGG, M., GARCIA-PINTADO, J., CLOKE, H. L., NEAL, J. C. & BATES, P. D. 2016. Improving the TanDEM-X Digital Elevation Model for flood modelling using flood extents from Synthetic Aperture Radar images. *Remote Sensing of Environment,* 173, 15-28.
MASUMOTO, T., HAI, P. T. & SHIMIZU, K. 2008. Impact of paddy irrigation levels on floods and water use in the Mekong River basin. *Hydrological Processes,* 22, 1321-1328.
MATAKI, M., KOSBY, K. C. & LAL, M. 2006. Baseline Climatology of Viti Levu (Fiji) and Current Climatic Trends. *Pacific Science,* 60, 49-68.
MATGEN, P., SCHUMANN, G., HENRY, J. B., HOFFMANN, L. & PFISTER, L. 2007. Integration of SAR-derived river inundation areas, high-precision topographic data and a river flow model toward near real-time flood management. *International Journal of Applied Earth Observation and Geoinformation,* 9, 247-263.
MAUNE, D. (ed.) 2001. *Digital Elevation Model Technologies and Applications: The DEM Users Manual,* Maryland: ASPRS.
MAUNE, D. (ed.) 2007. *Digital Elevation Model Technologies and Applications: The Dem Users Manual*: American Society for Photogrammetry and Remote Sensing.
MCGARIGAL, K., CUSHMAN, S. A., NEEL, M. C. & ENE, E. 2002. FRAGSTATS: Spatial Pattern Analysis Program for Categorical Maps. 4 ed. Amherst, Massachusetts.

MCMILLAN, H., KRUEGER, T. & FREER, J. 2012. Benchmarking observational uncertainties for hydrology: rainfall, river discharge and water quality. *Hydrological Processes,* 26, 4078-4111.
MENZE, B. H., UR, J. A. & SHERRATT, A. G. 2006. Detection of Ancient Settlement Mounds: Archaeological Survey Based on the SRTM Terrain Model. *Photogrammetric Engineering & Remote Sensing,* 72, 321-327.
MERSEL, M. K., SMITH, L. C., ANDREADIS, K. M. & DURAND, M. T. 2013. Estimation of river depth from remotely sensed hydraulic relationships. *Water Resources Research,* 49, 3165-3179.
MERTES, L. A. K. 1997. Documentation and significance of the perirheic zone on inundated floodplains. *Water Resources Research,* 33, 1749-1762.
MERWADE, V., COOK, A. & COONROD, J. 2008. GIS techniques for creating river terrain models for hydrodynamic modeling and flood inundation mapping. *Environmental Modelling & Software,* 23, 1300-1311.
MERZ, B., KREIBICH, H., SCHWARZE, R. & THIEKEN, A. 2010. Review article "Assessment of economic flood damage". *Natural Hazards and Earth System Science,* 10, 1697-1724.
MEYER, V., KUHLICKE, C., LUTHER, J., FUCHS, S., PRIEST, S., DORNER, W., SERRHINI, K., PARDOE, J., MCCARTHY, S., SEIDEL, J., PALKA, G., UNNERSTALL, H., VIAVATTENE, C. & SCHEUER, S. 2012. Recommendations for the user-specific enhancement of flood maps. *Natural Hazards and Earth System Sciences,* 12, 1701-1716.
MICHAELIDES, K. & CHAPPELL, A. 2009. Connectivity as a concept for characterising hydrological behaviour. *Hydrological Processes,* 23, 517-522.
MILIARESIS, G. C. & PARASCHOU, C. V. E. 2005. Vertical accuracy of the SRTM DTED level 1 of Crete. *International Journal of Applied Earth Observation and Geoinformation,* 7, 49-59.
MILLER, C. L. & LAFLAMME, R. A. 1958. The Digital Terrain Model- Theory & Application. *MIT Photogrammetry Laboratory*.
MINDERHOUD, P. S. J., COUMOU, L., ERBAN, L. E., MIDDELKOOP, H., STOUTHAMER, E. & ADDINK, E. A. 2018. The relation between land use and subsidence in the Vietnamese Mekong delta. *Sci Total Environ,* 634, 715-726.
MINDERHOUD, P. S. J., ERKENS, G., PHAM, V. H., BUI, V. T., ERBAN, L., KOOI, H. & STOUTHAMER, E. 2017. Impacts of 25 years of groundwater extraction on subsidence in the Mekong delta, Vietnam. *Environmental Research Letters,* 12.
MITAS, L. & MITASOVA, H. 1999. Spatial Interpolation. *In:* LONGLEY, P. A., GOODCHILD, M. F., MAGUIRE, D. J. & RHIND, D. W. (eds.) *Geographical Information Systems: principles, techniques, management and applications.* New York: Wiley.
MOFTAKHARI, H. R., AGHAKOUCHAK, A., SANDERS, B. F. & MATTHEW, R. A. 2017a. Cumulative hazard: The case of nuisance flooding. *Earth's Future,* 5, 214-223.
MOFTAKHARI, H. R., SALVADORI, G., AGHAKOUCHAK, A., SANDERS, B. F. & MATTHEW, R. A. 2017b. Compounding effects of sea level rise and fluvial flooding. *Proc Natl Acad Sci U S A,* 114, 9785-9790.
MONCKTON, C. 1994. *An Investigation into the spatial structure of error in digital elevation data,* London, UK, Taylor and Francis.
MOREIRA, A. The TanDEM-X Mission: A New Measurement of the Earth's Topography and Much More. The 18th International Radar Symposium IRS 2017, 2017 Prague, Czech Republic.
MORETTI, G. & ORLANDINI, S. 2018. Hydrography-Driven Coarsening of Grid Digital Elevation Models. *Water Resources Research,* 54, 3654-3672.
MORRIN, T. H. 1976. Chain-Link Compression of Arbitrary Black-White images *Computer Graphics and Image Processing,* 5, 172-189.
MOURATIDIS, A., BRIOLE, P. & KATSAMBALOS, K. 2010. SRTM 3″ DEM (versions 1, 2, 3, 4) validation by means of extensive kinematic GPS measurements: a case study from North Greece. *International Journal of Remote Sensing,* 31, 6205-6222.
MRC 2010a. Multi-functionality of Paddy Fields over the Lower Mekong Basin. Vientiene: Mekong River Commission.
MRC 2010b. State of the Basin Report 2010. Vientiane, Laos: Mekong River Commission.
MRC 2011a. Basin Development Plan Programme, Phase 2: Assessment of Basin-wide Development Scenarios. Vientiane, Laos: Mekong River Commission.
MRC 2011b. Flood Situtation Report 2011. Vientienne, Laos: Mekong River Commission.
MTAMBA, J., VAN DER VELDE, R., NDOMBA, P., ZOLTÁN, V. & MTALO, F. 2015. Use of Radarsat-2 and Landsat TM Images for Spatial Parameterization of Manning's Roughness Coefficient in Hydraulic Modeling. *Remote Sensing,* 7, 836-864.

MUKHERJEE, S., JOSHI, P. K., MUKHERJEE, S., GHOSH, A., GARG, R. D. & MUKHOPADHYAY, A. 2013. Evaluation of vertical accuracy of open source Digital Elevation Model (DEM). *International Journal of Applied Earth Observation and Geoinformation,* 21, 205-217.
MULDER, V. L., DE BRUIN, S., SCHAEPMAN, M. E. & MAYR, T. R. 2011. The use of remote sensing in soil and terrain mapping — A review. *Geoderma,* 162, 1-19.
MUNICHRE 2016. Natural Catastrophes 2016 Analysis, assessments, positions.
MUNICHRE 2018. Natural Catastrophes 2017.
MURILLO, M. L. & HUNTER, G. J. 1997. Assessing uncertainty due to elevation error in a landslide susceptibility model. *Transactions in GIS,* 2, 289-298.
NANSON, G. C. & CROKE, J. C. 1992. A genetic classification of floodplains. *Geomorphology,* 4, 459-486.
NARDI, F., VIVONI, E. R. & GRIMALDI, S. 2006. Investigating a floodplain scaling relation using a hydrogeomorphic delineation method. *Water Resources Research,* 42.
NASH, J. E. & SUTCLIFFE, J. V. 1970. River Flow Forecasting through Conceptual Models. Part 1 - A Discussion of Principles. *Journal of Hydrology,* 10, 282-290.
NASSIMI, D. & SAHNI, S. 1980. Finding Connected Components and Connected Ones on a Mesh-Connected Parallel Computer. *SIAM J. COMPUT,* 9, 744-757.
NEAL, J., DUNNE, T., SAMPSON, C., SMITH, A. & BATES, P. 2018. Optimisation of the two-dimensional hydraulic model LISFOOD-FP for CPU architecture. *Environmental Modelling & Software,* 107, 148-157.
NEAL, J., FEWTRELL, T. & TRIGG, M. 2009a. Parallelisation of storage cell flood models using OpenMP. *Environmental Modelling & Software,* 24, 872-877.
NEAL, J., KEEF, C., BATES, P., BEVEN, K. & LEEDAL, D. 2013. Probabilistic flood risk mapping including spatial dependence. *Hydrological Processes,* 27, 1349-1363.
NEAL, J., SCHUMANN, G. & BATES, P. 2012a. A subgrid channel model for simulating river hydraulics and floodplain inundation over large and data sparse areas. *Water Resources Research,* 48.
NEAL, J., SCHUMANN, G., FEWTRELL, T., BUDIMIR, M., BATES, P. & MASON, D. 2011. Evaluating a new LISFLOOD-FP formulation with data from the summer 2007 floods in Tewkesbury, UK. *Journal of Flood Risk Management,* 4, 88-95.
NEAL, J., VILLANUEVA, I., WRIGHT, N., WILLIS, T., FEWTRELL, T. & BATES, P. 2012b. How much physical complexity is needed to model flood inundation? *Hydrological Processes,* 26, 2264-2282.
NEAL, J. C., BATES, P. D., FEWTRELL, T. J., HUNTER, N. M., WILSON, M. D. & HORRITT, M. S. 2009b. Distributed whole city water level measurements from the Carlisle 2005 urban flood event and comparison with hydraulic model simulations. *Journal of Hydrology,* 368, 42-55.
NEAL, J. C., ODONI, N. A., TRIGG, M. A., FREER, J. E., GARCIA-PINTADO, J., MASON, D. C., WOOD, M. & BATES, P. D. 2015. Efficient incorporation of channel cross-section geometry uncertainty into regional and global scale flood inundation models. *Journal of Hydrology,* 529, 169-183.
NÉELZ, S. & PENDER, G. 2013. Benchmarking the latest generation of 2D hydraulic modelling packages. Bristol: Environment Agency.
NELSON, A., REUTER, H. I. & GESSLER, P. 2009. DEM production methods and sources. *Developments in soil science,* 33, 65-85.
NGO, H., PATHIRANA, A., ZEVENBERGEN, C. & RANASINGHE, R. 2018. An Effective Modelling Approach to Support Probabilistic Flood Forecasting in Coastal Cities—Case Study: Can Tho, Mekong Delta, Vietnam. *Journal of Marine Science and Engineering,* 6.
NGUYEN, A. D. & SAVENIJE, H. H. G. 2006. Salt intrusion in multi-channel estuaries: a case study in the Mekong Delta, Vietnam. *Hydrology and Earth System Sciences,* 10, 743-754.
NGUYEN, D., CLAUSS, K., CAO, S., NAEIMI, V., KUENZER, C. & WAGNER, W. 2015. Mapping Rice Seasonality in the Mekong Delta with Multi-Year Envisat ASAR WSM Data. *Remote Sensing,* 7, 15868-15893.
NGUYEN, D. B., GRUBER, A. & WAGNER, W. 2016. Mapping rice extent and cropping scheme in the Mekong Delta using Sentinel-1A data. *Remote Sensing Letters,* 7, 1209-1218.
NGUYEN, H. N., VU, K. T. & NGUYEN, X. N. 2007. Flooding in Mekong River Delta, Viet Nam. Human Development Report 2008.
NGUYEN, T. P., LUOM, T. T. & PARNELL, K. E. 2017. Existing strategies for managing mangrove dominated muddy coasts: Knowledge gaps and recommendations. *Ocean & Coastal Management,* 138, 93-100.

NHAN, N. H. 2016. Tidal regime deformation by sea level rise along the coast of the Mekong Delta. *Estuarine, Coastal and Shelf Science,* 183, 382-391.
NICHOLAS, A. P. & MITCHELL, C. A. 2003. Numerical simulation of overbank processes in topographically complex floodplain environments. *Hydrological Processes,* 17, 727-746.
NIENHUIS, J. H., TÖRNQVIST, T. E., JANKOWSKI, K. L., FERNANDES, A. M. & KEOGH, M. E. 2017. A New Subsidence Map for Coastal Louisiana. *GSA Today*, 60-61.
O'LOUGHLIN, F., TRIGG, M. A., SCHUMANN, G. J. P. & BATES, P. D. 2013. Hydraulic characterization of the middle reach of the Congo River. *Water Resources Research,* 49, 5059-5070.
O'LOUGHLIN, F. E., NEAL, J., YAMAZAKI, D. & BATES, P. D. 2016a. ICESat-derived inland water surface spot heights. *Water Resources Research,* 52, 3276-3284.
O'LOUGHLIN, F. E., PAIVA, R. C. D., DURAND, M., ALSDORF, D. E. & BATES, P. D. 2016b. A multi-sensor approach towards a global vegetation corrected SRTM DEM product. *Remote Sensing of Environment,* 182, 49-59.
OCAMPO, C. J., SIVAPALAN, M. & OLDHAM, C. 2006. Hydrological connectivity of upland-riparian zones in agricultural catchments: Implications for runoff generation and nitrate transport. *Journal of Hydrology,* 331, 643-658.
OKSANEN, J. 2006. *Digital Elevation Model Error in terrain analysis.* University of Helsinki.
OKSANEN, J. & SARJAKOSKI, T. 2005. Error propagation of DEM-based surface derivatives. *Computers & Geosciences,* 31, 1015-1027.
OKSANEN, J. & SARJAKOSKI, T. 2006. Uncovering the statistical and spatial characteristics of fine toposcale DEM error. *International Journal of Geographical Information Science,* 20, 345-369.
OLEA, R. A. 2006. A six-step practical approach to semivariogram modeling. *Stochastic Environmental Research and Risk Assessment,* 20, 307-318.
OPPERMAN, J. J., GALLOWAY, G. E., FARGIONE, J., MOUNT, J. F., RICHTER, B. D. & SECCHI, S. 2009. Sustainable Floodplains Through Large-Scale Reconnection to Rivers. *Science,* 326, 1487-1488.
ORR, S., PITTOCK, J., CHAPAGAIN, A. & DUMARESQ, D. 2012. Dams on the Mekong River: Lost fish protein and the implications for land and water resources. *Global Environmental Change,* 22, 925-932.
OTTINGER, M., CLAUSS, K. & KUENZER, C. 2016. Aquaculture: Relevance, distribution, impacts and spatial assessments – A review. *Ocean & Coastal Management,* 119, 244-266.
OZDEMIR, H., SAMPSON, C. C., DE ALMEIDA, G. A. M. & BATES, P. D. 2013. Evaluating scale and roughness effects in urban flood modelling using terrestrial LIDAR data. *Hydrology and Earth System Sciences,* 17, 4015-4030.
PALL, P., AINA, T., STONE, D. A., STOTT, P. A., NOZAWA, T., HILBERTS, A. G., LOHMANN, D. & ALLEN, M. R. 2011. Anthropogenic greenhouse gas contribution to flood risk in England and Wales in autumn 2000. *Nature,* 470, 382-5.
PAPPENBERGER, F., BEVEN, K. J., RATTO, M. & MATGEN, P. 2008. Multi-method global sensitivity analysis of flood inundation models. *Advances in Water Resources,* 31, 1-14.
PAPPENBERGER, F., MATGEN, P., BEVEN, K. J., HENRY, J.-B., PFISTER, L. & FRAIPONT, P. 2006. Influence of uncertain boundary conditions and model structure on flood inundation predictions. *Advances in Water Resources,* 29, 1430-1449.
PARK, E. & LATRUBESSE, E. M. 2017. The hydro-geomorphologic complexity of the lower Amazon River floodplain and hydrological connectivity assessed by remote sensing and field control. *Remote Sensing of Environment,* 198, 321-332.
PARK, J. M., LOONEY, C. G. & CHEN, H. C. 2000. Fast connected component labeling algorithm using a divide and conquer technique. *Computers and Their Applications,* 4, 4-7.
PASSALACQUA, P. 2017. The Delta Connectome: A network-based framework for studying connectivity in river deltas. *Geomorphology,* 277, 50-62.
PAUL, F. & HAEBERLI, W. 2008. Spatial variability of glacier elevation changes in the Swiss Alps obtained from two digital elevation models. *Geophysical Research Letters,* 35.
PAVELSKY, T. M. & SMITH, L. C. 2008. RivWidth: A Software Tool for the Calculation of River Widths From Remotely Sensed Imagery. *IEEE Geoscience and Remote Sensing Letters,* 5, 70-73.
PAWLOWICZ, R., BEARDSLEY, B. & LENTZ, S. 2002. Classical tidal harmonic analysis including error estimates in MATLAB using T TIDE. *Computers & Geosciences,* 28, 929-937.
PEBESMA, E. J. 2004. Multivariable geostatistics in S: the gstat package. *Computers & Geosciences,* 30, 683-691.

PEKEL, J. F., COTTAM, A., GORELICK, N. & BELWARD, A. S. 2016. High-resolution mapping of global surface water and its long-term changes. *Nature,* 540, 418-422.
PENDER, G. 2006. Briefing: Introducing the Flood Risk Management Research Consortium. *Proceedings of the Institution of Civil Engineers - Water Management,* 159, 3-8.
PENDER, G. & NEELZ, S. 2007. Use of computer models of flood inundation to facilitate communication in flood risk management. *Environmental Hazards,* 7, 106-114.
PERPINAN LAMIGUEIRO, O. & HIJMANS, R. J. 2018. rasterVis. 0.44 ed.
PHAN, L. K., VAN THIEL DE VRIES, J. S. M. & STIVE, M. J. F. 2015. Coastal Mangrove Squeeze in the Mekong Delta. *Journal of Coastal Research,* 300, 233-243.
PICKUP, G. & WARNER, R. F. 1976. Effects of Hydrologic Regime on Magnitude and Frequency of Dominant Discharge. *Journal of Hydrology,* 29, 51-75.
PIMAN, T., LENNAERTS, T. & SOUTHALACK, P. 2013. Assessment of hydrological changes in the lower Mekong Basin from Basin-Wide development scenarios. *Hydrological Processes,* 27, 2115-2125.
PINEL, S., BONNET, M.-P., SANTOS DA SILVA, J., MOREIRA, D., CALMANT, S., SATGÉ, F. & SEYLER, F. 2015. Correction of Interferometric and Vegetation Biases in the SRTMGL1 Spaceborne DEM with Hydrological Conditioning towards Improved Hydrodynamics Modeling in the Amazon Basin. *Remote Sensing,* 7, 16108-16130.
PLANET 2017. PlanetDEM 30 Plus.
PLAYNE, D. P. & HAWICK, K. 2018. A New Algorithm for Parallel Connected-Component Labelling on GPUs. *IEEE Transactions on Parallel and Distributed Systems,* 29, 1217-1230.
POFF, N. L., BROWN, C. M., GRANTHAM, T. E., MATTHEWS, J. H., PALMER, M. A., SPENCE, C. M., WILBY, R. L., HAASNOOT, M., MENDOZA, G. F., DOMINIQUE, K. C. & BAEZA, A. 2016. Sustainable water management under future uncertainty with eco-engineering decision scaling. *Nature Climate Change,* 6, 25-34.
POPESCU, I. 2012. Theoretical background: unsteady flow. *In:* DI BALDASSARRE, G. (ed.) *Floods in a Changing Climate: Inundation Modelling.* Cambridge: Cambridge University Press.
PRINGLE, C. 2001. Hydrologic Connectivity and the Management of Biological Reserves: A blobal Perspective. *Ecological Applications,* 11, 981-998.
PRINGLE, C. 2003. What is hydrologic connectivity and why is it ecologically important? *Hydrological Processes,* 17, 2685-2689.
PURVIS, M. J., BATES, P. D. & HAYES, C. M. 2008. A probabilistic methodology to estimate future coastal flood risk due to sea level rise. *Coastal Engineering,* 55, 1062-1073.
QUARTEL, S., KROON, A., AUGUSTINUS, P. G. E. F., VAN SANTEN, P. & TRI, N. H. 2007. Wave attenuation in coastal mangroves in the Red River Delta, Vietnam. *Journal of Asian Earth Sciences,* 29, 576-584.
QUINN, N., BATES, P. D. & SIDDALL, M. 2013. The contribution to future flood risk in the Severn Estuary from extreme sea level rise due to ice sheet mass loss. *Journal of Geophysical Research: Oceans,* 118, 5887-5898.
RAAFLAUB, L. D. & COLLINS, M. J. 2006. The effect of error in gridded digital elevation models on the estimation of topographic parameters. *Environmental Modelling & Software,* 21, 710-732.
RABUS, B., EINEDER, M., ROTH, A. & BAMLER, R. 2003. The shuttle radar topography mission—a new class of digital elevation models acquired by spaceborne radar. *ISPRS Journal of Photogrammetry and Remote Sensing,* 57, 241-262.
RÄSÄNEN, T. A., SOMETH, P., LAURI, H., KOPONEN, J., SARKKULA, J. & KUMMU, M. 2017. Observed river discharge changes due to hydropower operations in the Upper Mekong Basin. *Journal of Hydrology,* 545, 28-41.
REES, W. G. 2000. The accuracy of Digital Elevation Models interpolated to higher resolutions. *International Journal of Remote Sensing,* 21, 7-20.
RENAUD, F. G., LE, T. T. H., LINDENER, C., GUONG, V. T. & SEBESVARI, Z. 2015. Resilience and shifts in agro-ecosystems facing increasing sea-level rise and salinity intrusion in Ben Tre Province, Mekong Delta. *Climatic Change,* 133, 69-84.
REUTER, H. I., KERSEBAUM, K. C. & WENDROTH, O. 2005. Modelling of solar radiation influenced by topographic shading—evaluation and application for precision farming. *Physics and Chemistry of the Earth, Parts A/B/C,* 30, 143-149.
REXER, M. & HIRT, C. 2014. Comparison of free high resolution digital elevation data sets (ASTER GDEM2, SRTM v2.1/v4.1) and validation against accurate heights from the Australian National Gravity Database. *Australian Journal of Earth Sciences,* 61, 213-226.

RIJKE, J., VAN HERK, S., ZEVENBERGEN, C. & ASHLEY, R. 2012. Room for the River: delivering integrated river basin management in the Netherlands. *International Journal of River Basin Management,* 10, 369-382.
RINDERER, M., ALI, G. & LARSEN, L. G. 2018. Assessing structural, functional and effective hydrologic connectivity with brain neuroscience methods: State-of-the-art and research directions. *Earth-Science Reviews,* 178, 29-47.
RIZZOLI, P., MARTONE, M., GONZALEZ, C., WECKLICH, C., BORLA TRIDON, D., BRÄUTIGAM, B., BACHMANN, M., SCHULZE, D., FRITZ, T., HUBER, M., WESSEL, B., KRIEGER, G., ZINK, M. & MOREIRA, A. 2017. Generation and performance assessment of the global TanDEM-X digital elevation model. *ISPRS Journal of Photogrammetry and Remote Sensing,* 132, 119-139.
ROBINSON, N., REGETZ, J. & GURALNICK, R. P. 2014. EarthEnv-DEM90: A nearly-global, void-free, multi-scale smoothed, 90m digital elevation model from fused ASTER and SRTM data. *ISPRS Journal of Photogrammetry and Remote Sensing,* 87, 57-67.
RODRIGUEZ, E., MORRIS, C. S. & BELZ, J. E. 2006. A Global Assessment of the SRTM Performance. *Photogrammetric Engineering & Remote Sensing,* 72, 249-260.
ROSENFIELD, A. & PFALTZ, J. L. 1966. Sequential Operations in Digital Picture Processing *Journal of ACM,* 13, 471-494.
ROUGIER, J. & ZAMMIT-MANGION, A. 2016. Visualization for Large-scale Gaussian Updates. *Scandinavian Journal of Statistics,* 43, 1153-1161.
RUBIN, Z. K., KONDOLF, G. M. & CARLING, P. A. 2015. Anticipated geomorphic impacts from Mekong basin dam construction. *International Journal of River Basin Management,* 13, 105-121.
RUDORFF, C. M., MELACK, J. M. & BATES, P. D. 2014. Flooding dynamics on the lower Amazon floodplain: 1. Hydraulic controls on water elevation, inundation extent, and river-floodplain discharge. *Water Resources Research,* 50, 619-634.
SAKAMOTO, T., VAN NGUYEN, N., KOTERA, A., OHNO, H., ISHITSUKA, N. & YOKOZAWA, M. 2007. Detecting temporal changes in the extent of annual flooding within the Cambodia and the Vietnamese Mekong Delta from MODIS time-series imagery. *Remote Sensing of Environment,* 109, 295-313.
SAKSENA, S. & MERWADE, V. 2015. Incorporating the effect of DEM resolution and accuracy for improved flood inundation mapping. *Journal of Hydrology,* 530, 180-194.
SAMELA, C., ALBANO, R., SOLE, A. & MANFREDA, S. 2018. A GIS tool for cost-effective delineation of flood-prone areas. *Computers, Environment and Urban Systems,* 70, 43-52.
SAMELA, C., MANFREDA, S., PAOLA, F. D., GIUGNI, M., SOLE, A. & FIORENTINO, M. 2015. DEM-Based Approaches for the Delineation of Flood-Prone Areas in an Ungauged Basin in Africa. *Journal of Hydrologic Engineering,* 21.
SAMELA, C., TROY, T. J. & MANFREDA, S. 2017. Geomorphic classifiers for flood-prone areas delineation for data-scarce environments. *Advances in Water Resources,* 102, 13-28.
SAMET, H. & TAMMINEN, M. 1986. An improved approach to connected component labeling of images. *International Conference on Computer Vision And Pattern Recognition.*
SAMPSON, C. C., BATES, P. D., NEAL, J. C. & HORRITT, M. S. 2013. An automated routing methodology to enable direct rainfall in high resolution shallow water models. *Hydrological Processes,* 27, 467-476.
SAMPSON, C. C., FEWTRELL, T. J., DUNCAN, A., SHAAD, K., HORRITT, M. S. & BATES, P. D. 2012. Use of terrestrial laser scanning data to drive decimetric resolution urban inundation models. *Advances in Water Resources,* 41, 1-17.
SAMPSON, C. C., SMITH, A. M., BATES, P. D., NEAL, J. C., ALFIERI, L. & FREER, J. E. 2015. A high-resolution global flood hazard model. *Water Resources Research,* 51, 7358-7381.
SAMPSON, C. C., SMITH, A. M., BATES, P. D., NEAL, J. C. & TRIGG, M. A. 2016. Perspectives on Open Access High Resolution Digital Elevation Models to Produce Global Flood Hazard Layers. *Frontiers in Earth Science,* 3.
SANDERS, B. F. 2007. Evaluation of on-line DEMs for flood inundation modeling. *Advances in Water Resources,* 30, 1831-1843.
SANYAL, J., CARBONNEAU, P. & DENSMORE, A. L. 2013. Hydraulic routing of extreme floods in a large ungauged river and the estimation of associated uncertainties: a case study of the Damodar River, India. *Natural Hazards,* 66, 1153-1177.
SAUNDERS, W. 1999. Preparation of DEMs for use in environmental modeling analysis. *ESRI User Conference.* San Diego, CA.

SAVAGE, J., PIANOSI, F., BATES, P., FREER, J. & WAGENER, T. 2016a. Quantifying the importance of spatial resolution and other factors through global sensitivity analysis of a flood inundation model. *Water Resources Research,* 52, 9146-9163.
SAVAGE, J. T. S., BATES, P., FREER, J., NEAL, J. & ARONICA, G. 2016b. When does spatial resolution become spurious in probabilistic flood inundation predictions? *Hydrological Processes,* 30, 2014-2032.
SAYERS, P., PENNING-ROWSELL, E. C. & HORRITT, M. 2018. Flood vulnerability, risk, and social disadvantage: current and future patterns in the UK. *Regional Environmental Change,* 18, 339-352.
SCHALLER, N., KAY, A. L., LAMB, R., MASSEY, N. R., VAN OLDENBORGH, G. J., OTTO, F. E. L., SPARROW, S. N., VAUTARD, R., YIOU, P., ASHPOLE, I., BOWERY, A., CROOKS, S. M., HAUSTEIN, K., HUNTINGFORD, C., INGRAM, W. J., JONES, R. G., LEGG, T., MILLER, J., SKEGGS, J., WALLOM, D., WEISHEIMER, A., WILSON, S., STOTT, P. A. & ALLEN, M. R. 2016. Human influence on climate in the 2014 southern England winter floods and their impacts. *Nature Climate Change,* 6, 627-634.
SCHIRPKE, U., TASSER, E. & TAPPEINER, U. 2013. Predicting scenic beauty of mountain regions. *Landscape and Urban Planning,* 111, 1-12.
SCHMIDT, C. W. 2015. Delta Subsidence: An Imminent Threat to Coastal Populations. *Environ Health Perspect,* 123, A204-9.
SCHMUDDE, T. H. 1968. Floodplain. *In:* FAIRBRUDGE, R. W. (ed.) *The Encyclopaedia of Geomorphology.* Berlin: Springer.
SCHOORL, J. M., SONNEVELD, M. P. W. & VELDKAMP, A. 2000. Three-dimensional landscape process modelling: the effect of DEM resolution. *Earth Surface Processes and Landforms,* 25.
SCHREYER, J., GEIS, C. & LAKES, T. 2016. TanDEM-X for Large-Area Modeling of Urban Vegetation Height: Evidence from Berlin, Germany. *IEEE Journal of Selected Topics in Applied Earth Observations and Remote Sensing,* 9, 1876-1887.
SCHUMANN, G., MATGEN, P., HOFFMANN, L., HOSTACHE, R., PAPPENBERGER, F. & PFISTER, L. 2007. Deriving distributed roughness values from satellite radar data for flood inundation modelling. *Journal of Hydrology,* 344, 96-111.
SCHUMANN, G. J. P., BATES, P., NEAL, J. & ANDREADIS, K. M. 2014. Technology: Fight floods on a global scale. *Nature,* 507, 169.
SCHUMANN, G. J. P., NEAL, J. C., VOISIN, N., ANDREADIS, K. M., PAPPENBERGER, F., PHANTHUWONGPAKDEE, N., HALL, A. C. & BATES, P. D. 2013. A first large-scale flood inundation forecasting model. *Water Resources Research,* 49, 6248-6257.
SCHURR, F. M., PAGEL, J., CABRAL, J. S., GROENEVELD, J., BYKOVA, O., O'HARA, R. B., HARTIG, F., KISSLING, W. D., LINDER, H. P., MIDGLEY, G. F., SCHRÖDER, B., SINGER, A. & ZIMMERMANN, N. E. 2012. How to understand species' niches and range dynamics: a demographic research agenda for biogeography. *Journal of Biogeography,* 39, 2146-2162.
SCHWARTZ, J., SHARJR, M. & SIEGEL, A. 1985. An efficient algorithm for finding connected components in a binary image. New York University Robotics Research Tech Report.
SCOWN, M. W., THOMS, M. C. & DE JAGER, N. R. 2016. An index of floodplain surface complexity. *Hydrology and Earth System Sciences,* 20, 431-441.
SEPA 2011. Natural Flood Management Handbook. Stirling: Scottish Environmental Protection Agency.
SETO, K. C. 2011. Exploring the dynamics of migration to mega-delta cities in Asia and Africa: Contemporary drivers and future scenarios. *Global Environmental Change,* 21, S94-S107.
SHAMSUDDUHA, M., MARZEN, L. J., UDDIN, A., LEE, M. K. & SAUNDERS, J. A. 2008. Spatial relationship of groundwater arsenic distribution with regional topography and water-table fluctuations in the shallow aquifers in Bangladesh. *Environmental Geology,* 57.
SHAN, J. & TOTH, E. (eds.) 2008. *Topographic laser ranging and scanning, principles and processing,* Boca Raton, FL: Taylor & Francis.
SHEFFER, N. A., ENZEL, Y., BENITO, G., GRODEK, T., POART, N., LANG, M., NAULET, R. & CŒUR, D. 2003. Paleofloods and historical floods of the Ardèche River, France. *Water Resources Research,* 39.
SHI, X., GIROD, L., LONG, R., DEKETT, R., PHILIPPE, J. & BURKE, T. 2012. A comparison of LiDAR-based DEMs and USGS-sourced DEMs in terrain analysis for knowledge-based digital soil mapping. *Geoderma,* 170, 217-226.
SHORTRIDGE, A. 2006. Shuttle Radar Topography Mission Elevation Data Error and Its Relationship to Land Cover. *Cartography and Geographic Information Science,* 33, 65-75.

SHORTRIDGE, A. & MESSINA, J. 2011. Spatial structure and landscape associations of SRTM error. *Remote Sensing of Environment,* 115, 1576-1587.
SIEBERT, S., KUMMU, M., PORKKA, M., DÖLL, P., RAMANKUTTY, N. & SCANLON, B. R. 2015. A global data set of the extent of irrigated land from 1900 to 2005. *Hydrology and Earth System Sciences,* 19, 1521-1545.
SIMARD, M., PINTO, N., FISHER, J. B. & BACCINI, A. 2011. Mapping forest canopy height globally with spaceborne lidar. *Journal of Geophysical Research,* 116.
SMAJGL, A., TOAN, T. Q., NHAN, D. K., WARD, J., TRUNG, N. H., TRI, L. Q., TRI, V. P. D. & VU, P. T. 2015. Responding to rising sea levels in the Mekong Delta. *Nature Climate Change,* 5, 167-174.
SMITH, A., SAMPSON, C. & BATES, P. 2015. Regional flood frequency analysis at the global scale. *Water Resources Research,* 51, 539-553.
SMITH, M. J. & CLARK, C. D. 2005. Methods for the visualization of digital elevation models for landform mapping. *Earth Surface Processes and Landforms,* 30, 885-900.
SMITH, N. D., PÉREZ-ARLUCEA, M., EDMONDS, D. A. & SLINGERLAND, R. L. 2009. Elevation adjustments of paired natural levees during flooding of the Saskatchewan River. *Earth Surface Processes and Landforms,* 34, 1060-1068.
SMITH, R. A. E., BATES, P. D. & HAYES, C. 2011. Evaluation of a coastal flood inundation model using hard and soft data. *Environmental Modelling & Software*.
SOH, Y., ASHRAF, H., HAE, Y. & KIM, I. 2014. Fast parallel connected component labeling algorithms using CUDA based on 8-directional label selection. *International Journal of Latest Research in Science and Technology,* 3, 187-190.
SØRENSEN, R. & SEIBERT, J. 2007. Effects of DEM resolution on the calculation of topographical indices: TWI and its components. *Journal of Hydrology,* 347, 79-89.
SRINIVASEN, M., PETERSON, C., ANDRAL, A., DEJUS, M., HOSSAIN, F., CRETEAUX, J.-F. & BEIGHLEY, E. 2014. SWOT Applications Plan. 1 ed.: NASA Jet Propulsion Laboratory.
STATISTICS, F. B. O. 2010. Fiji Census of Population and Housing. Suva, Fiji: Fiji Bureau of Statistics.
STATISTICS, F. B. O. 2018. Population of Towns and Areas by Sex (2007 census).
STEPHENS, E., SCHUMANN, G. & BATES, P. 2014. Problems with binary pattern measures for flood model evaluation. *Hydrological Processes,* 28, 4928-4937.
STIEGLITZ, M., SHAMAN, J., MCNAMARA, J., ENGEL, V., SHANLEY, J. & KLING, G. W. 2003. An approach to understanding hydrologic connectivity on the hillslope and the implications for nutrient transport. *Global Biogeochemical Cycles,* 17, n/a-n/a.
STRICK, R. J. P. 2016. *Floodplain Geomorphology and Topography in Large Rivers.* Doctor of Philosophy, University of Brighton.
STRICK, R. J. P., ASHWORTH, P. J., AWCOCK, G. & LEWIN, J. 2018. Morphology and spacing of river meander scrolls. *Geomorphology,* 310, 57-68.
SU, Y., GUO, Q., MA, Q. & LI, W. 2015. SRTM DEM Correction in Vegetated Mountain Areas through the Integration of Spaceborne LiDAR, Airborne LiDAR, and Optical Imagery. *Remote Sensing,* 7, 11202-11225.
SUWANDANA, E., KAWAMURA, K., SAKUNO, Y., KUSTIYANTO, E. & RAHARJO, B. 2012. Evaluation of ASTER GDEM2 in Comparison with GDEM1, SRTM DEM and Topographic-Map-Derived DEM Using Inundation Area Analysis and RTK-dGPS Data. *Remote Sensing,* 4, 2419-2431.
SUZUKI, K., HORIBA, I. & SUGIE, N. 2003. Linear-time connected-component labeling based on sequential local operations. *Computer Vision and Image Understanding,* 89, 1-23.
SYVITSKI, J. P. M., KETTNER, A. J., OVEREEM, I., HUTTON, E. W. H., HANNON, M. T., BRAKENRIDGE, G. R., DAY, J., VÖRÖSMARTY, C., SAITO, Y., GIOSAN, L. & NICHOLLS, R. J. 2009. Sinking deltas due to human activities. *Nature Geoscience,* 2, 681-686.
SYVITSKI, J. P. M., OVEREEM, I., BRAKENRIDGE, G. R. & HANNON, M. 2012. Floods, floodplains, delta plains — A satellite imaging approach. *Sedimentary Geology,* 267-268, 1-14.
SYVITSKI, J. P. M. & SAITO, Y. 2007. Morphodynamics of deltas under the influence of humans. *Global and Planetary Change,* 57, 261-282.
SZABO, S., BRONDIZIO, E., RENAUD, F. G., HETRICK, S., NICHOLLS, R. J., MATTHEWS, Z., TESSLER, Z., TEJEDOR, A., SEBESVARI, Z., FOUFOULA-GEORGIOU, E., DA COSTA, S. & DEARING, J. A. 2016. Population dynamics, delta vulnerability and environmental change: comparison of the Mekong, Ganges–Brahmaputra and Amazon delta regions. *Sustainability Science,* 11, 539-554.

TACHIKAWA, T., HATO, M., KAKU, M. & IWASAKI, A. 2011a. Characteristics of ASTER GDEM version 2. *Geoscience and remote sensing symposium (IGARSS).* IEEE.
TACHIKAWA, T., KAKU, M., IWASAKI, A., GESCH, D. B., OIMOEN, M., ZHANG, Z., DANIELSON, J. J., KRIEGER, T., CURTIS, B., HAASE, J., ABRAMS, M., CRIPPEN, R. & CARABAJAL, C. C. 2011b. ASTER Global Digital Elevation Model Version 2 – Summary of Validation Results. NASA.
TADONO, T., ISHIDA, H., ODA, F., NAITO, S., MINAKAWA, K. & IWAMOTO, H. 2014. Precise Global DEM Generation by ALOS PRISM. *ISPRS Annals of Photogrammetry, Remote Sensing and Spatial Information Sciences,* II-4, 71-76.
TADONO, T., NAGAI, H., ISHIDA, H., ODA, F., NAITO, S., MINAKAWA, K. & IWAMOTO, H. 2016. Generation of the 30 M-Mesh Global Digital Surface Model by Alos Prism. *ISPRS - International Archives of the Photogrammetry, Remote Sensing and Spatial Information Sciences,* XLI-B4, 157-162.
TAKAGI, H., THAO, N. & ANH, L. 2016. Sea-Level Rise and Land Subsidence: Impacts on Flood Projections for the Mekong Delta's Largest City. *Sustainability,* 8.
TAKAGI, H., THAO, N., ESTEBAN, M., TAM, T. T., KNAEPEN, H. L., MIKAMI, T. & YAMAMOTO, L. 2013. Coastal Disaster Risk in Southern Vietnam: The Problems of Coastal Development and the Need for Better Coastal Planning. *Background Paper prepared for the Global Assessment Report on Disaster Risk Reduction 2013.* Geneva, Switzerland: UNISDR.
TAKAKU, J. & TADONO, T. Quality updates of 'AW3D' global DSM generated from ALOS PRISM. Geoscience and remote Sensing Symposium (IGARSS), 2017 Fort Worth, TX, USA. IEEE.
TAKAKU, J., TADONO, T., TSUTSUI, K. & ICHIKAWA, M. 2016. Validation of "Aw3d" Global Dsm Generated from Alos Prism. *ISPRS Annals of Photogrammetry, Remote Sensing and Spatial Information Sciences,* III-4, 25-31.
TALAGRAND, O., VAUTARD, R. & STRAUSS, B. 1997. Evaluation of probabilistic prediction systems. *ECMWF Workshop on Predictability.* Reading, United Kingdom.
TARAKEGN, T. H. & SAYAMA, T. 2013. Correction of SRTM artefacts by fourier transform for flood inundation modelling. *Journal of Japan Society of Civil Engineers, Ser. B1 (Hydraulic Engineering),* 69, 193-I.
TARPANELLI, A., BROCCA, L., MELONE, F. & MORAMARCO, T. 2013. Hydraulic modelling calibration in small rivers by using coarse resolution synthetic aperture radar imagery. *Hydrological Processes,* 27, 1321-1330.
TAYLOR, J. 1997. *Introduction to error analysis, the study of uncertainties in physical measurements,* Sausalito, CA, University Science Books.
TEAM, R. C. 2018. R: A Language and Environment for Statistical Computing. 3.4.4 ed. Vienna, Austria: R Foundation for Statistical Computing.
TENG, J., JAKEMAN, A. J., VAZE, J., CROKE, B. F. W., DUTTA, D. & KIM, S. 2017. Flood inundation modelling: A review of methods, recent advances and uncertainty analysis. *Environmental Modelling & Software,* 90, 201-216.
TERRY, J. P. 2007. River Hydrology & Floods. *Tropical Cyclones: Climatology and Impacts in the South Pacific.* Springer.
TERRY, J. P., GARIMELLA, S. & KOSTASCHUK, R. A. 2002. Rates of floodplain accretion in a tropical island river system impacted by cyclones and large floods. *Geomorphology,* 42, 171-182.
TESSLER, Z. D., VOROSMARTY, C. J., GROSSBERG, M., GLADKOVA, I., AIZENMAN, H., SYVITSKI, J. P. & FOUFOULA-GEORGIOU, E. 2015. ENVIRONMENTAL SCIENCE. Profiling risk and sustainability in coastal deltas of the world. *Science,* 349, 638-43.
TETZLAFF, D., SOULSBY, C., BACON, P. J., YOUNGSON, A. F., GIBBINS, C. & MALCOLM, I. A. 2007. Connectivity between landscapes and riverscapes—a unifying theme in integrating hydrology and ecology in catchment science? *Hydrological Processes,* 21, 1385-1389.
THOMAS, B. 2012. Nadi LiDAR Survey Report for the Secretariat of the South Pacific Community Applied Geoscience and Technology Division (SOPAC). Suva, Fiji: Network Mapping Aerial Laser Survey.
THOMAS, I. A., JORDAN, P., SHINE, O., FENTON, O., MELLANDER, P. E., DUNLOP, P. & MURPHY, P. N. C. 2017. Defining optimal DEM resolutions and point densities for modelling hydrologically sensitive areas in agricultural catchments dominated by microtopography. *International Journal of Applied Earth Observation and Geoinformation,* 54, 38-52.
THOMPSON, J. A., BELL, J. C. & BUTLER, C. A. 2001. Digital elevation model resolution: effects on terrain attribute calculation and quantitative soil-landscape modeling. *Geoderma,* 100, 67-89.

TOBLER, W. R. 1970. A computer movie simulating urban growth in the Detroit Region. *Economic Geography,* 46, 234-240.
TOCKNER, K., F, M. & WARD, J. V. 2000. An extension of the flood pulse concept. *Hydrological Processes,* 14, 2861-2883.
TOCKNER, K., PENNETZDORFER, D., REINER, N., SCHIEMER, F. & WARD, J. V. 1999. Hydrological connectivity, and the exchange of organic matter and nutrients in a dynamic river–floodplain system (Danube, Austria). *Freshwater Biology,* 41, 521-535.
TOCKNER, K. & STANFORD, J. A. 2002. Riverine flood plains: present state and future trends. *Environmental Conservation,* 29.
TRAN, D. D., VAN HALSEMA, G., HELLEGERS, P., LUDWIG, F. & WYATT, A. 2018a. Questioning triple rice intensification on the Vietnamese mekong delta floodplains: An environmental and economic analysis of current land-use trends and alternatives. *J Environ Manage,* 217, 429-441.
TRAN, D. D., VAN HALSEMA, G., HELLEGERS, P. J. G. J., LUDWIG, F. & SEIJGER, C. 2018b. Stakeholders' assessment of dike-protected and flood-based alternatives from a sustainable livelihood perspective in An Giang Province, Mekong Delta, Vietnam. *Agricultural Water Management,* 206, 187-199.
TRAN, D. D. & WEGER, J. 2017. Barriers to Implementing Irrigation and Drainage Policies in An Giang Province, Mekong Delta, Vietnam. *Irrigation and Drainage*.
TRI, V. K. 2012. Hydrology and hydraulic infrastructure systems in the Mekong Delta, Vietnam. *The Mekong Delta System.* Dordrecht: Springer.
TRI, V. P. D., TRUNG, N. H. & THANH, V. Q. 2013. Vulnerability to Flood in the Vietnamese Mekong Delta: Mapping and Uncertainty Assessment. *Journal of Environmental Science and Engineering* B, 229-237.
TRIET, N. V. K., DUNG, N. V., FUJII, H., KUMMU, M., MERZ, B. & APEL, H. 2017. Has dyke development in the Vietnamese Mekong Delta shifted flood hazard downstream? *Hydrology and Earth System Sciences,* 21, 3991-4010.
TRIGG, M. A., BATES, P. D., WILSON, M. D., SCHUMANN, G. & BAUGH, C. 2012. Floodplain channel morphology and networks of the middle Amazon River. *Water Resources Research,* 48.
TRIGG, M. A., BIRCH, C. E., NEAL, J. C., BATES, P. D., SMITH, A., SAMPSON, C. C., YAMAZAKI, D., HIRABAYASHI, Y., PAPPENBERGER, F., DUTRA, E., WARD, P. J., WINSEMIUS, H. C., SALAMON, P., DOTTORI, F., RUDARI, R., KAPPES, M. S., SIMPSON, A. L., HADZILACOS, G. & FEWTRELL, T. J. 2016. The credibility challenge for global fluvial flood risk analysis. *Environmental Research Letters,* 11.
TRIGG, M. A., MICHAELIDES, K., NEAL, J. C. & BATES, P. D. 2013. Surface water connectivity dynamics of a large scale extreme flood. *Journal of Hydrology,* 505, 138-149.
TURNBULL, L., WAINWRIGHT, J. & BRAZIER, R. E. 2008. A conceptual framework for understanding semi-arid land degradation: ecohydrological interactions across multiple-space and time scales. *Ecohydrology,* 1, 23-34.
UNISDR 2015. The Human Cost of Weather Related Disasters. Geneva: UNISDR.
UYSAL, M., TOPRAK, A. S. & POLAT, N. 2015. DEM generation with UAV Photogrammetry and accuracy analysis in Sahitler hill. *Measurement,* 73, 539-543.
VAN DE SANDE, B., LANSEN, J. & HOYNG, C. 2012. Sensitivity of Coastal Flood Risk Assessments to Digital Elevation Models. *Water,* 4, 568-579.
VAN NIEL, K. P., LAFFAN, S. W. & LEES, B. 2004. Effect of error in the DEM on environmental variables for predictive vegetation modelling. *Journal of Vegetation Science,* 15, 747-756.
VAN, P. D. T., POPESCU, I., VAN GRIENSVEN, A., SOLOMATINE, D. P., TRUNG, N. H. & GREEN, A. 2012. A study of the climate change impacts on fluvial flood propagation in the Vietnamese Mekong Delta. *Hydrology and Earth System Sciences,* 16, 4637-4649.
VAN STAVEREN, M. F., VAN TATENHOVE, J. P. M. & WARNER, J. F. 2018. The tenth dragon: controlled seasonal flooding in long-term policy plans for the Vietnamese Mekong delta. *Journal of Environmental Policy & Planning,* 20, 267-281.
VARGA, M. & BAŠIĆ, T. 2015. Accuracy validation and comparison of global digital elevation models over Croatia. *International Journal of Remote Sensing,* 36, 170-189.
VAZE, J., TENG, J. & SPENCER, G. 2010. Impact of DEM accuracy and resolution on topographic indices. *Environmental Modelling & Software,* 25, 1086-1098.
VEREGIN, H. 1997. The Effects of Vertical Error in Digital Elevation Models on the Determination of Flow-path Direction. *Cartography and Geographic Information Systems,* 24, 67-79.

VIDON, P. G. F. & HILL, A. R. 2004. Landscape controls on the hydrology of stream riparian zones. *Journal of Hydrology,* 292, 210-228.
VIETNAM, K. O. T. N. A. T. S. R. O. 2013. Mekong Delta Plan.
WAHL, T., JAIN, S., BENDER, J., MEYERS, S. D. & LUTHER, M. E. 2015. Increasing risk of compound flooding from storm surge and rainfall for major US cities. *Nature Climate Change,* 5, 1093-1097.
WAINWRIGHT, J., TURNBULL, L., IBRAHIM, T. G., LEXARTZA-ARTZA, I., THORNTON, S. F. & BRAZIER, R. E. 2011. Linking environmental régimes, space and time: Interpretations of structural and functional connectivity. *Geomorphology,* 126, 387-404.
WALKER, W. S., KELLNDORFER, J. M. & PIERCE, L. E. 2007. Quality assessment of SRTM C- and X-band interferometric data: Implications for the retrieval of vegetation canopy height. *Remote Sensing of Environment,* 106, 428-448.
WANG, W., YANG, X. & YAO, T. 2012. Evaluation of ASTER GDEM and SRTM and their suitability in hydraulic modelling of a glacial lake outburst flood in southeast Tibet. *Hydrological Processes,* 26, 213-225.
WARD, D. P., HAMILTON, S. K., JARDINE, T. D., PETTIT, N. E., TEWS, E. K., OLLEY, J. M. & BUNN, S. E. 2013a. Assessing the seasonal dynamics of inundation, turbidity, and aquatic vegetation in the Australian wet-dry tropics using optical remote sensing. *Ecohydrology,* 6, 312-323.
WARD, J. & STANFORD, J. A. 1995. Ecological connectivity in alluvial river ecosystems and its disruption by flow regulation. *Regulated Rivers: research & management,* 11, 105-119.
WARD, J. V. 1989. The four-dimensional nature of lotic ecosystems. *Journal of the North American Benthological Society,* 8, 2-8.
WARD, P. J., JONGMAN, B., WEILAND, F. S., BOUWMAN, A., VAN BEEK, R., BIERKENS, M. F. P., LIGTVOET, W. & WINSEMIUS, H. C. 2013b. Assessing flood risk at the global scale: model setup, results, and sensitivity. *Environmental Research Letters,* 8.
WASSMANN, R., HIEN, N. X., HOANH, C. T. & TUONG, T. P. 2004. Sea Level Rise Affecting the Vietnamese Mekong Delta: Water Elevation in the Flood Season and Implications for Rice Production. *Climatic Change,* 66, 89-107.
WECHSLER, S. P. 2000. *Effect of DEM Uncertainty on Topographic Parameters.* PhD Thesis, State University of New York.
WECHSLER, S. P. 2003. Perceptions of digital elevation model uncertainty by DEM users. *URISA-Washington DC,* 15, 57-64.
WECHSLER, S. P. 2007. Uncertainties associated with digital elevation models for hydrologic applications: a review. *Hydrology and Earth System Sciences,* 11, 1481-1500.
WECHSLER, S. P. & KNOLL, C. N. 2006. Quantifying DEM Uncertainty and its Effect on Topographic Parameters. *Photogrammetric Engineering & Remote Sensing,* 9, 1081-1090.
WENDI, D., LIONG, S.-Y., SUN, Y. & DOAN, C. D. 2016. An innovative approach to improve SRTM DEM using multispectral imagery and artificial neural network. *Journal of Advances in Modeling Earth Systems,* 8, 691-702.
WESSEL, B., HUBER, M., WOHLFART, C., MARSCHALK, U., KOSMANN, D. & ROTH, A. 2018. Accuracy assessment of the global TanDEM-X Digital Elevation Model with GPS data. *ISPRS Journal of Photogrammetry and Remote Sensing,* 139, 171-182.
WEST, H., HORSWELL, M. & QUINN, N. 2018. Exploring the sensitivity of coastal inundation modelling to DEM vertical error. *International Journal of Geographical Information Science,* 32, 1172-1193.
WESTER, T., WASKLEWICZ, T. & STALEY, D. 2014. Functional and structural connectivity within a recently burned drainage basin. *Geomorphology,* 206, 362-373.
WESTERN, A. W., BLÖSCHL, G. & GRAYSON, R. B. 2001. Toward capturing hydrologically significant connectivity in spatial patterns. *Water Resources Research,* 37, 83-97.
WEYDAHL, D. J., SAGSTUEN, J., DICK, Ø. B. & RØNNING, H. 2007. SRTM DEM accuracy assessment over vegetated areas in Norway. *International Journal of Remote Sensing,* 28, 3513-3527.
WIDAYATI, A., LUSIANA, B., SUYAMTO, D. & VERBIST, B. 2004. Uncertainty and Effects of Resolution of Digital Elelvation Model and its Derived Features: Case Study of Sumberjaya, Sumatera, Indonesia. *International Archives of Photogrammetry Remote Sensing* 25, 1013-1018.
WILKINS, R. W., HODGES, D. A., LAURIENTI, P. J., STEEN, M. & BURDETTE, J. H. 2014. Network science and the effects of music preference on functional brain connectivity: from Beethoven to Eminem. *Sci Rep,* 4, 6130.

WILKS, D. S. 2011. *Statistical methods in the atmospheric sciences,* Oxford, Elsevier.
WILLIAMS, G. P. 1978. Bankfull discharge of rivers. *Water Resources Research,* 14, 1141-1154.
WILSON, J. P. 2012. Digital terrain modeling. *Geomorphology,* 137, 107-121.
WILSON, M., BATES, P., ALSDORF, D., FORSBERG, B., HORRITT, M., MELACK, J., FRAPPART, F. & FAMIGLIETTI, J. 2007. Modeling large-scale inundation of Amazonian seasonally flooded wetlands. *Geophysical Research Letters,* 34.
WILSON, M. D. & ATKINSON, P. M. 2005. Prediction Uncertainty in Elevation and its Effect on Flood Inundation Modelling. *In:* ATKINSON, P. M., FOODY, G. M., DARBY, S. & WU, F. (eds.) *Geodynamics.* Andover: CRC Press.
WILSON, M. D. & ATKINSON, P. M. 2007. The use of remotely sensed land cover to derive floodplain friction coefficients for flood inundation modelling. *Hydrological Processes,* 21, 3576-3586.
WING, O. E. J., BATES, P. D., SAMPSON, C. C., SMITH, A. M., JOHNSON, K. A. & ERICKSON, T. A. 2017. Validation of a 30 m resolution flood hazard model of the conterminous United States. *Water Resources Research,* 53, 7968-7986.
WING, O. E. J., BATES, P. D., SMITH, A. M., SAMPSON, C. C., JOHNSON, K. A., FARGIONE, J. & MOREFIELD, P. 2018. Estimates of present and future flood risk in the conterminous United States. *Environmental Research Letters,* 13.
WINSEMIUS, H. C., AERTS, JEROEN C. J. H., VAN BEEK, LUDOVICUS P. H., BIERKENS, MARC F. P., BOUWMAN, A., JONGMAN, B., KWADIJK, JAAP C. J., LIGTVOET, W., LUCAS, PAUL L., VAN VUUREN, DETLEF P. & WARD, PHILIP J. 2015. Global drivers of future river flood risk. *Nature Climate Change,* 6, 381-385.
WISDOM 2016. WISDOM Project Dataset. *In:* CENTER, G. A. (ed.).
WISE, S. 2000. Assessing the quality for hydrological applications of digital elevation models derived from contours. *Hydrological Processes,* 14, 1909-1929.
WISE, S. 2007. Effect of differing DEM creation methods on the results from a hydrological model. *Computers & Geosciences,* 33, 1351-1365.
WISE, S. 2011. Cross-validation as a means of investigating DEM interpolation error. *Computers & Geosciences,* 37, 978-991.
WOHL, E. 2017. Connectivity in rivers. *Progress in Physical Geography,* 41, 345-362.
WOLOCK, D. M. & PRICE, C. V. 1994. Effects of digital elevation model map scale and data resolution on a topography-based watershed model. *Water Resources Research,* 30, 3041-3052.
WONG, J. S., FREER, J. E., BATES, P. D., SEAR, D. A. & STEPHENS, E. M. 2015. Sensitivity of a hydraulic model to channel erosion uncertainty during extreme flooding. *Hydrological Processes,* 29, 261-279.
WOOD, M., HOSTACHE, R., NEAL, J., WAGENER, T., GIUSTARINI, L., CHINI, M., CORATO, G., MATGEN, P. & BATES, P. 2016. Calibration of channel depth and friction parameters in the LISFLOOD-FP hydraulic model using medium-resolution SAR data and identifiability techniques. *Hydrology and Earth System Sciences,* 20, 4983-4997.
WOODROW, K., LINDSAY, J. B. & BERG, A. A. 2016. Evaluating DEM conditioning techniques, elevation source data, and grid resolution for field-scale hydrological parameter extraction. *Journal of Hydrology,* 540, 1022-1029.
WU, K., OTOO, E. & SHOSHANI, A. 2005. Optimizing Connected Component Labeling Algorithms. *Medical Imaging 2005: Image Processing,* 5747, 1965-1977.
WU, K., OTOO, E. & SUZUKI, K. 2009. Optimizing two-pass connected-component labeling algorithms. *Pattern Analysis and Applications,* 12, 117-135.
WU, S., LI, J. & HUANG, G. H. 2008. A study on DEM-derived primary topographic attributes for hydrologic applications: Sensitivity to elevation data resolution. *Applied Geography,* 28, 210-223.
YAMAZAKI, D., BAUGH, C. A., BATES, P. D., KANAE, S., ALSDORF, D. E. & OKI, T. 2012. Adjustment of a spaceborne DEM for use in floodplain hydrodynamic modeling. *Journal of Hydrology,* 436-437, 81-91.
YAMAZAKI, D., IKESHIMA, D., TAWATARI, R., YAMAGUCHI, T., O'LOUGHLIN, F., NEAL, J. C., SAMPSON, C. C., KANAE, S. & BATES, P. D. 2017. A high-accuracy map of global terrain elevations. *Geophysical Research Letters*.
YAMAZAKI, D., O'LOUGHLIN, F., TRIGG, M. A., MILLER, Z. F., PAVELSKY, T. M. & BATES, P. D. 2014a. Development of the Global Width Database for Large Rivers. *Water Resources Research,* 50, 3467-3480.

YAMAZAKI, D., SATO, T., KANAE, S., HIRABAYASHI, Y. & BATES, P. D. 2014b. Regional flood dynamics in a bifurcating mega delta simulated in a global river model. *Geophysical Research Letters,* 41, 3127-3135.
YAN, K., DI BALDASSARRE, G., SOLOMATINE, D. P. & SCHUMANN, G. J. P. 2015a. A review of low-cost space-borne data for flood modelling: topography, flood extent and water level. *Hydrological Processes,* 29, 3368-3387.
YAN, K., TARPANELLI, A., BALINT, G., MORAMARCO, T. & BALDASSARRE, G. D. 2015b. Exploring the Potential of SRTM Topography and Radar Altimetry to Support Flood Propagation Modeling: Danube Case Study. *Journal of Hydrologic Engineering,* 20, 04014048.
YANG, P., AMES, D. P., FONSECA, A., ANDERSON, D., SHRESTHA, R., GLENN, N. F. & CAO, Y. 2014. What is the effect of LiDAR-derived DEM resolution on large-scale watershed model results? *Environmental Modelling & Software,* 58, 48-57.
YEO, S. 2015. Refining the historical flood series for Ba, Fiji. *Risk Frontiers Technical Report.* Australia: Macquarie University,.
YILMAZ, M., USUL, N. & AKYUREK, A. 2004. Modeling the propagation of DEM uncertainty in flood inundation. *ESRI User Conference.*
YOON, Y., DURAND, M., MERRY, C. J., CLARK, E. A., ANDREADIS, K. M. & ALSDORF, D. E. 2012. Estimating river bathymetry from data assimilation of synthetic SWOT measurements. *Journal of Hydrology,* 464-465, 363-375.
YU, D. & LANE, S. N. 2006. Urban fluvial flood modelling using a two-dimensional diffusion-wave treatment, part 1: mesh resolution effects. *Hydrological Processes,* 20, 1541-1565.
YU, D. & LANE, S. N. 2011. Interactions between subgrid-scale resolution, feature representation and grid-scale resolution in flood inundation modelling. *Hydrological Processes,* 25, 36-53.
ZANCHI, A., FRANCESCA, S., STEFANO, Z., SIMONE, S. & GRAZIANO, G. 2009. 3D reconstruction of complex geological bodies: Examples from the Alps. *Computers & Geosciences,* 35, 49-69.
ZANDBERGEN, P. A. 2008. Positional Accuracy of Spatial Data: Non-Normal Distributions and a Critique of the National Standard for Spatial Data Accuracy. *Transactions in GIS,* 12, 103-130.
ZANDBERGEN, P. A. 2010. Accuracy Considerations in the Analysis of Depressions in Medium-Resolution Lidar DEMs. *GIScience & Remote Sensing,* 47, 187-207.
ZANOBETTI, D., LONGERÉ, H., PREISSMANN, A. & CUNGE, J. A. 1970. Mekong delta mathematical model program construction. *American Society of Civil Engineers, Journal of the Waterways and Harbors Division 96*, 181-199.
ZEBKER, H. A. & GOLDSTEIN, R. M. 1986. Topographic mapping from interferometric synthetic aperture radar observations. *Journal of Geophysical Research,* 91.
ZEVENBERGEN, C., RIJKE, J., VAN HERK, S., LUDY, J. & ASHLEY, R. 2013. Room for the River: International relevance. *Water Governance,* 3.
ZHANG, J. & GOODCHILD, M. F. 2002. *Uncertainty in Geographical Information,* London, Taylor & Francis.
ZHANG, J. X., CHANG, K. T. & WU, J. Q. 2008. Effects of DEM resolution and source on soil erosion modelling: a case study using the WEPP model. *International Journal of Geographical Information Science,* 22, 925-942.
ZHANG, K., LIU, H., LI, Y., XU, H., SHEN, J., RHOME, J. & SMITH, T. J. 2012. The role of mangroves in attenuating storm surges. *Estuarine, Coastal and Shelf Science,* 102-103, 11-23.
ZHANG, W. & MONTGOMERY, D. R. 1994. Digital elevation model grid size, landscape representation, and hydrologic simulations. *Water Resources Research,* 30, 1019-1028.
ZHANG, X., DRAKE, N. A., WAINWRIGHT, J. & MULLIGAN, M. 1999. Comparison of slope estimates from low resolution DEMs: Scaling issues and a fractal method for their solution. *Earth Surface Processes and Landforms,* 24, 763-779.
ZHANG, Y., XIAN, C., CHEN, H., GRIENEISEN, M. L., LIU, J. & ZHANG, M. 2016. Spatial interpolation of river channel topography using the shortest temporal distance. *Journal of Hydrology,* 542, 450-462.
ZHAO, T., SHAO, Q. & ZHANG, Y. 2017. Deriving Flood-Mediated Connectivity between River Channels and Floodplains: Data-Driven Approaches. *Sci Rep,* 7, 43239.
ZHAO, X., HE, L., YAO, B. & CHAO, Y. 2015. A New Connected-Component Labeling Algorithm. *IEICE Transactions on Information and Systems,* E98.D, 2013-2016.
ZHAO, X., SU, Y., HU, T., CHEN, L., GAO, S., WANG, R., JIN, S. & GUO, Q. 2018. A global corrected SRTM DEM product for vegetated areas. *Remote Sensing Letters,* 9, 393-402.

ZHOU, H., SUN, J., TURK, G. & REHG, J. M. 2007. Terrain synthesis from digital elevation models. *IEEE Trans Vis Comput Graph,* 13, 834-48.
ZISCHG, A. 2018. Floodplains and Complex Adaptive Systems—Perspectives on Connecting the Dots in Flood Risk Assessment with Coupled Component Models. *Systems,* 6.
ZSCHEISCHLER, J., WESTRA, S., VAN DEN HURK, B. J. J. M., SENEVIRATNE, S. I., WARD, P. J., PITMAN, A., AGHAKOUCHAK, A., BRESCH, D. N., LEONARD, M., WAHL, T. & ZHANG, X. 2018. Future climate risk from compound events. *Nature Climate Change,* 8, 469-477.